

DOCTORAL THESIS

Development of Ti-Eggshell Composite for Bio-Implants Applications

Riddhi Hirenkumar Shukla

TALLINN UNIVERSITY OF TECHNOLOGY
DOCTORAL THESIS
10/2025

Development of Ti-Eggshell Composite for Bio-Implants Applications

RIDDHI HIRENKUMAR SHUKLA



TALLINN UNIVERSITY OF TECHNOLOGY

School of Engineering

Department of Mechanical and Industrial Engineering

This dissertation was accepted for the defence of the degree 13/01/2025

Supervisor:

Prof. Prashanth Konda Gokuldoss
Department of Mechanical and Industrial Engineering
Tallinn University of Technology
Tallinn, Estonia

Opponents:

Prof. Jürgen Eckert
Erich Schmid Institute of Materials Science
Austrian Academy of Sciences
Leoben, Austria

Prof Geethapriyan Thangamani
Department of Applied Science and Technology
Politecnico di Torino
Torino, Italy

Defence of the thesis: 21/02/2025, Tallinn

Declaration:

Hereby I declare that this doctoral thesis, my original investigation and achievement, submitted for the doctoral degree at Tallinn University of Technology has not been submitted for a doctoral or equivalent academic degree.

Riddhi Shukla

signature



European Union
European Regional
Development Fund



Investing
in your future

Copyright: Riddhi Hirenkumar Shukla, 2025

ISSN 2585-6898 (publication)

ISBN 978-9916-80-255-7 (publication)

ISSN 2585-6901 (PDF)

ISBN 978-9916-80-256-4 (PDF)

DOI <https://doi.org/10.23658/taltech.10/2025>

Printed by Koopia Niini & Rauam

Shukla, R. (2025). *Development of Ti-Eggshell Composite for Bio-Implants Applications* [TalTech Press]. <https://doi.org/10.23658/taltech.10/2025>

TALLINNA TEHNIKAÜLIKOOL
DOKTORITÖÖ
10/2025

Ti-munakoore komposiidi väljatöötamine bioimplantaatide rakenduste jaoks

RIDDHI HIRENKUMAR SHUKLA



Dedicated to

My beloved parents and Sister

Contents

List of publications	9
Author's contribution to the publications	10
Introduction	11
Abbreviations	13
Terms	14
Symbols	15
1 Literature review	16
1.1 Additive Manufacturing	16
1.1.1 Selective laser melting / Laser powder bed fusion	16
1.1.2 Metallic bioimplants.....	21
1.1.3 Lattice designs for orthopedic bone implant applications.....	24
1.2 Chicken eggshell and ceramics for bioimplants	25
1.3 Fabrication of bio-ceramics by SPS	26
1.4 Problem statement and hypothesis of the research.....	28
1.5 Objectives.....	29
2 Experimental details.....	30
2.1 Fabrication of Ti6Al4V and CP-Ti by LPBF	30
2.2 Fabrication of eggshell and Ti-eggshell composite by SPS.....	30
2.3 Structural characterization of the samples	31
2.4 Microstructural characterization of the samples.....	31
2.5 Mechanical testing of the samples	31
2.6 Cytotoxicity and bacterial study of the Ti-eggshell composites.....	32
3 Fabrication of Ti6Al4V Specimens by LPBF	34
3.1 Characterization of the feedstock Ti6Al4V powder	34
3.2 Characterization of Ti6Al4V fabricated by LPBF.....	34
3.3 Mechanical testing of LPBF Ti6Al4V samples	36
3.4 Summary	40
4 Fabrication of CP-Ti by LPBF process	41
4.1 Characterization of the feedstock CP-Ti powder	41
4.2 Characterization of CP-Ti produced by LPBF.....	42
4.3 Mechanical testing of CP-Ti produced by LPBF	43
4.4 Summary	47
5 Eggshell densification by SPS	49
5.1 Feedstock characterization of eggshell powder.....	49
5.2 SPS of eggshell powder	50
5.3 Characterization of eggshell compacts	54
5.4 Summary	58
6 Fabrication of eggshell-based composite.....	59
6.1 Microarchitecture of CP-Ti lattice	59
6.2 Characterization of the Ti-eggshell composite.....	60
6.3 Cytotoxicity and bacterial study of the Ti-eggshell composite	65
6.4 Summary	68

7 Conclusion and outlook of the thesis.....	69
7.1 Conclusions	69
7.2 Outlook of the thesis.....	69
List of figures	71
List of tables	74
References	75
Acknowledgments.....	87
Abstract.....	88
Lühikokkuvõte.....	89
Appendix	91
Curriculum vitae.....	124
Elulookirjeldus.....	125

List of publications

The list of author's publications, on the basis of which the thesis has been prepared:

- I Kumar Yadav, M., **Hiren Shukla, R.**, & Prashanth, K. G. (2023). A comprehensive review on development of waste derived hydroxyapatite (HAp) for tissue engineering application. *Materials Today: Proceedings*. <https://doi.org/10.1016/j.matpr.2023.04.669>
- II **Shukla, R.**, Sokkalingam, R., & Prashanth, K. G. (2023). Densification of the eggshell powder by spark plasma sintering. *Journal of Alloys and Compounds*, 962, 171079. <https://doi.org/10.1016/j.jallcom.2023.171079>
- III **Shukla, R.**, Yadav, M. K., Madruga, L. Y. C., Jaymani, J., Popat, K., Wang, Z., Xi, L., & Prashanth, K. G. (2024). A novel Ti-eggshell-based composite fabricated by combined additive manufacturing-powder metallurgical routes as bioimplants. *Ceramics International*. <https://doi.org/10.1016/j.ceramint.2024.12.073>

Other publications

- IV **Shukla, R.**; Prashanth, K.G. (2022). Ti6Al4V Coating on 316L Substrate by Laser-based Fusion Process. *Transactions of the Indian Institute of Metals*. DOI: 10.1007/s12666-022-02748-6
- V Baskaran, J.; Muthukannan, D.; **Shukla, R.**; Konda Gokuldoss, P. (2024). Manufacturability and deformation studies on a novel metallic lattice structure fabricated by Selective Laser Melting. *Vacuum*, 222, #113065. DOI: 10.1016/j.vacuum.2024.113065
- VI Yadav, M.K., **Shukla, R.**, Xi, L., Wang, Z., Konda Gokuldoss, P. (2025). Metallic multimaterials fabricated by combining additive manufacturing and powder metallurgy (under review in *Journal of composite science*)

Author's Contribution to the Publications

Contribution to the papers in this thesis are:

- I Co-author. Partially drafting- Original manuscript, Formal analysis, Reviewing, Editing.
- II First author. Investigation, Methodology, Formal analysis, Manuscript formation.
- III First author. Conceptualization, Experiments, Investigation, Methodology, and Manuscript formation.

Introduction

The increasing prevalence of arthritis, accidents, and osteoporosis has heightened the demand for orthopedic implants that facilitate bone healing and restore disrupted healing processes (Stewart et al., 2019). These implants can be fabricated from metals, ceramics, polymers, or a combination thereof, depending on the specific requirements and location of the bone injury (Li et al., 2017). For load-bearing applications, the implants must exhibit biocompatibility, excellent corrosion resistance, and a favorable combination of mechanical characteristics including strength, fatigue resistance, Young's modulus, ductility, and wear resistance (Geetha et al., 2009).

Commercially pure titanium (CP-Ti) is an unalloyed titanium variant containing approximately 0.1–0.3% oxygen, depending on the grade. CP-Ti is known for its ductility, reduced elastic modulus (105 GPa) (Geetha et al., 2009), and enhanced biocompatibility and corrosion resistance compared to the commonly used Ti6Al4V alloy, making it a promising candidate for biomedical applications. However, there exists a significant challenge in orthopedic implant design related to Young's modulus mismatch between metallic implants and human cortical bone. The modulus of human cortical bone ranges between 10 GPa and 30 GPa (Geetha et al., 2009). This mismatch can lead to a phenomenon known as stress shielding, where the implant absorbs more stress than the surrounding bone, causing bone resorption and necessitating revision surgeries. To address this, two main strategies have been explored: develop alloys with a lower elastic modulus (Sarraf et al., 2022; L.-C. Zhang et al., 2016) and design porous materials that can mimic the mechanical properties of bone (Lopez-Heredia et al., 2008). Recent advancements in additive manufacturing (AM) have revolutionized the production of orthopedical implants, particularly in the development of porous structures. AM allows for the precise control of porosity, enabling the fabrication of implants that can be customized to meet patient-specific requirements. The incorporation of porosity into implants can significantly reduce their density and modulus, thereby reducing stress shielding (Gokuldoss et al., 2017; S. Liu & Shin, 2019; X. P. Tan et al., 2017). However, the inherent bio-inertness of titanium-based implants limits their functionality, particularly in terms of bioactivity and the ability to integrate seamlessly with bone tissue.

On the other hand, ceramics, particularly bioactive ceramics like calcium carbonate (CaCO_3), have garnered attention for their biocompatibility, bioresorbability, and ability to promote osseointegration. CaCO_3 is naturally found in bone alongside hydroxyapatite and collagen, making it a suitable candidate for bone repair applications. Furthermore, CaCO_3 offers the advantage of releasing therapeutic ions, such as Ca^{+2} , during degradation, which can enhance bone healing and offer antibacterial properties (Kumar et al., 2015; Vuola et al., 1998). Eggshells, a common waste in the food industry, are rich in CaCO_3 (94–95%), along with traces of other minerals (Cree & Rutter, 2015; Hincke et al., 2012; Mahdavi et al., 2021; Zaman et al., 2018). Despite their potential, eggshells are largely discarded, posing environmental challenges due to the release of harmful gases during decomposition (Freire & Holanda, 2006; R. Shukla et al., 2023; Tangboriboon et al., 2012). This research aims to valorize eggshell waste by incorporating it into orthopedic implants, thus addressing both environmental concerns and the need for sustainable materials in biomedical applications. However, the brittleness of ceramics poses a significant challenge, particularly in load-bearing applications, where mechanical failure is a critical risk (Chu et al., 2006; Kumar, Dhara, et al., 2013; Kumar et al., 2015; Kumar, Webster, et al., 2013).

Considering these challenges, this research explores a novel approach to developing biocomposites that combine the mechanical strength of metals with the bioactivity of ceramics. Specifically, this thesis investigates the potential of utilizing eggshells in combination with Ti-based structures, fabricated using a hybrid method (laser powder bed fusion (LPBF) and spark plasma sintering (SPS)). The innovative aspect of this research lies in the utilization of CaCO_3 from eggshells – a readily available and sustainable resource – into Ti-based implants, thereby contributing to a circular economy and promoting green manufacturing. The proposed Ti-eggshell composite not only aims to harness the bioactivity and antibacterial properties of CaCO_3 but also seeks to overcome the limitations of current Ti-based implants, particularly their susceptibility to bacterial infections. Implant-associated infections (IAI) remain a significant challenge in orthopedic surgery, often leading to implant failure and necessitating further interventions (Ul-Haq et al., 2024). By integrating CaCO_3 , which exhibits inherent antibacterial properties, the composite material developed in this study aims to reduce the risk of IAI and enhance the overall longevity and performance of the implant.

The objective of this thesis is to advance the development of sustainable orthopedic implants by integrating green manufacturing practices and circular economy principles. This study aims to address the challenges associated with traditional Ti-based implants, which often suffer from issues such as poor interfacial bonding, and stress shielding. Additionally, the present thesis explores the integration of AM techniques to fabricate these bio-implants with tailored porosity and mechanical properties combined with powder metallurgical techniques.

The primary focus of this thesis is to produce a bioactive, antibacterial, and natural bone-mimicking composite. The thesis starts with a literature overview of the materials and processes used in this thesis followed by an experimental method. Chapters 3 and 4 elaborate on the structure-processing-properties of the Ti6Al4V and CP-Ti manufactured by LPBF. Chapter 5 emphasizes the optimization of the densification of eggshells by SPS. The combination of Chapter 4 and Chapter 5 by producing a Ti-eggshell composite is elaborated in Chapter 6. The produced composite was tested for mechanical and biological testing.

Abbreviations

ACP	Amorphous calcium phosphate
ADSCs	Adipose-derived stem cells
AM	Additive Manufacturing
ASTM	American Society for Testing and Materials
ATR	Attenuated Total Reflection
BCC	Body-centred closed-pack structure
CAD	Computer-Aided Design
CFU	Colony Forming Units
CP-Ti	Commercially Pure- Titanium
CRSS	Critical resolved shear stress
DI	De-ionized water
EDS	Energy Dispersive X-ray spectroscopy
ES	Eggshell
FTIR	Fourier Transform Infrared Spectroscopy
GND	Geometry Necessary Dislocation
HAp	Hydroxyapatite
HCP	Hexagonal closed-pack crystal structure
HSD	Honestly significant difference
IAI	Implant associated infection
IFT	inverse fast Fourier transformation image
LDH	Lactate dehydrogenase
LOF	Lack of Fusion
LPBF	Laser powder bed fusion
PBS	Phosphate Buffer Solution
SAED	Selected area diffraction pattern
SEM	Scanning electron microscopy
SLM	Selective laser melting
SPS	Spark plasma sintering
TEM	Transmission electron microscopy
TGA	Thermo-gravimetry analysis
Ti6Al4V	Ti-6Al-4V with extra low interstitial (ELI)
TSB	Tryptic Soy broth
XRD	X-ray diffraction analysis
XRF	X-ray Florence spectroscopy

Terms

Biomaterials	Materials used for bio-implant applications
Bioactivity	The ability of a material to interact with biological tissues, often promoting healing or tissue regeneration.
Biodegradation	The natural breakdown of materials by biological agents, enabling safe absorption or removal from the body.
Bioinert	Materials that remain stable and non-reactive in the body, avoiding any interaction with surrounding tissues.
Bioresorbable	Materials that dissolve in a controlled manner, providing the therapeutic agent (e.g., Ca^{+2} , PO_4^{-3}) during degradation.
Dislocation	A linear crystalline defect around which there is atomic misalignment.
Dislocation density	The total dislocation length per unit volume of material; alternately, the number of dislocations that intersect a unit area of a random surface section
Ductility/ fracture strain	A measure of a material's ability to undergo appreciable plastic deformation before fracture; may be expressed as percent elongation (%EL) or percent reduction in area (%RA) from a tensile test.
Engineering strain	The change in gauge length of a specimen (in the direction of an applied stress) divided by its original gauge length.
Engineering stress	The instantaneous load applied to a specimen is divided by its cross-sectional area before any deformation.
Osseointegration	The direct bonding between living bone and an implant, creating a stable and lasting connection.
Plastic deformation	Deformation that is permanent or nonrecoverable after the release of the applied load.
Slip	Plastic deformation as the result of dislocation motion; also, the shear displacement of two adjacent planes of atoms.
Slip system	The combination of a crystallographic plane and, within that plane, a crystallographic direction along which slip (i.e., dislocation motion) occurs.
True strain	The natural logarithm of the ratio of instantaneous gauge length to the original gauge length of a specimen being deformed by a uniaxial force.
True stress	The instantaneous applied load is divided by the instantaneous cross-sectional area of a specimen.
Ultimate tensile strength (UTS)	The maximum engineering stress, in tension, may be sustained without fracture.
Yield strength (YS)	The stress required to produce a very slight yet specified amount of plastic strain; a strain offset of 0.002 mm/mm (0.2%) is commonly known as Proof Strength.
β -transus temperature	$\alpha \rightarrow \beta$ transformation temperature

Symbols

α	HCP Titanium
α'	Martensite
β	BCC Titanium
μm	micrometer
\AA	Angstrom
Al	Aluminium
C	Carbon
Cl	Chlorin
E	Elastic modulus
HV _{0.05}	Vickers hardness value at 50 g load
K	Potassium
mm	millimeter
Na	Sodium
nm	nanometer
O	Oxygen
S	Sulphur
Sr	Strontium
V	Vanadium

1 Literature review

This chapter presents the theoretical foundation essential for comprehending the research conducted in this dissertation. It begins with an overview of the principles of AM processes, with a particular emphasis on the LPBF process. A detailed examination of the SLM process is provided, followed by a discussion on the SPS process. Additionally, the chapter explores the lattice designs employed in orthopedic bio-implants, highlighting their general characteristics, microstructural formation, and the fundamental metallurgy of LPBF Ti6Al4V and CP-Ti. The chapter concludes with an introduction to biomaterials like HAp and CaCO₃.

1.1 Additive Manufacturing

AM also referred to as 3D printing is a layer-by-layer manufacturing technique. This approach starkly contrasts with subtractive manufacturing techniques, which remove material from a solid block to create the desired shape.

During AM fabrication, three primary steps are involved as illustrated in Figure 1.1:

1. Firstly, the desired CAD model is developed and tessellated. Here, tessellation involves the fragmentation of the CAD model into layer-by-layer data based on the layer thickness employed.
2. Next, the tessellated geometry is transmitted to the AM machine. In this step, process parameters are fixed based on the alloy to be fabricated.
3. In the final step, the material is deposited layer by layer based on the developed 3D CAD model and given process parameters.

Certain AM methods or designs may necessitate post-processing steps, such as surface finishing and removal of support structure, etc. As per ISO/ ASTM 52900, AM can be classified into many subcategories. However, LPBF is a commonly used technology for metals and is further discussed in the following subsection (Gibson et al., 2010).

1.1.1 Selective laser melting / Laser powder bed fusion

Among various AM techniques, SLM or LPBF has garnered particular attention due to its capability to produce high-precision, complex metallic parts directly from powder materials. LPBF operates by utilizing a high-powered laser to selectively melt and fuse metallic powders. When the laser is irradiated onto the powder, it is heated by absorption, and if sufficient power is applied, the material melts, forming a liquid melt pool. This molten pool then rapidly solidifies which eventually constitutes the final product. After scanning the cross-section of a layer, the building platform is lowered based on the employed layer thickness, and a new layer of powder is deposited. This cycle is repeated until the entire product is complete. After the process is completed, the unused powder is collected, sieved, and can be reused. To mitigate the curling of the material caused by the accumulation of thermal stresses during the SLM process, the part is constructed on a solid substrate. Due to the high reactivity of titanium alloys, the process must be performed under an inert argon atmosphere.

A typical layout of an LPBF machine is illustrated in Figure 1.2. This process enables the production of parts with intricate geometries, internal features, and customized properties that would be challenging or impossible to achieve through conventional manufacturing methods. The capability to produce near-net-shape parts with minimal waste makes LPBF a highly efficient and sustainable manufacturing option. Additionally, the development of new materials and alloys tailored for LPBF has expanded the range

of applications, enabling the creation of parts with superior performance characteristics. (Asiva Noor Rachmayani, 2017; Kant, 2024). Recent literature has extensively explored various aspects of LPBF, including the optimization of process parameters, material properties, and post-processing techniques. Table 1.1 briefly describes various process parameters used during the LPBF process.

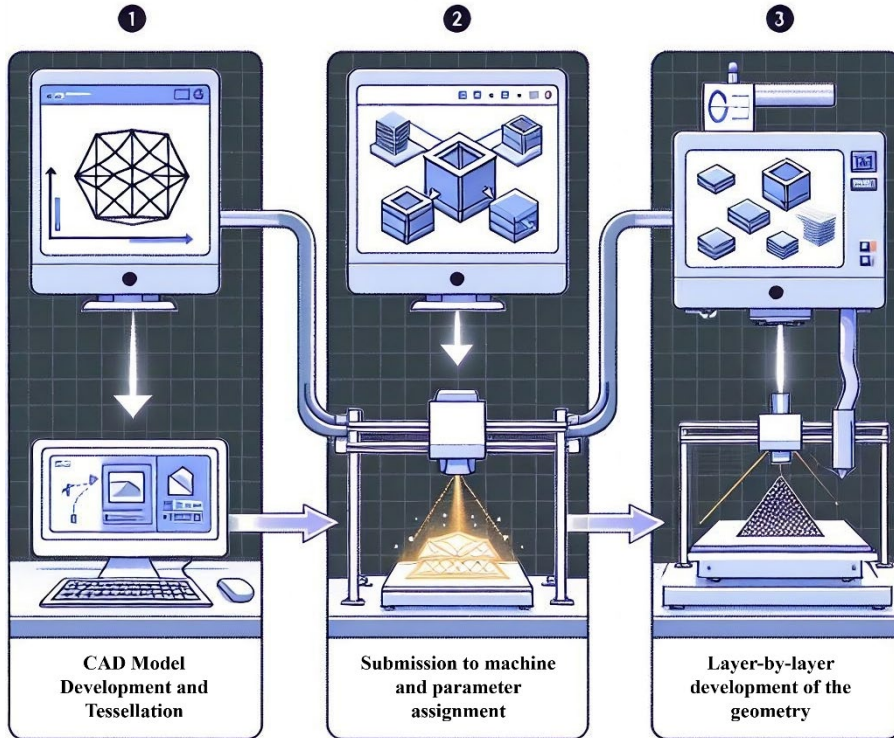


Figure 1.1. Schematics illustrating the additive manufacturing process showing the different steps involved. Step 1. CAD model development and tessellation followed by Step 2. Fixing the process parameter and Step 3: fabrication of the material layer-by-layer.

Microstructure refers to the arrangement of phases and grains within a metal, which directly influences their properties. The microstructure is largely determined by the manufacturing processes employed and the, employed process parameters play a critical role. These parameters not only affect the morphology of grains but also dictate the microstructural features, especially for Ti-based alloys. Epitaxial growth, a process where a new grain grows over a previously solidified grain, typically results in columnar grains that align in a direction opposite to the heat flow in direction. While this columnar structure can enhance mechanical properties along the grain growth direction, it may also introduce anisotropy, where material properties vary depending on their orientation. Microstructure provides a clear link between manufacturing processes and the resulting mechanical, physical, and chemical properties. The LPBF process exhibits distinct macroscopic and microscopic structures, due to its unique thermal process, which differs significantly from traditional manufacturing methods (T. Zhang & Liu, 2022).

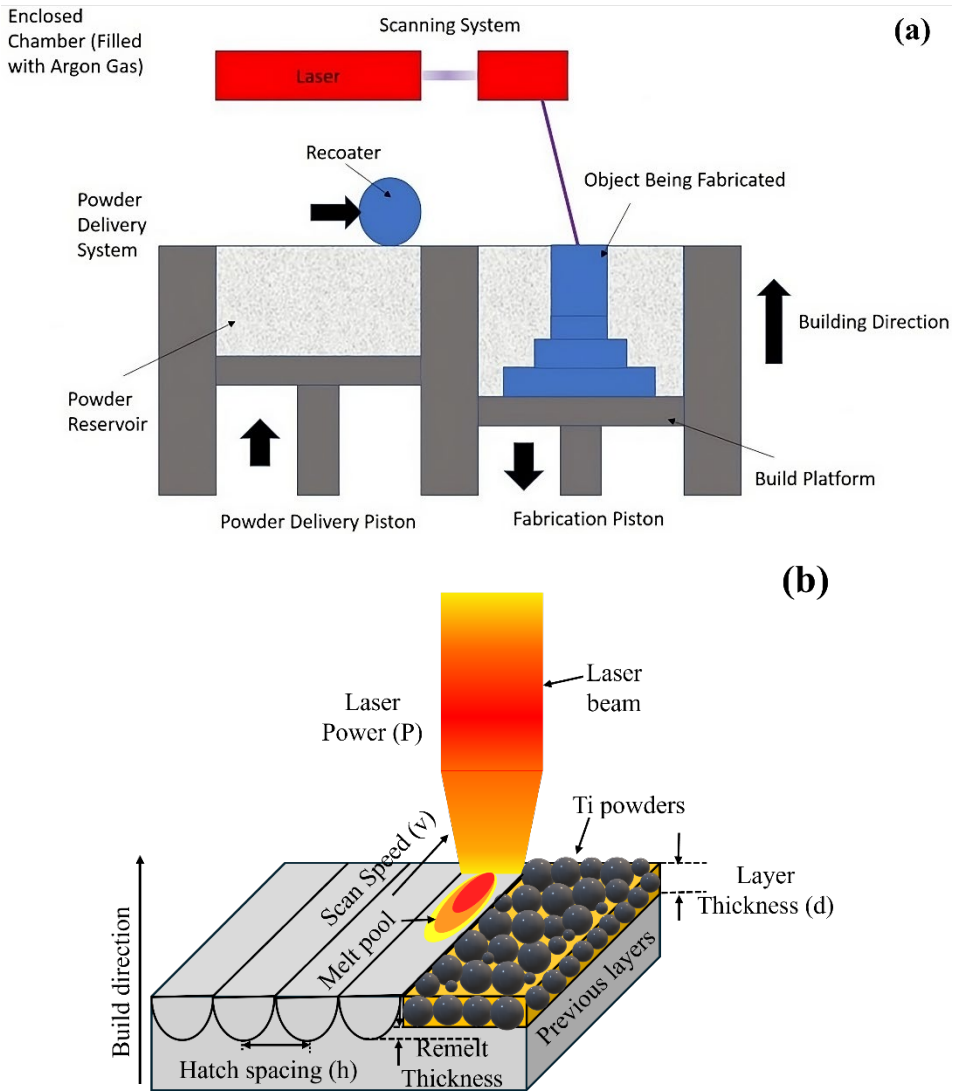


Figure 1.2. Schematics illustrating the (a) laser powder bed fusion process (Jiao et al., 2018), (b) laser-powder interaction during the laser powder bed fusion process.

Table 1.1. Table showing the list of processing parameters that could influence the LPBF process (El Wakil, 2019; Gulbrandsen-Dahl et al., 2024; Pandey et al., 2022; Singla et al., 2021).

Parameter Category	Parameters	Description	Impact	Potential Defects
Laser Parameters	Laser Power (P)	Energy provided by the laser per unit time.	Affects melt pool size, penetration, and defect formation (e.g., spatter).	High power: spatter, keyholing; Low power: lack of fusion.
Laser Parameters	Laser Spot Size	Diameter of the laser beam.	Influences resolution and alignment precision.	Incorrect spot size: poor surface finish, lack of detail.
Laser Parameters	Scan Speed (v)	Speed at which the laser moves over the powder bed.	Impacts melt pool size, cooling rate, and heat input.	High speed: lack of fusion; Low speed: overheating, distortion.
Laser Parameters	Hatch Spacing (h)	Distance between adjacent laser scan lines.	Ensures complete melting and fusion between layers.	Incorrect spacing: unmelted zones, porosity.
Powder Characteristics	Particle Size Distribution	Range of particle sizes in the powder.	Affects surface finish, packing density, and flowability.	Wide distribution: poor surface quality; Narrow: powder clogging.
Powder Characteristics	Powder Shape	Morphology of powder particles (e.g., spherical, irregular).	Spherical powders improve flowability and packing density; irregular shapes can cause uneven layering.	Irregular shape: poor flowability, inconsistent layer thickness, porosity.
Powder Characteristics	Powder Flowability	Ease with which powder flows and spreads.	Affects uniformity of powder layers and packing density.	Poor flowability: inconsistent layers, poor surface finish, porosity.

Powder Characteristics	Apparent Density	The bulk density of the powder, considering the voids between particles. Usually, 50% to 70% of the true density.	Affects packing density and the overall density of the final part.	Low apparent density: high porosity, weak mechanical properties.
Powder Characteristics	Powder Layer Thickness (t)	Thickness of each deposited powder layer.	Balances resolution, surface finish, and build time.	Thick layers: lack of fusion; Thin layers: extended build time.
Powder Characteristics	Powder Material	Type of metallic powder used (e.g., titanium, aluminum)	Determines melting point, thermal conductivity, and optical absorptivity.	Material-specific defects like oxidation, contamination.
Thermal Management	Pre-heat Temperature	Temperature of the build platform before and during the build.	Reduces thermal gradients and residual stresses.	Insufficient pre-heating: warping, delamination.
Thermal Management	Cooling Rate	Speed at which the part cools post-laser exposure.	Influences residual stress, micro-cracking, and material properties.	Fast cooling: high residual stresses, cracks; Slow cooling: grain coarsening.
Scanning Strategy	Scan Pattern	Path followed by the laser (e.g., unidirectional, bidirectional).	Affects residual stress distribution and part distortion.	Inconsistent patterns: uneven stress distribution, distortion
Scanning Strategy	Layer Rotation	Rotation of scan pattern between successive layers.	Helps reduce residual stresses.	No rotation: anisotropic properties, distortion
Environmental Consideration	Atmosphere	Gas environment (e.g., argon, nitrogen) used to prevent oxidation.	Prevents contamination and oxidation.	Poor atmosphere control: oxidation, contamination.

Environmental Consideration	Humidity & Temperature Control	Consistent environmental conditions during the build.	Ensures reproducibility and part quality.	Inconsistent conditions: moisture absorption, oxidation.
Post-Processing Processes	Heat Treatment	Thermal treatments applied after the build process.	Relieves residual stresses and enhances material properties.	Incorrect treatment: retained stresses, undesired microstructure
Post-Processing Processes	Surface Finishing	Processes like machining, polishing, or blasting.	Improves surface quality and dimensional accuracy.	Inadequate finishing: rough surfaces, dimensional inaccuracies.

During AM, alloys undergo complex physical processes and thermal histories, including intense Marangoni flow, temperature gradients, and extreme cooling rates. These factors influence the grain morphology, leading to unique microstructural features and higher defect densities compared to cast counterparts (T. Zhang & Liu, 2022). Additionally, AM offers the fabrication of compositionally heterogeneous alloys that were previously not possible using other conventional fabrication processes (S. Liu & Shin, 2019; Z. Wang et al., 2019). However, LPBF has significant drawbacks in terms of time and cost. The layer-by-layer deposition and solidification process is time-consuming, with build times depending on the material and geometry. Furthermore, the need for high-quality spherical powder, typically produced by expensive atomization techniques, makes production costly and limits its use to specific materials/alloys. Consequently, LPBF is primarily used in aerospace and biomedical implant production, where intricate shapes and a balance between density and properties are essential (T. Zhang & Liu, 2022).

1.1.2 Metallic bioimplants

Titanium and its alloys have become indispensable materials across a multitude of industries due to their remarkable properties, including a high strength-to-weight ratio, excellent corrosion resistance, and outstanding biocompatibility, making them suitable for a wide range of applications, particularly in the aerospace, medical, and dental sectors (Srivatsan & Sudarshan, 2015). Ti has a melting point of 1668 °C, 4.51 g/cm³ density, and two allotropic crystal structures. At room temperature, Ti shows a hexagonal close-packed (HCP) crystal structure known as the α -phase ($a = 2.9504 \pm 0.0004 \text{ \AA}$, $c = 4.6832 \pm 0.0004 \text{ \AA}$, and $c/a = 1.5873$) (Joshi, 2006). This phase remains up to 882 °C. Beyond this temperature, Ti undergoes a phase transformation to a body-centered cubic (bcc) structure known as the β -phase ($a = 3.28 \pm 0.003 \text{ \AA}$). This transformation is crucial in the development of Ti-based alloys, as the balance between the α and β phases can be used to tailor the mechanical properties of the material. Hereafter, α will be used for HCP and β for BCC (Donachie, 2000; Srivatsan & Sudarshan, 2015).

Upon cooling through the β transition temperature, the β phase transforms into various equilibrium or nonequilibrium phases, depending on the cooling rate and alloying elements. Rapid cooling (water or oil quenching) can transform the β phase to martensite

(α' - hcp or α'' orthorhombic phases) (Donachie, 2000; Zheng et al., 2022). The tendency to form α'' over α' increases with the concentration of β -stabilizer (Donachie, 2000). In contrast, slower cooling transforms the β phase through nucleation and growth into the Widmanstätten α structure. The morphology of the Widmanstätten α phase can vary from a colony of similarly aligned α laths to a basket-weave pattern, depending on the cooling rate or alloying addition, with finer lamellar structures forming at higher cooling rates. During slow cooling, the α phase may also precipitate along prior β grain boundaries (Donachie, 2000; Joshi, 2006; Zheng et al., 2022). Additionally, the microstructure may retain small amounts of β phase, with the quantity of retained β increasing as the solute content rises.

Generally, bio-implants are manufactured from SS316L (Elastic Modulus (E) close to 210 GPa), Co-Cr (E around 230 GPa), and Ti-based alloys (E approximately 100–110 GPa) (Geetha et al., 2009). Since the development of biocompatible and high strength-to-weight ratio Ti6Al4V ELI (extra low interstitial impurity content) alloy, it has become the preferred choice and has been widely used. Ti6Al4V ELI can be manufactured easily, and the microstructure can be altered easily. However, alloying elements like Al and V pose long-term issues in the human body, such as Alzheimer's disease, and other neurological side-effects making it not the ideal candidate for bio-implant applications (Attar et al., 2020; Prakasam et al., 2017; Sarraf et al., 2022).

1.1.2.1 CP-Ti based bioimplants

CP-Ti is an unalloyed commercially pure- Ti containing, 0-0.4% oxygen. Based on the oxygen content and as per ASTM F67-13(2017), it is divided into different grades. The CP-Ti Grade 1 has the lowest oxygen content of 0.18% and it is soft and ductile, with a typical Ultimate Tensile Strength (UTS) of 240 MPa and Yield Strength (YS) of 170 MPa. The CP-Ti Grade 2 has 0.25% oxygen content and has moderate strength and ductility, with UTS and YS values of 345 MPa and 275 MPa, respectively. The CP-Ti Grade 3 and Grade 4 have a higher oxygen content of 0.35% and 0.40% respectively, resulting in increased strength but reduced ductility. Grade 3 exhibits a UTS of 450 MPa and YS of 380 MPa, while Grade 4 shows the highest strength with a UTS of 550 MPa and YS of 485 MPa (Depboylu et al., 2022; Williams, 2002).

The limited amount of slip systems in CP-Ti (HCP) complicates dislocation movements compared to BCC and FCC crystal structures. This limitation makes CP-Ti less malleable and more prone to issues like anisotropy and poor formability, especially at room temperature. During LPBF processing, due to limited melt pool stability and inferior surface finishing, CP-Ti poses manufacturability issues. However, researchers have reported the successful fabrication of CP-Ti using LPBF. Attar et al. (Attar et al., 2014) varied the energy density to identify the optimized parameters. This research has investigated the mechanical properties (including compressive properties, tensile properties, and microhardness) of CP-Ti (Grade 2). The report by Gu et al. (Gu et al., 2012) has demonstrated the effect of the scan speed on densification, achieving nearly fully dense (99.5%) parts without post-treatment. Their experiments showed that optimal LPBF parameters not only improved the hardness and strength of CP-Ti but also maintained its ductility, making it competitive with the traditionally manufactured counterparts. The cooling rate during LPBF, influenced by factors such as energy input and substrate temperature, significantly affects the microstructure of the SLM CP-Ti. The SLM CP-Ti typically, results in a refined α' martensite, which enhances their mechanical properties, particularly yield strength. (T. Zhang & Liu, 2022)

1.1.2.2 Ti6Al4V-based bioimplants

As the name suggests, Ti6Al4V is an alloy of Ti having 6% Al, and 4% V commonly known as Ti Grade 5 or Ti64. In trace amounts (0.25%), it may contain oxygen, and nitrogen-like impurities. These interstitials increase the possibility of embrittlement, potent to fail under complex mechanical and biochemical stresses encountered in the human body. This led to the development of the biomedical grade Ti6Al4V grade 23 with extra low-interstitial (ELI) (0.13%). Titanium Grade 23 was developed to meet the stringent requirements of the medical industry, especially for orthopedic and dental implants. The primary mechanical advantage of Grade 23 over Grade 5 lies in its enhanced ductility and toughness, while maintaining high strength. The UTS and YS of Grade 23 are slightly lower than those of Grade 5 due to reduced interstitial hardening, but the trade-off is acceptable for applications where toughness and elongation are more critical. The lower interstitial content in Grade 23 reduces the risk of adverse biological reactions, making it highly biocompatible. This characteristic is particularly important for medical implants, where the material needs to integrate well with human tissues without causing inflammation or rejection. Additionally, the corrosion resistance of the alloy in physiological environments is enhanced, further supporting its use in long-term implants. In contrast, due to the reduction of interstitials, it is very difficult to machine this alloy and hence expensive. However, the requirement of the biochemical and mechanical properties justifies the usage of Grade 23 over Grade 5. As per ASTM standards, Ti6Al4V (ELI) Grade 23 is the medical grade Ti6Al4V and hence in this study, Ti6Al4V implies Ti6Al4V (ELI) Grade 23 and not grade 5 until and unless specified (Donachie, 2000).

In Ti6Al4V, Al is the α -stabilizer and V is a β -phase stabilizer. This combination puts Ti6Al4V alloy in the $\alpha+\beta$ category. In general, Ti6Al4V shows the basket-weave-like widmenstatten $\alpha+\beta$ microstructure at room temperature. However, the microstructure strongly depends on the thermal history and cooling rates. For example, slow cooling results in the above-mentioned $\alpha+\beta$ microstructure; while fast cooling results in α' martensitic structure. Ti6Al4V, with its mix of α and β phases, can be more readily processed at both low and high temperatures, offering more flexibility in manufacturing. The behavior of Ti6Al4V alloy during cooling is critical in determining its microstructure and, consequently, its mechanical properties. When the alloy is cooled rapidly from a temperature above the β -transus (the temperature above which the β phase is stable), a martensitic transformation occurs. Specifically, at cooling rates exceeding 410 K/s, the β phase transforms into α' (alpha prime) martensite. This transformation is diffusionless taking place without the movement of atoms over large distances, resulting in a highly refined microstructure (Donachie, 2000; Zheng et al., 2022).

The formation of α' martensite leads to a significant increase in the YS of the alloy, often exceeding 1100 MPa due to the morphology of the martensitic phase. However, an increase in the strength is at the cost of ductility ranging between 5% and 10%. This reduced ductility is a consequence of the brittle nature of the martensitic structure, which limits the alloy's ability to deform plastically before fracturing. In contrast, if the cooling rate is relatively slow, below 20 K/s, the transformation from the β phase to the α phase takes place through diffusional precipitation. This process allows for the formation of a more equiaxed and coarser α phase, which is typically associated with improved ductility but lower YS compared to the martensitic microstructure (Donachie, 2000; Zheng et al., 2022).

The ability to tailor the microstructure of Ti6Al4V through controlled cooling and heat treatment allows for the customization of mechanical properties to suit specific

applications. During AM processes like LPBF, the inherent rapid cooling favors the formation of α' martensite. As a result, LPBF-processed Ti6Al4V typically exhibits high strength but relatively low ductility, necessitating post-processing heat treatments if a balanced set of mechanical properties is desired. (Gupta et al., 2021; S. Liu & Shin, 2019; Neikter et al., 2018; Singla et al., 2021; T. Zhang & Liu, 2022)

1.1.3 Lattice designs for orthopedic bone implant applications

AM has emerged as a transformative technology in the biomedical field, particularly in the design and fabrication of orthopedic bone implants. The ability to create complex, patient-specific geometries with precise control over the internal architecture has opened new possibilities for improving the performance and functionality of the implants. Among the various design strategies, lattice structures have gained significant attention due to their potential to mimic the mechanical and biological properties of the natural bone. The difference in Young's modulus between natural bone and implant creates a stress-shielding effect on the surrounding bone, leading to bone resorption and the need for revision surgery. To reduce stress shielding, it is necessary to lower Young's modulus, for which two approaches are commonly used. The first involves developing alloys with an elastic modulus in the range of natural bone, such as β -Ti. However, it does not meet the requirement of a strength-modulus trade-off. The second approach involves the production of porous materials, which has gained considerable attention in the recent years. In porous materials, the presence of porosity (open/closed) can significantly reduce the density of the implant, and its Young's modulus, resulting in a reduced stress-shielding effect (McGregor et al., 2021).

Lattice structures in orthopedic implants are characterized by their open, porous features, which can be tailored to match the stiffness and strength of bone while promoting osseointegration and vascularization. These designs are typically composed of repeating unit cells that can be systematically varied in size, shape, and orientation to achieve desired mechanical and biological outcomes. The concept of using lattice structures in bone implants is rooted in the need to address the limitations of traditional solid implants, such as stress shielding, poor integration with the host tissue, and the risk of implant loosening over time. Lattice structures offer a means to tune the mechanical properties of the implant, ensuring load transfer to the surrounding bone and reducing the risk of implant failure. Additionally, the interconnected porosity of lattice designs provides pathways for bone ingrowth and nutrient transport, enhancing the biological integration of the implant (Khan & Riccio, 2024; McGregor et al., 2021; Tao & Leu, 2016).

Despite their advanced material properties, Ti-based load-bearing implants, such as hip and knee prostheses, face high failure rates. For example, ~600,000 knee replacement surgeries performed as of 2011 experienced implant failure within 15 years. Major factors contributing to these failures include interfacial instability and aseptic loosening. Failures in load-bearing implants generally fall into three primary categories: (1) inadequate interfacial bonding between the implant surface and bone tissue, (2) stress shielding due to the significant modulus mismatch between the implant (110–120 GPa for Ti-based alloys) and human cortical bone (10–30 GPa), and (3) wear-induced osteolysis resulting from the excessive release of metal ions around the bone-implant interface (Bandyopadhyay et al., 2017). To enhance the in vivo longevity of implants, improvements can be made by strengthening the interfacial bond between the implant and bone tissue and by reducing the effective modulus of the implant. One effective strategy involves incorporating a bioceramic coating on the implant surface. Porous materials can reduce

the effective modulus of the implant and promote biological fixation by allowing bone growth into the porous structure. This process, known as osseointegration, facilitates a mechanical interlock that improves the stability and performance of the implant. However, limited interfacial strength between the base material and coating, along with potential coating fractures during service, can lead to significant clinical complications (Kumar et al., 2015). In the following section such biomaterials and their fabrication by SPS are discussed.

1.2 Chicken eggshell and ceramics for bioimplants

Chicken eggs are a daily food ingredient and are widely consumed in Europe and worldwide as a rich source of CaCO_3 . Approximately 7.0 million tones of eggs were annually used in Europe alone in 2018 (Gautron et al., 2022). The inner core of the egg and the thin protein layer of the egg (albumin) are useful for food processing (Hicks et al., 2023), while 11% of the egg is made up of a ceramic shell (eggshell) ~ 2000 tons/day is discarded as it is not directly useful for food production. This eggshell layer contains potential nutrients and elements as mentioned in Table 1.2. Eggshells are essentially composites of calcite crystals encased in a protein matrix. Like various mollusk shells, such as those from mussels and oysters, eggshells contain around 88 g of CaCO_3 per 100 g of dry weight. This CaCO_3 can be readily converted into calcium forms used to synthesize HAp (Kumar Yadav et al., 2023).

Table 1.2. Chemical composition of the eggshell (Cree & Rutter, 2015; Hincke, 2012; Mahdavi et al., 2021; R. Shukla et al., 2023; Zaman et al., 2018).

Chemical Composition	Amount
Calcium carbonate (CaCO_3)	94–95 %
Calcium phosphate ($\text{Ca}_3(\text{PO}_4)_2$)	$\sim 1\%$
Magnesium carbonate (MgCO_3)	$\sim 1\%$
sodium (Na)	1512 ppm
magnesium (Mg)	3472–4500 ppm
strontium (Sr)	320–411 ppm
potassium (K)	525 ppm
sulfur (S)	589 ppm
Organic matter	$\sim 4\%$

HAp ($\text{Ca}_{10}(\text{PO}_4)_6(\text{OH})_2$) is a prominent bioceramic due to its excellent biocompatibility, non-toxicity, and ability to promote osteointegration and osteoconduction. Its chemical and structural similarity to natural bone supports bone regeneration and integration with host tissue. HAp releases calcium and phosphate ions in biological fluids, which aids in cell proliferation and bone metabolism. While synthetic HAp, produced through methods like mechanochemical reactions, wet chemical precipitation, hydrothermal processes, and sol-gel techniques, is often considered superior due to its controlled composition and absence of contaminants, it is also expensive. Natural sources, such as xenogeneic bone (e.g., bovine) used for HAp production, offer a more cost-effective alternative and can be enhanced through thermal and mechanical processing (Kumar Yadav et al., 2023).

CaCO_3 is found in the natural bone along with HAp and collagen, making it easy to osseointegrate. The main advantage of using CaCO_3 -based implants is their bioresorbability. Bioresorbable materials also degrade like biodegradable materials but

also release a controlled amount of Ca^{+2} and PO_4^{-3} , which act as therapeutic agents to heal bone injuries and increase bactericidal activity (Kumar et al., 2015; Vuola et al., 1998). Disposal of eggshells not only results in the loss of these elements but also poses waste disposal issues. Dumping in land costs money, the decomposition of organic matter from the eggshell produces ammonia, methane, and hydrogen sulfide-like foul-smelling gases, as well as microbial action of the eggshell, threatens environmental concerns (Freire & Holanda, 2006; R. Shukla et al., 2023; Tangboriboon et al., 2012). Utilizing eggshells as food calcium supplements has not eliminated waste disposal issues. Researchers have tried to use eggshells in different products such as wall tiles (Freire & Holanda, 2006), Cd- and Pb-like heavy metal removal (Tizo et al., 2018) Pd@CaO solar photocatalytic fabrication for wastewater treatment (Nassar & Alotaibi, 2021), and polymer composite (Hanumantharaju et al., 2022; Homavand et al., 2024; Leclair et al., 2021; Owuamanam & Cree, 2020). Despite these efforts, the utilization of eggshell waste remains a major concern. This research aims to utilize eggshell waste in orthopedic bio-implants to produce sustainable bio-implants.

Several studies have reported the densification of CaCO_3 using powder metallurgical and sintering. However, at temperatures exceeding 800–900 °C, CaCO_3 tends to decompose into calcium oxide (CaO) and carbon dioxide (CO_2) through calcination. This instability during high-temperature processing presents difficulties in achieving proper densification and complicates the fabrication of bone-grafting implants. (Baqain et al., 2023; Combes et al., 2006; Cree & Pliya, 2019; Naemchan et al., 2008a; R. Shukla et al., 2023; Wan et al., 2021; Zaman et al., 2018). To overcome these challenges, researchers have explored the use of dopants or sintering aids to stabilize CaCO_3 and achieve densification without decomposition. For instance, Tetrad and Assollant (Tetard et al., 2014) doped CaCO_3 with Lithium Phosphate (Li_3PO_4), attaining 98% relative density at 700 °C using a pressureless sintering technique. Urabe et al. (Chróścicka et al., 2016) employed LiF as an additive to enhance CaCO_3 densification, while Vlasov et al. (Vlasov & Poroskova, 1997) incorporated 1–2% Lithium Carbonate (Li_2CO_3) into the aragonite phase of CaCO_3 , identifying 620–650 °C as the optimal sintering temperature range. Smirnov et al. (Smirnov et al., 2012) utilized ammonium carbonate to lower the sintering temperature of CaCO_3 , and Ito et al. (Ito et al., 2017) succeeded in producing a 99% dense compact using a eutectic mixture of KF-NaF-LiF system with CaCO_3 and. Despite this research, there remains limited data on the densification of CaCO_3 . The objective of the present study is to produce bio-implants from eggshells, for which eggshell powder must be densified.

1.3 Fabrication of bio-ceramics by SPS

SPS (refer to Figure 1.3) also known as Field-Assisted Sintering Technique (FAST), is a powder consolidation method that leverages the simultaneous application of uniaxial pressure and pulsed direct current to achieve rapid sintering of materials at relatively low temperatures. SPS is renowned for its ability to produce materials with superior properties. The principle of SPS involves the generation of spark discharges between powder particles, which results in localized high temperatures and electric fields. These conditions facilitate rapid densification and grain growth, allowing the production of fully dense materials with fine microstructures in a matter of minutes. This rapid sintering process not only enhances the mechanical properties of the materials but also preserves the intrinsic characteristics of the powders, such as nanostructures and phase compositions.

Recent studies have delved into the mechanisms underlying SPS, exploring the roles of electric fields, current effects, and thermal gradients in the sintering process. The optimization of process parameters such as temperature, pressure, and pulsed current has been a major focus, as these factors critically influence the densification kinetics, microstructural evolution, and resultant material properties. Moreover, SPS has been instrumental in the development of novel materials, including high-entropy alloys, refractory metals, and advanced ceramics. One of the notable advantages of SPS is its ability to sinter materials with complex compositions, which is challenging for conventional sintering methods. The rapid processing times and lower sintering temperatures also result in energy savings and reduced environmental impact, aligning with the growing emphasis on sustainable manufacturing practices. However, challenges such as inhomogeneous temperature distribution, limited scalability, and the need for specialized equipment remain areas of active research.

SPS is a promising method compared to conventional methods as compaction and sintering occur simultaneously. This not only achieves a higher density but also reduces the sintering time and lowers the sintering temperature. By extending its benefits, it is possible to avoid or limit the decomposition and crystallization phenomena happening in these eggshells (Han et al., 2019; Kawagoe et al., 2008; Orrù et al., 2009; Oza et al., 2021). SPS has been utilized to produce HAp (Kawagoe et al., 2008), tricalcium phosphate implants, and bioglass[®] owing to its densification at comparatively low temperatures. Moreover, SPS can consolidate a wide variety of materials from amorphous alloys, crystalline materials, composites, and functionally graded materials, etc. (Kamboj et al., 2019; Rahmani et al., 2019, 2020, 2022a; N. Singh et al., 2021; Sokkalingam et al., 2020; Surreddi et al., 2010). For instance, Mechay et al. (Mechay et al., 2014) used SPS to produce HAp-based bone implants and observed suppression of the sintering temperature from 1300 °C to 900 °C as compared to conventional sintering techniques.

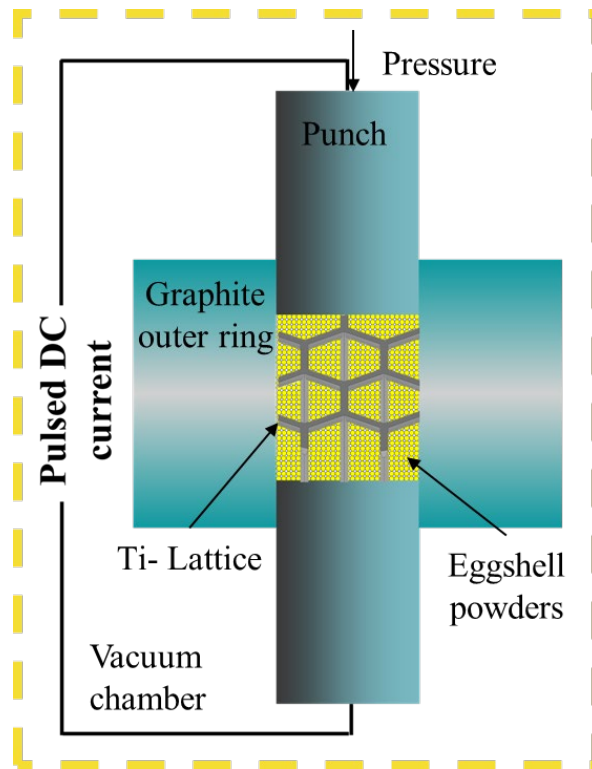


Figure 1.3. Schematic of the spark plasma sintering (SPS) process, illustrating the simultaneous application of uniaxial pressure and pulsed electric current to the powder compact.

1.4 Problem statement and Hypothesis of the research

CP-Ti-based metallic implants are beneficial for providing ductility and support essential for bone healing. However, the higher Young's Modulus induces a stress-shielding effect. To address this, porous CP-Ti implants have been developed using advanced LPBF technology. Albeit these implants have limitations of bioinert behavior and implant-associated infections. Moreover, to easily integrate with the natural bone, bioactivity is crucial. On the other hand, bioceramics such as eggshells possess excellent bioactivity owing to a similar chemical composition to the natural bone. However inferior ductility and concomitant brittleness limit its usage in bio-implants. Moreover, the coating of the bioactive material also faces several challenges due to interfacial bonding and detachment of the coating from the interface.

This study hypothesizes that by integrating a bioceramic eggshell with a porous CP-Ti implant produced using LPBF and densified through SPS, a composite implant with the following enhanced properties will be achieved:

- The bio-implant aims to promote sustainability by repurposing eggshell waste, thereby supporting sustainability and circular economy goals 3, 6 (partially), 9, 12, 13, and 15.
- The implant is expected to achieve a Young's Modulus comparable to natural cortical bone, thereby reducing the stress-shielding effect often seen with traditional implants.

- The combined CP-Ti and eggshell composition is anticipated to provide greater ductility compared to bioceramics like eggshells.
- The porous structure of the metallic implant will be filled with bioresorbable CaCO_3 , allowing for the controlled release of therapeutic agents (in this case Ca^{+2}) during degradation. This release is expected to enhance osseointegration and confer antibacterial properties, addressing IAI risks.

1.5 Objectives

This study represents a critical advancement in developing advanced bio-implants by integrating principles of circular economy and green manufacturing. It offers a sustainable approach to addressing the challenges of orthopedics implantology, contributing to both environmental stewardship and technological innovation. The present research focuses on the following objectives:

- To assess the potential of using eggshell waste as a bioceramic additive, contributing to circular economy principles in bio-implantology.
- To investigate and compare the mechanical properties of Ti6Al4V and CP-Ti fabricated by LPBF, providing insights into material selection for orthopedic implants.
- To establish the structure-processing-property relationships for the CP-Ti produced by LPBF, enabling the understanding of its properties for use in medical implants.
- To achieve maximum density the SPS parameters for eggshells, aiming to achieve maximum density.
- To develop and characterize Ti-eggshell composites that provide both mechanical durability and effective biological performance, ensuring the suitability of the implants for long-term use in orthopedic applications.
- To investigate the mechanisms of bacterial adhesion and growth on the implant surface, aiming to enhance the antibacterial properties.

2 Experimental details

2.1 Fabrication of Ti6Al4V and CP-Ti by LPBF

Ti6Al4V and CP-Ti specimens were fabricated using LPBF Process (SLM Solutions GmbH Realizer SLM-280 device) equipped with a 700 W fiber laser, spot size $\sim 80 \mu\text{m}$, and 20–75 μm layer thickness. The device offers a build envelope of $280 \times 280 \times 350 \text{ mm}^3$ and utilizes a single 1070 nm yttrium scanning laser ($1 \times 700 \text{ W}$). A custom-designed smaller build platform (D100 mm) made from CP-Ti, along with a re-coater, was employed for printing the samples. The scanning parameters for both materials, shown in Table 2.1, were selected based on literature recommendations for CP-Ti (Attar et al., 2014) and optimized parameters provided by SLM Solutions for Ti6Al4V. An Ar atmosphere was maintained throughout the process to reduce oxygen levels to less than 100 ppm. After printing, samples were cut from the build plate by wire EDM.

Table 2.1. The processing parameters employed to fabricate CP-Ti and Ti6Al4V samples using the LPBF process.

Processing parameters	Ti6Al4V	CP-Ti
Laser Power (W)	275	165
Scan Speed (mm/ s)	1100	138
Hatch Spacing (μm)	120	110
Hatch Rotation ($^\circ$)	90	72
Layer Thickness (μm)	30	50

2.2 Fabrication of eggshell and Ti-eggshell composite by SPS

Commercial eggshell powders were densified using SPS (HPD 10-GB, FCT System GmbH, Germany). A 10 mm diameter graphite mold, equipped with graphite spacers, was employed to prevent a reaction between the graphite mold and the sample. The SPS device is placed under the glove box and hence the SPS process takes place under vacuum. A uniaxial pressure of 50 MPa was applied, along with simultaneous heating. The heating rate was set at $100 \text{ }^\circ\text{C}/\text{min}$, with a 5 min holding period at the desired temperatures (i.e., $250 \text{ }^\circ\text{C}$, $500 \text{ }^\circ\text{C}$, $750 \text{ }^\circ\text{C}$, $850 \text{ }^\circ\text{C}$, $950 \text{ }^\circ\text{C}$, and $1000 \text{ }^\circ\text{C}$, respectively). The sintering temperature was monitored using a K-type thermocouple placed into the graphite mold wall. During the SPS process, parameters such as the piston movement (punch displacement), pressure, current, voltage, and temperature were meticulously recorded. The instantaneous change in the punch displacement was calculated using Eq. 2.1, and this instantaneous change in the punch position was directly related to the instantaneous relative density (hereafter relative density) of the sample using Eq. 2.2.

$$L = L_f + \Delta L_{max} - \Delta L \dots \dots \dots \quad (\text{Eq. 2.1})$$

$$D = \left(\frac{L_f}{L}\right) D_f \dots \dots \dots \quad (\text{Eq. 2.2})$$

where L (mm) and L_f (mm) are the instantaneous and final heights of the sintered compacts, while ΔL_{max} (mm) and ΔL (mm) represent the maximum and instantaneous upper punch displacement, respectively. D (%) and D_f (%) denote the instantaneous and final relative densities of the powder compact (Bernard-Granger & Guizard, 2007; L. Huang et al., 2021; Q. Yang et al., 2021). To fabricate the Ti-eggshell composite, the eggshell powder was added to the lattice structure and subjected to SPS. The parameters combination optimized in Chapter 5 was used to sinter the Ti-eggshell composite.

2.3 Structural characterization of the samples

Thermogravimetric analysis (TGA) of the eggshell powder was performed using a NETZSCH STA 449 F3 Jupiter, covering a temperature range from room temperature to 1200 °C, with a heating rate of 20 K/min under a nitrogen atmosphere. About 9.5 mg of eggshell powder was used in alumina crucibles without a lid for the analysis. To investigate the structure and functional groups present in the sintered compacts, the infrared spectra for Fourier transform infrared (FTIR) were measured using a Platinum-ATR Alpha FTIR spectrometer (Bruker Optic GmbH, Germany) using the attenuated total reflection (ATR) technique in the wavelength range between 50 cm⁻¹ and 2500 cm⁻¹. The chemical composition of Ti6Al4V and eggshell feedstock powder was determined using X-ray Florence (XRF) (Rigaku Primus II XRF spectrometer) was used to identify.

Structural characterization of the samples was carried out using X-ray diffraction (XRD) analysis. The XRD analysis was performed using the Rigaku Smart Lab system with Cu-K α radiation ($\lambda = 1.5406 \text{ \AA}$), operating at a step size of 0.02, and a scan speed of 5°/min from 20–65°. The dislocation density values were calculated from the XRD patterns using the conventional Williamson-Hall equation. The crystallographic data were also calculated from the XRD patterns.

2.4 Microstructural characterization of the samples

To determine the microstructure of the bulk LPBF samples, solids with 5 mm diameter and 5 mm height were produced along with the lattice. They were mounted in epoxy and followed by the standard metallographic procedures: grinding and polishing with different grades of emery paper to remove all the scratches and mechanical imperfections. The polished surface was etched using a Kroll's reagent observed under optical microscopy (Leica Microsystems) and high-resolution – scanning electron microscope (HR-SEM) (model – Zeiss Gemini SEM 450). Whereas to characterize SEM of the sintered compacts, polishing up to 4000-grid SiC paper was performed. ImageJ was used to investigate and extract the statistical data such as powder particle size and achieved theoretical density in compacts from SEM images. The feedstock Ti6Al4V, CP-Ti, and eggshell powders were also examined under SEM for determining particle shape and size distribution. The microstructure of the Ti-eggshell composite was examined using an HR-SEM fitted with an EDS setup (INCA pental FETX3, Oxford instrument).

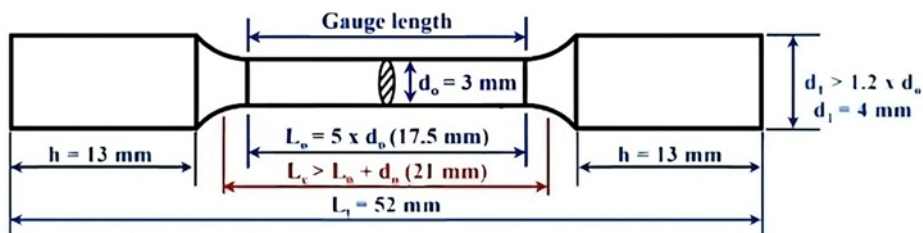
High-resolution imaging was carried out using a transmission electron microscope (TEM, Tecnai G2 F20, FEI, Germany) equipped with a high-angle annular dark-field (HAADF) TEM using an FEI 80-300, and nano-diffraction.

2.5 Mechanical testing of the samples

The microhardness of the eggshell compacts was evaluated using an Indentec 5030 kV (Indentec Hardness Testing Machines Limited, West Midlands, UK), applying a load of 50 g and dwell time of 10 s. Due to the presence of porosity in the compacts SPS at 250 °C and 500 °C measurement of the indentation size was affected, consequently, the hardness value. Hence, these compacts were excluded from the hardness test.

The tensile specimens were manufactured with the parameters mentioned in Table 2.1 as per the ASTM standard: ASTM E8 / E8M- 13 a. The dimensions of the tensile specimen are shown in Figure 2.1. Room temperature uniaxial tensile test was conducted using an Instron test 5567 screw-driven universal testing machine at different strain rates

from $1 \times 10^{-2} \text{ s}^{-1}$, $1 \times 10^{-3} \text{ s}^{-1}$, and $1 \times 10^{-4} \text{ s}^{-1}$. At least three tensile and compressive samples were tested under each condition. In accordance with the ASTM E9-09 standard, cylindrical samples with a diameter of 10 mm and a height of 15 mm were prepared, maintaining the specified height-to-diameter ratio of 1:1.5 for compression testing. The compressive test was conducted on the same Instron test 5567 screw-driven universal testing machine at a strain rate of 10^{-3} s^{-1} along the building direction.



Sample dimensions redesigned according to the standard: ASTM: E8/E8M – 13a

Figure 2.1. A schematic sketch showing the dimensions of the tensile samples fabricated as per the -ASTM: E8 /E8M– 13a standards (reproduced from (Karimi et al., 2021)).

2.6 Cytotoxicity and bacterial study of the Ti-eggshell composites

To compare the performance of the Ti-eggshell composite, eggshell compact produced by SPS, and bulk CP-Ti (solids of 10 mm diameter and 6 mm height) were utilized. For cytotoxicity assessment, samples were immersed in α -MEM media (10% fetal bovine serum and 1% penicillin-streptomycin solution). After 24 h, the solution was centrifuged, filtered, and added to the cell culture. Adipose-derived stem cells (ADSCs) at passage 6 were cultured in flasks containing the α -MEM media. The cytotoxicity of samples was determined using a lactate dehydrogenase (LDH) assay (CyQUANTTM LDH Cytotoxicity Assay Kit). When the cells reached 80% confluency, 20,000 cells/mL were seeded into each well of a 24-well plate containing the filtered solution from different samples and incubated for 24 h at 37 °C and 5% CO₂, a 50 μL solution from each well was transferred to a 96-well plate, and the standard protocols were followed to assess cytotoxicity. Cells grown in the polystyrene well plate were considered as positive control and cells exposed to lysis buffer served as negative control. The absorbance was measured at 490 nm and 680 nm using a microplate reader (FLUOstar Omega, BMG LABTECH, Cary, NC, USA). The quantitative data were analyzed using two-way ANOVA analysis, followed by post-hoc Tukey's honestly significant difference (HSD) test, with statistical significance set at $p < 0.05$, using the origin software.

The antibacterial activity was evaluated using bacterial cultures of gram-negative *pseudomonas aeruginosa* (ATCC 10145, referred to as *P. aeruginosa*) and gram-positive *staphylococcus aureus* (ATCC 6538, referred to as *S. aureus*) bacteria. They were cultivated in 8 mL tryptic soy broth (TSB) from Sigma-Aldrich followed by incubating for 12 h at 37 °C. The bacterial solution was diluted until an optical density reading of 0.52 was reached, corresponding to a concentration of 10^9 colony-forming units (CFU)/mL of TSB solution, measured at a wavelength of 562 nm. The surfaces were cleaned with deionized (DI) water, sterilized under UV light for 60 min and transferred to 24-well plates. 500 μL bacteria solution (10^6 CFU/mL) was added, and well plates were then incubated at 37 °C for 6 h and 24 h, respectively. After incubation, the bacterial solution was removed,

and the surfaces were rinsed with phosphate-buffered saline (PBS). Bacteria on the surfaces were fixed by immersing the samples in a fixative solution (3% glutaraldehyde, 0.1 M sucrose, and 0.1 M sodium cacodylate in DI water) for 45 min. Once the bacteria were fixed, they were allowed to sit in a buffer solution (fixative solution without glutaraldehyde) for 10 min, followed by immersion in 35%, 50%, 70%, and 100% ethanol for 10 min each. The dried samples were stored in a desiccator. Prior to imaging, the surfaces were coated with 10 nm gold (Au) to improve the conductivity of the sample. Bacterial morphology and biofilm formation on different samples were analyzed using FE-SEM (JEOL JSM-6500).

3 Fabrication of Ti6Al4V Specimens by LPBF

This chapter explains the structure-processing-properties correlation in LPBF-fabricated Ti6Al4V and the mechanical properties of the Ti6Al4V are compared with CP-Ti to evaluate the best possible composition for biomedical applications.

3.1 Characterization of the feedstock Ti6Al4V powder

Table 3.1 shows the composition of the Ti6Al4V powder (ASTM grade 23) containing 5.5–6.5 % Al, 3.5–4.5 % V, and a reduced amount of O (0.13) along with other trace elements.

Table 3.1. Composition of the feedstock Ti6Al4V powder.

Elements	Ti	Al	V	Fe	O	N	H
wt. %	Bal.	5.5–6.5	3.5–4.5	0–0.25	0–0.13	0–0.05	0–0.012

Figure 3.1 shows the feedstock characterization of the Ti6Al4V powder. In the present study, gas-atomized Ti6Al4V powder (Figure 3.1-(a,b)) was used, showing the presence of spherical-shaped particles along with minor satellites. These satellites present on large particles are due to the collision of the fine particles and partially molten particles as a result of gas circulation in the atomizing chamber (Sun et al., 2017). The particle size distribution plot displayed in Figure 3.1-(c) indicates the presence of a wide range of particle sizes, with a mean particle size (d_{50}) of $24 \pm 18 \mu\text{m}$. Figure 3.1-(d) exhibits the XRD pattern of the Ti6Al4V powder revealing reveals major peaks at 35.06° ($10\bar{1}0$), 38.36° ($000\bar{2}$), 40.11° ($10\bar{1}1$), 53.62° ($10\bar{1}2$), and 63.62° ($11\bar{2}0$), respectively corresponding to the HCP (α/α') crystal structure having the space group: P63/mmc (194).

3.2 Characterization of Ti6Al4V fabricated by LPBF

As illustrated in Figure 3.2-(a), the XRD patterns of LPBF Ti6Al4V exhibit major peaks consistent with those of the original Ti6Al4V powder, indicating the presence of the HCP (α/α') crystal structure. Notably, there is no evidence of the BCC (β) phase. In conventional processing, such as casting, and SPS (N. Singh et al., 2021), both HCP α -Ti and BCC β -Ti are typically observed due to the allotropic transformation of titanium above its transition temperature ($\sim 882^\circ\text{C}$). During cooling, the reverse transformation does not fully occur due to the β -stabilizing effect of V, leading to a dual-phase microstructure consisting of both α and β phases (N. Singh et al., 2021). However, in LPBF-processed Ti6Al4V, the cooling rate ranges between 10^5 – 10^6 K/s, preventing the formation of either the α or β phases and instead resulting in the formation of a supercooled α' martensitic structure. The optical microscopy image in Figure 3.2-(b) and the SEM image in Figure 3.2-(c) reveal an acicular martensitic structure, corroborating the XRD analysis. Both the α and α' phases exhibit an HCP crystal structure with similar lattice parameters. Hence, the XRD peaks revealing the HCP structure correspond to the martensite structure. Additionally, the rapid thermal cycles inherent to the LPBF process refine the microstructure, producing secondary and tertiary martensite, as shown in Figure 3.2-(d). Yang et al. (Yang et al., 2016) claimed this refinement to the repeated heating and cooling cycles during LPBF, which can induce secondary martensite in regions that have already undergone initial martensitic transformation, leading to more refined martensitic variants.

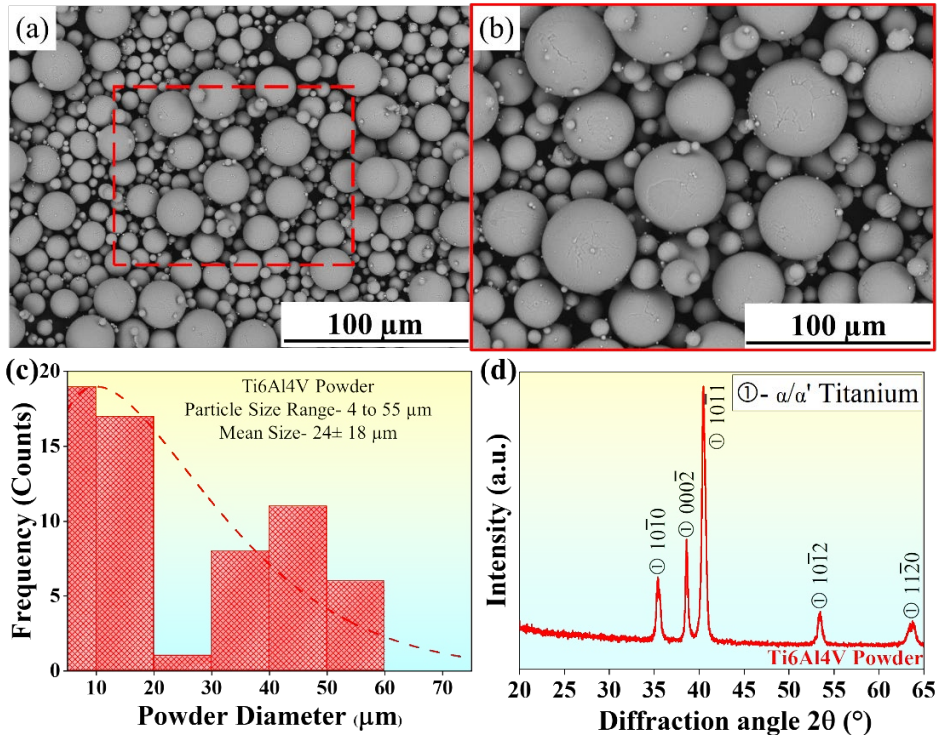


Figure 3.1. Feedstock characterization: Scanning electron microscopy image of the Ti6Al4V powder at (a) lower magnification, and (b) higher magnification. (c) Plot showing the particle size distribution of the employed gas-atomized Ti6Al4V powders where the average particle size is observed to be $24 \pm 18 \mu\text{m}$, and (d) the corresponding X-ray diffraction pattern of the Ti6Al4V powder.

The rapid cooling in LPBF generates a high density of dislocations within the martensitic structure, which act as nucleation sites for further martensitic transformations, particularly for secondary and tertiary martensite (Yang et al., 2016). Twinning within the martensitic structure also contributes to the refinement process, as it accommodates strain during transformation and provides additional interfaces for the nucleation of finer martensitic variants. These thermal cycles increase the density of dislocations and twins, resulting in shorter martensitic structures compared to the primary martensite. Furthermore, martensite can be classified based on the dimensions of its major and minor axes: primary martensite typically has a major axis greater than $20 \mu\text{m}$ and a minor axis varying in the range $1 \mu\text{m}$ and $3 \mu\text{m}$; secondary martensite has a major axis ranging between $10 \mu\text{m}$ and $20 \mu\text{m}$ and a minor axis ranging between -100 nm and 900 nm ; tertiary martensite is even smaller in dimensions, with a major axis ranging between $1 \mu\text{m}$ - $10 \mu\text{m}$ and a minor axis ranging between 20 nm and -90 nm . Quartic martensite, which is even finer, was not identified in the present microstructure (S. Liu & Shin, 2019; J. Yang et al., 2016).

In addition to the microstructure, Figure 3.2-(c) reveals spherical-shaped porosity in the Ti6Al4V, which is known as the gas porosity. This is commonly observed in the LPBF samples, that ranges from 0.1–0.3 %. The main reason behind this spherical porosity is due to the entrapment of gases that may come from gas flow or adsorbed gases in feedstock powder (Qian et al., 2016) or due to the presence of porosity in the gas-atomized powder.

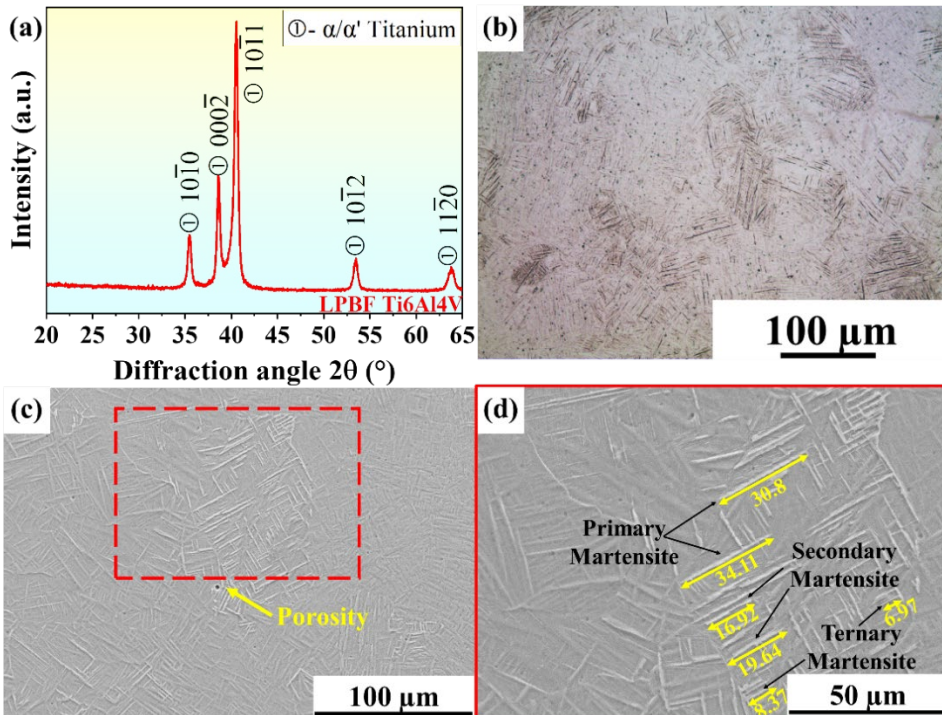


Figure 3.2. (a) The X-ray diffraction pattern, (b) optical microscopy image, scanning electron microscopy image at (c) lower magnification, and (d) higher magnification of the LPBF-fabricated Ti6Al4V sample.

3.3 Mechanical testing of LPBF Ti6Al4V samples

Figure 3.3 shows the tensile and compressive curves of the LPBF Ti6Al4V samples. Ti6Al4V (refer Figure 3.3-(a)) revealed the YS of 1180 ± 10 MPa and UTS of 1275 ± 12 MPa. The fracture strain was observed to be 7 ± 1 MPa and Young's Modulus of about 106 ± 0.8 GPa. These results are in the range of the previously reported results of LPBF Ti6Al4V (Krakhmalev et al., 2016; Prashanth et al., 2017; Vrancken et al., 2012). The LPBF Ti6Al4V shows hardness in the range of $412 \text{ HV}_{0.05}$. Such high hardness increased tensile strength and reduced ductility are attributed to the presence of the martensitic structure. On the negative side, an increase in mechanical properties increases Young's Modulus. Young's Modulus is the primary criterion for selecting a load-bearing implant, since it will widen the gap between natural bone and implant leading to the stress-shielding effect. In addition to the hardness data, as shown in Figure 3.3-(b) compressive yield strength was observed to be 1404 ± 1 MPa, and compressive ultimate strength was found to be 1820 ± 10 MPa with a fracture strain about $18 \pm 1\%$.

Figure 3.4 shows the fractography images of the LPBF Ti6Al4V samples after tensile test. The fracture surface reveals a mixed mode of the fracture with feature, where both dimples (correspond to plastic deformation) and with quasi-cleavage facets are observed. As shown in the low magnification fractography image in Figure 3.4-(a), the fracture morphology observed in the central region is ductile with a fibrous texture, dominated by dimples. These dimples are indicative of micro-void coalescence, which occurs during plastic deformation.

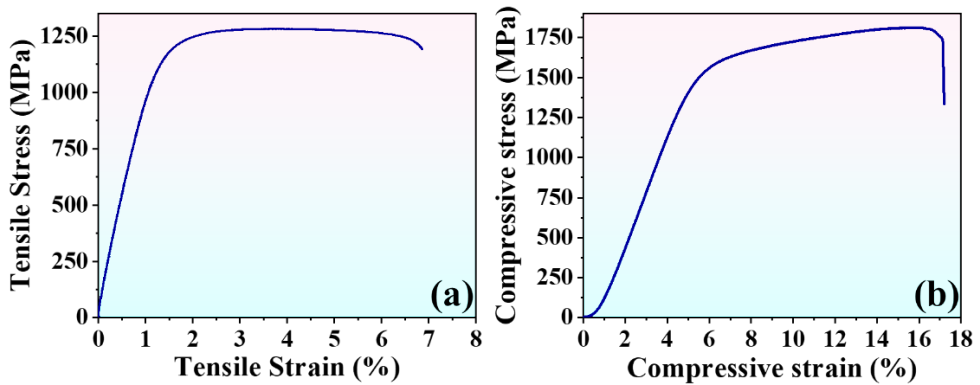


Figure 3.3. Room temperature mechanical properties of the LPBF Ti6Al4V alloy under (a) Tension and, (b) Compression.

The outer regions show smooth morphology, where localized shear stresses are concentrated. This combination of ductile and shear regions suggests a mixed mode of fracture typical for LPBF Ti6Al4V under tensile loading. Figure 3.4-(b, c) features quasi-cleavage facets along with localized dimple structures. The dimples arise from the nucleation, growth, and coalescence of microvoids, typical for ductile metals. The higher magnification image Figure 3.4-(c) reveals variations in dimple sizes, suggesting differences in local plasticity and void formation during the tensile test. Quasi-cleavage facets are intermediate to ductile and brittle fracture. In LPBF Ti6Al4V alloys, this is a common feature due to the presence of martensitic needles observed in the initial microstructure. When crack propagates, it progresses through the martensitic colony and produces these quasi-cleavage structures. These structures hampers ductility as compared to the conventional counterpart (Krakhmalev et al., 2016; Prashanth et al., 2017). However, the primary β grain boundary, fusion boundary, or such interface changes the direction of the crack propagation and delays the failure of the material (Krakhmalev et al., 2016; Shifeng et al., 2014). Similar quasi-cleavage facets are visible in Figure 3.4-(e) as well along with localized dimple structure showing localized plastic deformation with brittle fracture. On the other hand, Figure 3.4-(d, f) are higher magnification images of the localized deformed area showing various sizes of the dimple. However, in the image Figure 3.4-(f), dimples are shallow and elongated compared to Figure 3.4-(d) shows the shear lip characteristics. Whereas (Figure 3.4-(d)), the presence of larger dimples indicates that significant energy was absorbed before the final fracture. This also indicates grain boundary fracture or void formation at larger inclusions or defects, leading to the initiation of cracks under tensile loading. Overall, this fractography highlights the mixed-mode failure, influenced by micro-void coalescence, quasi-cleavage facets, and localized plastic deformation, characteristic of LPBF Ti6Al4V under tensile loading.

There exists a debate about the best possible candidate between Ti6Al4V and CP-Ti for bio-implants. It is very difficult to choose between these two materials (Shah et al., 2016) as CP-Ti does not contain any toxic content but is difficult to manufacture compared to Ti6Al4V. Due to the revolutionization in the manufacturing field, where the Ti6Al4V composition was coined, ease in the fabrication of Ti6Al4V was realized.

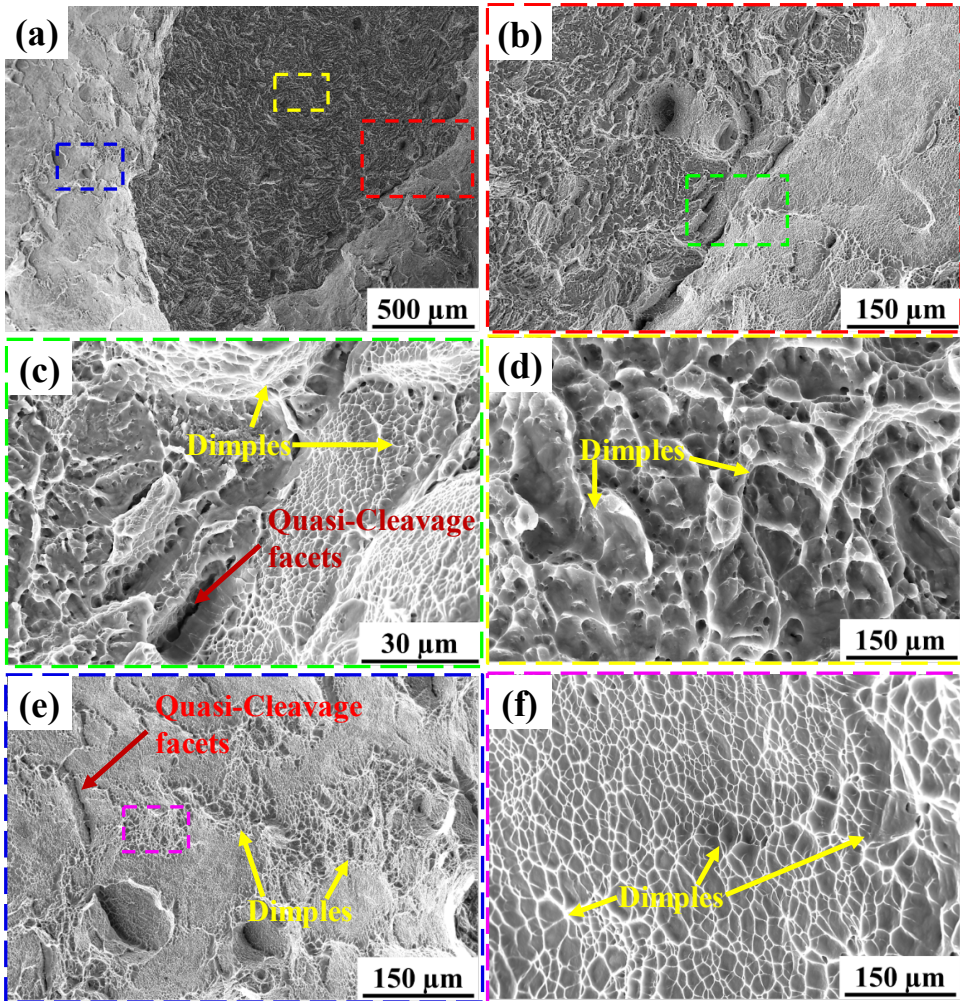


Figure 3.4. Fractography images of LPBF Ti6Al4V samples after tensile test. (a) A low magnification overview of the fracture surface, (b) a higher magnification image revealing dimple and quasi-cleavage facets, and corresponding (c) higher magnification image showing fine dimples (d) higher magnification image from the center (e) Lower magnification image from the, and corresponding (f) higher magnification image revealing varying dimple size indicating localized plastic deformation.

As a rule of thumb, CP-Ti is used for low-strength applications such as an oral implant, and maxillofacial implants, whereas Ti6Al4V is used for load-bearing applications. However, several case studies reported that neurological disorders result due to the presence of toxic elements like Al and V (Abdel-Hady Gepreel & Niinomi, 2013; Attar et al., 2020; Prakasam et al., 2017; Sarraf et al., 2022; X. Wang et al., 2016). As shown in Table 3.2, the tensile and compressive strength of the Ti6Al4V is ~ 10 times higher than the natural compact bone, while for CP-Ti, these values are around five times higher. Additionally, the present result shows that LPBF CP-Ti implants exhibit lower hardness and compressive strength compared to their Ti6Al4V counterparts. Despite this, Steinemann (Steinemann, 2000) reported that CP-Ti provides better integration to the bone perhaps due to the enhanced corrosion rate compared to Ti6Al4V (Steinemann,

2000; Williams, 2002). This supports the argument that CP-Ti is a more suitable material for orthopedic bio-implant applications than Ti6Al4V. Therefore, in the present research, CP-Ti is selected instead of Ti6Al4V. Moreover, as indicated in Table 3.2, numerous studies have demonstrated that CP-Ti can be effectively manufactured using LPBF, further supporting its viability for its use in orthopedic applications.

Table 3.2. Comparison of Young's Modulus and tensile properties of the natural bone, Ti6Al4V and CP-Ti fabricated by various manufacturing methods.

Material	Processing Method	YS (MPa)	UTS (MPa)	Fracture Strain (%)	E (GPa)	Ref.
Cortical Bone	-	-	135 ± 16	-	18 ± 4	(X. Wang et al., 2016)
ASTM F136-13 – Annealed wrought Ti6Al4V	Wrought followed by annealing	≥ 760	≥ 825	≥ 8	-	(ASTM International, 2021)
Ti6Al4V	Wrought	830–1070	920–1140	10–15	100–110	(Bartolomeu et al., 2022)
ASTM F3302 – 18 AM Ti alloys*	LPBF	≥ 795	≥ 860	≥ 10	-	(ASTM International, 2018)
ASTM F3302 – 18 AM Ti alloys*	LPBF	≥ 380	≥ 450	≥ 18	-	(ASTM International, 2018)
Ti6Al4V	LPBF	1180 ± 10	1275 ± 12	7 ± 1	106 ± 1	This work
Ti6Al4V	LPBF	1250 ± 15	1355 ± 20	8 ± 1	-	(Prashanth et al., 2017)
Ti6Al4V	LPBF	1110 ± 9	1267 ± 5	7 ± 1	109 ± 3	(Vrancken et al., 2012)
Ti6Al4V	LPBF	1098 ± 2	1265 ± 5	9 ± 1	-	(Krakhmalev et al., 2016)
CP-Ti Grade 2	LPBF	555 ± 3	757 ± 13	20 ± 2	-	(Attar et al., 2014)
CP-Ti Grade 2	LPBF	500	650	17	-	(Barbas et al., 2012)
CP-Ti Grade 1	LPBF	533 ± 3	714 ± 4	18 ± 1	-	(D. W. Wang et al., 2019)
CP-Ti Grade	LPBF	-	766	28	-	(Kang et al., 2017)
CP-Ti Grade	LPBF	445	542	20	-	(Depboylu et al., 2023)
CP-Ti Grade 2	LPBF	732 ± 6	630	20 ± 1	-	(Tao et al., 2020)

CP-Ti Grade	LPBF	792 ± 5	990 ± 10	6 ± 1	-	(Zhou et al., 2019)
CP-Ti Grade	LPBF	502 ± 2	-	34 ± 1	-	(J. Zhang et al., 2021)
CP-Ti Grade 2	LPBF (Micro-tensile)	600–680	780–850	12-16	-	(Wysocki et al., 2017)

3.4 Summary

This chapter provides an in-depth analysis of the mechanical properties of LPBF Ti6Al4V and its correlation with microstructure. The LPBF process induces a martensitic structure, which is linked to the quasi-cleavage and brittle fracture observed in the fractography images, potentially explaining the reduced ductility. However, some regions exhibited ductile fracture (where dimples are observed). The microstructural modification results in improved hardness, as well as higher tensile and compressive strength. This, in turn, raises Young's Modulus of the material, leading to a greater mismatch with natural bone and exacerbating the stress-shielding effect. Hence, comparing these outcomes with the CP-Ti, it reveals that CP-Ti offers superior biological and corrosion properties compared to Ti6Al4V, despite its reduced mechanical properties – a benefit in matching the mechanical properties of natural bone. The primary challenge of CP-Ti is its manufacturing complexity, which can be mitigated by using LPBF instead of traditional methods. Several studies have demonstrated that CP-Ti can be easily manufactured at optimized energy densities using LPBF. However, there remains a gap in the literature regarding the deformation behavior of CP-Ti at various strain rates and its relationship with microstructure and properties. Therefore, the next chapter will focus on exploring the processing-microstructure-property relationship of CP-Ti produced via LPBF.

4 Fabrication of CP-Ti by LPBF process

As discussed in Chapter 3, LPBF CP-Ti may be preferred over Ti6Al4V for load-bearing implants, especially considering the stress-shielding effect. However, there lack of information in the regarding the CP-Ti such as the effect of the strain rate on their mechanical properties and its correlation to the microstructure. Hence, this chapter explains the structure-processing-properties correlation of LPBF CP-Ti.

4.1 Characterization of the feedstock CP-Ti powder

Figure 4.1 illustrates the characterization of the feedstock powder used in this study. Gas-atomized CP-Ti powder was utilized (as depicted in Figure 4.1-(a,b)), where the particles exhibit a predominantly spherical shape with wider particle size distribution. Minor satellite particles attached to the boundaries of larger particles are also observed. These satellite particles are typical of gas-atomized powder formed due to the collision of fine and partially molten particles caused by gas circulation within the atomizing chamber (Sun et al., 2017). The particle size distribution (shown in Figure 4.1-(c)) reveals a broad range with a mean size (d_{50}) of $29 \pm 13 \mu\text{m}$. Additionally, the XRD pattern presented in Figure 4.1-(d) displays prominent peaks at 35.06° ($10\bar{1}0$), 38.36° ($000\bar{2}$), 40.11° ($10\bar{1}1$), 53.62° ($10\bar{1}2$), and 63.62° ($11\bar{2}0$), respectively corresponding to the HCP (α/α') crystal structure with the space group $P63/mmc$ (194).

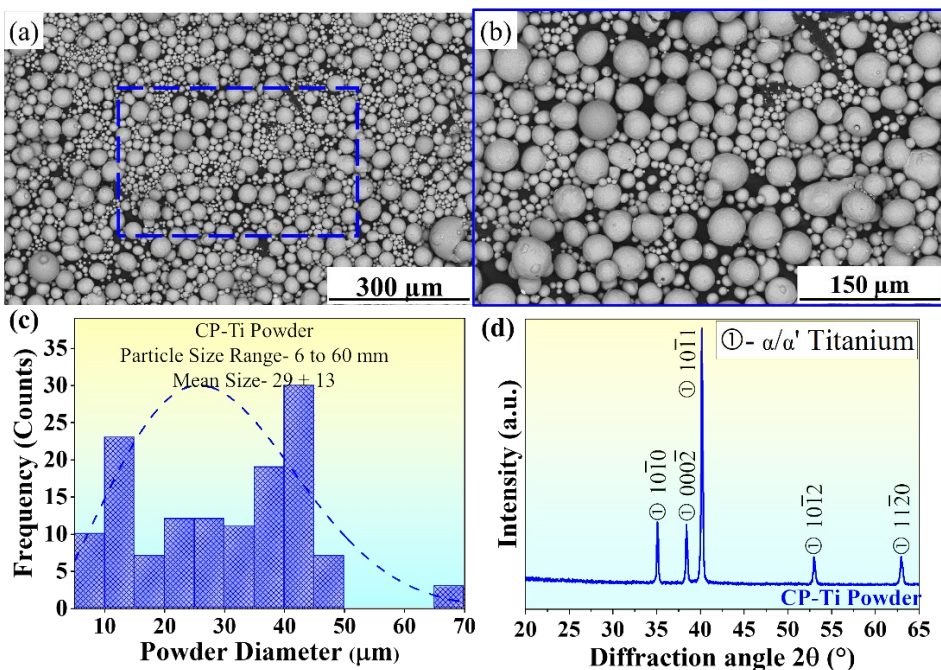


Figure 4.1. Feedstock characterization Scanning electron microscopy image of the CP-Ti powder at (a) lower magnification, and (b) higher magnification. (c) Plot showing the particle size distribution of the gas-atomized CP-Ti powders where the average particle size is observed to be $29 \pm 13 \mu\text{m}$ (d) X-ray diffraction pattern of the CP-Ti powder showing the presence of the HCP phase.

4.2 Characterization of CP-Ti produced by LPBF

As shown in Figure 4.2-(a), the XRD pattern of the LPBF CP-Ti reveals the presence of HCP α/α' structure. LPBF CP-Ti exhibits major peaks consistent with those of the original CP-Ti powder, indicating the presence of the HCP (α/α') crystal structure. As shown in Figure 4.2-(b), the microstructure shows the presence of porosity, which can be further categorized based on the shape of the pore. As mentioned in the previous chapter, the spherical porosity correlates to the gas entrapment and is hence known as gas porosity. Whereas irregular-shaped pores are formed due to the lack of fusion during the process (improper process parameters) known as the Lack of fusion (LOF) pores. The SEM images (Figure 4.2-(c)) reveal the presence of an acicular martensitic structure, corroborating the XRD results. Both the α and α' phases exhibit HCP crystal structure with similar lattice parameters. The rapid thermal cycles inherent to the LPBF process refine the microstructure, producing secondary and tertiary martensite (Figure 4.2-(c)) as explained in the earlier chapter.

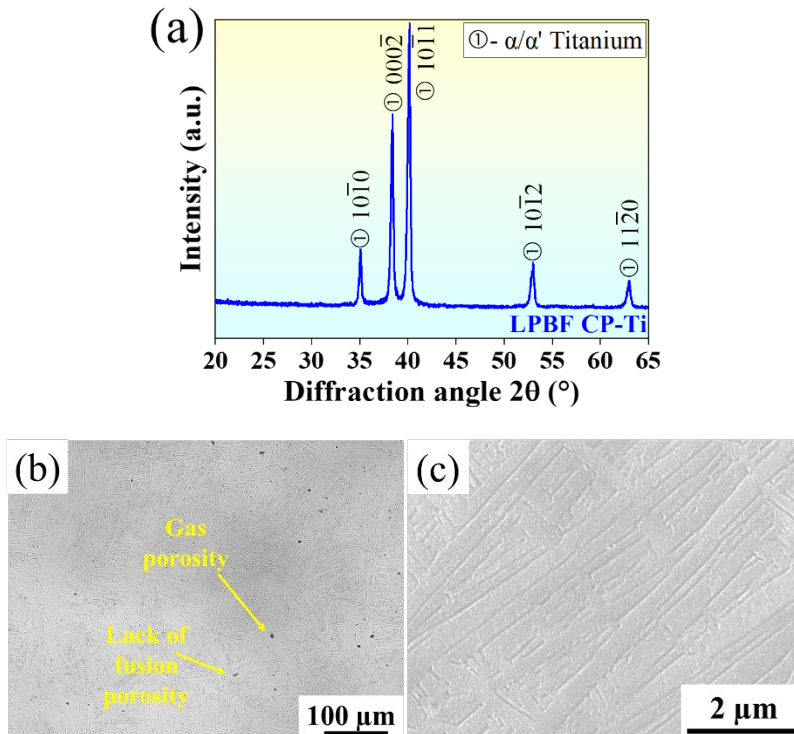


Figure 4.2. (a) X-ray diffraction pattern of the LPBF CP-Ti sample (b) Optical Microscopy image showing the presence of porosity and (c) higher magnification scanning electron microscopy image of the LPBF CP-Ti sample.

Figure 4.3 exhibits TEM images of the LPBF-processed CP-Ti. The selected area diffraction pattern (SAED) of LPBF CP-Ti (refer to Figure 4.3-(a)) displays a characteristic HCP pattern, indicative of martensitic phase formation in the case of CP-Ti. The SAED pattern, captured along the $[2\bar{1}\bar{1}0]$ zone axis, exhibits an angle of $\sim 28.62^\circ$ between the planes AB and $\sim 61.38^\circ$ between planes BC. The SEAD pattern aligns with the XRD and SEM analyses, where α' martensitic structure is identified as the primary phase in the

LPBF CP-Ti lattice. The bright field image (refer to Figure 4.3-(b)) illustrates various crystal defects within the LPBF CP-Ti, such as line defects in the form of dislocations. In addition to that, other surface defects such as the grain boundaries and twins/twin boundaries are also present in the LPBF-fabricated CP-Ti. These defects can be owing to the extreme cooling conditions during the LPBF processing of materials. Figure 4.3-(c) illustrates the inverse fast Fourier transformation image (IFT) showing the presence of numerous edge dislocations, including both positive and negative edge dislocations that formed during the solidification process. These edge dislocations can be attributed to the thermal cycling intrinsic to the LPBF process. Predictably, the negative edge dislocation induces the generation of tensile stress on the microstructure and the positive edge dislocation causes compressive stress in return. As shown in Figure 4.3 (c) on the entire surface, multiple positive and negative edge dislocations co-exist, which forms a series of dislocation grids.

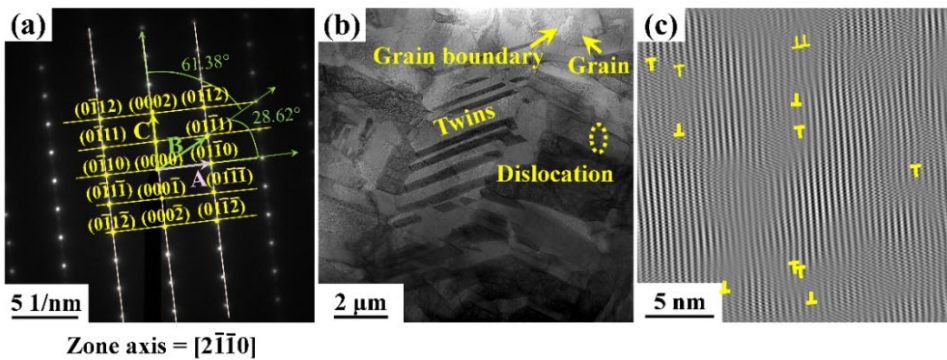


Figure 4.3. The transmission electron microscopy images of the CP-Ti fabricated by laser power-bed fusion process. (a) Selected area diffraction pattern confirming the presence of a hexagonally closed packed structure. (b) Bright-field image showing the presence of imperfections like grain boundaries, twins, and dislocations. (c) Inverse Fourier-filtered image showing the presence of multiple edge dislocations (R. Shukla et al., 2024).

4.3 Mechanical testing of CP-Ti produced by LPBF

The mechanical properties are quite important for predicting the performance of the CP-Ti under different loading applications. Figure 4.4-(a) shows the engineering tensile stress-strain curve as a function of different strain rates and Figure 4.4-(b) shows the true stress-strain curves of the LPBF CP-Ti. The mechanical properties data is summarized in Table 4.1 and compared with previously reported results in Table 3.2.

Slip systems refer to the combination of a slip plane and a slip direction along which dislocation motion occurs, leading to plastic deformation. In crystalline materials, slip generally occurs on planes with the highest atomic density, as these planes offer the least resistance to dislocation motion. In HCP materials, like that of α -Ti, the slip systems are more limited compared to face-centered cubic (FCC) or body-centered cubic (BCC) structures due to the lower symmetry of the HCP lattice. The HCP unit cell with two lattice parameters: a (in the basal plane) and c (along the c -axis). The c/a ratio, for CP-Ti, is ~ 1.587 , which influences the ease of slip in different directions. Ti contains three slip systems, basal plane, prismatic plane, and pyramidal plane. The basal plane (0001), the highest atomic density plane in the HCP structure is parallel to the base of the

hexagonal unit cell (refer to Figure 4.4-(c)). Also, it is the plane of closest atomic packing. In this plane, the atoms are arranged in a hexagonal pattern, and the distance between adjacent atoms is minimized, making it the densest plane in the HCP structure. As the slip direction is $\langle 1\bar{1}20 \rangle$, hence, $(0001) \langle 1\bar{1}20 \rangle$ is the most common and easiest slip system in the HCP material due to the low critical resolved shear stress (CRSS) required for dislocation motion. The easy slip along the basal plane is responsible for the ductility of the HCP material at lower temperatures. However, because slip is limited to certain planes and directions, HCP metals like Ti can exhibit anisotropy in mechanical properties, with different strengths and ductility along different crystallographic directions. Due to the limited number of slip systems in the HCP structure (compared to FCC materials), HCP metals like Ti can exhibit limited ductility. To accommodate more complex deformations, mechanisms such as twinning, where a portion of the crystal lattice reorients itself to accommodate strain can become active. Twinning in Ti often occurs on the $(10\bar{1}2)$ plane and allows for additional deformation along the c-axis. At higher temperatures and higher strain rates, the activation of additional slip systems, including prismatic and pyramidal slip, helps to overcome the limitations imposed by the HCP structure, leading to higher yield strength and improved ductility. Prismatic planes, which are $(10\bar{1}0)$ planes. These planes are perpendicular to the c-axis and contain the $\langle 11\bar{2}0 \rangle$ direction. $(10\bar{1}0) \langle 11\bar{2}0 \rangle$ is another important slip system, particularly when basal slip alone cannot accommodate the imposed deformation. Pyramidal planes, which can be $(10\bar{1}1)$, $(11\bar{2}1)$, and other higher-index planes. Pyramidal slip systems are less favorable than basal or prismatic slip due to higher CRSS, but they become active at higher stress levels and are essential for accommodating deformation along the c-axis (Salem et al., 2003; Z. Wang et al., 2019).

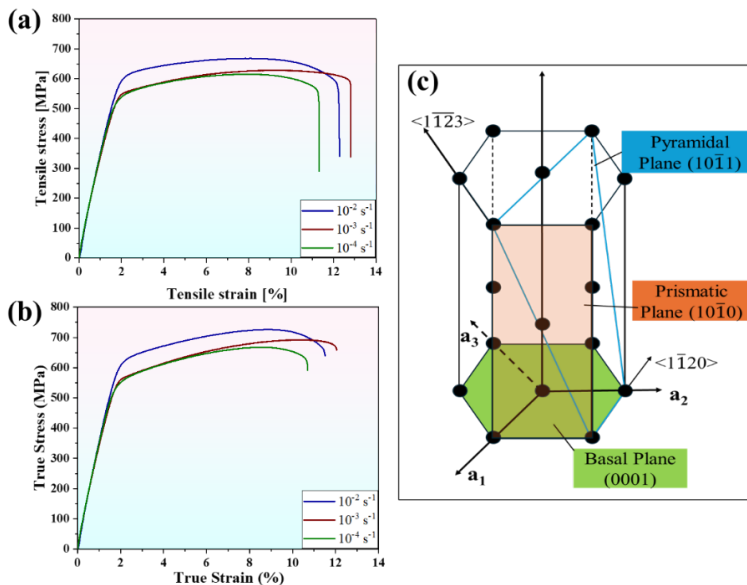


Figure 4.4. Mechanical properties for the CP-Ti produced by LPBF. Room temperature tensile stress-strain curves as a function of different strain rates (a) Engineering stress-strain and (b) True tensile stress-strain curves. (c) Schematic illustration of the hexagonal crystal structure showing various planes and directions.

In general, there are several strengthening mechanisms that explain the strengthening of crystalline materials. However, only a few strengthening mechanisms work for the LPBF CP-Ti. The first strengthening mechanism is solid solution strengthening. Despite having only 0.05% oxygen, owing to interstitial site occupation of the oxygen, strength improves as compared to the purer grade of Ti. (Dong et al., 2020; Yu et al., 2015) have reported that oxygen hinders the screw dislocation motion of the Ti and provides solid solution strengthening. Another strengthening mechanism is the grain boundary strengthening. Due to grain refinement, the number of grain boundaries increases, which perturbs dislocation motion. This dislocation motion is responsible for the plastic deformation and resulting strength of the material. Due to the increase in the number of grain boundaries, dislocation motion is arrested, which results in a reduction in ductility due to a reduction in plasticity and increase in strength. The most important strengthening mechanism is the martensitic formation. In summary, the yield strength in CP-Ti is primarily controlled by the initial activation of the slip systems, with the basal slip system playing a key role. As the material undergoes further deformation, additional slip systems and twinning mechanisms contribute to strain hardening, which in turn increases the UTS. The microstructural features such as grain size and α' plates, influenced by LPBF, further influence the strength by affecting dislocation motion and the activation of several hardening mechanisms.

Table 4.1. Table furnishing the Youngs Modulus, ductility, Yield Strength, and the ultimate tensile Strength for the CP-Ti produced by LPBF as a function of different strain rates.

Strain Rate (s⁻¹)	YS (MPa)	UTS (MPa)	True UTS (MPa)	Fracture Strain (%)
10 ⁻²	593.63	667.75	726.22	12.20
10 ⁻³	534.66	628.39	692.20	12.80
10 ⁻⁴	516.42	615.31	667.20	11.32

As shown in Figure 4.5, the compressive yield strength of LPBF CP-Ti is observed to be 678± 16 MPa. In addition, the sample during compressive test bulges and do not fracture until 50 % deformation. This is advantageous for bone implants, as orthopedic implants typically endure compressive loads. The observed higher deformability under compressive stress reduces the likelihood of premature failure, making it a beneficial for implant materials. As mentioned earlier, the HCP phase in CP-Ti has a limited number of slip systems. Compressive load requires a limited number of slip systems compared to tensile load. Hence CP-Ti shows better compression properties compared to tensile properties. CP-Ti shows hardness in the range of 260 ± 15 HV_{0.05}, which is aligned with the results reported in the literature (refer to Table 3.2). During conventional processing, CP-Ti or Ti6Al4V cannot achieve such high hardness. As discussed, such higher hardness is attributed to the presence of martensitic microstructure.

Figure 4.6 illustrates the fracture surface of tensile-deformed LPBF CP-Ti, highlighting several microstructural features that influence its mechanical performance. The image reveals the presence of unmelted particles and microporosity, which are prominent along the periphery of the fractured sample. These defects significantly compromise the ductility of the LPBF CP-Ti, leading to premature failure under tensile stress. Notably, samples tested at different strain rates exhibit similar fracture strains, suggesting that the observed imperfections are intrinsic to the material rather than testing conditions.

These imperfections are common in additively manufactured materials, where incomplete fusion during processing results in micro defects, compromising the mechanical properties of the material. (Attar et al., 2014) and (D. W. Wang et al., 2019)

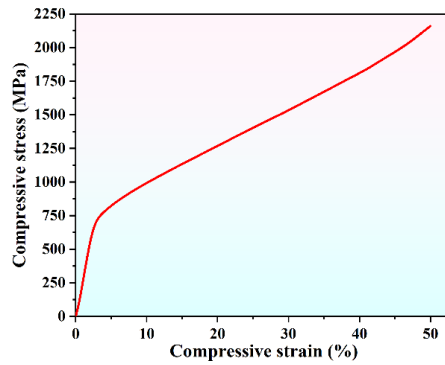


Figure 4.5. Compression stress-strain curve of the LPBF CP-Ti sample.

have also reported similar results in LPBF CP-Ti. In other areas of the fracture surface, a combination of smooth regions (quasi-cleavage fracture) and dimples are observed. (D. W. Wang et al., 2019) further explained that the quasi-cleavage facets are due to cleaved acicular α' -Ti grains. The surface also exhibited isolated, randomly distributed microscopic voids. (Attar et al., 2014; Kang et al., 2017; D. W. Wang et al., 2019). (Attar et al., 2014) concluded that nucleation and growth of the microvoids led to the formation of microscopic cracks, which propagated along the stress axis. (D. W. Wang et al., 2019) also corroborated above mentioned behavior in the LPBF CP-Ti.

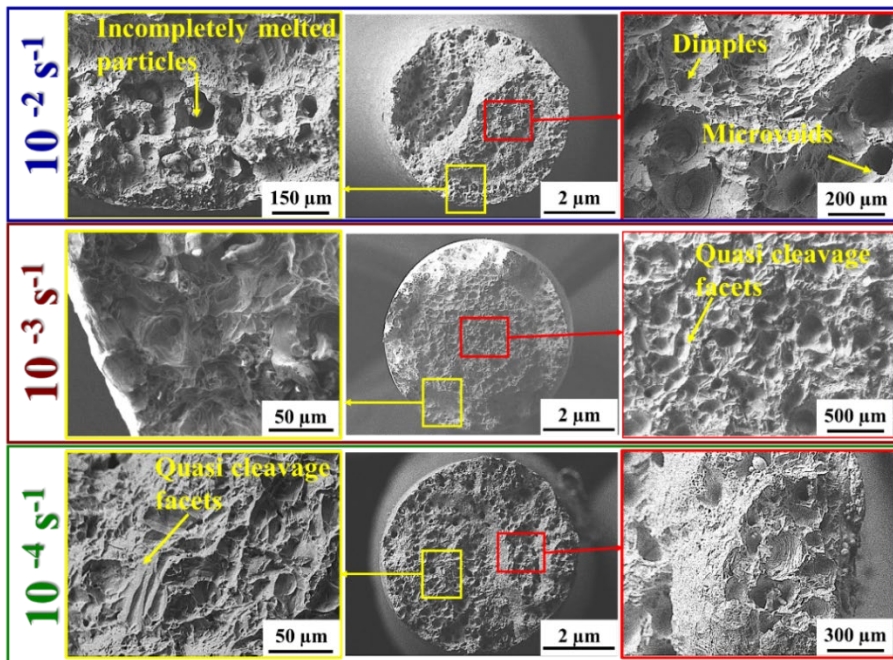


Figure 4.6. Scanning electron microscopy fractography images of the LPBF processed CP-Ti samples after the tensile test as a function of different strain rates.

4.4 Summary

The LPBF CP-Ti samples exhibit a martensitic structure offering high strength in these materials. This martensite strengthening resulted in improved tensile strength. Moreover, CP-Ti showed improved compressive strength and higher deformability in compression compared to the same material manufactured using conventional processing. This gives an advantage to use LPBF CP-Ti for load-bearing implants.

However, it is noteworthy that the compressive strength and resultant Young's modulus of CP-Ti are considerably higher than those of natural bone, may lead to stress-shielding effect. This issue may be addressed by fabricating porous CP-Ti lattices. The LPBF technique facilitates the production of such porous structures, allowing for the optimization of mechanical properties to closely match those of natural bone (Alkentar et al., 2023; Van Bael et al., 2012). This approach is further explored in Chapter 6. Mechanical properties are crucial for addressing the stress-shielding and strengthening perspective for load-bearing applications. However, the bio-inert behavior of the Ti-based implant always perturbed the sole use of the Ti-based alloys. Conversely, ceramics-based biomaterials are known for their biocompatibility, corrosion resistance, and compressive strength, making them suitable for hard tissue applications.

Bio-active ceramics, such as HAp (Kumar Yadav et al., 2023), tri-calcium phosphate (Yadav et al., 2022), amorphous calcium phosphate (ACP) (Ma et al., 2023), or CaCO_3 shows demonstrate superior bioactivity (RYAN et al., 2006). Notably, CaCO_3 is the primary component of natural bone, coexisting with HAp and collagen, making, it easy to osseointegrate. The main advantage of using CaCO_3 -based implants is their bioresorbability. Bioresorbable materials also degrade like biodegradable materials but also release a controlled amount of Ca^{+2} and PO_4^{-3} , which act as therapeutic agents to

heal bone injuries and increase bactericidal activity (Kumar et al., 2015; Vuola et al., 1998). However, implants made from these ceramics are prone to brittle failure and have inferior mechanical properties, which limits their usage as a bio-implant. Nevertheless, the inherent brittleness of ceramics poses a significant risk of early-stage implant failure under load-bearing conditions. This creates a critical need for biomaterials that offer both mechanical durability and effective biological performance (Kumar et al., 2015), (Chu et al., 2006; Kumar, Dhara, et al., 2013; Kumar, Webster, et al., 2013). This has led to growing interest in biocomposites that combine the strength and ductility of metals with the bioactivity of ceramics. As discussed earlier in chapter 1, eggshells are an excellent source of CaCO_3 , however, standardized manufacturing methods for their use remain undeveloped. Moreover, to date no data is reporting the SPS technique to produce eggshells/ CaCO_3 bone implants Hence, the densification of the eggshell powder by SPS is elaborated in the next chapter.

5 Eggshell densification by SPS

This chapter discusses the sintering behavior of the calcium carbonate-rich eggshell and determines the optimum sintering temperature for its consolidation.

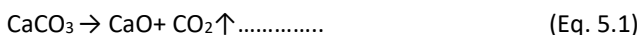
5.1 Feedstock characterization of eggshell powder

Table 5.1 details the chemical composition of the feedstock eggshell powder, which is a calcareous biomaterial. In other words, the eggshell powder primarily consists of calcium carbonate (CaCO₃), with calcium (Ca), carbon (C), and oxygen (O) being the predominant elements, constituting approximately 32 wt.%, 48 wt.%, and 19 wt.%, respectively (Hincke, 2012). In addition to these basic elements, the analysis also confirmed the presence of other elements like magnesium (Mg) and silicon (Si), along with trace amounts of aluminum (Al), chlorine (Cl), sodium (Na), iron (Fe), phosphorus (P), sulfur (S), and strontium (Sr) (Tangboriboon et al., 2012).

Table 5.1. X-ray fluorescence analysis showing the composition of the raw eggshell powder.

Elements	C	O	Na	Mg	Al	Si	P	S	Cl	Ca	Fe	Sr
Concentration (wt.%)	19.30	47.51	0.16	0.36	0.19	0.35	0.17	0.19	0.08	31.58	0.05	0.05

Figure 5.1 presents the characterization of the eggshell powder used in this study. The SEM images (Figure 5.1-(a)) reveal that the eggshell powder contains a broad particle size distribution having irregularly shaped particles, which is commonly present in eggshell powders (Awogbemi et al., 2020). A higher-resolution SEM image of a single large particle (Figure 5.1-(b)) shows the presence of open pores, which are naturally occurring in eggshells, allowing gas exchange through micropores between the crystalline calcite structures (Y. Huang et al., 2020). The particle size distribution of the raw eggshell powder is depicted in Figure 5.1-(c), with sizes ranging from 0.50 μm to 52.00 μm and an average particle size of 18 ± 12.00 μm, indicating a wide distribution. TGA was conducted to assess the thermal stability of the eggshell powder. The mass loss with increasing temperature, shown in Figure 5.1-(d), occurs in three distinct stages under ambient pressure. The initial mass loss of 0.8%, observed between room temperature and approximately 250°C, is attributed to moisture removal from the powder (Cree & Pliya, 2019; Pedavoah et al., 2018; V. Singh & Sharma, 2017). Eggshells consist of a composite structure of non-calcifying membranes (organic matter) and a calcified shell matrix (mainly CaCO₃). The organic matter, being metastable, decomposes within the temperature range of 250 °C to 650 °C, leading to a second mass loss of about 7.6% (Cree & Pliya, 2019; Engin et al., 2006; Naemchan et al., 2008b; Pedavoah et al., 2018; V. Singh & Sharma, 2017). The third stage, showing a mass loss of ~48.9%, corresponds to the decomposition of CaCO₃, with calcination occurring between 800 °C and 900 °C, depending on the source and heating conditions (Hossain & Roy, 2018). The calcination reaction is shown in Eq. 5. Post-calcination, CaO, which is white, porous, and fragile, is formed (Tangboriboon et al., 2012).



XRD analysis was performed on the eggshell powder before and after TGA to identify the phases present. The XRD pattern of the unprocessed eggshell powder (Figure 5.1-(e)) displays peaks at 23.05° (012), 29.41° (104), 35.98° (110), 39.42° (113), 43.17° (202), 47.52° (018), and 48.58° (116), consistent with the calcite (CaCO₃) phase, which is in line with other studies (Onwubu et al., 2019). Calcite, one of the three polymorphs of CaCO₃, is the most thermodynamically stable at room temperature and atmospheric pressure, exhibiting a rhombohedral crystal structure (R $\bar{3}$ c) (Chang et al., 2017). The most intense diffraction peak at 29.41° corresponds to the (104) plane, confirming the presence of calcite (Hoque, 2013). CaO being hygroscopic, rapidly absorbs moisture from the atmosphere and converts to portlandite, also known as hydrated lime (Usta et al., 2022). The portlandite phase has a hexagonal crystal structure (P $\bar{3}$ m1) with a:c ratio of 1:1.36 (Esquivias et al., 2018). The appearance of portlandite supports the decomposition of CaCO₃ to CaO and its subsequent hydration to Ca(OH)₂, as outlined in Eq. 5.1 and 5.2.



5.2 SPS of eggshell powder

The relative density obtained during the SPS process was plotted against various parameters, including sintering time (Figure 5.2), sintering temperature (Figure 5.3), and holding time (Figure 5.4). These plots provide valuable insights into the densification process. As illustrated in Figure 5.2, the densification process during SPS occurs in multiple stages, each influenced by the applied pressure and temperature. The initial stage involves the application of pressure during the pre-sintering or pre-pressing step, where the powders are subjected to 50 MPa of pressure prior to heating. This step plays a crucial role in the densification process by facilitating the fragmentation, rearrangement, and improved contact between particles. The increased contact area between particles during this stage enhances the activation energy required for neck growth, which subsequently leads to densification as the necks between particles expand and the compact becomes more cohesive. Therefore, a greater number of contact points during this stage contributes significantly to the overall densification process (Rahaman, 2014).

Following the pre-pressing step, the actual sintering process begins, where a high electric current is passed through the compact, generating heat through the Joule heating phenomenon. The SPS process theorizes that this current flows between adjacent particles, creating plasma and electric arcs that increase the sintering temperature, promote neck formation, and reduce porosity (L. Huang et al., 2022). This stage is critical for achieving densification, as demonstrated by the changes in densification with temperature shown in Figure 5.3. Temperature is a key driving force in the sintering process, as it influences the activation energy of the sintering mechanisms. There are six primary sintering mechanisms at play, three of which contribute to densification. The non-densifying mechanisms, which include surface diffusion, lattice diffusion from the surface, and vapor transport, primarily result in particle growth without contributing to overall densification. In contrast, the densifying mechanisms – grain boundary diffusion, lattice diffusion from the grain boundary, and plastic flow – are responsible for the significant shrinkage and densification of the compact, as evidenced in Figure 5.3.

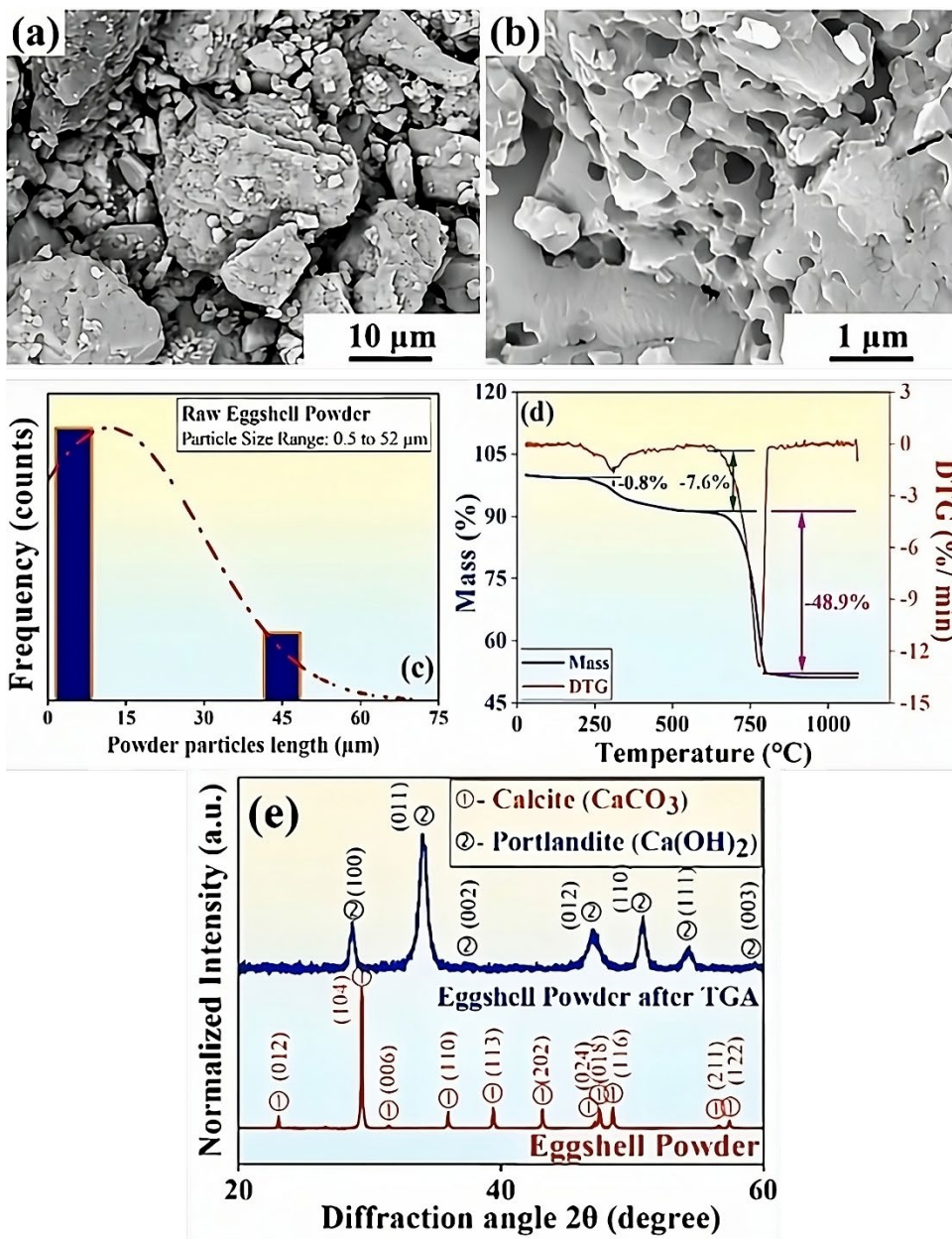


Figure 5.1. Characterization of the feedstock eggshell powder (a), (b) scanning electron microscopy images, (c) particle size measurement plot, (d) thermogravimetric analysis plot, and (e) X-ray diffraction patterns of the eggshell powder (adapted from (R. Shukla et al., 2023)).

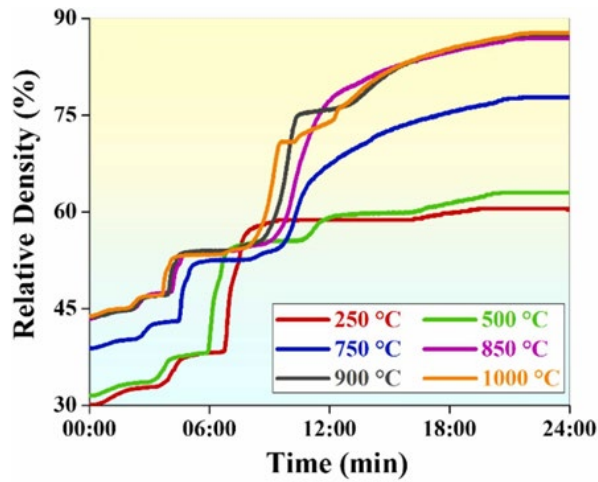


Figure 5.2. Densification curves obtained for different spark plasma sintered samples as a function of sintering time (adapted from (R. Shukla et al., 2023)).

The competition between these mechanisms is strongly temperature-dependent, with higher sintering temperatures favoring the densifying mechanisms, leading to higher relative densities (L. Huang et al., 2022). Throughout the sintering process, the applied pressure of 50 MPa persists, further enhancing particle contacts and driving the densifying mechanisms. However, the non-densifying mechanisms are largely unaffected by the applied pressure and its impact on the compact structure (Shrivastava et al., 2021). Additionally, the simultaneous occurrence of particle fragmentation and sintering alters the surface area of the particles, thereby influencing the kinetics of the sintering process. These changes can affect the decomposition or recrystallization temperatures (Bellucci et al., 2018). Overall, the application of pressure during the hot consolidation process plays a crucial role in altering transformation temperatures and mechanisms.

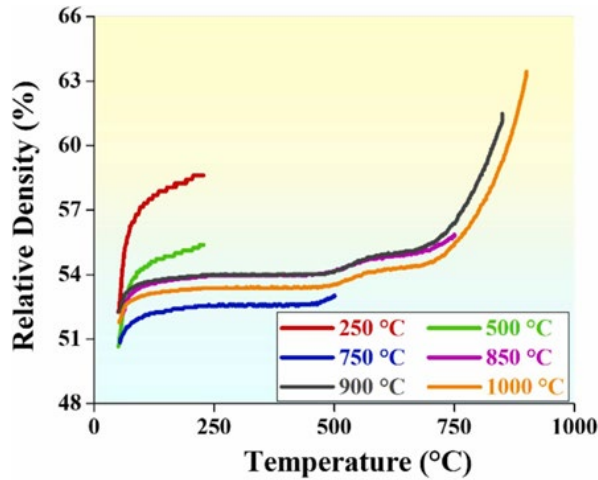


Figure 5.3. Densification curves obtained for different spark plasma sintered samples as a function of temperature (adapted from (R. Shukla et al., 2023)).

Once the desired sintering temperature is reached, the samples are held at that temperature for a specified duration. Figure 5.4 illustrates the effect of holding temperature on relative density. At relatively low sintering temperatures, such as 250 °C and 500 °C, changes in relative density are minimal. However, at higher holding temperatures, the increase in density is primarily due to the elevated temperature rather than the duration of holding. This indicates that densifying mechanisms become more prominent at higher temperatures, whereas holding time has a negligible effect (Kermani et al., 2014). The final stage of the SPS process involves cooling, during which thermal shrinkage further densifies the compact. As shown in Figure 5.3, the extent of thermal shrinkage and the corresponding changes in densification are highly dependent on the sintering temperature. Higher sintering temperatures result in greater expansion of the compact, leading to more significant changes in relative density compared to lower temperatures. Consequently, at lower sintering temperatures (250 °C and 500 °C), changes in relative density are minimal, resulting in a relatively flat curve. In contrast, higher sintering temperatures (850 °C, 900 °C, and 1000 °C) yield more pronounced changes in relative density (Rahaman, 2014).

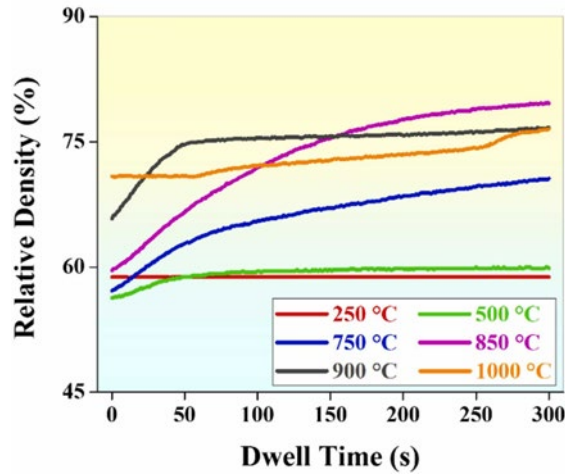


Figure 5.4. Densification curves obtained for different spark plasma sintered samples as a function of dwell time (adapted from (R. Shukla et al., 2023)).

5.3 Characterization of eggshell compacts

Figure 5.5 presents SEM images of the eggshell samples sintered at six different temperatures. These images clearly highlight the differences in density and porosity among the samples sintered at 250 °C, 500 °C, 750 °C, and 850 °C. As observed, the eggshell powder sintered at 250 °C and 500 °C retained individual particle structures even after the SPS process, indicating insufficient densification at these temperatures (63% and 60% relative density, respectively). As the sintering temperature increased, the compact became denser due to the activation of various sintering mechanisms and the reduction of particle boundaries, which almost disappear at 850 °C. However, even at this temperature, a network of closed porosity was still present (R. Shukla et al., 2020). The densities achieved are mentioned in Table 5.2.

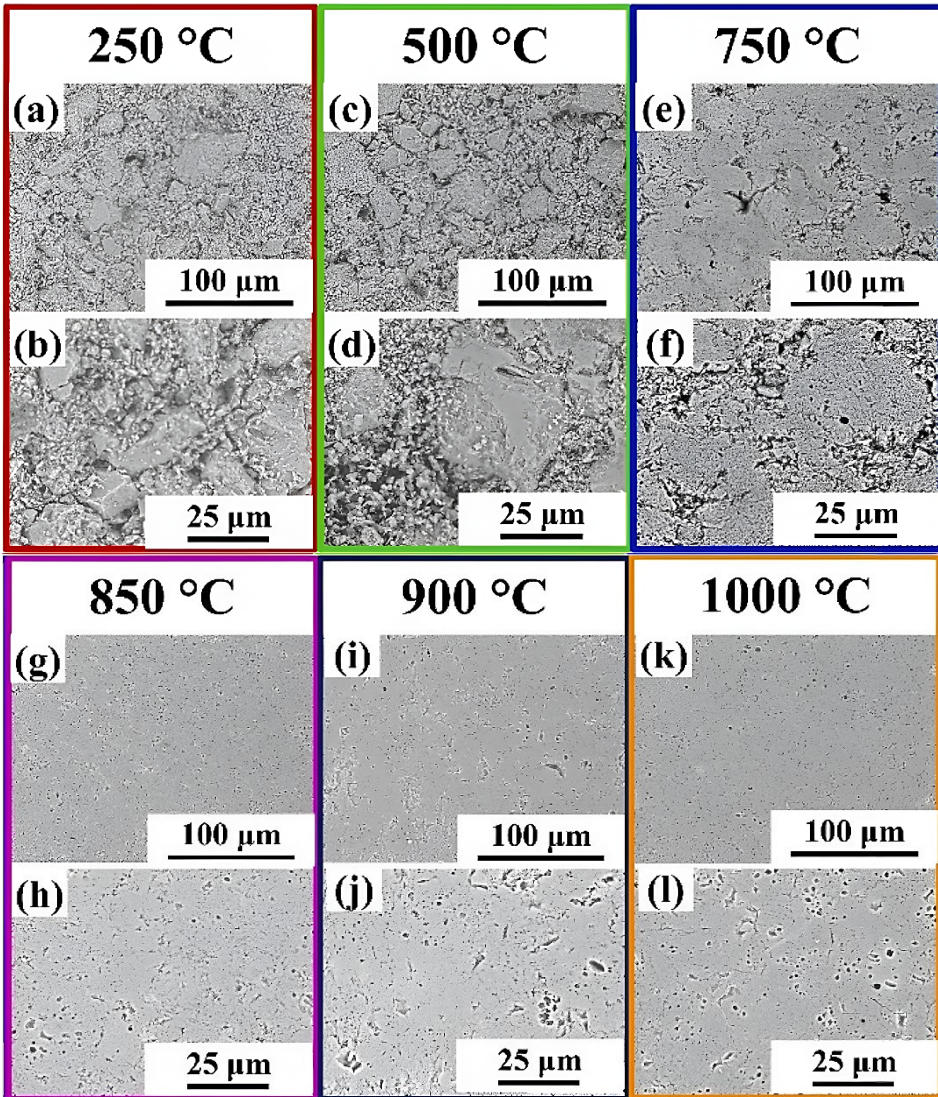


Figure 5.5. Scanning electron microscopy images of the eggshell powder sintered at various temperatures (a), (b) 250 °C, (c), (d) 500 °C, (e), (f) 750 °C, (g), (h) 850 °C, (i), (j) 900 °C, and (k), (l) 1000 °C, respectively (adapted from (R. Shukla et al., 2023)).

Table 5.2. Achieved sinter density at various sintering temperatures.

Sintering Temperature	250 °C	500 °C	750 °C	850 °C	900 °C	1000 °C
Achieved Density (%)	60 ± 1	63 ± 2	78 ± 0.1	87 ± 1	88 ± 3	88 ± 3

Figure 5.6 presents the XRD patterns of the eggshell powder sintered at various temperatures. The XRD patterns, as depicted in Figure 5.6, reveal the crystalline structure of the sintered compacts. The prominent peaks observed in the XRD graph confirm the rhombohedral crystal structure, which corresponds to the calcite phase of calcium carbonate (CaCO_3). Notably, all major peaks are concentrated around 29° , aligning with

the (104) plane of the calcite phase. Despite the sintering process being conducted at temperatures exceeding the typical decomposition temperature of CaCO_3 (800 °C), no additional peaks were detected that would indicate the presence of calcium oxide (CaO) or calcium hydroxide ($\text{Ca}(\text{OH})_2$). This suggests that during SPS, the decomposition temperature of CaCO_3 shifts above 1000 °C. These XRD results clearly indicate that the sintered compacts are predominantly composed of the calcite phase, with no evidence of phase transformation (Tangboriboon et al., 2012).

The FTIR spectra, shown in Figure 5.7, provide detailed information regarding the various stretching and bending vibrations of the functional groups present in the sintered eggshell compacts. Across all sintering temperatures, the FTIR spectra demonstrates the presence of consistent functional groups, with no significant differences observed. The FTIR analysis of the eggshell powder identified four major peaks at 1410 cm^{-1} , 1084 cm^{-1} , 873 cm^{-1} , and 712 cm^{-1} , which are characteristic of the carbonate group (Naemchan et al., 2008b; Yilmaz et al., 2019). Eggshells primarily consist of CaCO_3 , where the ionic bond between calcium and carbonate ions is complemented by covalent bonds within the carbonate group. In carbonates, the carbon atom is covalently bonded to three oxygen atoms, and this C-O bond is responsible for the vibrations detected in the FTIR spectra (Wong, 1991) (Shafiu Kamba et al., 2013).

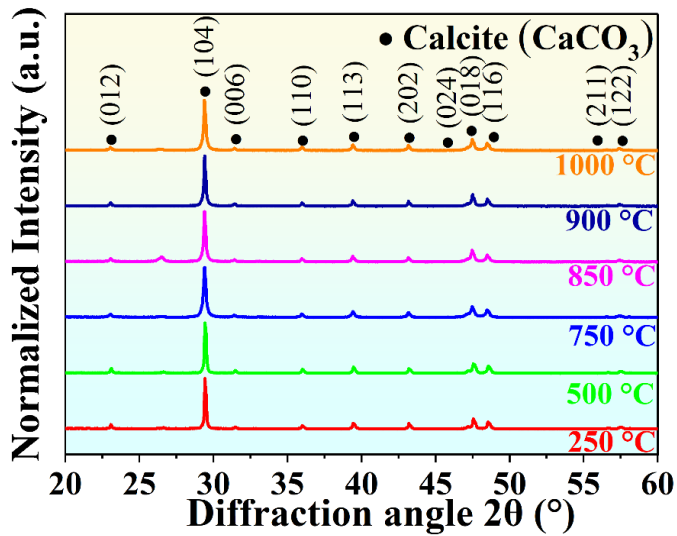


Figure 5.6. X-ray diffraction patterns of the eggshell powder spark plasma sintered at 250 °C, 500 °C, 750 °C, 850 °C, 900 °C, and 1000 °C, respectively (adapted from (R. Shukla et al., 2023)).

The symmetric vibration (ν_1), typically found at 1083 cm^{-1} , was weakly present in the eggshell powder and diminished further with increasing sintering temperatures, as evidenced by a decrease in peak intensity, which is consistent with previous reports on CaCO_3 (Kim et al., 2021). A prominent peak at 1410 cm^{-1} corresponds to the asymmetric stretching (ν_3) of the carbonate ion (CO_3^{2-}), characterized by molecules moving towards and away from each other with varying intensities in different directions (Fleet, 2009). Asymmetric stretching can be identified as the to-and-fro moment of molecules towards each other, similar to symmetric stretching, but with different intensities in each direction (Khan et al., 2001). Additionally, sharp and narrow peaks at 712 cm^{-1} and 873 cm^{-1} were observed, corresponding to symmetric bending (in-plane

bending, ν_4) and asymmetric bending (out-of-plane bending, ν_2) respectively (Fleet, 2009). These FTIR spectra corroborate previous findings and confirm the presence of carbonate ions, even in compacts sintered at elevated temperatures such as 1000 °C. The presence of trace elements like magnesium (Mg) and sodium (Na) in the eggshells, which may exist in carbonate forms along with calcium carbonate, is likely responsible for variations in peak intensity relative to sintering temperature.

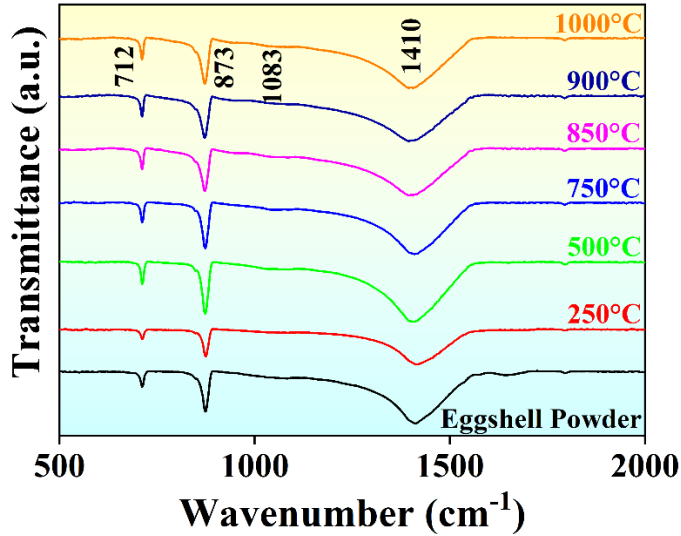


Figure 5.7. Fourier-transformed infrared spectroscopy traces of the eggshell powder spark plasma sintered at 250 °C, 500 °C, 750 °C, 850 °C, 900 °C, and 1000 °C, respectively (adapted from (R. Shukla et al., 2023)).

The microhardness test results for the sintered eggshell compacts are depicted in Figure 5.8. Among the tested samples, the compact sintered at 850 °C exhibited the highest microhardness value of $157 \pm 6 \text{ HV}_{0.05}$. Conversely, compacts sintered at 750 °C, 900 °C, and 1000 °C displayed similar hardness values of 149 ± 5 , 149 ± 7 , and $148 \pm 8 \text{ HV}_{0.05}$, respectively. This indicates that increasing the sintering temperature beyond 850°C does not significantly influence the microhardness of the eggshell compacts. The hardness values are closely associated with the density of the compacts, and since compacts sintered at 850 °C, 900 °C, and 1000 °C exhibited similar theoretical densities (and comparable porosity levels), their hardness values were nearly identical. Also, it is interesting to note that all these samples show the presence of similar phases that are also attributed to the presence of similar (Gong, 2003; Tang & Gong, 2013)(Gong, 2003; Tang & Gong, 2013). Notably, the hardness values are consistent with those reported for pure calcite phases (105–140 HV) (Pandya et al., 1983; Wong, 1991).

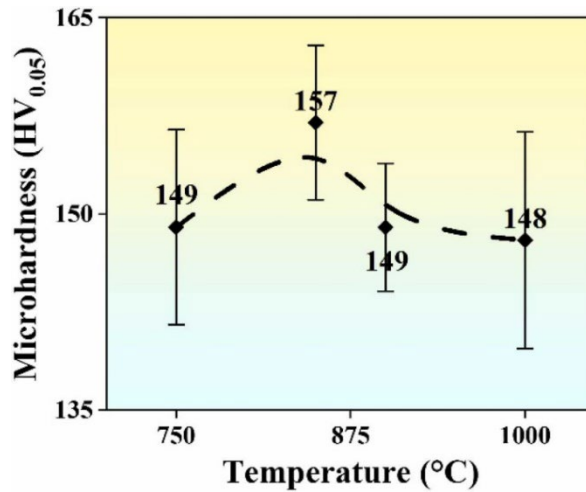


Figure 5.8. Microhardness values of the spark plasma sintered eggshell powder at different temperatures: 750 °C, 850 °C, 900 °C, and 1000 °C (adapted from (R. Shukla et al., 2023)).

5.4 Summary

Sintering is highly temperature-dependent, with higher sintering temperatures leading to denser samples through porosity reduction. Consequently, the SPS graph for eggshell powder sintered at higher temperatures (850 °C, 900 °C, and 1000 °C) in Figure 5.3 reflects the highest achievable density. Both XRF and XRD analyses confirm the dominance of the calcite phase (CaCO_3) as the major phase, even in samples sintered at temperatures up to 1000 °C. According to TGA, the decomposition of CaCO_3 into CaO should commence at 800 °C, which could complicate the production of pore-free, dense samples at temperatures exceeding 800°C. However, the concurrent application of pressure and heat during the SPS process appears to alter the kinetics of this decomposition reaction (Bellucci et al., 2018). The XRD and FTIR analyses of eggshell samples sintered above 800 °C (850 °C, 900 °C, and 1000 °C) showed that the calcite phase remained unchanged, with no evidence of calcination, like the original eggshell powder. This suggests that the decomposition reaction temperature has been elevated, preventing decomposition even at 1000 °C. Moreover, the optimal balance of densification and microhardness was achieved at 850 °C, with no significant improvement observed upon increasing the sintering temperature to 900 °C or 1000 °C. It is also noteworthy that sintering the eggshell powder at higher temperatures did not yield an optimal combination of mechanical properties. Thus, 850 °C is determined to be the optimal sintering temperature for eggshell powder compaction, enabling the production of dense compacts without the addition of reactive phases.

This chapter finalized the optimum sintering parameters for the consolidation of eggshell powder by SPS. The optimum sintering temperature and pressure is found to be 850 °C and 50 MPa pressure, respectively. These findings establish a foundational step towards the fabrication of Ti-eggshell composites. The next chapter will focus on the fabrication of CP-Ti lattice structures and their integration with eggshell powder to create the Ti-eggshell composite.

6 Fabrication of eggshell-based composite

This chapter discusses the production of Ti-eggshell composite and hence involves processing parameters and properties optimized in Chapters 4 and 5. As discussed in Chapter 4, to produce implants with desired mechanical properties, porous lattices are involved. Hence the first part of the chapter discusses the fabrication of CP-Ti lattice LPBF, which in the later part of the chapter integrated with the eggshell powder to fabricate novel Ti-eggshell composite. The structure- mechanical properties correlation was established for the composite. In addition to this, the produced composite was tested for the bacterial and cytotoxicity studies. The mechanisms involved in bacterial adhesion and growth will be elucidated.

6.1 Microarchitecture of CP-Ti lattice

The microarchitecture of the lattice structure designed to fabricate CP-Ti using LPBF is furnished in Figure 6.1. In the current study, a hexagonal truss-like structure, or a hexagonal prism structure (hereafter HXP) was selected for implant design because, the HXP structure (with 60–70% porosity (Li et al., 2009; X. P. Tan et al., 2017)) provides Young's modulus in the range of the cortical bone (7–30 GPa) (Hameed et al., 2021) and offers good compressibility and energy absorptivity (Choy et al., 2017). The HXP lattice includes both vertical and horizontal struts, which are better achievable than inclined struts by LPBF (Li et al., 2009; Van Bael et al., 2012).

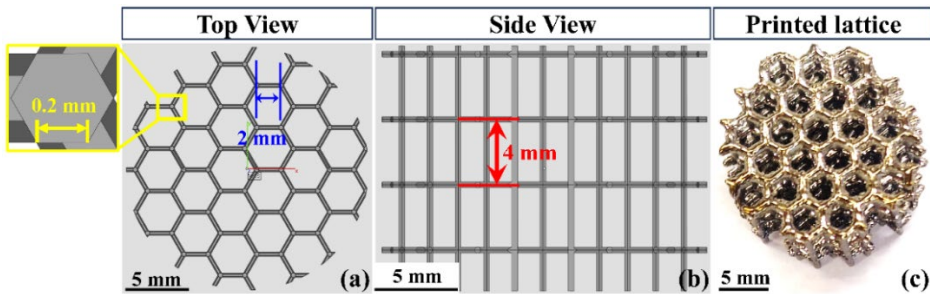


Figure 6.1. Micro-architecture of the lattice structure, (a) Computer-aided design (CAD) showing the top view of the lattice and the inset showing the structure of an individual strut, (b) CAD design showing the side view of the lattice, and (c) optical microscopy image of the printed CP-Ti lattice (adapted from (R. Shukla et al., 2024)).

Figure 6.1 (a, b) show the CAD design of the HXP lattice designed using SolidWorks. As shown in the top view (Figure 6.1-(a)), the unit cell is 2 mm in length with a strut thickness of 0.2 mm (inset attached in Figure 6.1-(a)). Notably, the individual struts are also hexagonal with a strut thickness of 0.2 mm as it is the minimum possible feature achievable using the LPBF method. The thin strut size was chosen to reduce the volume fraction of CP-Ti in the composite and to increase the volume fraction of eggshell powder. A hexagonal prism varies from a honeycomb structure in terms of its side view, as it has a truss-like structure (as seen in Figure 6.1-(b)) rather than a wall-like structure. The distance between two hexagonal layers is kept at 4 mm, resulting in a unit cell width-to-height ratio of 1:2. The relative density of the lattice structure was calculated by dividing the lattice structure volume of the unit cell by the total volume of the unit

cell. (du Plessis et al., 2018) This calculation yielded a relative density of 36%. Figure 6.1-(c) displays an optical image of the CP-Ti lattice produced using the LPBF method replicating the CAD design within experimental limits.

6.2 Characterization of the Ti-eggshell composite

Figure 6.2 presents the XRD patterns for LPBF-fabricated CP-Ti, SPS eggshell compacts, and Ti-eggshell composites. The XRD pattern of LPBF CP-Ti and eggshell compact reveals prominent peaks of the CP-Ti and eggshell as mentioned in the preceding chapters. CP-Ti exhibits peaks at 35.06° (100), 38.36° (002), and 40.11° (101) which correspond to the hexagonal close-packed (HCP) crystal structure of titanium, specifically associated with the space group $P63/mmc$ (194) (Attar et al., 2014). The XRD pattern of the SPS-fabricated eggshell compact (Figure 6.2) displays major peaks at 29.40° (104), 47.46° (018), and 48.51° (116). The most intense peak at (104) confirms the presence of the calcite phase of calcium carbonate, which possesses a rhombohedral crystal structure belonging to the $R\bar{3}c$ space group (Chang et al., 2017; Hoque, 2013; Onwubu et al., 2019). The XRD pattern of the Ti-eggshell composite, as shown in Figure 6.2, confirms the presence of both CP-Ti (HCP structure) and calcite phases, with no additional peaks observed, indicating that no interfacial reaction occurred during the SPS process.

The dislocation density values for the CP-Ti strut after LPBF processing were calculated to be $3.8 \pm 1 \times 10^{15} \text{ m}^{-3}$. Such high dislocation densities are characteristic of LPBF-processed materials. Similar high dislocation density were also observed in alloys like Al-based, Ti-based, Co-based, and Ag-based. The rapid cooling rate during LPBF resembles the quick quenching of the material, leading to the formation of metastable phases with a high concentration of geometrically necessary dislocations (GNDs). The lattice parameters for the martensitic phase are determined to be $a = 2.9506 \text{ \AA}$, and $c = 4.6850 \text{ \AA}$, resulting in a c/a ratio of ~ 1.5878 . This ratio is notably lower than the ideal value of 1.633 indicating that the dimensions along the c -axis are considerably smaller than those along the a -axis. In contrast to the quenching effect in LPBF, during the composite fabrication process via SPS, the CP-Ti lattice and eggshell powders are heated to 850°C (below the beta transus temperature) for 5 min followed by slow cooling inside a graphite die, resembling an annealing process. As a result, the CP-Ti undergoes an annealing-like treatment during composite fabrication. Consequently, the dislocation density after the fabrication process decreases to $6 \pm 2 \times 10^{14} \text{ m}^{-3}$. The lattice parameters of CP-Ti also change, with a and c values of 2.9508 \AA and 4.6882 \AA , respectively, resulting in a c/a ratio of 1.5888. Generally, the c/a ratio of Ti is observed to be 1.5888, which is still lower than the ideal hcp c/a ratio of 1.633.

The microstructural analysis in Figure 6.3 (a, b) further confirms the presence of a martensitic structure (α'), characterized by observable martensitic plates. As discussed in Chapter 4, due to the rapid cooling inherent in the LPBF process, the solidification conditions favor the formation of a martensitic phase with this HCP structure (Attar et al., 2015). This microstructure is consistent with findings reported by Attar et al. (Attar et al., 2014) and Gu et al. (Gu et al., 2012) in their studies on LPBF-fabricated CP-Ti. During the LPBF process, the multiple scans induce multiple cooling cycles, which further refine the martensitic structure. The modified martensite can be classified based on the dimensions of its major and minor axes. As indicated by black arrows in Figure 6.3-(a, b), martensitic plates with a major axis exceeding $20 \mu\text{m}$ are identified as primary

martensite, those with dimensions between 10 μm and 20 μm are classified as secondary martensite, and plates with major axes ranging from 1 μm to 10 μm are termed ternary martensite (J. Yang et al., 2016).

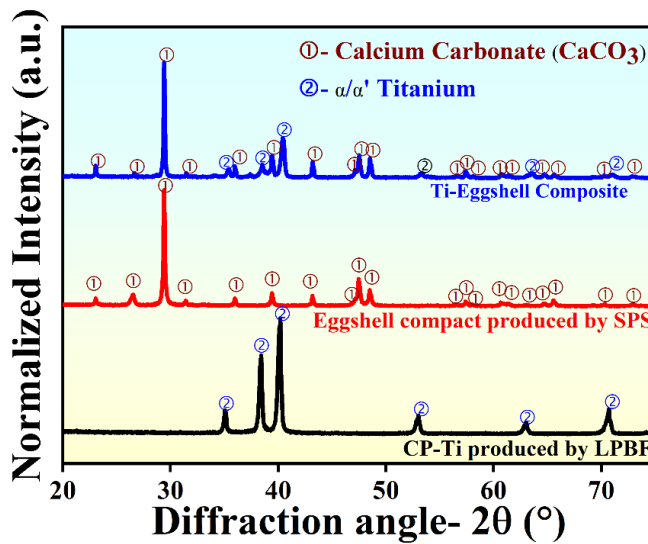


Figure 6.2. XRD of CP-Ti produced by LPBF, Eggshell compact produced by SPS, and Ti-eggshell composite (adapted from (R. Shukla et al., 2024)).

The SEM image in Figure 6.3-(c) of the SPS-fabricated eggshell compact reveals noticeable porosity, with the compacts achieving a density of $87 \pm 1\%$ similar to those mentioned in Chapter 5 (R. Shukla et al., 2023). In Figure 6.4-(a), the SEM image shows the CP-Ti lattice before undergoing SPS consolidation. The average strut length deviated by approximately 23% from the CAD design. However, post-SPS (Figure 6.4-(b)), the average strut length remained consistent, although with greater deviation. Notably, Figure 6.4-(b) illustrates that the strut lengths varied, with some areas elongating while others contracted, likely due to the thermal and mechanical energies applied during the SPS process. The strut width also increased post-SPS, resulting in a reduced distance between parallel struts. The applied pressure of 50 MPa during SPS to densify the lattice contributed to these dimensional changes (Rahmani et al., 2022). Additionally, the edges of the struts exhibited waviness rather than being straight, a common geometric imperfection observed in horizontal struts, often involving overhanging features. Overhanging features during LPBF typically lead to irregular surfaces and wavy edges. These geometric imperfections, including strut waviness, dimensional and geometric deviations, and particle adhesion, are more pronounced in thin-wall or strut structures, primarily due to gravitational effects and heat transfer properties. Moreover, necking at nodal points was observed, a typical defect when up to five struts converge at a single point. Necking contributes to deviations from the original design and affects individual strut lengths (L. Liu et al., 2017). In this design, three struts merge from a single plane, while two struts converge from a perpendicular plane. Table 6.1 compares the original strut dimensions from the CAD design, the dimensions post-LPBF fabrication, and the changes after SPS consolidation. The table highlights minor dimensional variations between the CAD model and the fabricated sample, attributable to the process capabilities. Further changes in the strut dimensions post-SPS, already discussed, are related to the

combined effects of thermal and mechanical energies during the consolidation process. As illustrated in Figure 6.4-(c), the interface of the composite material (CP-Ti and eggshell) shows no defects such as porosity, likely due to the controlled processing parameters during SPS consolidation. Furthermore, no new phase formation is observed at the interface, indicating the absence of thermal reactions leading to intermetallic phase formation, which corroborates the XRD findings.

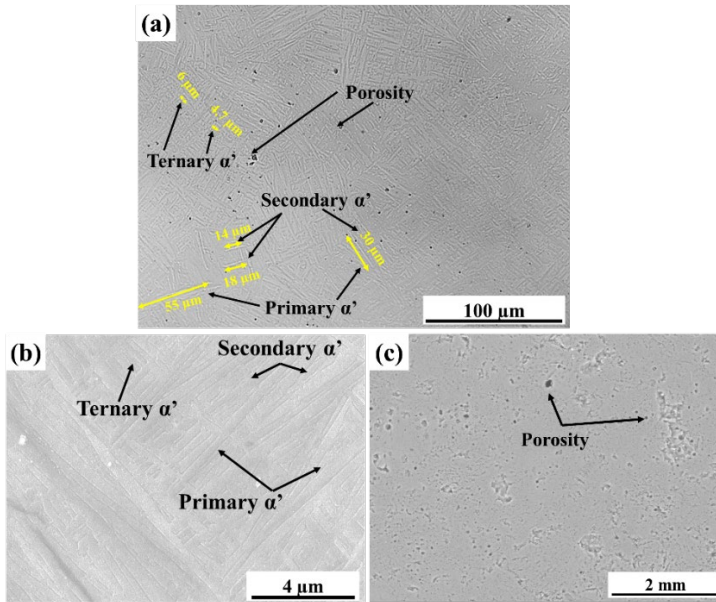


Figure 6.3. (a) Optical Microscopy image, (b) SEM image of CP-Ti produced by LPBF, (c) SEM image of the eggshell (adapted from (R. Shukla et al., 2024)).

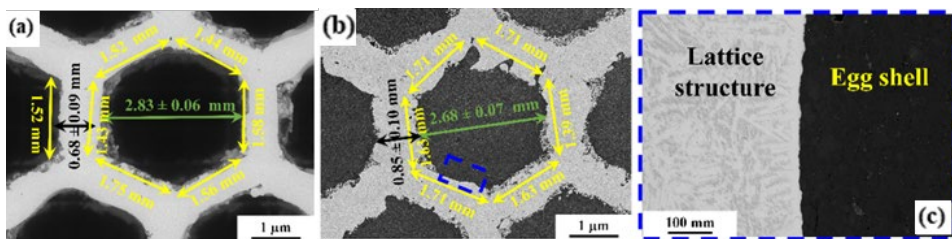


Figure 6.4. (a) SEM image of the CP-Ti lattice before SPS; (b) SEM image of the CP-Ti-eggshell composite, (c) higher magnification SEM image of the CP-Ti-eggshell composite interface (adapted from (R. Shukla et al., 2024)).

Table 6.1. Table showing the average dimensions (length, width, and distance between two parallel struts) observed for the struts calculated from the SEM images and their variations as a function of processing conditions (adapted from (R. Shukla et al., 2024)).

Description	Average length of the strut (n = 10) (mm)	Average width of the strut (n = 10) (mm)	Average distance between two parallel struts (n = 10) (mm)
CAD Design	2.0	0.5–0.7	3.1–3.2
As-built lattice	1.54 ± 0.09	0.68 ± 0.09	2.83 ± 0.06
Lattice after SPS	1.54 ± 0.15	0.85 ± 0.10	2.68 ± 0.07

The energy-dispersive X-ray (EDX) mapping of the Ti-eggshell composites is furnished in Figure 6.5. It can be observed that the composite samples show the presence of elements like Ti, Ca, C, and O. The lattice rich in Ti is surrounded by the elements Ca, C, and O, which correspond to the CaCO₃ phase. Although several O and C signals were detected within the Ti lattice regions, these signals might be attributed to the lower X-ray energies associated with O and C elements. In particular, the presence of CaCO₃ in the sample, which is not a good conductor, could lead to charging effects during analysis. The charging effects can cause spurious signals or noise, especially from low-energy X-ray emissions (such as those from O and C), which might then be erroneously attributed to the Ti lattice regions. The interaction volume in non-conductive areas can exacerbate this issue, leading to interference with the true material signals. It is noteworthy to mention that the interfacial reaction between CP-Ti lattice and eggshell powder is absent and there is no diffusion at the interface under the optimized SPS conditions.

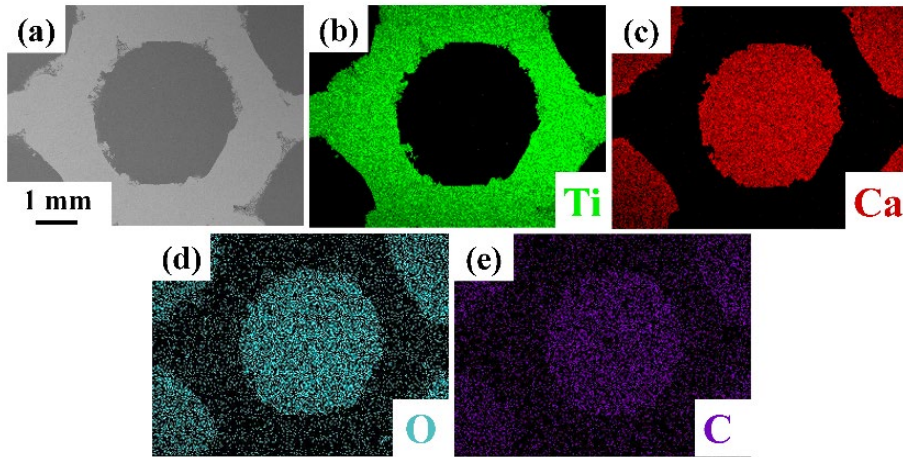


Figure 6.5. The energy dispersive X-ray (EDX) maps taken along the Ti-eggshell composite (a) secondary electron image of the composite material. The EDX maps show the presence of elements like (b) Ti (CP-Ti lattice) and (c) Ca, (d) O, and (e) C (from eggshell) (adapted from (R. Shukla et al., 2024)).

Figure 6.6-(a) presents the room-temperature uniaxial engineering compressive stress-strain curves for LPBF-fabricated CP-Ti, SPS-fabricated eggshell compacts, and the Ti-eggshell composite. The yield strength (σ_y) for the CP-Ti sample is approximately 38 ± 2 MPa, while the eggshell compact exhibits a σ_y of 155 ± 15 MPa, and the Ti-eggshell

composite displays a σ_y of 123 ± 34 MPa (refer to Table 6.2). The post-compression test images of the samples are provided as insets in Figure 6.6-(a), with enlarged views shown in Figure 6.6-(b-d). The CP-Ti lattice after fracture exhibits a plateau, a characteristic compressive behavior for porous structures according to ISO 13314 standards (Choy et al., 2017). The presence of a smooth plateau region further confirms the ductile nature of the lattice (X. P. Tan et al., 2017). The fracture image of the hexagonal Ti lattice indicates that the struts of the top layer and the layer directly beneath it are bent at angles of 75° and 65° , respectively, but in opposite directions, a phenomenon known as sequential bending. The hexagonal lattice structure consists only of struts oriented either parallel (vertical struts) or perpendicular (horizontal struts) to the loading direction, without any struts angled relative to the loading direction. Choy et al. (Choy et al., 2017) previously reported that the horizontal struts remain unaffected by the compressive load due to their orientation, while the vertical struts support the horizontal ones, leading to the vertical struts bending at an angle of 75° (Choy et al., 2017) However, beyond the second layer from the top (Figure 6.6-(b)), the layer thickness remains consistent at 4 mm, as designed, owing to the sequential bending pattern (X. Huang et al., 2023).

The ‘saw-tooth’ pattern observed in the plastic region is characteristic of brittle ceramic materials, often resulting from the initiation and propagation of micro-cracks, which ultimately lead to material failure. In the fractured eggshell sample (Figure 6.6-(a, c)), this serrated pattern is indicative of brittle fracture (Pelleg, 2014). The Ti-eggshell composite (Figure 6.6-(a, d)) exhibited a combination of the compressive behaviors of both CP-Ti and the eggshell. Specifically, it showed an increase in yield strength similar to that of the eggshell compact, while its Young’s modulus decreased, resembling the CP-Ti lattice. Consequently, the Ti-eggshell composite achieved a compressive yield strength of approximately 123 ± 34 MPa and Young’ modulus of around 47 ± 1 GPa, values that align closely with those of natural cortical bone (compressive yield strength of 100–130 MPa and Young’s modulus of 5–30 GPa) (X. Wang et al., 2016). The optical image of the Ti-eggshell composite post-compression test (Figure 6.6-(d)) reveals a compressive failure at an angle of approximately 45° , attributed to shear forces, which in this context is referred to as diagonal shear, consistent with a brittle fracture.

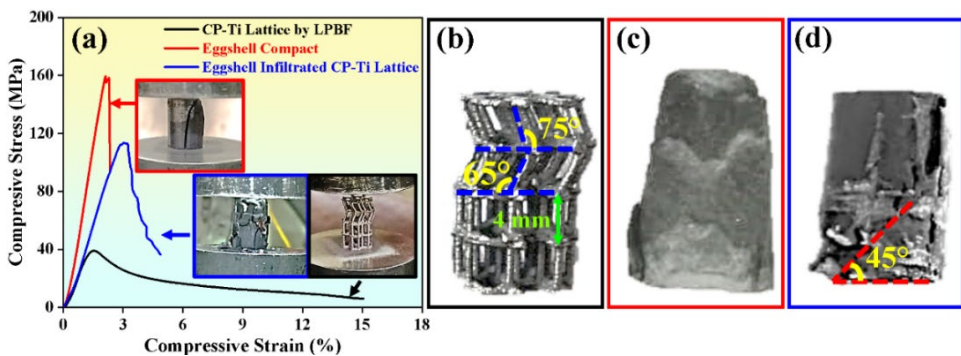


Figure 6.6. (a) Room temperature uniaxial compressive stress-strain curves observed for the LPBF-fabricated CP-Ti lattice, eggshell compact, and CP-Ti-eggshell composites and the inset shows the fractured image of the samples. Optical images of the samples showing fractured impact after the compression test (b) LPBF-processed CP-Ti lattice (c) SPS-made eggshell compacts, and (d) Ti-eggshell composite (adapted from (R. Shukla et al., 2024)).

Table 6.2. Table furnishing the Youngs Modulus and the Yield Strength for the CP-Ti lattice, consolidated, and Ti-eggshell composites (adapted from (R. Shukla et al., 2024)).

Description	Youngs Modulus (GPa)	Yield Strength (MPa)
CP-Ti	38 ± 1	37 ± 2
Eggshell	87 ± 11	155 ± 15
Composite – Ti+ Eggshell	47 ± 2	123 ± 34

6.3 Cytotoxicity and bacterial study of the Ti-eggshell composite

Figure 6.7 underscores the potential of the Ti-eggshell composite for biomedical applications, particularly where both mechanical strength and biocompatibility are critical. Lactate dehydrogenase (LDH) is an intracellular enzyme that serves as an indicator of cytotoxicity, with its release signifying cell lysis due to contact with a material. Elevated levels of LDH enzyme in the surrounding medium directly indicate cytotoxicity, while lower absorbance readings suggest greater cytocompatibility (Baghersad et al., 2023). As depicted in Figure 6.7 the cytotoxicity profiles of CP-Ti, eggshell, and Ti-eggshell composite were evaluated using adipose-derived stem cells (ADSCs). Among these, the eggshell exhibited the lowest absorbance, indicating the least LDH release, while the CP-Ti and the Ti-eggshell composite displayed similar absorbance levels. Nonetheless, all the tested samples showed significantly lower cytotoxicity than the cytotoxic control and no statistical difference from the polystyrene control.

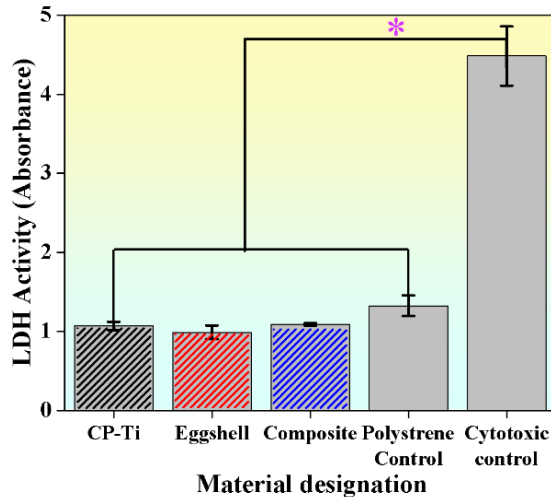


Figure 6.7. The cytotoxicity analysis for the LPBF-processed CP-Ti lattice, eggshell compact, and Ti-eggshell composite on human adipose-derived stem cells. (* $p \leq 0.05$) (adapted from (R. Shukla et al., 2024)).

Figure 6.8 presents SEM images of the bacterial strains *Staphylococcus aureus* (ATCC 6538) and *Pseudomonas aeruginosa* (ATCC 10145) after 6 and 24 hours of incubation, respectively. The images reveal that bacterial growth is most pronounced on the CP-Ti surface, followed by the Ti-eggshell composite and eggshell compacts. Notably, the CP-Ti surface supports significant bacterial colonization, with evident biofilm formation observed after 24 hours for both bacterial strains. In contrast, the eggshell compact shows a marked reduction in bacterial growth, likely due to the antibacterial

properties of CaCO_3 , which is particularly effective against *Pseudomonas aeruginosa*. The Ti-eggshell composite, which features both eggshell and CP-Ti surfaces, demonstrates reduced bacterial proliferation overall. While the CP-Ti regions within the composite exhibit more bacterial growth than the eggshell regions, the total bacterial presence on the composite is significantly lower than on CP-Ti alone, and importantly, no biofilm formation is detected. The underlying mechanisms of antibacterial activity and bacterial interaction with these surfaces are further elaborated in Figure 6.9.

Pseudomonas aeruginosa (*P. aeruginosa*) and *Staphylococcus aureus* (*S. aureus*) are well-known representatives of gram-negative and gram-positive bacteria, respectively (Lee et al., 2019). The interaction between bacterial cell walls and material surfaces begins with the cell wall, the first barrier of defense. Gram-negative bacteria, such as *P. aeruginosa*, have a highly complex cell wall structure characterized by a thin layer of peptidoglycan, while gram-positive bacteria like *S. aureus* have a thicker peptidoglycan layer (Madruga et al., 2020).

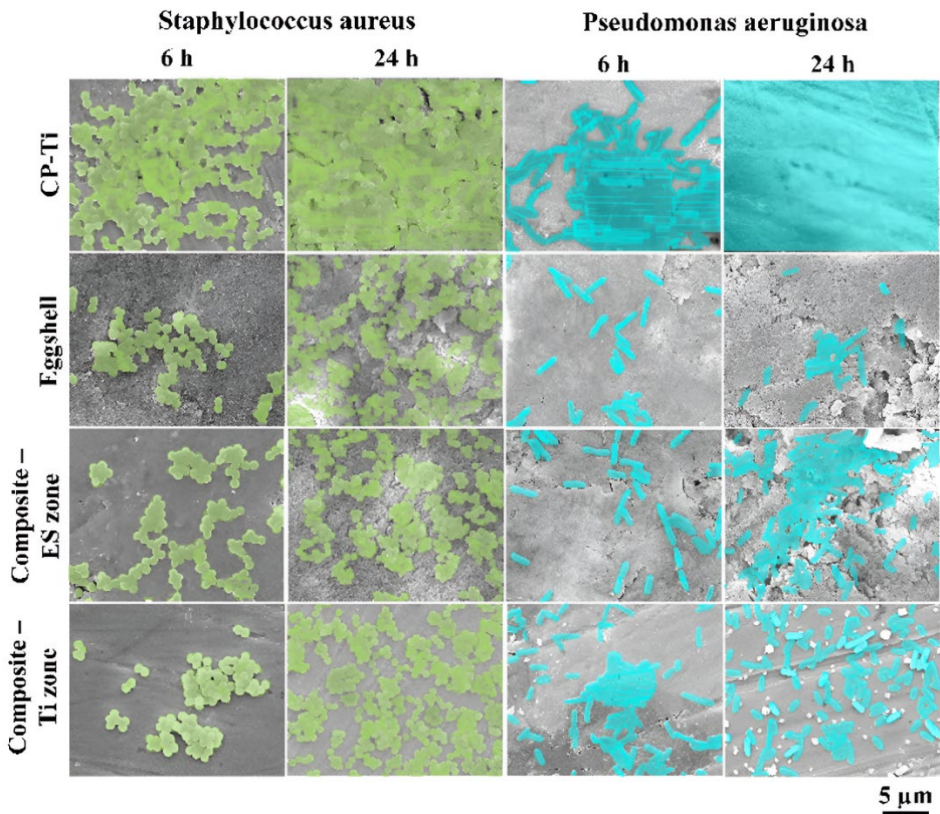


Figure 6.8. Scanning electron microscopy images of the *Staphylococcus aureus* bacteria (false-coloured green) and *Pseudomonas aeruginosa* bacteria (false-coloured cyan) for the LPBF-fabricated CP-Ti, SPS-made eggshell Compact, and the Ti-eggshell composite (abbreviated as composite) (adapted from (R. Shukla et al., 2024)).

According to the literature, calcium ions can interact and bind with the cell walls of both types of bacteria, potentially disrupting energy transport processes (Thomas & Rice, 2014). Additionally, these ions may permeate the cell wall and interact with the bacterial cytoplasmic membrane, affecting cellular processes. In bacterial cells, the proton pump plays a critical role by constantly exchanging H^+ ions (protons), a process essential for the synthesis of adenosine triphosphate (ATP). Eggshells are predominantly composed of calcium carbonate ($CaCO_3$), specifically consisting of Ca^{+2} and CO_3^{-2} ions held together by ionic bonds. $CaCO_3$ is highly alkaline, and upon contact with a bacterial solution containing water (H_2O), it readily reacts with H^+ ions, leading to the formation of HCO_3^- and OH^- ions. This reaction creates a proton-depleted zone as H^+ ions are consumed to neutralize $CaCO_3$. The proton gradient across the bacterial cell membrane, essential for ATP production via the electron transport chain (ETC), is thereby disrupted (as illustrated in Figure 6.9). ATP is a powerhouse of the cell, and interference in ATP synthesis can severely impair bacterial growth, and metabolism, and ultimately lead to bacterial death. Thus, the alkaline nature of $CaCO_3$ effectively inhibits bacterial growth and biofilm formation in eggshell-based bio-implants (Nostro et al., 2012; S. K. Shukla & Rao, 2013; J. Tan et al., 2018). In contrast, CP-Ti lacks ions capable of generating a proton-depleted zone, and titanium is less alkaline than calcium. Although an alkaline environment generally inhibits bacterial growth, the absence of such ion-mediated interactions in CP-Ti results in lower bactericidal activity. However, the incorporation of eggshells into the Ti matrix enhances the bactericidal properties of the composite. This finding suggests that the Ti-eggshell composite holds promise as a material for fabricating bactericidal surfaces and implants.

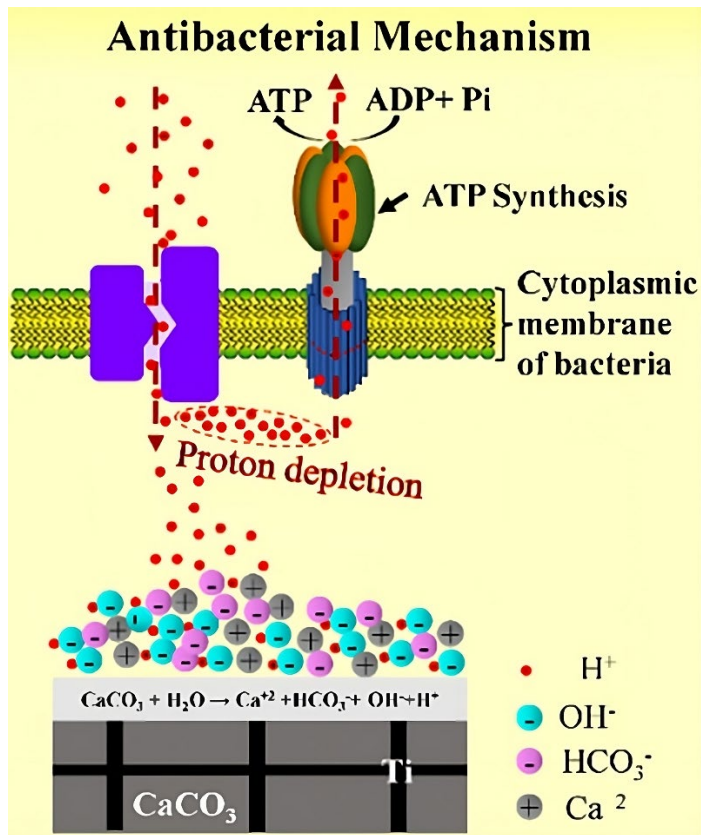


Figure 6.9. Schematic diagram illustrating the micro-surface detailing the mechanism involved in the antibacterial behavior of the Ti-eggshell composite (adapted from (R. Shukla et al., 2024)).

6.4 Summary

This chapter reports the successful fabrication of Ti-eggshell composites using a combined approach of LPBF and SPS. The resulting composite demonstrated Young's modulus and compressive strength within the range of natural bone, marking a significant achievement in fabricating a bone-mimicking material. Additionally, the produced composite exhibits non-cytotoxic characteristics and possesses antibacterial properties, attributed to the presence of ions that create a proton-depleted zone, effectively disrupting ATP synthesis.

7 Conclusion and outlook of the thesis

7.1 Conclusions

This study successfully demonstrates the valorization of eggshell waste into bio-implant material, incorporating circular economy principles. The following conclusions are drawn from the results:

- While Ti6Al4V is preferred for high-load applications due to its superior mechanical properties, CP-Ti is a viable alternative for applications where biocompatibility is critical. The higher compressive strength and hardness of Ti6Al4V support the choice of CP-Ti for bio-implants prioritizing biocompatibility.
- The LPBF process successfully fabricated CP-Ti with improved mechanical properties compared to conventional methods. This improvement is attributed to the formation of martensitic microstructures. Mechanical testing revealed the formation of twins and provided insights into the deformation mechanisms. Fracture surface analysis showed dimples, microvoids, and quasi-cleavage facets, with microvoid growth leading to microscopic cracks, increased strength, but reduced fracture strain.
- SPS testing indicated that sintering above 850 °C did not improve density, with an optimal density of ~87% achieved at 850 °C.
- The Ti-eggshell composite was successfully fabricated by combining AM and powder metallurgy (LPBF+SPS). CP-Ti hexagonal lattice structures were produced via LPBF, with a metastable martensitic phase and dislocations due to rapid cooling during manufacturing.
- Compression testing showed that the CP-Ti lattice failed by sequential bending, the eggshell compact failed by brittle fracture, and the Ti-eggshell composite failed via diagonal shear. The composite exhibited compressive strength and Young's modulus matching that of natural human cortical bone.
- The Ti-eggshell composite was non-cytotoxic to ADSCs, confirming its safety for use as a biomaterial. The composite also demonstrated significant antibacterial activity against both Gram-negative (*Pseudomonas aeruginosa*) and Gram-positive (*Staphylococcus aureus*) bacteria, attributed to the disruption of the proton pump by the eggshell.
- The successful incorporation of eggshell waste into CP-Ti lattice structures aligns with circular economy principles. The resulting Ti-eggshell composite offers mechanical properties comparable to natural human bone and shows excellent biocompatibility and antibacterial properties, making it a promising candidate for orthopedic and biomedical applications.

7.2 Outlook of the thesis

- The interface study between the Ti and eggshell should be further study to establish a full understanding of the composite.
- The tribological, fatigue, and further testing according to ASTM standards should be done to standardize this composite.
- The human body can absorb the limited number of ions released from such implants. Calcium carbonate releases Ca^{+2} and CO_3^{-2} ions. These ions are non-toxic and therapeutic agents. However, the in-vivo testing of the eggshell-based implant

should be considered to evaluate adverse reactions due to extra dosage or rapid degradation of these ions.

- The interaction with the blood should be considered in evaluating effective bone-healing and interaction of the implant.

List of figures

Figure 1.1. Schematics illustrating the additive manufacturing process showing the different steps involved. Step 1. CAD model development and tessellation followed by Step 2. Fixing the process parameter and Step 3: fabrication of the material layer-by-layer.	17
Figure 1.2. Schematics illustrating the (a) laser powder bed fusion process (Jiao et al., 2018), (b) laser-powder interaction during the laser powder bed fusion process.	18
Figure 1.3. Schematic of the spark plasma sintering (SPS) process, illustrating the simultaneous application of uniaxial pressure and pulsed electric current to the powder compact.	28
Figure 2.1. A schematic sketch showing the dimensions of the tensile samples fabricated as per the -ASTM: E8 /E8M– 13a standards (reproduced from (Karimi et al., 2021)). ...	32
Figure 3.1. Feedstock characterization: Scanning electron microscopy image of the Ti6Al4V powder at (a) lower magnification, and (b) higher magnification. (c) Plot showing the particle size distribution of the employed gas-atomized Ti6Al4V powders where the average particle size is observed to be $24 \pm 18 \mu\text{m}$, and (d) the corresponding X-ray diffraction pattern of the Ti6Al4V powder.....	35
Figure 3.2. (a) The X-ray diffraction pattern, (b) optical microscopy image, scanning electron microscopy image at (c) lower magnification, and (d) higher magnification of the LPBF-fabricated Ti6AL4V sample.....	36
Figure 3.3. Room temperature mechanical properties of the LPBF Ti6Al4V alloy under (a) Tension and, (b) Compression.	37
Figure 3.4. Fractography images of LPBF Ti6Al4V samples after tensile test. (a) A low magnification overview of the fracture surface, (b) a higher magnification image revealing dimple and quasi-cleavage facets, and corresponding (c) higher magnification image showing fine dimples (d) higher magnification image from the center (e) Lower magnification image from the, and corresponding -(f) higher magnification image revealing varying dimple size indicating localized plastic deformation.	38
Figure 4.1. Feedstock characterization Scanning electron microscopy image of the CP-Ti powder at (a) lower magnification, and (b) higher magnification. (c) Plot showing the particle size distribution of the gas-atomized CP-Ti powders where the average particle size is observed to be $29 \pm 13 \mu\text{m}$ (d) X-ray diffraction pattern of the CP-Ti powder showing the presence of the HCP phase.....	41
Figure 4.2. (a) X-ray diffraction pattern of the LPBF CP-Ti sample (b) Optical Microscopy image showing the presence of porosity and (c) higher magnification scanning electron microscopy image of the LPBF CP-Ti sample.....	42
Figure 4.3. The transmission electron microscopy images of the CP-Ti fabricated by laser power-bed fusion process. (a) Selected area diffraction pattern confirming the presence of a hexagonally closed packed structure. (b) Bright-field image showing the presence of imperfections like grain boundaries, twins, and dislocations. (c) Inverse Fourier-filtered image showing the presence of multiple edge dislocations.	43
Figure 4.4. Mechanical properties for the CP-Ti produced by LPBF. Room temperature tensile stress-strain curves as a function of different strain rates (a) Engineering stress-strain and (b) True tensile stress-strain curves. (c) Schematic illustration of the hexagonal crystal structure showing various planes and directions.....	44
Figure 4.5. Compression stress-strain curve of the LPBF CP-Ti sample.	46

Figure 4.6. Scanning electron microscopy fractography images of the LPBF processed CP-Ti samples after the tensile test as a function of different strain rates.	47
Figure 5.1. Characterization of the feedstock eggshell powder (a), (b) scanning electron microscopy images, (c) particle size measurement plot, (d) thermogravimetric analysis plot, and (e) X-ray diffraction patterns of the eggshell powder (adapted from (R. Shukla et al., 2023)).	51
Figure 5.2. Densification curves obtained for different spark plasma sintered samples as a function of sintering time (adapted from (R. Shukla et al., 2023)).	52
Figure 5.3. Densification curves obtained for different spark plasma sintered samples as a function of temperature (adapted from (R. Shukla et al., 2023)).	53
Figure 5.4. Densification curves obtained for different spark plasma sintered samples as a function of dwell time (adapted from (R. Shukla et al., 2023)).	54
Figure 5.5. Scanning electron microscopy images of the eggshell powder sintered at various temperatures (a), (b) 250 °C, (c), (d) 500 °C, (e), (f) 750 °C, (g), (h) 850 °C, (i), (j) 900 °C, and (k), (l) 1000 °C, respectively (adapted from (R. Shukla et al., 2023)).	55
Figure 5.6. X-ray diffraction patterns of the eggshell powder spark plasma sintered at 250 °C, 500 °C, 750 °C, 850 °C, 900 °C, and 1000 °C, respectively (adapted from (R. Shukla et al., 2023)).	56
Figure 5.7. Fourier-transformed infrared spectroscopy traces of the eggshell powder spark plasma sintered at 250 °C, 500 °C, 750 °C, 850 °C, 900 °C, and 1000 °C, respectively (adapted from (R. Shukla et al., 2023)).	57
Figure 5.8. Microhardness values of the spark plasma sintered eggshell powder at different temperatures: 750 °C, 850 °C, 900 °C, and 1000 °C (adapted from (R. Shukla et al., 2023)).	58
Figure 6.1. Micro-architecture of the lattice structure, (a) Computer-aided design (CAD) showing the top view of the lattice and the inset showing the structure of an individual strut, (b) CAD design showing the side view of the lattice, and (c) optical microscopy image of the printed CP-Ti lattice (adapted from (R. Shukla et al., 2024)).	59
Figure 6.2. XRD of CP-Ti produced by LPBF, Eggshell compact produced by SPS, and Ti-eggshell composite (adapted from (R. Shukla et al., 2024)).	61
Figure 6.3. (a) Optical Microscopy image, (b) SEM image of CP-Ti produced by LPBF, (c) SEM image of the eggshell (adapted from (R. Shukla et al., 2024)).	62
Figure 6.4. (a) SEM image of the CP-Ti lattice before SPS; (b) SEM image of the CP-Ti-eggshell composite, (c) higher magnification SEM image of the CP-Ti-eggshell composite interface (adapted from (R. Shukla et al., 2024)).	62
Figure 6.5. The energy dispersive X-ray (EDX) maps taken along the Ti-eggshell composite (a) secondary electron image of the composite material. The EDX maps show the presence of elements like (b) Ti (CP-Ti lattice) and (c) Ca, (d) O, and (e) C (from eggshell) (adapted from (R. Shukla et al., 2024)).	63
Figure 6.6. (a) Room temperature uniaxial compressive stress-strain curves observed for the LPBF-fabricated CP-Ti lattice, eggshell compact, and CP-Ti-eggshell composites and the inset shows the fractured image of the samples. Optical images of the samples showing fractured impact after the compression test (b) LPBF-processed CP-Ti lattice (c) SPS-made eggshell compacts, and (d) Ti-eggshell composite (adapted from (R. Shukla et al., 2024)).	64
Figure 6.7. The cytotoxicity analysis for the LPBF-processed CP-Ti lattice, eggshell compact, and Ti-eggshell composite on human adipose-derived stem cells. (* $p \leq 0.05$) (adapted from (R. Shukla et al., 2024)).	65

Figure 6.8. Scanning electron microscopy images of the *Staphylococcus aureus* bacteria (false-coloured green) and *Pseudomonas aeruginosa* bacteria (false-coloured cyan) for the LPBF-fabricated CP-Ti, SPS-made eggshell Compact, and the Ti-eggshell composite (abbreviated as composite) (adapted from (R. Shukla et al., 2024)). 66

Figure 6.9. Schematic diagram illustrating the micro-surface detailing the mechanism involved in the antibacterial behavior of the Ti-eggshell composite (adapted from (R. Shukla et al., 2024))..... 68

List of tables

Table 1.1. Table showing the list of processing parameters that could influence the LPBF process (El Wakil, 2019; Gulbrandsen-Dahl et al., 2024; Pandey et al., 2022; Singla et al., 2021).	19
Table 1.2. Chemical composition of the eggshell (Cree & Rutter, 2015; Hincke et al., 2012; Mahdavi et al., 2021; Zaman, Mostari, Mahmood, et al., 2018).	25
Table 2.1. The processing parameters employed to fabricate CP-Ti and Ti6Al4V samples using the LPBF process.....	30
Table 3.1. Composition of the feedstock Ti6Al4V powder.....	34
Table 3.2. Comparison of Young’s Modulus and tensile properties of the natural bone, Ti6Al4V and CP-Ti fabricated by various manufacturing methods.	39
Table 4.1. Table furnishing the Youngs Modulus, ductility, Yield Strength, and the ultimate tensile Strength for the CP-Ti produced by LPBF as a function of different strain rates.	45
Table 5.1. X-ray fluorescence analysis showing the composition of the raw eggshell powder.	49
Table 5.2. Achieved sinter density at various sintering temperatures.	55
Table 6.1. Table showing the average dimensions (length, width, and distance between two parallel struts) observed for the struts calculated from the SEM images and their variations as a function of processing conditions (adapted from (R. Shukla et al., 2024)).	63
Table 6.2. Table furnishing the Youngs Modulus and the Yield Strength for the CP-Ti lattice, consolidated, and Ti-eggshell composites (adapted from (R. Shukla et al., 2024)).	65

References

- Abdel-Hady Gepreel, M., & Niinomi, M. (2013). Biocompatibility of Ti-alloys for long-term implantation. *Journal of the Mechanical Behavior of Biomedical Materials*, 20, 407–415. <https://doi.org/10.1016/j.jmbbm.2012.11.014>
- Alkentar, R., Kladovasilakis, N., Tzetzis, D., & Mankovits, T. (2023). Effects of Pore Size Parameters of Titanium Additively Manufactured Lattice Structures on the Osseointegration Process in Orthopedic Applications: A Comprehensive Review. *Crystals*, 13(1), 113. <https://doi.org/10.3390/cryst13010113>
- Asiva Noor Rachmayani. (2017). *Additive Manufacturing Handbook* (A. B. Badiru, V. V. Valencia, & D. Liu, Eds.). CRC Press. <https://doi.org/10.1201/9781315119106>
- ASTM International. (2018). *ASTM F3302 – 18: Standard for Additive Manufacturing – Finished Part Properties – Standard Specification for Titanium Alloys via Powder Bed Fusion*. ASTM Standards; ASTM International. <https://doi.org/10.1520/F3302-18.Copyright>
- ASTM International. (2021). *ASTM F136 – 13 Standard Specification for Wrought Titanium-6Aluminum-4Vanadium ELI (Extra Low Interstitial) Alloy for Surgical Implant Applications (UNS R56401)*. ASTM International; ASTM International. <https://doi.org/10.1520/F0136-13.2>
- Attar, H., Calin, M., Zhang, L. C., Scudino, S., & Eckert, J. (2014). Manufacture by selective laser melting and mechanical behavior of commercially pure titanium. *Materials Science and Engineering: A*, 593, 170–177. <https://doi.org/10.1016/j.msea.2013.11.038>
- Attar, H., Ehtemam-Haghighi, S., Soro, N., Kent, D., & Dargusch, M. S. (2020). Additive manufacturing of low-cost porous titanium-based composites for biomedical applications: Advantages, challenges and opinion for future development. *Journal of Alloys and Compounds*, 827, 154263. <https://doi.org/10.1016/j.jallcom.2020.154263>
- Attar, H., Prashanth, K. G., Chaubey, A. K., Calin, M., Zhang, L. C., Scudino, S., & Eckert, J. (2015). Comparison of wear properties of commercially pure titanium prepared by selective laser melting and casting processes. *Materials Letters*, 142, 38–41. <https://doi.org/10.1016/j.matlet.2014.11.156>
- Awogbemi, O., Inambao, F., & Onuh, E. I. (2020). Modification and characterization of chicken eggshell for possible catalytic applications. *Heliyon*, 6(10), e05283. <https://doi.org/10.1016/j.heliyon.2020.e05283>
- Baghersad, S., Madruga, L. Y. C., Martins, A. F., Popat, K. C., & Kipper, M. J. (2023). Expanding the Scope of an Amphoteric Condensed Tannin, Tanfloc, for Antibacterial Coatings. *Journal of Functional Biomaterials*, 14(11), 554. <https://doi.org/10.3390/jfb14110554>
- Bandyopadhyay, A., Shivaram, A., Tarafder, S., Sahasrabudhe, H., Banerjee, D., & Bose, S. (2017). In Vivo Response of Laser Processed Porous Titanium Implants for Load-Bearing Implants. *Annals of Biomedical Engineering*, 45(1), 249–260. <https://doi.org/10.1007/s10439-016-1673-8>
- Baqain, M., Rüstü Yörük, C., Nešumajev, D., Järvik, O., & Konist, A. (2023). Ash characterisation formed under different oxy-fuel circulating fluidized bed conditions. *Fuel*, 338(September 2022), 1–16. <https://doi.org/10.1016/j.fuel.2022.127244>

- Bartolomeu, F., Gasik, M., Silva, F. S., & Miranda, G. (2022). Mechanical Properties of Ti6Al4V Fabricated by Laser Powder Bed Fusion: A Review Focused on the Processing and Microstructural Parameters Influence on the Final Properties. *Metals*, 12(6), 986. <https://doi.org/10.3390/met12060986>
- Bellucci, D., Salvatori, R., Cannio, M., Luginina, M., Orrù, R., Montinaro, S., Anesi, A., Chiarini, L., Cao, G., & Cannillo, V. (2018). Bioglass and bioceramic composites processed by Spark Plasma Sintering (SPS): biological evaluation Versus SBF test. *Biomedical Glasses*, 4(1), 21–31. <https://doi.org/10.1515/bglass-2018-0003>
- Bernard-Granger, G., & Guizard, C. (2007). Spark plasma sintering of a commercially available granulated zirconia powder: I. Sintering path and hypotheses about the mechanism(s) controlling densification. *Acta Materialia*, 55(10), 3493–3504. <https://doi.org/10.1016/J.ACTAMAT.2007.01.048>
- Chang, R., Kim, S., Lee, S., Choi, S., Kim, M., & Park, Y. (2017). Calcium Carbonate Precipitation for CO₂ Storage and Utilization: A Review of the Carbonate Crystallization and Polymorphism. *Frontiers in Energy Research*, 5(JUL). <https://doi.org/10.3389/fenrg.2017.00017>
- Choy, S. Y., Sun, C.-N., Leong, K. F., & Wei, J. (2017). Compressive properties of Ti-6Al-4V lattice structures fabricated by selective laser melting: Design, orientation and density. *Additive Manufacturing*, 16, 213–224. <https://doi.org/10.1016/j.addma.2017.06.012>
- Chróścicka, A., Jaegermann, Z., Wychowański, P., Ratajska, A., Sadło, J., Hoser, G., Michałowski, S., & Lewandowska-Szumiel, M. (2016). Synthetic Calcite as a Scaffold for Osteoinductive Bone Substitutes. *Annals of Biomedical Engineering*, 44(7), 2145–2157. <https://doi.org/10.1007/s10439-015-1520-3>
- Chu, C., Xue, X., Zhu, J., & Yin, Z. (2006). In vivo study on biocompatibility and bonding strength of Ti/Ti–20 vol.% HA/Ti–40 vol.% HA functionally graded biomaterial with bone tissues in the rabbit. *Materials Science and Engineering: A*, 429(1–2), 18–24. <https://doi.org/10.1016/J.MSEA.2006.03.099>
- Combes, C., Miao, B., Bareille, R., & Rey, C. (2006). Preparation, physical–chemical characterisation and cytocompatibility of calcium carbonate cements. *Biomaterials*, 27(9), 1945–1954. <https://doi.org/10.1016/J.BIOMATERIALS.2005.09.026>
- Cree, D., & Pliya, P. (2019). Effect of elevated temperature on eggshell, eggshell powder and eggshell powder mortars for masonry applications. *Journal of Building Engineering*, 26, 100852. <https://doi.org/10.1016/j.jobe.2019.100852>
- Cree, D., & Rutter, A. (2015). Sustainable Bio-Inspired Limestone Eggshell Powder for Potential Industrialized Applications. *ACS Sustainable Chemistry and Engineering*, 3(5), 941–949. <https://doi.org/10.1021/ACSSUSCHEMENG.5B00035>
- Depboylu, F. N., Yasa, E., Poyraz, Ö., Minguella-Canela, J., Korkusuz, F., & De los Santos López, M. A. (2022). Titanium based bone implants production using laser powder bed fusion technology. *Journal of Materials Research and Technology*, 17, 1408–1426. <https://doi.org/10.1016/j.jmrt.2022.01.087>
- Donachie, M. J. (2000). Titanium. In *ASM International* (Vol. 99, Issue 5). ASM International. <https://doi.org/10.31399/asm.tb.ttg2.9781627082693>
- Dong, Y. P. P., Tang, J. C. C., Wang, D. W. W., Wang, N., He, Z. D. D., Li, J., Zhao, D. P. P., & Yan, M. (2020). Additive manufacturing of pure Ti with superior mechanical performance, low cost, and biocompatibility for potential replacement of Ti-6Al-4V. *Materials & Design*, 196, 109142. <https://doi.org/10.1016/J.MATDES.2020.109142>

- du Plessis, A., Yadroitsava, I., & Yadroitsev, I. (2018). Ti6Al4V lightweight lattice structures manufactured by laser powder bed fusion for load-bearing applications. *Optics & Laser Technology*, *108*, 521–528. <https://doi.org/10.1016/J.OPTLASTEC.2018.07.050>
- El Wakil, S. D. (2019). Processes and Design for Manufacturing. In *Processes and Design for Manufacturing* (3rd ed.). CRC Press. <https://doi.org/10.1201/9780429506635>
- Engin, B., Demirtaş, H., & Eken, M. (2006). Temperature effects on egg shells investigated by XRD, IR and ESR techniques. *Radiation Physics and Chemistry*, *75*(2), 268–277. <https://doi.org/10.1016/j.radphyschem.2005.09.013>
- Esquivias, L., Morales-Flórez, V., & Santos, A. (2018). Carbon dioxide sequestration by phosphogypsum based procedure. In *Carbon Dioxide Sequestration in Cementitious Construction Materials* (pp. 199–223). Elsevier. <https://doi.org/10.1016/B978-0-08-102444-7.00009-5>
- Fleet, M. E. (2009). Infrared spectra of carbonate apatites: v2-Region bands. *Biomaterials*, *30*(8), 1473–1481. <https://doi.org/10.1016/j.biomaterials.2008.12.007>
- Freire, M. N., & Holanda, J. N. F. (2006). Characterization of avian eggshell waste aiming its use in a ceramic wall tile paste. *Cerâmica*, *52*(324), 240–244. <https://doi.org/10.1590/S0366-69132006000400004>
- Gautron, J., Dombre, C., Nau, F., Feidt, C., & Guillier, L. (2022). Review: Production factors affecting the quality of chicken table eggs and egg products in Europe. *Animal*, *16*, 100425. <https://doi.org/10.1016/J.ANIMAL.2021.100425>
- Geetha, M., Singh, A. K., Asokamani, R., & Gogia, A. K. (2009). Ti based biomaterials, the ultimate choice for orthopaedic implants – A review. *Progress in Materials Science*, *54*(3), 397–425. <https://doi.org/10.1016/j.pmatsci.2008.06.004>
- Gibson, I., Rosen, D. W., & Stucker, B. (2010). Additive Manufacturing Technologies. In *Additive Manufacturing Technologies: Rapid Prototyping to Direct Digital Manufacturing*. Springer US. <https://doi.org/10.1007/978-1-4419-1120-9>
- Gokuldoss, P. K., Kolla, S., & Eckert, J. (2017). Additive manufacturing processes: Selective laser melting, electron beam melting and binder jetting-selection guidelines. *Materials*, *10*(6), 672. <https://doi.org/10.3390/ma10060672>
- Gong, J. (2003). Comment on “Measurement of hardness on traditional ceramics”, H. Kim and T. Kim, J. Eur. Ceram. Soc., *22*, 1437–1445 (2002). *Journal of the European Ceramic Society*, *23*(10), 1769–1772. [https://doi.org/10.1016/S0955-2219\(02\)00398-9](https://doi.org/10.1016/S0955-2219(02)00398-9)
- Gu, D., Hagedorn, Y.-C., Meiners, W., Meng, G., Batista, R. J. S., Wissenbach, K., & Poprawe, R. (2012). Densification behavior, microstructure evolution, and wear performance of selective laser melting processed commercially pure titanium. *Acta Materialia*, *60*(9), 3849–3860. <https://doi.org/10.1016/j.actamat.2012.04.006>
- Gulbrandsen-Dahl, S., Dreyer, H. C., Hinrichsen, E. L., Holtskog, H., Martinsen, K., Raabe, H., & Sziebig, G. (2024). Digitalization and Sustainable Manufacturing. In *Sustainability (Switzerland)* (Vol. 11, Issue 1). Routledge. <https://doi.org/10.4324/9781032693415>
- Gupta, S. K., Shahidsha, N., Bahl, S., Kedaria, D., Singamneni, S., Yarlagadda, P. K. D. V., Suwas, S., & Chatterjee, K. (2021). Enhanced biomechanical performance of additively manufactured Ti-6Al-4V bone plates. *Journal of the Mechanical Behavior of Biomedical Materials*, *119*, 104552. <https://doi.org/10.1016/j.jmbbm.2021.104552>

- Hameed, P., Liu, C.-F., Ummethala, R., Singh, N., Huang, H.-H., Manivasagam, G., & Prashanth, K. G. (2021). Biomorphic porous Ti6Al4V gyroid scaffolds for bone implant applications fabricated by selective laser melting. *Progress in Additive Manufacturing*, 6(3), 455–469. <https://doi.org/10.1007/s40964-021-00210-5>
- Han, Y. H., Gao, R., Bajpai, I., Kim, B. N., Yoshida, H., Nieto, A., Son, H. W., Yun, J., Jang, B. K., Jhung, S., Jingming, Z., Hwang, K. H., Chen, F., Shackelford, J. F., & Kim, S. (2019). Spark plasma sintered bioceramics – from transparent hydroxyapatite to graphene nanocomposites: a review. *https://doi.org/10.1080/17436753.2019.1691871*, 119(2), 57–74. <https://doi.org/10.1080/17436753.2019.1691871>
- Hanumantharaju, H. G., Prashanth, K. P., Ramu, B., Venkatesh, N., & Chethan, G. R. (2022). 3D Printing of Biopolymer Composites Investigation on Effect of Egg Shell Particles on Polylactic Acid Matrix. *Biointerface Research in Applied Chemistry*, 13(3), 251. <https://doi.org/10.33263/BRIAC133.251>
- Hicks, M., Anamthawat-Jónsson, K., Einarsson, Á., & Þórsson, Æ. Þór. (2023). The identification of bird eggshell by scanning electron microscopy. *Journal of Archaeological Science*, 151, 105712. <https://doi.org/10.1016/j.jas.2022.105712>
- Hincke, M. T. (2012). The eggshell: structure, composition and mineralization. *Frontiers in Bioscience*, 17(1), 1266. <https://doi.org/10.2741/3985>
- Hincke, M. T., Nys, Y., Gautron, J., Mann, K., Rodriguez-Navarro, A. B., & Mckee, M. D. (2012). The eggshell: structure, composition and mineralization. *Frontiers in Bioscience*, 17, 1266.
- Homavand, A., Cree, D. E., & Wilson, L. D. (2024). Polylactic Acid Composites Reinforced with Eggshell/CaCO₃ Filler Particles: A Review. *Waste*, 2(2), 169–185. <https://doi.org/10.3390/waste2020010>
- Hoque, M. E. (2013). Processing and Characterization of Cockle Shell Calcium Carbonate (CaCO₃) Bioceramic for Potential Application in Bone Tissue Engineering. *Journal of Material Science & Engineering*, 02(04), 4. <https://doi.org/10.4172/2169-0022.1000132>
- Hossain, S. S., & Roy, P. K. (2018). Study of physical and dielectric properties of bio-waste-derived synthetic wollastonite. *Journal of Asian Ceramic Societies*, 6(3), 289–298. <https://doi.org/10.1080/21870764.2018.1508549>
- Huang, L., Pan, Y., Zhang, J., Du, Y., & Zhang, Y. (2022). Spark plasma sintering of W-30Si refractory targets: Microstructure, densification and mechanical properties. *International Journal of Refractory Metals and Hard Materials*, 105, 105833. <https://doi.org/10.1016/j.ijrmhm.2022.105833>
- Huang, L., Pan, Y., Zhang, J., Du, Y., Zhang, Y., & Zhang, S. (2021). Densification, grain growth mechanism and mechanical properties of Mo10Nb refractory targets fabricated by SPS. *International Journal of Refractory Metals and Hard Materials*, 99, 105575. <https://doi.org/10.1016/j.IJRMHM.2021.105575>
- Huang, X., Ding, S., Lang, L., & Gong, S. (2023). Compressive response of selective laser-melted lattice structures with different strut sizes based on theoretical, numerical and experimental approaches. *Rapid Prototyping Journal*, 29(2), 209–217. <https://doi.org/10.1108/RPJ-12-2021-0339>
- Huang, Y., Ji, Y., Kang, Z., Li, F., Ge, S., Yang, D.-P., Ruan, J., & Fan, X. (2020). Integrating eggshell-derived CaCO₃/MgO nanocomposites and chitosan into a biomimetic scaffold for bone regeneration. *Chemical Engineering Journal*, 395, 125098. <https://doi.org/10.1016/j.cej.2020.125098>

- Ito, J., Matsushima, Y., Unuma, H., Horiuchi, N., Yamashita, K., & Tajika, M. (2017). Preparation and properties of pressureless-sintered dense calcite ceramics. *Materials Chemistry and Physics*, *192*, 304–310. <https://doi.org/10.1016/J.MATCHEMPHYS.2017.01.062>
- Jiao, L., Chua, Z. Y., Moon, S. K., Song, J., Bi, G., & Zheng, H. (2018). Femtosecond Laser Produced Hydrophobic Hierarchical Structures on Additive Manufacturing Parts. *Nanomaterials*, *8*(8), 601. <https://doi.org/10.3390/nano8080601>
- Joshi, V. A. (2006). *Titanium Alloys*. CRC Press. <https://doi.org/10.1201/9781420006063>
- Kamboj, N., Rodríguez, M. A., Rahmani, R., Prashanth, K. G., & Hussainova, I. (2019). Bioceramic scaffolds by additive manufacturing for controlled delivery of the antibiotic vancomycin. *Proceedings of the Estonian Academy of Sciences*, *68*(2), 185–190. <https://doi.org/10.3176/proc.2019.2.10>
- Kang, N., Yuan, H., Coddet, P., Ren, Z., Bernage, C., Liao, H., & Coddet, C. (2017). On the texture, phase and tensile properties of commercially pure Ti produced via selective laser melting assisted by static magnetic field. *Materials Science and Engineering: C*, *70*, 405–407. <https://doi.org/10.1016/J.MSEC.2016.09.011>
- Kant, R. (2024). Modern Materials and Manufacturing Techniques. In *Modern Materials and Manufacturing Techniques*. CRC Press. <https://doi.org/10.1201/9781032703046>
- Karimi, J., Suryanarayana, C., Okulov, I., & Prashanth, K. G. (2021). Selective laser melting of Ti6Al4V: Effect of laser re-melting. *Materials Science and Engineering: A*, *805*, 140558. <https://doi.org/10.1016/J.MSEA.2020.140558>
- Kawagoe, D., Ishijima, T., & Kimura, K. (2008). Densification Behavior of Various Hydroxyapatite Powders by Spark Plasma Sintering. *Transactions of the Materials Research Society of Japan*, *33*(4), 915–917. <https://doi.org/10.14723/TMRSJ.33.915>
- Kermani, M., Razavi, M., Rahimpour, M. R., & Zakeri, M. (2014). The effect of mechanical alloying on microstructure and mechanical properties of MoSi₂ prepared by spark plasma sintering. *Journal of Alloys and Compounds*, *593*, 242–249. <https://doi.org/10.1016/J.JALLCOM.2014.01.041>
- Khan, N., Dollimore, D., Alexander, K., & Wilburn, F. W. (2001). The origin of the exothermic peak in the thermal decomposition of basic magnesium carbonate. *Thermochimica Acta*, *367–368*, 321–333. [https://doi.org/10.1016/S0040-6031\(00\)00669-9](https://doi.org/10.1016/S0040-6031(00)00669-9)
- Khan, N., & Riccio, A. (2024). A systematic review of design for additive manufacturing of aerospace lattice structures: Current trends and future directions. *Progress in Aerospace Sciences*, *149*, 101021. <https://doi.org/10.1016/J.PAEROSCI.2024.101021>
- Kim, Y., Caumon, M. C., Barres, O., Sall, A., & Cauzid, J. (2021). Identification and composition of carbonate minerals of the calcite structure by Raman and infrared spectroscopies using portable devices. *Spectrochimica Acta Part A: Molecular and Biomolecular Spectroscopy*, *261*, 119980. <https://doi.org/10.1016/J.SAA.2021.119980>
- Krakhmalev, P., Fredriksson, G., Yadroitsava, I., Kazantseva, N., Du Plessis, A., & Yadroitsev, I. (2016). Deformation Behavior and Microstructure of Ti6Al4V Manufactured by SLM. *Physics Procedia*, *83*, 778–788. <https://doi.org/10.1016/J.PHPRO.2016.08.080>

- Kumar, A., Biswas, K., & Basu, B. (2015). Hydroxyapatite-titanium bulk composites for bone tissue engineering applications. *Journal of Biomedical Materials Research Part A*, *103*(2), 791–806. <https://doi.org/10.1002/jbm.a.35198>
- Kumar, A., Dhara, S., Biswas, K., & Basu, B. (2013). In vitro bioactivity and cytocompatibility properties of spark plasma sintered HA-Ti composites. *Journal of Biomedical Materials Research Part B: Applied Biomaterials*, *101B*(2), 223–236. <https://doi.org/10.1002/jbm.b.32829>
- Kumar, A., Webster, T. J., Biswas, K., & Basu, B. (2013). Flow cytometry analysis of human fetal osteoblast fate processes on spark plasma sintered hydroxyapatite–titanium biocomposites. *Journal of Biomedical Materials Research Part A*, *101*(10), 2925–2938. <https://doi.org/10.1002/jbm.a.34603>
- Kumar Yadav, M., Hiren Shukla, R., & Prashanth, K. G. (2023). A comprehensive review on development of waste derived hydroxyapatite (HAp) for tissue engineering application. *Materials Today: Proceedings*. <https://doi.org/10.1016/j.matpr.2023.04.669>
- Leclair, J.-P., Borges, N., Cree, D., & Hof, L. A. (2021). Towards Circular Manufacturing: Repurposing Eggshell Waste As Filler For Poly Lactic Acid Feedstock For 3D Printing. *Progress in Canadian Mechanical Engineering. Volume 4*, 1–6. <https://doi.org/10.32393/csme.2021.120>
- Lee, J. S., Lee, S. J., Yang, S. Bin, Lee, D., Nah, H., Heo, D. N., Moon, H.-J., Hwang, Y.-S., Reis, R. L., Moon, J.-H., & Kwon, I. K. (2019). Facile preparation of mussel-inspired antibiotic-decorated titanium surfaces with enhanced antibacterial activity for implant applications. *Applied Surface Science*, *496*, 143675. <https://doi.org/10.1016/j.apsusc.2019.143675>
- Li, X., Gao, P., Wan, P., Pei, Y., Shi, L., Fan, B., Shen, C., Xiao, X., Yang, K., & Guo, Z. (2017). Novel Bio-functional Magnesium Coating on Porous Ti6Al4V Orthopaedic Implants: In vitro and In vivo Study. *Scientific Reports 2017 7:1*, *7*(1), 1–11. <https://doi.org/10.1038/srep40755>
- Li, X., Wang, C., Zhang, W., & Li, Y. (2009). Fabrication and characterization of porous Ti6Al4V parts for biomedical applications using electron beam melting process. *Materials Letters*, *63*(3–4), 403–405. <https://doi.org/10.1016/j.matlet.2008.10.065>
- Liu, L., Kamm, P., García-Moreno, F., Banhart, J., & Pasini, D. (2017). Elastic and failure response of imperfect three-dimensional metallic lattices: the role of geometric defects induced by Selective Laser Melting. *Journal of the Mechanics and Physics of Solids*, *107*, 160–184. <https://doi.org/10.1016/j.jmps.2017.07.003>
- Liu, S., & Shin, Y. C. (2019). Additive manufacturing of Ti6Al4V alloy: A review. *Materials & Design*, *164*, 107552. <https://doi.org/10.1016/j.matdes.2018.107552>
- Lopez-Heredia, M. A., Goyenvalle, E., Aguado, E., Pilet, P., Leroux, C., Dorget, M., Weiss, P., & Layrolle, P. (2008). Bone growth in rapid prototyped porous titanium implants. *Journal of Biomedical Materials Research - Part A*, *85*(3), 664–673. <https://doi.org/10.1002/jbm.a.31468>
- Ma, Q., Rubenis, K., Sigurjónsson, Ó. E., Hildebrand, T., Standal, T., Zemjane, S., Locs, J., Loca, D., & Haugen, H. J. (2023). Eggshell-derived amorphous calcium phosphate: Synthesis, characterization and bio-functions as bone graft materials in novel 3D osteoblastic spheroids model. *Smart Materials in Medicine*, *4*, 522–537. <https://doi.org/10.1016/j.smaim.2023.04.001>

- Madruza, L. Y. C., Sabino, R. M., Santos, E. C. G., Popat, K. C., Balaban, R. de C., & Kipper, M. J. (2020). Carboxymethyl-kappa-carrageenan: A study of biocompatibility, antioxidant and antibacterial activities. *International Journal of Biological Macromolecules*, *152*, 483–491. <https://doi.org/10.1016/j.ijbiomac.2020.02.274>
- Mahdavi, S., Amirsadeghi, A., Jafari, A., Niknezhad, S. V., & Bencherif, S. A. (2021). Avian Egg: A Multifaceted Biomaterial for Tissue Engineering. *Industrial and Engineering Chemistry Research*, *60*(48), 17348–17364. <https://doi.org/10.1021/acs.iecr.1c03085>
- McGregor, M., Patel, S., McLachlin, S., & Mihaela Vlasea. (2021). Architectural bone parameters and the relationship to titanium lattice design for powder bed fusion additive manufacturing. *Additive Manufacturing*, *47*, 102273. <https://doi.org/10.1016/J.ADDMA.2021.102273>
- Mechay, A., Elfeki, H., Schoenstein, F., Tétard, F., & Jouini, N. (2014). Effect of spark plasma sintering process on the microstructure and mechanical properties of Nano crystalline hydroxyapatite ceramics prepared by hydrolysis in polyol medium. *International Journal of Advanced Chemistry*, *2*(2), 80–84. <https://doi.org/10.14419/ijac.v2i2.2393>
- Naemchan, K., Meejoo, S., Onreabroy, W., & Limsuwan, P. (2008a). Temperature effect on chicken egg shell investigated by XRD, TGA and FTIR. *Advanced Materials Research*, *55–57*, 333–336. <https://doi.org/10.4028/WWW.SCIENTIFIC.NET/AMR.55-57.333>
- Naemchan, K., Meejoo, S., Onreabroy, W., & Limsuwan, P. (2008b). Temperature effect on chicken egg shell investigated by XRD, TGA and FTIR. *Advanced Materials Research*, *55–57*, 333–336. <https://doi.org/10.4028/WWW.SCIENTIFIC.NET/AMR.55-57.333>
- Nassar, A. M., & Alotaibi, N. F. (2021). Eggshell recycling for fabrication of Pd@CaO, characterization and high-performance solar photocatalytic activity. *Environmental Science and Pollution Research*, *28*(3), 3515–3523. <https://doi.org/10.1007/S11356-020-10751-X/FIGURES/11>
- Neikter, M., Åkerfeldt, P., Pederson, R., Antti, M. L., & Sandell, V. (2018). Microstructural characterization and comparison of Ti-6Al-4V manufactured with different additive manufacturing processes. *Materials Characterization*, *143*, 68–75. <https://doi.org/10.1016/J.MATCHAR.2018.02.003>
- Nostro, A., Cellini, L., Di Giulio, M., D'Arrigo, M., Marino, A., Blanco, A. R., Favalaro, A., Cutroneo, G., & Bisignano, G. (2012). Effect of alkaline pH on staphylococcal biofilm formation. *APMIS*, *120*(9), 733–742. <https://doi.org/10.1111/j.1600-0463.2012.02900.x>
- Onwubu, S. C., Mhlungu, S., & Mdluli, P. S. (2019). In vitro evaluation of nanohydroxyapatite synthesized from eggshell waste in occluding dentin tubules. *Journal of Applied Biomaterials & Functional Materials*, *17*(2), 228080001985176. <https://doi.org/10.1177/2280800019851764>
- Orrù, R., Licheri, R., Locci, A. M., Cincotti, A., & Cao, G. (2009). Consolidation/synthesis of materials by electric current activated/assisted sintering. *Materials Science and Engineering: R: Reports*, *63*(4–6), 127–287. <https://doi.org/10.1016/J.MSER.2008.09.003>
- Owuamanam, S., & Cree, D. (2020). Progress of Bio-Calcium Carbonate Waste Eggshell and Seashell Fillers in Polymer Composites: A Review. *Journal of Composites Science*, *4*(2), 70. <https://doi.org/10.3390/jcs4020070>

- Oza, M. J., Schell, K. G., Bucharsky, E. C., Laha, T., & Roy, S. (2021). Developing a hybrid Al–SiC-graphite functionally graded composite material for optimum composition and mechanical properties. *Materials Science and Engineering: A*, *805*, 140625. <https://doi.org/10.1016/J.MSEA.2020.140625>
- Pandey, P. M., Singh, N. K., & Singh, Y. (2022). Additive Manufacturing. In *Sustainability (Switzerland)* (Vol. 11, Issue 1). CRC Press. <https://doi.org/10.1201/9781003258391>
- Pandya, J. R., Bhagia, L. J., & Shah, A. J. (1983). Microhardness of rhombohedral crystals: Calcite and sodium nitrate. *Bulletin of Materials Science*, *5*(1), 79–82. <https://doi.org/10.1007/BF02822352>
- Pedavoah, M.-M., Badu, M., Boadi, N. O., Awudza, J. A. M., Pedavoah, M.-M., Badu, M., Boadi, N. O., & Awudza, J. A. M. (2018). Green Bio-Based CaO from Guinea Fowl Eggshells. *Green and Sustainable Chemistry*, *8*(2), 208–219. <https://doi.org/10.4236/GSC.2018.82015>
- Pelleg, J. (2014). Deformation in Ceramics. In *Mechanical Properties of Ceramics* (1st ed., Vol. 213, pp. 281–350). Springer Cham. https://doi.org/10.1007/978-3-319-04492-7_4
- Prakasam, M., Locs, J., Salma-Ancane, K., Loca, D., Largeteau, A., & Berzina-Cimdina, L. (2017). Biodegradable Materials and Metallic Implants—A Review. *Journal of Functional Biomaterials*, *8*(4), 44. <https://doi.org/10.3390/jfb8040044>
- Prashanth, K. G., Damodaram, R., Maity, T., Wang, P., & Eckert, J. (2017). Friction welding of selective laser melted Ti6Al4V parts. *Materials Science and Engineering: A*, *704*, 66–71. <https://doi.org/10.1016/J.MSEA.2017.08.004>
- Qian, M., Xu, W., Brandt, M., & Tang, H. P. (2016). Additive manufacturing and postprocessing of Ti-6Al-4V for superior mechanical properties. *MRS Bulletin*, *41*(10), 775–784. <https://doi.org/10.1557/MRS.2016.215>
- Rahaman, M. N. (2014). Ceramic Processing and Sintering. In *Sintering of Ceramics* (second). Marcel Dekker Inc.
- Rahmani, R., Antonov, M., Kollo, L., Holovenko, Y., & Prashanth, K. G. (2019). Mechanical behavior of Ti6Al4V scaffolds filled with CaSiO₃ for implant applications. *Applied Sciences (Switzerland)*, *9*(18), 3844. <https://doi.org/10.3390/app9183844>
- Rahmani, R., Brojan, M., Antonov, M., & Prashanth, K. G. (2020). Perspectives of metal-diamond composites additive manufacturing using SLM-SPS and other techniques for increased wear-impact resistance. *International Journal of Refractory Metals and Hard Materials*, *88*, 105192. <https://doi.org/10.1016/j.ijrmhm.2020.105192>
- Rahmani, R., Kamboj, N., Brojan, M., Antonov, M., & Prashanth, K. G. (2022a). Hybrid metal-ceramic biomaterials fabricated through powder bed fusion and powder metallurgy for improved impact resistance of craniofacial implants. *Materialia*, 101465. <https://doi.org/10.1016/J.MTLA.2022.101465>
- Rahmani, R., Kamboj, N., Brojan, M., Antonov, M., & Prashanth, K. G. (2022b). Hybrid metal-ceramic biomaterials fabricated through powder bed fusion and powder metallurgy for improved impact resistance of craniofacial implants. *Materialia*, *24*, 101465. <https://doi.org/10.1016/j.mtla.2022.101465>
- RYAN, G., PANDIT, A., & APATSIDIS, D. (2006). Fabrication methods of porous metals for use in orthopaedic applications. *Biomaterials*, *27*(13), 2651–2670. <https://doi.org/10.1016/j.biomaterials.2005.12.002>
- Salem, A. A., Kalidindi, S. R., & Doherty, R. D. (2003). Strain hardening of titanium: role of deformation twinning. *Acta Materialia*, *51*, 4225–4237. [https://doi.org/10.1016/S1359-6454\(03\)00239-8](https://doi.org/10.1016/S1359-6454(03)00239-8)

- Sarraf, M., Rezvani Ghomi, E., Alipour, S., Ramakrishna, S., & Liana Sukiman, N. (2022). A state-of-the-art review of the fabrication and characteristics of titanium and its alloys for biomedical applications. *Bio-Design and Manufacturing*, 5(2), 371–395. <https://doi.org/10.1007/s42242-021-00170-3>
- Shafiu Kamba, A., Ismail, M., Tengku Ibrahim, T. A., & Zakaria, Z. A. B. (2013). Synthesis and characterisation of calcium carbonate aragonite nanocrystals from cockle shell powder (anadara granosa). *Journal of Nanomaterials*, 2013. <https://doi.org/10.1155/2013/398357>
- Shah, F. A., Trobos, M., Thomsen, P., & Palmquist, A. (2016). Commercially pure titanium (cp-Ti) versus titanium alloy (Ti6Al4V) materials as bone anchored implants — Is one truly better than the other? *Materials Science and Engineering: C*, 62, 960–966. <https://doi.org/10.1016/J.MSEC.2016.01.032>
- Shifeng, W., Shuai, L., Qingsong, W., Yan, C., Sheng, Z., & Yusheng, S. (2014). Effect of molten pool boundaries on the mechanical properties of selective laser melting parts. *Journal of Materials Processing Technology*, 214(11), 2660–2667. <https://doi.org/10.1016/J.JMATPROTEC.2014.06.002>
- Shrivastava, A., Kumar, T., Shukla, R., & Chaudhuri, P. (2021). Li₂TiO₃ pebble fabrication by freeze granulation & freeze drying method. *Fusion Engineering and Design*, 168, 112411. <https://doi.org/10.1016/J.FUSENGDES.2021.112411>
- Shukla, R., Shrivastava, A., & Chaudhuri, P. (2020). Effect of sintering parameters on surface morphology of Li₂TiO₃ compacts. *Twenty Second DAE-BRNS Symposium on Thermal Analysis - Thermal Techniques for Advanced Materials*. https://inis.iaea.org/search/search.aspx?orig_q=RN:51088475
- Shukla, R., Sockalingam, R., & Prashanth, K. G. (2023). Densification of the eggshell powder by spark plasma sintering. *Journal of Alloys and Compounds*, 962, 171079. <https://doi.org/10.1016/j.jallcom.2023.171079>
- Shukla, R., Yadav, M. K., Madruga, L. Y. C., Jayaraj, J., Popat, K., Wang, Z., Xi, L., & Prashanth, K. G. (2024). A novel Ti-eggshell-based composite fabricated by combined additive manufacturing-powder metallurgical routes as bioimplants. *Ceramics International*. <https://doi.org/10.1016/J.CERAMINT.2024.12.073>
- Shukla, S. K., & Rao, T. S. (2013). Effect of calcium on Staphylococcus aureus biofilm architecture: A confocal laser scanning microscopic study. *Colloids and Surfaces B: Biointerfaces*, 103, 448–454. <https://doi.org/10.1016/j.colsurfb.2012.11.003>
- Singh, N., Ummethala, R., Karamched, P. S., Sockalingam, R., Gopal, V., Manivasagam, G., & Prashanth, K. G. (2021). Spark plasma sintering of Ti6Al4V metal matrix composites: Microstructure, mechanical and corrosion properties. *Journal of Alloys and Compounds*, 865, 158875. <https://doi.org/10.1016/J.JALLCOM.2021.158875>
- Singh, V., & Sharma, Y. C. (2017). Low cost guinea fowl bone derived recyclable heterogeneous catalyst for microwave assisted transesterification of Annona squamosa L. seed oil. *Energy Conversion and Management*, 138, 627–637. <https://doi.org/10.1016/J.ENCONMAN.2017.02.037>
- Singla, A. K., Banerjee, M., Sharma, A., Singh, J., Bansal, A., Gupta, M. K., Khanna, N., Shahi, A. S., & Goyal, D. K. (2021). Selective laser melting of Ti6Al4V alloy: Process parameters, defects and post-treatments. *Journal of Manufacturing Processes*, 64, 161–187. <https://doi.org/10.1016/J.JMAPRO.2021.01.009>

- Smirnov, V. V., Bakunova, N. V., Barinov, S. M., Gol'Dberg, M. A., Kutsev, S. V., & Shvorneva, L. I. (2012). Effect of ripening time on the sintering of CaCO₃ powders and the properties of the resultant ceramics. *Inorganic Materials*, 48(5), 544–548. <https://doi.org/10.1134/S0020168512040164>
- Sokkalingam, R., Tarraste, M., Surreddi, K. B., Mikli, V., Muthupandi, V., Sivaprasad, K., & Prashanth, K. G. (2020). Powder metallurgy of Al_{0.1}CoCrFeNi high-entropy alloy. *Journal of Materials Research*, 35(21), 2835–2847. <https://doi.org/10.1557/jmr.2020.272>
- Srivatsan, T. S., & Sudarshan, T. S. (2015). Additive Manufacturing. In T. S. Srivatsan & T. S. Sudarshan (Eds.), *CRC Press* (Vol. 68, Issue 7). CRC Press. <https://doi.org/10.1201/b19360>
- Steinemann, S. G. (2000). Titanium-the material of choice? The foreign body. *Periodontology*, 17, 7–21. <https://doi.org/10.1111/j.1600-0757.1998.tb00119.x>
- Stewart, C., Akhavan, B., Wise, S. G., & Bilek, M. M. M. (2019). A review of biomimetic surface functionalization for bone-integrating orthopedic implants: Mechanisms, current approaches, and future directions. *Progress in Materials Science*, 106, 100588. <https://doi.org/10.1016/J.PMATSCI.2019.100588>
- Sun, P., Fang, Z. Z., Zhang, Y., & Xia, Y. (2017). Review of the Methods for Production of Spherical Ti and Ti Alloy Powder. *JOM*, 69(10), 1853–1860. <https://doi.org/10.1007/s11837-017-2513-5>
- Surreddi, K. B., Scudino, S., Sakaliyska, M., Prashanth, K. G., Sordelet, D. J., & Eckert, J. (2010). Crystallization behavior and consolidation of gas-atomized Al₈₄Gd₆Ni₇Co₃ glassy powder. *Journal of Alloys and Compounds*, 491(1–2), 137–142. <https://doi.org/10.1016/j.jallcom.2009.10.178>
- Tan, J., Wang, D., Cao, H., Qiao, Y., Zhu, H., & Liu, X. (2018). Effect of Local Alkaline Microenvironment on the Behaviors of Bacteria and Osteogenic Cells. *ACS Applied Materials & Interfaces*, 10(49), 42018–42029. <https://doi.org/10.1021/acsami.8b15724>
- Tan, X. P., Tan, Y. J., Chow, C. S. L., Tor, S. B., & Yeong, W. Y. (2017). Metallic powder-bed based 3D printing of cellular scaffolds for orthopaedic implants: A state-of-the-art review on manufacturing, topological design, mechanical properties and biocompatibility. *Materials Science and Engineering: C*, 76, 1328–1343. <https://doi.org/10.1016/j.msec.2017.02.094>
- Tang, Q., & Gong, J. (2013). Effect of porosity on the microhardness testing of brittle ceramics: A case study on the system of NiO–ZrO₂. *Ceramics International*, 39(8), 8751–8759. <https://doi.org/10.1016/J.CERAMINT.2013.04.061>
- Tangboriboon, N., Kunanuruksapong, R., & Sirivat, A. (2012). Preparation and properties of calcium oxide from eggshells via calcination. *Materials Science-Poland*, 30(4), 313–322. <https://doi.org/10.2478/s13536-012-0055-7>
- Tao, W., & Leu, M. C. (2016). Design of lattice structure for additive manufacturing. *International Symposium on Flexible Automation, ISFA 2016*, 325–332. <https://doi.org/10.1109/ISFA.2016.7790182>
- Tetard, F., Bernache-assollant, D., & Saint-etienne, M. (2014). *Calcium carbonate densification with Li₃PO₄. January 1995*.
- Thomas, K. J., & Rice, C. V. (2014). Revised model of calcium and magnesium binding to the bacterial cell wall. *BioMetals*, 27(6), 1361–1370. <https://doi.org/10.1007/s10534-014-9797-5>

- Tizo, M. S., Andre, L., Blanco, V., Cagas, C. Q., Rangel, B., Dela Cruz, B., Encoy, J. C., Guntung, J. V., Arazo, R. O., Irvin, V., & Mabayo, F. (2018). Efficiency of calcium carbonate from eggshells as an adsorbent for cadmium removal in aqueous solution. *Original Research Article*. <https://doi.org/10.1016/j.serj.2018.09.002>
- Ul Haq, I., Khan, T. A., & Krukiewicz, K. (2024). Etiology, pathology, and host-impaired immunity in medical implant-associated infections. *Journal of Infection and Public Health*, *17*(2), 189–203. <https://doi.org/10.1016/J.JIPH.2023.11.024>
- Usta, M. C., Yörük, C. R., Uibu, M., Hain, T., Gregor, A., & Trikkel, A. (2022). CO₂ Curing of Ca-Rich Fly Ashes to Produce Cement-Free Building Materials. *Minerals* *2022*, *Vol. 12*, Page 513, *12*(5), 513. <https://doi.org/10.3390/MIN12050513>
- Van Bael, S., Chai, Y. C., Truscetto, S., Moesen, M., Kerckhofs, G., Van Oosterwyck, H., Kruth, J.-P., & Schrooten, J. (2012). The effect of pore geometry on the in vitro biological behavior of human periosteum-derived cells seeded on selective laser-melted Ti6Al4V bone scaffolds. *Acta Biomaterialia*, *8*(7), 2824–2834. <https://doi.org/10.1016/j.actbio.2012.04.001>
- Vlasov, A. S., & Poroskova, A. A. (1997). Sintering of calcium carbonate in the presence of lithium carbonate additive. *Glass and Ceramics*, *54*(11), 11–12. <https://doi.org/10.1007/BF02766759>
- Vrancken, B., Thijs, L., Kruth, J. P., & Van Humbeeck, J. (2012). Heat treatment of Ti6Al4V produced by Selective Laser Melting: Microstructure and mechanical properties. *Journal of Alloys and Compounds*, *541*, 177–185. <https://doi.org/10.1016/J.JALLCOM.2012.07.022>
- Vuola, J., Taurio, R., Göransson, H., & Asko-Seljavaara, S. (1998). Compressive strength of calcium carbonate and hydroxyapatite implants after bone-marrow-induced osteogenesis. *Biomaterials*, *19*(1–3), 223–227. [https://doi.org/10.1016/S0142-9612\(97\)00211-1](https://doi.org/10.1016/S0142-9612(97)00211-1)
- Wan, M. chen, Qin, W., Lei, C., Li, Q. hong, Meng, M., Fang, M., Song, W., Chen, J. hua, Tay, F., & Niu, L. na. (2021). Biomaterials from the sea: Future building blocks for biomedical applications. *Bioactive Materials*, *6*(12), 4255–4285. <https://doi.org/10.1016/J.BIOACTMAT.2021.04.028>
- Wang, D. W., Zhou, Y. H., Shen, J., Liu, Y., Li, D. F., Zhou, Q., Sha, G., Xu, P., Ebel, T., & Yan, M. (2019). Selective laser melting under the reactive atmosphere: A convenient and efficient approach to fabricate ultrahigh strength commercially pure titanium without sacrificing ductility. *Materials Science and Engineering: A*, *762*, 138078. <https://doi.org/10.1016/J.MSEA.2019.138078>
- Wang, X., Xu, S., Zhou, S., Xu, W., Leary, M., Choong, P., Qian, M., Brandt, M., & Xie, Y. M. (2016). Topological design and additive manufacturing of porous metals for bone scaffolds and orthopaedic implants: A review. *Biomaterials*, *83*, 127–141. <https://doi.org/10.1016/j.biomaterials.2016.01.012>
- Wang, Z., Xiao, Z., Tse, Y., Huang, C., & Zhang, W. (2019). Optimization of processing parameters and establishment of a relationship between microstructure and mechanical properties of SLM titanium alloy. *Optics & Laser Technology*, *112*, 159–167. <https://doi.org/10.1016/j.optlastec.2018.11.014>
- Williams, D. F. (2002). Titanium in medicine. In *Biomaterials* (Vol. 23, Issue 18). [https://doi.org/10.1016/s0142-9612\(02\)00111-4](https://doi.org/10.1016/s0142-9612(02)00111-4)
- Wong, T. (1991). *Knoop microhardness anisotropy on the cleavage plane of single crystals with the calcite structure*.

- Yadav, M. K., Pandey, V., Mohanta, K., & Singh, V. K. (2022). A low-cost approach to develop silica doped Tricalcium Phosphate (TCP) scaffold by valorizing animal bone waste and rice husk for tissue engineering applications. *Ceramics International*, *48*(17), 25335–25345. <https://doi.org/10.1016/J.CERAMINT.2022.05.207>
- Yang, J., Yu, H., Yin, J., Gao, M., Wang, Z., & Zeng, X. (2016). Formation and control of martensite in Ti-6Al-4V alloy produced by selective laser melting. *Materials & Design*, *108*, 308–318. <https://doi.org/10.1016/j.matdes.2016.06.117>
- Yang, Q., Cheng, D. L., Zhang, F. G., Shi, Q. W., Chen, Z., Wang, M. L., Zhong, S. Y., Wu, Y., & Wang, H. W. (2021). Spark plasma sintering mechanisms of the Al-Zn-Mg-Cu alloys and TiB₂/Al-Zn-Mg-Cu composites. *Materials Characterization*, *172*, 110825. <https://doi.org/10.1016/J.MATCHAR.2020.110825>
- Yilmaz, P., Öztürk Er, E., Bakirdere, S., Ülgen, K., & Özbek, B. (2019). Application of supercritical gel drying method on fabrication of mechanically improved and biologically safe three-component scaffold composed of graphene oxide/chitosan/hydroxyapatite and characterization studies. *Journal of Materials Research and Technology*, *8*(6), 5201–5216. <https://doi.org/10.1016/J.JMRT.2019.08.043>
- Yu, Q., Qi, L., Tsuru, T., Traylor, R., Rugg, D., Morris, J. W., Asta, M., Chrzan, D. C., & Minor, A. M. (2015). Origin of dramatic oxygen solute strengthening effect in titanium. *Science*, *347*(6222), 635–639. https://doi.org/10.1126/SCIENCE.1260485/SUPPL_FILE/YU-SM.PDF
- Zaman, T., Mostari, Mst. S., Mahmood, Md. A. Al, & Rahman, Md. S. (2018). Evolution and characterization of eggshell as a potential candidate of raw material. *Cerâmica*, *64*(370), 236–241. <https://doi.org/10.1590/0366-69132018643702349>
- Zhang, L.-C., Attar, H., Calin, M., & Eckert, J. (2016). Review on manufacture by selective laser melting and properties of titanium based materials for biomedical applications. *Materials Technology*, *31*(2), 66–76. <https://doi.org/10.1179/1753555715Y.0000000076>
- Zhang, T., & Liu, C. T. (2022). Design of titanium alloys by additive manufacturing: A critical review. *Advanced Powder Materials*, *1*(1), 100014. <https://doi.org/10.1016/J.APMATE.2021.11.001>
- Zheng, Y., Banerjee, R., Wang, Y., Fraser, H., & Banerjee, D. (2022). Pathways to Titanium Martensite. *Transactions of the Indian Institute of Metals*, *75*(4), 1051–1068. <https://doi.org/10.1007/s12666-022-02559-9>

Acknowledgments

I would like to express my deepest gratitude to the Estonian Research Council and the ETAG21021 project, Waste-to-resource: eggshells as a source for next-generation biomaterials for bone regeneration (1.04.2021–31.03.2024), led by Principal Investigator Prof. Prashanth Konda Gokuldoss from Tallinn University of Technology, School of Engineering, Department of Mechanical and Industrial Engineering (partner), funded by the EEA/Norway/Iceland (Lichtenstein) Grant. The financial support of 205,250 EUR made this research possible, and I am deeply thankful for this opportunity.

My heartfelt thanks go to Prof. Prashanth Konda Gokuldoss for entrusting me with this research and for his unwavering support, insight, and guidance throughout. His mentorship has been the cornerstone of my development as a researcher. Special thanks also to Prof. Jayaraj Jaymani, whose invaluable guidance significantly shaped my research. I am grateful to both professors' families for their warmth and hospitality.

I am especially grateful to Mr. Mayank Kumar Yadav for his help with mechanical testing and technical insights. I also thank my co-authors and colleagues Dr. Sokkalingam Rathinavelu, Dr. Jagdeesh Bhaskaran, and Miss Shangavi Subramanian for their support and companionship. I am grateful to my colleague Ms. Sibel Yöyler, Mrs. Mansoureh, and her family, especially my tiny friend Abtin, for bringing warmth and joy to this journey.

I am deeply indebted to Prof. Ketul C. Popat for hosting me at Colorado State University, USA, and for his guidance during the in-vitro study. His encouragement, expertise, and patience are deeply appreciated. I am especially thankful to Dr. Liszt Yeltsin Coutinho Madruga for teaching and assisting throughout all the tests. My time there was made so much smoother thanks to the support of Mr. Aniruddha Vijay Savargaonkar, Mr. Abhishek Bhattacharjee, and the rest of my colleagues and friends at Colorado State University.

My sincere thanks go to Dr. Rocio Rojas, Dr. Jüri Majak, and Dr. Kristo Karjust for their valuable feedback, and to Dr. Le Liu, Dr. Marek Tarraste, Dr. Rainer Traksmäa, Dr. Mart Viljus, Mr. Hans Vallner for their guidance in the practical aspects of my work. I am deeply grateful to Dr. Mart Konles and Dr. Märt Kolnes for their continuous help, and to Mrs. Ruth Kulbas, Mrs. Laivi Väljaots, Mr. Mykola Semeniuk, and the Department of Mechanical and Industrial Engineering staff for their support. Thanks also to Prof. Oliver Järvik and Dr. Kaia Tõnsuaadu for their help with TGA and FTIR analyses.

To my family—my mother, father, and sister—your unwavering love, encouragement, and belief in me have been my foundation, and I dedicate this achievement to you. You are the reason I have come this far. I am also grateful to Lord Ganesha, my uncle Mr. Kaushik Pandit, and my family doctor for always being with us in our highs and lows.

My deepest thanks also go to my master's thesis supervisors, Mr. Aroh Shrivastava, Dr. Parithosh Chaudhuri, and Dr. Vandana Rao, especially Mr. Aroh Shrivastava, for inspiring and supporting me throughout my research journey. I am grateful to my friends Mr. Meet Oza, Mr. Shreyas Patil, Mr. Vijay Solanki, and Mr. Sunilkumar Prajapati, whose support and motivation carried me through the highs and lows. Finally, I would like to acknowledge God and my late grandparents, whose love and wisdom continue to inspire me, along with my friends, teachers, and all those who have supported me throughout my academic journey.

I would also like to express my gratitude to the programs that supported me during my research, including Dora Plus, Erasmus+, SPARC, and Euroteq. My appreciation goes out to everyone involved in these funding agencies for making this journey possible.

Abstract

Development of Ti-eggshell composite for bio-implants applications

The demand for orthopedic implants has escalated due to an increase in the incidence of arthritis, accidents, and osteoporosis. Bio-implants for load-bearing applications require biocompatibility, corrosion resistance, and a balance of mechanical properties such as strength, fatigue resistance, Young's Modulus, and wear resistance. Commercially pure titanium (CP-Ti) is widely considered for biomedical applications due to its superior ductility, biocompatibility, and corrosion resistance. However, its mismatch with the elastic modulus (100–105 GPa) compared to natural bone (10–30 GPa) leads to stress shielding, which can cause bone resorption and implant failure. To address these limitations, recent advancements in additive manufacturing (AM) have facilitated the development of porous titanium structures that mimic the mechanical properties of natural bone, reducing stress shielding. Despite these advancements, the bio-inert nature of titanium hampers its ability to fully integrate with bone tissues and promote osseointegration.

In contrast, ceramics, such as calcium carbonate (CaCO_3), have demonstrated significant potential for biomedical applications due to their bioactivity, bioresorbability, and osseointegration capabilities. CaCO_3 is present naturally in bone and hence can promote bone healing by releasing essential ions (Ca^{2+} , PO_4^{3-}) and even exhibit antibacterial properties. Eggshells, which are 94–95% calcium carbonate, represent a significant and underutilized bio-waste. This research aims to valorize eggshell waste by incorporating it into orthopedic implants, creating a composite material that combines the bioactivity of CaCO_3 with the mechanical strength of titanium. This novel approach addresses both the environmental challenge of waste disposal and the limitations of current titanium implants, particularly their high Young's modulus and susceptibility to bacterial infections.

Mechanical testing of the Ti-eggshell composite revealed compressive strength (123 ± 34 MPa) and Young's modulus (47 ± 1 GPa), values within the range of natural human cortical bone (compressive yield strength = 100–130 MPa, and Young's modulus = 5–30 GPa respectively), demonstrating the potential for use in load-bearing orthopedic implants. Additionally, cytotoxicity tests showed that the composite was non-toxic to adipose-derived stem cells (ADSCs), confirming its biocompatibility. Importantly, the Ti-eggshell composite exhibited antibacterial activity against both gram-negative (*Pseudomonas aeruginosa*) and gram-positive (*Staphylococcus aureus*) bacteria, significantly reducing the risk of implant-associated infections (IAs).

The innovative combination of titanium and eggshell in this study offers a promising solution for orthopedic implants by reducing stress shielding, enhancing osseointegration, and providing antibacterial protection. Moreover, by utilizing a bio-waste material in the form of eggshells, this research promotes a circular economy approach in biomedical manufacturing, aligning with green and sustainable practices. The valorization of eggshell waste into high-performance bio-implants represents a significant advancement in both environmental stewardship and the development of next-generation orthopedic materials.

Lühikokkuvõte

Ti-munakoore komposiidi väljatöötamine bioimplantaatide rakenduste jaoks

Nõudlus ortopeediliste implantaatide järele on suurenenud artriidi, õnnetusjuhtumite ja osteoporoosi esinemissageduse suurenemise tõttu. Kandvate rakenduste jaoks mõeldud bioimplantaadid nõuavad biosobivust, korrosioonikindlust ja mehaaniliste omaduste, nagu tugevus, väsimuskindlus, Youngi moodul ja kulumiskindlus, tasakaalu. Kaubanduslikult puhast titaani (CP-Ti) peetakse laialdaselt biomeditsiinilisteks rakendusteks tänu selle suurepärasele plastilisusele, biosobivusele ja korrosioonikindlusele. Kuid selle ebakõla elastsusmooduliga (100–105 GPa) võrreldes loodusliku luuga (10–30 GPa) põhjustab pingearvestuse, mis võib põhjustada luu resorptsiooni ja implantaadi ebaõnnestumist. Nende piirangute lahendamiseks on hiljutised edusammud lisandite tootmises (AM) hõlbustanud poorsete titaanstruktuuride väljatöötamist, mis jäljendavad loodusliku luu mehaanilisi omadusi, vähendades stressivarjestust. Vaatamata nendele edusammudele takistab titaani bioinertne olemus selle võimet täielikult luukoega integreeruda ja soodustada luude integratsiooni.

Seevastu keraamika, nagu kaltsiumkarbonaat (CaCO_3), on näidanud märkimisväärset potentsiaali biomeditsiinilistes rakendustes tänu nende bioaktiivsusele, bioresorbeerumisele ja luude integreerumisvõimele. CaCO_3 esineb luus loomulikult ja võib seega soodustada luude paranemist, vabastades olulisi ioone (Ca^{2+} , PO_4^{3-}) ja avaldada isegi antibakteriaalseid omadusi. Munakoored, mis on 94–95% kaltsiumkarbonaadist, kujutavad endast märkimisväärset ja alakasutatud biojätmeid. Selle uuringu eesmärk on väärtustada munakoore jätmeid, lisades need ortopeedilistesse implantaatidesse, luues komposiitmaterjali, mis ühendab CaCO_3 bioaktiivsuse titaani mehaanilise tugevusega. See uudne lähenemisviis käsitleb nii jätmete kõrvaldamisega seotud keskkonnaprobleeme kui ka praeguste titaanimplantaatide piiranguid, eriti nende kõrget Youngi moodulit ja vastuvõtlikkust bakteriaalsetele infektsioonidele.

Ti-munakoore komposiidi mehaaniline testimine näitas survetugevust (123 ± 34 MPa) ja Youngi moodulit (47 ± 1 GPa), mis jäävad inimese loomuliku kortikaalse luu vahemikku (survevolupiir = 100–130 MPa ja Youngi moodul = vastavalt 5–30 GPa), mis näitab potentsiaali kasutada kandvates ortopeedilistes implantaatides. Lisaks näitasid tsütotoksilisuse testid, et komposiit ei olnud rasvast pärinevatele tüvirakkudele (ADSC) toksiline, kinnitades selle biosobivust. Oluline on see, et Ti-munakoore komposiidil oli antibakteriaalne toime nii gramnegatiivsete (*Pseudomonas aeruginosa*) kui ka grampositiivsete (*Staphylococcus aureus*) bakterite vastu, vähendades oluliselt implantaadiga seotud infektsioonide (IAI) riski.

Selle uuringu uuenduslik titaani ja munakoore kombinatsioon pakub ortopeediliste implantaatide jaoks paljulubavat lahendust, vähendades stressikaitset, suurendades luude integratsiooni ja pakkudes antibakteriaalset kaitset. Lisaks sellele, kasutades biojätmeid munakoorte kujul, edendab see uurimus biomeditsiinilises tootmises ringmajandust, mis on kooskõlas roheliste ja säästvate tavadega. Munakoorejätmete väärtustamine suure jõudlusega bioimplantaatideks on oluline edasiminekuks nii keskkonnajuhtimises kui ka järgmise põlvkonna ortopeediliste materjalide väljatöötamises.

Appendix

Publication I

Kumar Yadav, M., **Hiren Shukla, R.**, & Prashanth, K. G. (2023). A comprehensive review on development of waste derived hydroxyapatite (HAp) for tissue engineering application. Materials Today: Proceedings. <https://doi.org/10.1016/j.matpr.2023.04.669>



Contents lists available at ScienceDirect

Materials Today: Proceedings

journal homepage: www.elsevier.com/locate/matpr

A comprehensive review on development of waste derived hydroxyapatite (HAp) for tissue engineering application

Mayank Kumar Yadav^{a,*}, Riddhi Hiren Shukla^a, K.G. Prashanth^{a,b,c,*}

^aDepartment of Mechanical and Industrial Engineering, Tallinn University of Technology, Ehitajate tee 5, 19086 Tallinn, Estonia

^bErich Schmid Institute of Materials Science, Austrian Academy of Sciences, Jahnstrasse 12, 8700 Leoben, Austria

^cCBCMT, School of Mechanical Engineering, Vellore Institute of Technology, Vellore 630014, Tamil Nadu, India

ARTICLE INFO

Article history:
Available online xxxxx

Keywords:
Waste Bone
Waste management
Hydroxyapatite
Tricalcium phosphate
Biomaterials

ABSTRACT

The present review article is a comprehensive study on the development and utilization of materials derived from biological wastes like animal waste bone, eggshells, fish scale, etc. These waste materials are calcium rich and can act as a precursor for the development of highly bioactive hydroxyapatite (HAp), tri-calcium phosphate (TCP), and calcium. The developed HAp and TCP can be utilized in the field of bone tissue engineering. The concept of valorization of these wastes into bioactive materials is a promising solution for waste management and an approach towards sustainable development.

Copyright © 2023 Elsevier Ltd. All rights reserved.

Selection and peer-review under responsibility of the scientific committee of the International Conference on Materials and Manufacturing for Sustainable Developments – 2022.

1. Introduction

It has been estimated that around 4.89 billion livestock population is present globally [1] which produces 16–20 Million Metric Tons/Year of animal waste worldwide through different sources like slaughterhouse, restaurants, etc [2,3]. Bones, horns, seashells, fish scales, eggshells, etc are some of the major parts which are generally discarded. As the demand for industrial and agricultural products is increasing the amount of organic waste produced is also increasing. The vast amount of biological waste produced is left unattended or disposed of in landfills, which can spread infectious diseases through the emission of foul smell and the tendency of pollutants to leach into the environment [4,5]. The fertility of the agricultural land is also affected by these wastes [6]. To mitigate the problem associated with these types of waste proper waste management practices are required which involves additional cost. In other words, the disposal of this biological waste is a challenge for the scientific community as it creates a hindrance to environmental protection and sustainable development. If these waste materials are processed and recycled efficiently, they have the potential to be a source of extra revenue and will directly impact the economy of the country. Researchers throughout the world

are working vigorously to obtain a sustainable solution for valorizing these waste materials. Many researchers have reported the application of these waste materials in different fields like Transesterification of biodiesel, Tissue Engineering applications, Drug delivery, etc. In different research findings it is concluded that if these waste materials are treated specifically, they have the potential to be converted into a source of calcium phosphate [7,8].

Hydroxyapatite (HAp) with chemical formula $\text{Ca}_{10}(\text{PO}_4)_6(\text{OH})_2$, a member of the calcium phosphate family is considered one of the most suitable bioceramics materials due to its biocompatibility, non-toxicity, osteointegration, and osteoconduction properties [9,10]. The chemical and structural properties of HAp are similar to that of natural bone and therefore it can promote bone regeneration and biological fixation with the host tissue without any supplements [11]. When HAp is introduced in biological fluid, they release Ca^{2+} and PO_4^{4-} ions upon dissolution which helps in cell proliferation and bone metabolism [12,13]. Synthetic HAp produced through different chemical methods like mechanochemical reaction, wet chemical precipitation, hydrothermal conversion emulsion, and solgel methods is considered superior [14] with respect to those derived from natural sources as mentioned above. But most of these above-mentioned methods are costly and lack some beneficial trace elements [15–17]. HAp derived from xenogeneic (derived from different species) bone sources like bovine bone is always considered a good option with respect to that of allogeneic bone (derived from the same species) [18–22] because of ease of

* Corresponding authors at: Department of Mechanical and Industrial Engineering, Tallinn University of Technology, Ehitajate tee 5, 19086 Tallinn, Estonia.

E-mail addresses: mayada@taltech.ee (M. Kumar Yadav), kprashanth@gmail.com (K.G. Prashanth).

<https://doi.org/10.1016/j.matpr.2023.04.669>

2214-7853/Copyright © 2023 Elsevier Ltd. All rights reserved.

Selection and peer-review under responsibility of the scientific committee of the International Conference on Materials and Manufacturing for Sustainable Developments – 2022.

availability and improvement in biological constituent and structure due to thermal and mechanical processing [22-24]. Table 1 lists different methods utilized to develop HAp using different animals' wastes bone, scale, and shells. The extent of the global research activity in the field of development of natural source bio-material especially by utilizing animal waste bones has created a scope for developing HAp. Considering the potential advantages of waste-derived HAp, the present review article is an approach to review the synthesis methods of HAp through different waste sources and its application in tissue engineering.

2. Animal bone waste: A source of natural hydroxyapatite (HAp)

Bio wastes like left-out bones of bovine, lamb, goat, pig, fish bone and scale, etc generally consist of proteins, lipids, collagens and polysaccharides as organic, and calcium phosphate (CaP) as inorganic constituents. These waste materials are widely used for the synthesis of HAp [22,30]. The synthesis of HAp from these wastes generally involves the removal of moisture and organic contents via different techniques. Thermal treatment, subcritical water treatment, and alkaline heat hydrolysis are some of the methods which are practiced for the development of HAp from bio-wastes. In the alkaline hydrolysis method, microbial biodegradation of keratin takes place through hydrolysis of isolated thermoactinomycete strains [31]. Since keratin and collagen are similar proteins due to their fibrous structure, Barakat et al. [25] performed alkaline hydrolysis of collagen and other organic content of bovine bones. In this method, grounded bone was mixed with 25 wt% of sodium hydroxide solution with a solid-to-liquid weight ratio of 1:40 followed by heating at 250 °C for 5 h. The SEM and TEM results revealed the formation of pure HAp nanoparticles at lower temperatures. In subcritical water treatment method pressurized hot water is employed which changes the solvent polarity, surface tension, and viscosity [32]. As the temperature increases the dielectric constant of water reduces resulting in a reduction in polarity and thus many organic compounds like collagen, protein, etc can be extracted [33]. This method is also known as the pressurized low-polarity water method. Apart from the above-mentioned two methods, there is another conventional method that is most widely used and commonly known as the thermal treatment method. Ofudje et al. synthesized waste-derived HAp by simple heat treatment of pig bone in the temper-

ature range of 600 to 1000 °C [29]. C.Y. Ooi et al. [22] examined the properties of HAp derived from bovine bone sintered at different temperatures between 400 and 1200 °C. The XRD results show that as the sintering temperature increases above 700 °C the crystallinity of the HAp phase enhances. At higher sintering temperatures i.e., 1100 °C and 1200 °C a phenomenon of phase transformation HAp to β -tricalcium phosphate (TCP) was observed [22]. The effect of calcination on the microstructural behavior of HAp derived from human and animal bone was studied by Figueiredo et al. and a similarity are drawn between allograft and xenograft samples [34]. Piccirillo et al. [35] for the first time utilised different parts of the same fish to synthesize HAp and chloroapatite by using fish bone and scale respectively. It is also important to note that the sintered bones form a mixture of HAp and β -TCP and as the temperature increases the content of β -TCP also increases [35]. The mechanism of phase transformation from HAp to TCP was explained by Shih et al. [36]. During high-temperature sintering phenomenon of decomposition and dehydroxylation takes place resulting in the formation of TCP (α and β) [36]. Thus, from the above observations and findings through different research work it can be concluded that waste bone obtained from different animal sources can be utilized for the development of HAp and TCP based materials suitable for biomedical applications.

3. Calcium derived from eggshell and other anthropogenic waste sources

An eggshell (ES) is basically a composite of calcite crystals that is surrounded by a protein framework [37]. Along with ES various mollusk shells like mussels, cuttlebone, oysters, snail shells, etc are mainly composed of calcium carbonate (CaCO_3), according to Soares et al. [38] ES contains about 88 g of CaCO_3 per 100 g of air-dried eggshells. This CaCO_3 can be easily converted to another form of Ca which can be used to synthesize HAp [39]. Calcium Phosphate (CaP) derived from ES shows in vitro biocompatibility and the scaffolds fabricated using CaP shows osteoinductive properties which are favourable for bone tissue engineering applications [40]. The fabrication of HAp using ES involves an essential reaction with Phosphorus precursor. There are two different methods based on the processing of raw precursor i.e., CaCO_3 . The first method is direct synthesis in which ES is directly treated with

Table 1
List of different animal waste and method for the development of HAp.

Waste Material	Method	Application	Major Conclusion	Ref.
Bovine bone	Thermal Decomposition	Production of pure HAp	65% average yield of HAp	[28]
Bovine bone	Subcritical water process	Production of pure HAp	Very small amount of nanoparticle HAp produced	[28]
Bovine bone	Alkaline Hydrothermal process	Production of pure HAp	Very small amount of nanoparticle HAp produced	[28]
Chicken bone	Simple calcination process	Guided bone regeneration	Chicken bone derived HAp can be used as an osteogenic filler to augments and can change the biological behaviour of chitosan membrane.	[26]
Lates HAp powder derived by	Calcarifer fish bone sintering fish bone at 1200 °C non-cytotoxic behaviour	Simple calcination process [27]	Biomedical application	
Fish Bone	Thermal treatment at 800–1050 °C for HAp preparation and polymeric sponge method for scaffold preparation	Highly porous 3D scaffold for tissue engineering application	Porosity of the scaffold was $85 \pm 0.4\%$ and compressive and bending strength was 0.13 ± 0.007 MPa and 1.72 ± 0.02 MPa respectively.	[37]
Pig Bone	Bone powder were calcined at different temperatures i.e., 600 °C, 800 °C and 1000 °C	Tissue engineering application	Development of HAp based scaffold with 65% porosity suitable for tissue engineering application	[22]
Fish Scale	By calcining fish scale between 200 °C and 1200 °C	Biomedical application	Crystallite size of fish scale derived HAp increases with the increase in temperature.	[25]

phosphorus-based reagents [41,42]. Another method also known as indirect synthesis involves the conversion of CaCO_3 into different calcium-based products like calcium oxide, calcium hydroxide, calcium chloride, etc. CaCO_3 can be converted into calcium-based products by direct heat treatment at different temperatures, by dissolving CaCO_3 in acids [43–47]. Wu, Et al. [41] prepared HAp by ball milling dicalcium phosphate dihydrate along with ES powder for 1 h followed by high temperature sintering at 1200 °C for 1 h. Prabakaran et al. [44] successfully synthesized nano-HAp by hydrothermal method using a cationic surfactant as a regulator of nucleation and grain growth. The microstructure of the developed HAp crystals depends on the processing route. Different shapes of HAp like rods, needles, flower-like shapes, etc are reported in different research work [45]. The effect of sintering time and temperature on the morphology of HAp crystal is shown in Fig. 1.

4. Production of HAp by valorizing fish bone and fish scale waste

The production of fish is increasing due to exponential growth in its demand. It is estimated that annually 91 million tons of fish are caught worldwide out of which 50–60% of it is consumed by humans and the remaining by-products are treated as waste which creates environmental-related issues as discussed earlier in the

introduction section. Considering this fact number of research studies are focused on the conversion of fish bone and scale waste into HAp [49]. There are different methods of synthesis of HAp by using fish waste, in general, this method involves washing of waste in running water and boiling followed by chemical treatment to remove protein [50]. Deb et al. [51] observed that HAp produced by acid-treated fish waste posse's smaller crystallite size with the interconnected porous network with respect to alkaline and acid alkaline-treated fish waste. Further, the chemically treated wastes are calcined at different temperatures to get different crystallite sizes and morphology of HAp powders. Barramundi, catfish, croaker, cod, salmon, sardine, tuna, yellowtail, etc are some of the common fish species whose waste parts are used for HAp synthesis [52]. Goto et al. [53] studied the effect of the presence of different trace elements like sodium, potassium, and magnesium on the thermal stability of HAp derived from different fish bone. The amount of Magnesium for different fish bone was in the order of: hoarse mackerel (0.21 mmol g^{-1}) > greater amberjack (0.15 mmol g^{-1}) > tuna = yellowtail (0.13 mmol g^{-1}). Tuna fish sintered at temperature above than 800 °C produces highly crystalline HAp with have higher value of Ca/P ratio and low magnesium content [53]. In another study conducted by Pujie Shi and co-workers reports the presence of carbonate ion (CO_3^{2-}) in all the fish bone i.e., rainbow trout, salmon except cod fish bone [54]. Huang et al. stud-

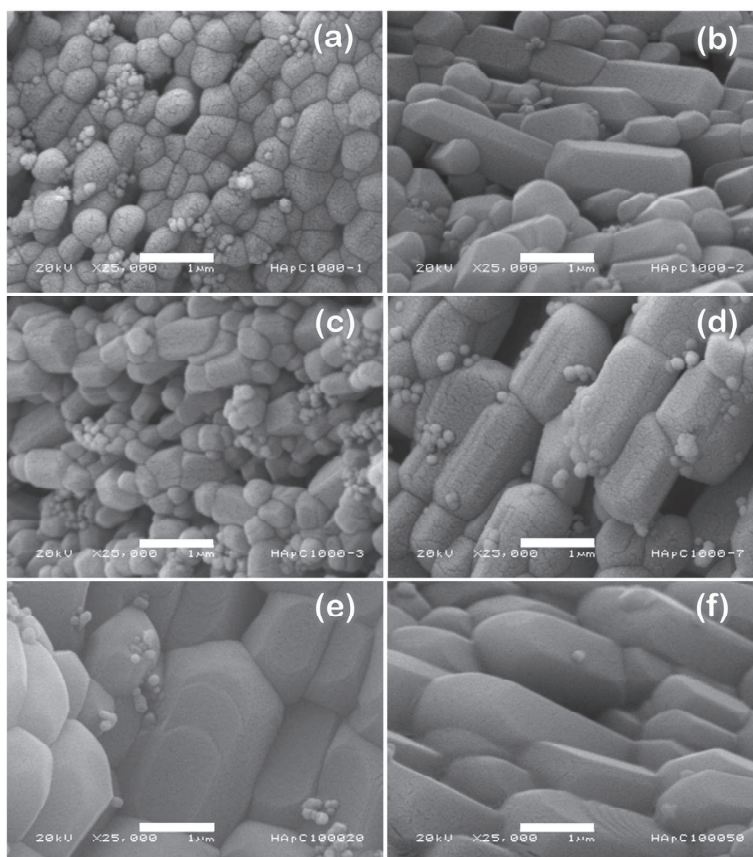


Fig. 1. SEM micrographs representing morphological transformation of samples calcined at 1000 °C for 1, 2, 3, 7, 20, and 50 h [48].

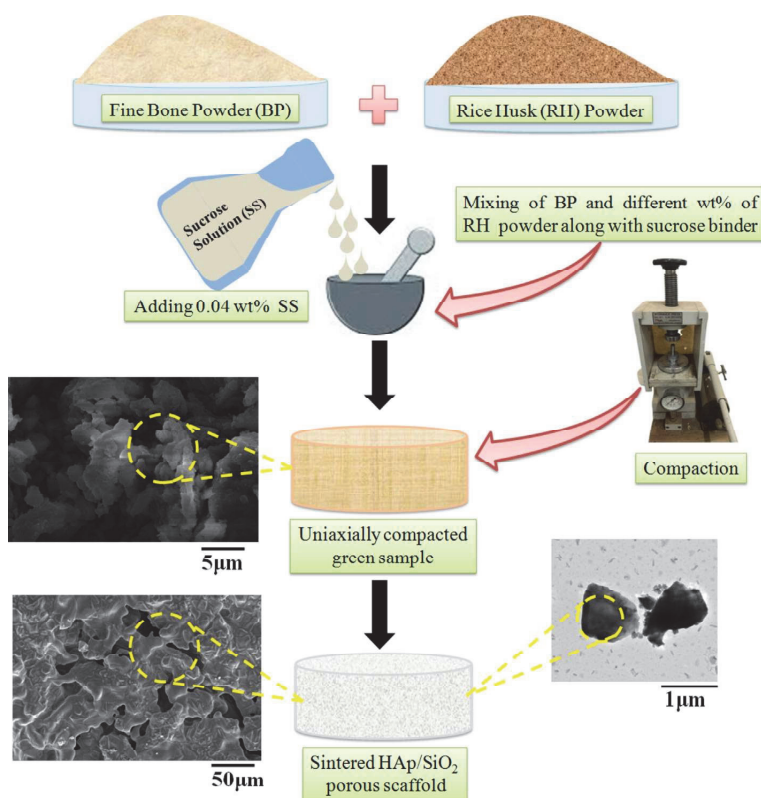


Fig. 2. Schematic diagram of the process involved in the development of HAp based scaffolds [3].

Table 2

Property comparison of 3D scaffold synthesized using different animal waste bone with respect to that of human cortical bone [3].

Type of bone	Space holder used	Binder used	Processing condition	Porosity (%)	Compressive Strength (MPa)	Ref.
Human cortical bone	NA	NA	NA	5–10	80–120	[55,56]
Bovine bone	Commercial sugar	NA	900 °C	76.7 ± 0.6	1.3 ± 0.09	[57]
Fish bone	High-density polyethylene sponge	PVA	Initial Sintering at 600 °C Final Sintering 1200 °C	85 ± 0.4	0.13 ± 0.007 MPa	[58]
Fish scale	Sponge replication	Starch	1000–1400 °C, 2hr	35	800 MPa	[38]
Pig bone	Ammonium bicarbonate	NA	600–1000 °C	65	NA	[22]
Fish bone	solvent casting particulate leaching technique/ NaCl (SH)	Ethanol (as solvent)	1200 °C, 3 hr	75 ± 0.8	7.26 ± 0.45	[39]
Bovine one	3D Printing	Glycerine (solvent)	900 °C	NA	3.22 ± 0.13 to 5.71 ± 0.43	[40]
Mixed bone waste	Rice Husk	Sucrose Solution	1000–1400 °C, 2 hr	34–61	0.22–4.1	[3]

ied the behaviour of HAp derived through enzymatic hydrolysis with Ca/P ratio of 1.76 through thermal treatment at 800 °C for 4 h.

5. Utilization of waste derived HAp for the development of 3D scaffold for tissue engineering application

Bone graft surgeries like autograft, allograft, xenograft, etc which involve the replacement of degenerated natural surfaces with the help of tissue, or organs of a donor of the same species or of different species are increasing. To reconstruct these damaged

tissues, bone tissue engineering can act as a substitute for conventional medical practices. In bone tissue engineering scaffolds are designed with the aim to proliferate bone tissues. Scaffold acts as a temporary extracellular matrix that promotes cell migration, proliferation, and differentiation [57,61] Biocompatibility, high porosity with interconnected pore structures, bioresorbability, osteoinduction, osteoconduction, and osteointegration are some of the important features of bio-scaffolds [62–65]. Since the structural and chemical resemblance of HAp is like that of natural bone, therefore the application of HAp has gained attention in the field of

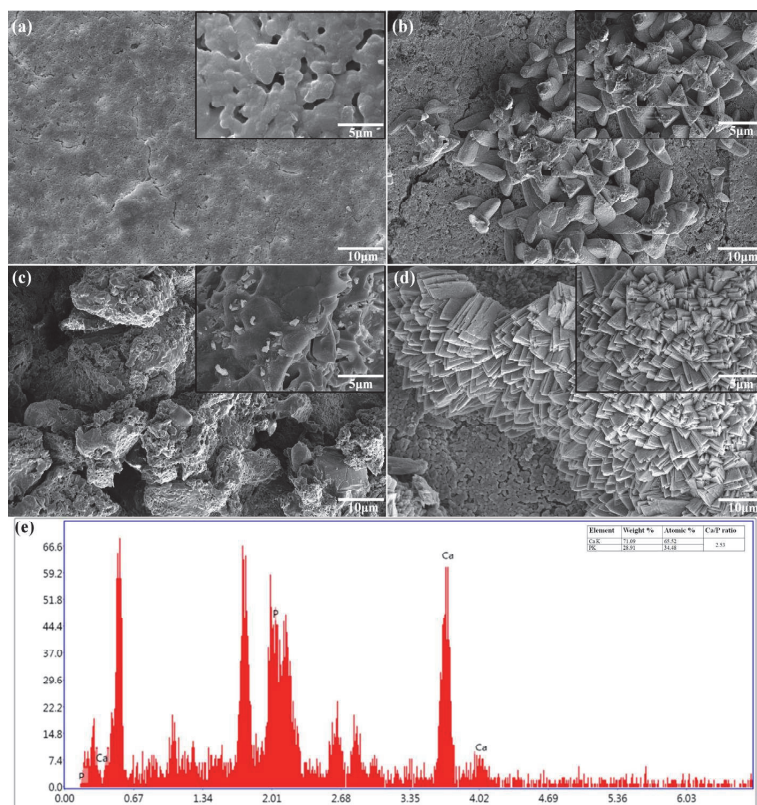


Fig. 3. SEM and EDS image of HAp based scaffold sintered at elevated temperature and immersed in simulated body fluid for different time periods [3].

bone tissue engineering. The elemental composition of HAp derived from different animal bone varies for example HAp derived from bovine bone contains 52.25 wt% CaO and 38.37 wt% P₂O₅ whereas HAp derived from Tengiri fish bones contains 49.84 wt % CaO and 26.195 wt% P₂O₅ [20,66,67]. The calcination temperature of porous waste bone plays a major role in the osteoconductive property of the scaffold. A study conducted by Rhee et al. [68] concludes that HAp derived at 600 °C shows better osteoconductivity with respect to that of samples sintered at 1000 °C, the main reason behind this phenomenon is the depletion of carbonate ion and increase in crystallinity of HAp synthesized at 1000 °C. The above research finding is also supported by several other studies highlighting the role of carbonate ions and particle size in osteoblast activity [69,70]. Synthesis of porous 3D scaffolds for bone tissue engineering using different materials is reported by different researchers. In our recent research work [3] we fabricated a porous HAp-SiO₂ 3D scaffold using waste bone obtained from different sources like restaurants, slaughterhouses, etc. Along with the use of rice husk powder as a space holder material as shown in Fig. 2. The scaffold posse's porosity of 34–61% based on sintering temperature and weight percent of rice husk. The compressive strength of the developed scaffold was up to 4.1 MPa. The obtained properties of the developed scaffold are comparable to that of natural bone and hence can be used for tissue engineering applications. Table 2 lists the comparative analysis of porosity and mechanical properties of HAp-based 3D scaffold fabricated using different animal bone waste with that of human cortical bone. Similarly, Naga et al.

[28] fabricated a highly porous ceramic scaffold using thermally treated fishbone by polymeric sponge method. The overall process involves three stages starting with the extraction of pure HAp of average particle size 50–80 nm from the fishbone skeleton, followed by the formation of a highly porous HAp scaffold using a polymeric sponge and heat treatment at 900 °C. Mechanical and structural characterization revealed that the scaffold posse's porosity is in the range of 85 ± 0.4% with a pore diameter in the range of 1–3 µm along with bending and compressive strength of 1.72 ± 0.02 Mpa and 0.13 ± 0.007 MPa respectively. Weeraphat et al. [50] studied the physicochemical, bioactivity, and biological properties of HAp which is derived from fish scale, and compared it with that of chemically synthesized HAp. It was concluded that fish scale-derived HAp consists of flat plate nanocrystals with sizes of 15–20 nm whereas chemically derived HAp has crystals in the range of 100 nm. Biocompatibility and bioactivity studies also suggest that fish scale-derived HAp has the potential to be used as an alternate for bone scaffold or regenerative materials (see Fig. 3).

6. Conclusion and future perspective

Animal bone waste derived from different sources contains valuable precursors which can be utilized for the development of HAp-based materials as they are rich in calcium. In this review, different methods of development of HAp using different types of animal waste like bones, shells, scales, etc are discussed. Generally, HAp can be derived from calcium phosphate and calcium sources

thermal decomposition, subcritical water process, and alkaline hydrothermal process. The properties of 3D scaffold developed from waste-derived HAp possess mechanical and biological properties like that of natural bone and thus can be utilized for the development of biomaterials. The concept of valorization of animal waste by synthesizing HAp is an idea to reduce the cost of HAp-based biomaterials and also a strategy for effective waste management. It is beneficial to conduct future research in the field of bone regeneration using animal waste bone as a scaffold. It is important to investigate the biodegradation properties of the scaffold, as well as conduct an in-depth analysis of degradation products. Comprehensive studies on properties such as porosity and compressive strength of the scaffold, along with in-vitro and in-vivo analysis, are important.

Data availability

Data will be made available on request.

Declaration of Competing Interest

The authors declare that they have no known competing financial interests or personal relationships that could have appeared to influence the work reported in this paper.

Acknowledgments

The authors acknowledge financial support from the Baltic Research Programme project no. EEA-RESEARCH-85 "Waste-to-resource: eggshells as a source for next generation biomaterials for bone regeneration (EGGSHELL)" under the EEA Grant of Iceland, Liechtenstein, and Norway no. EEZ/BPP/VIAA/2021/1.

References

- [1] Advances in biomaterial production from animal derived waste _ Enhanced Reader, (n.d.).
- [2] Y. Liu, J. Chen, Phosphorus Cycle, Encyclopedia of Ecology. (2014) 181–191. Doi: 10.1016/B978-0-12-409548-9.09043-6.
- [3] M.K. Yadav, V. Pandey, K. Mohanta, V.K. Singh, A low-cost approach to develop silica doped Tricalcium Phosphate (TCP) scaffold by valorizing animal bone waste and rice husk for tissue engineering applications, *Ceram Int.* (2022), <https://doi.org/10.1016/j.ceramint.2022.05.207>.
- [4] M.J. Quina, M.A.R. Soares, R. Quinta-Ferreira, Applications of industrial eggshell as a valuable anthropogenic resource, *Resour Conserv Recycl.* 123 (2017) 176–186, <https://doi.org/10.1016/j.resconrec.2016.09.027>.
- [5] H. Yamamura, V.H.P. da Silva, P.L.M. Ruiz, V. Ussui, D.R.R. Lazar, A.C.M. Renno, D.A. Ribeiro, Physico-chemical characterization and biocompatibility of hydroxyapatite derived from fish waste, *J Mech Behav Biomed Mater.* 80 (2018) 137–142, <https://doi.org/10.1016/j.jmbm.2018.01.035>.
- [6] M. Boutinguiza, J. Pou, R. Comesaña, F. Lusquinos, A. de Carlos, B. León, Biological hydroxyapatite obtained from fish bones, *Materials Science and Engineering: C.* 32 (2012) 478–486, <https://doi.org/10.1016/j.msec.2011.11.021>.
- [7] K. Fukui, N. Arimitsu, S. Kidoguchi, T. Yamamoto, H. Yoshida, Synthesis of calcium phosphate hydrogel from waste incineration fly ash and bone powder, *J Hazard Mater.* 163 (2009) 391–395, <https://doi.org/10.1016/j.jhazmat.2008.06.103>.
- [8] G.S. Kumar, E.K. Giriya, M. Venkatesh, G. Karunakaran, E. Kolesnikov, D. Kuznetsov, One step method to synthesize flower-like hydroxyapatite architecture using mussel shell bio-waste as a calcium source, *Ceram Int.* 43 (2017) 3457–3461, <https://doi.org/10.1016/j.ceramint.2016.11.163>.
- [9] M.R. Nikpour, S.M. Rabiee, M. Jahanshahi, Synthesis and characterization of hydroxyapatite/chitosan nanocomposite materials for medical engineering applications, *Compos B Eng.* 43 (2012) 1881–1886, <https://doi.org/10.1016/j.compositesb.2012.01.056>.
- [10] P. Nasker, A. Samanta, S. Rudra, A. Sinha, A.K. Mukhopadhyay, M. Das, Effect of fluorine substitution on sintering behaviour, mechanical and bioactivity of hydroxyapatite, *J Mech Behav Biomed Mater.* 95 (2019) 136–142, <https://doi.org/10.1016/j.jmbm.2019.03.032>.
- [11] G. Turnbull, J. Clarke, F. Picard, P. Riches, L. Jia, F. Han, B. Li, W. Shu, 3D bioactive composite scaffolds for bone tissue engineering, *Bioact Mater.* 3 (2018) 278–314, <https://doi.org/10.1016/j.bioactmat.2017.10.001>.
- [12] M. Sepantafar, H. Mohammadi, R. Maheronnaghsh, L. Tayebi, H. Baharvand, Single phased silicate-containing calcium phosphate bioceramics: Promising biomaterials for periodontal repair, *Ceram Int.* 44 (2018) 11003–11012, <https://doi.org/10.1016/j.ceramint.2018.03.050>.
- [13] A. Hoppe, N.S. Güldal, A.R. Boccacini, A review of the biological response to ionic dissolution products from bioactive glasses and glass-ceramics, *Biomaterials.* 32 (2011) 2757–2774, <https://doi.org/10.1016/j.biomaterials.2011.01.004>.
- [14] Synthetic materials used for the substitution of bone defects: Critical review, *Annals of Oral & Maxillofacial Surgery*, (n.d.), <https://www.oapublishinglondon.com/article/398> (accessed July 31, 2022).
- [15] D.K. Pattanayak, R. Dash, R.C. Prasad, B.T. Rao, T.R. Rama Mohan, Synthesis and sintered properties evaluation of calcium phosphate ceramics, *Materials Science and Engineering C.* 27 (2007) 684–690, <https://doi.org/10.1016/j.msec.2006.06.021>.
- [16] S. Koutsopoulos, Synthesis and characterization of hydroxyapatite crystals: A review study on the analytical methods, 2002.
- [17] M. Akram, ● Rashid, A. Imran, S. ● Wan, A. Wan, I. ● Rafoqat Hussain, Extracting hydroxyapatite and its precursors from natural resources, (n.d.). Doi: 10.1007/s10853-013-7864-x.
- [18] S. Joschek, B. Nies, R. Krotz, A. Göpferich, Chemical and physicochemical characterization of porous hydroxyapatite ceramics made of natural bone, *Biomaterials.* 21 (2000) 1645–1658, [https://doi.org/10.1016/S0142-9612\(00\)00036-3](https://doi.org/10.1016/S0142-9612(00)00036-3).
- [19] R. Murugan, S. Ramakrishna, K. Panduranga Rao, Nanoporous hydroxy-carbonate apatite scaffold made of natural bone, *Mater Lett.* 60 (2006) 2844–2847, <https://doi.org/10.1016/j.matlet.2006.01.104>.
- [20] K. Haberko, M.M. Bučko, J. Brzezińska-Miecznik, M. Haberko, W. Moggawa, T. Panz, A. Pyda, J. Zarebski, Natural hydroxyapatite—its behaviour during heat treatment, *J Eur Ceram Soc.* 26 (2006) 537–542, <https://doi.org/10.1016/j.jeurceramsoc.2005.07.033>.
- [21] R. Murugan, P. Rao, T.S.S. Kumar, Heat-deproteinated xenogeneic bone from slaughterhouse waste: Physico-chemical properties, 2003.
- [22] C.Y. Ooi, M. Hamdi, S. Ramesh, Properties of hydroxyapatite produced by annealing of bovine bone, *Ceram Int.* 33 (2007) 1171–1177, <https://doi.org/10.1016/j.ceramint.2006.04.001>.
- [23] S.A. Essien Etok Eugenia Valsami-Jones AE Timothy J Wess AE Jennifer C Hiller AE Clark A Maxwell AE Keith D Rogers AE David A C Manning AE Margaret L White AE Elisa Lopez-Capel AE Matthew J Collins AE Mike Buckley AE Kirsty E H Penkman AE Stephen L Woodgate, Structural and chemical changes of thermally treated bone apatite, (n.d.). Doi: 10.1007/s10853-007-1993-z.
- [24] J.C. Hiller, T.J.U. Thompson, M.P. Evison, A.T. Chamberlain, T.J. Wess, Bone mineral change during experimental heating: An X-ray scattering investigation, *Biomaterials.* 24 (2003) 5091–5097, [https://doi.org/10.1016/S0142-9612\(03\)00427-7](https://doi.org/10.1016/S0142-9612(03)00427-7).
- [25] N.A.M. Barakat, M.S. Khil, A.M. Omran, F.A. Sheikh, H.Y. Kim, Extraction of pure natural hydroxyapatite from the bovine bones bio waste by three different methods, *J Mater Process Technol.* 209 (2009) 3408–3415, <https://doi.org/10.1016/j.jmatprotec.2008.07.040>.
- [26] S.L. Bee, Z.A.A. Hamid, Characterization of chicken bone waste-derived hydroxyapatite and its functionality on chitosan membrane for guided bone regeneration, *Compos B Eng.* 163 (2019) 562–573, <https://doi.org/10.1016/j.compositesb.2019.01.036>.
- [27] A. Pal, S. Paul, A.R. Choudhury, V.K. Balla, M. Das, A. Sinha, Synthesis of hydroxyapatite from Lates calcarifer fish bone for biomedical applications, *Mater Lett.* 203 (2017) 89–92, <https://doi.org/10.1016/j.matlet.2017.05.103>.
- [28] S.M. Naga, H.F. El-Maghraby, E.M. Mahmoud, M.S. Talaat, A.M. Ibrahim, Preparation and characterization of highly porous ceramic scaffolds based on thermally treated fish bone, *Ceram Int.* 41 (2015) 15010–15016, <https://doi.org/10.1016/j.ceramint.2015.08.057>.
- [29] E.A. Ofudje, A. Rajendran, A.I. Adeogun, M.A. Idowu, S.O. Kareem, D.K. Pattanayak, Synthesis of organic derived hydroxyapatite scaffold from pig bone waste for tissue engineering applications, *Advanced Powder Technology.* 29 (2018) 1–8, <https://doi.org/10.1016/j.apt.2017.09.008>.
- [30] S. Paul, A. Pal, A.R. Choudhury, S. Bodhak, V.K. Balla, A. Sinha, M. Das, Effect of trace elements on the sintering effect of fish scale derived hydroxyapatite and its bioactivity, *Ceram Int.* 43 (2017) 15678–15684, <https://doi.org/10.1016/j.ceramint.2017.08.127>.
- [31] A. Gousterova, D. Braikova, I. Goshev, P. Christov, K. Tishinov, E. Vasileva-Tonkova, T. Haertel, P. Nedkov, Degradation of keratin and collagen containing wastes by newly isolated thermoactinomycetes or by alkaline hydrolysis, *Lett Appl Microbiol.* 40 (2005) 335–340, <https://doi.org/10.1111/j.1472-765X.2005.01692.X>.
- [32] Y. Yang, M. Belghazi, A. Lagadec, D.J. Miller, S.B. Hawthorne, Elution of organic solutes from different polarity sorbents using subcritical water, *J Chromatogr A.* 810 (1998) 149–159, [https://doi.org/10.1016/S0021-9673\(98\)00222-2](https://doi.org/10.1016/S0021-9673(98)00222-2).
- [33] Y. Han, S. Li, X. Wang, L. Jia, J. He, Preparation of hydroxyapatite rod-like crystals by protein precursor method, *Mater Res Bull.* 42 (2007) 1169–1177, <https://doi.org/10.1016/j.matresbull.2006.09.003>.
- [34] M. Figueiredo, A. Fernando, G. Martins, J. Freitas, F. Judas, F. Figueiredo, Effect of the calcination temperature on the composition and microstructure of hydroxyapatite derived from human and animal bone, *Ceram Int.* 36 (2010) 2383–2393, <https://doi.org/10.1016/j.ceramint.2010.07.016>.
- [35] C. Piccirillo, R.C. Pullar, D.M. Tobaldi, P.M.L. Castro, M.M.E. Pintado, Hydroxyapatite and chlorapatite derived from sardine by-products, *Ceram Int.* 40 (2014) 13231–13240, <https://doi.org/10.1016/j.ceramint.2014.05.030>.

- [36] S.F. Ou, S.Y. Chiou, K.L. Ou, Phase transformation on hydroxyapatite decomposition, *Ceram Int.* 39 (2013) 3809–3816, <https://doi.org/10.1016/j.ceramint.2012.10.221>.
- [37] S. Meski, S. Ziari, H. Khireddine, F. Yataghane, N. Ferguene, Elaboration of the hydroxyapatite with different precursors and application for the retention of the lead, *Water Science and Technology.* 63 (2011) 2087–2096, <https://doi.org/10.2166/wst.2011.210>.
- [38] M.A.R. Soares, M.J. Quina, R.M. Quinta-Ferreira, Immobilisation of lead and zinc in contaminated soil using compost derived from industrial eggshell, *J Environ Manage.* 164 (2015) 137–145, <https://doi.org/10.1016/j.jenvman.2015.08.042>.
- [39] Y. Hou, A. Shavandi, A. Carne, A.A. Bekhit, T.B. Ng, R.C.F. Cheung, A.E. din A. Bekhit, Marine shells: Potential opportunities for extraction of functional and health-promoting materials, <http://dx.doi.org/10.1080/10643389.2016.1202669>, 46 (2016) 1047–1116, Doi: 10.1080/10643389.2016.1202669.
- [40] M.F.M.A. Zamri, R. Bahru, R. Amin, M.U. Aslam Khan, S.I.A. Razak, S.A. Hassan, M.R.A. Kadir, N.H.M. Nayan, Waste to health: A review of waste derived materials for tissue engineering, *J Clean Prod.* 290 (2021), <https://doi.org/10.1016/j.jclepro.2021.125792>.
- [41] S.C. Wu, H.C. Hsu, S.K. Hsu, Y.C. Chang, W.F. Ho, Effects of heat treatment on the synthesis of hydroxyapatite from eggshell powders, *Ceram Int.* 41 (2015) 10718–10724, <https://doi.org/10.1016/j.ceramint.2015.05.006>.
- [42] S.C. Wu, H.C. Hsu, Y.N. Wu, W.F. Ho, Hydroxyapatite synthesized from oyster shell powders by ball milling and heat treatment, *Mater Charact.* 62 (2011) 1180–1187, <https://doi.org/10.1016/j.matchar.2011.09.009>.
- [43] B. Chaudhuri, B. Mondal, D.K. Modak, K. Pramanik, B.K. Chaudhuri, Preparation and characterization of nanocrystalline hydroxyapatite from egg shell and K₂HPO₄ solution, *Mater Lett.* 97 (2013) 148–150, <https://doi.org/10.1016/j.matlet.2013.01.082>.
- [44] K. Prabakaran, S. Rajeswari, Spectroscopic investigations on the synthesis of nano-hydroxyapatite from calcined eggshell by hydrothermal method using cationic surfactant as template, *Spectrochim Acta A Mol Biomol Spectrosc.* 74 (2009) 1127–1134, <https://doi.org/10.1016/j.saa.2009.09.021>.
- [45] N.K. Nga, N.T. Thuy Chau, P.H. Viet, Facile synthesis of hydroxyapatite nanoparticles mimicking biological apatite from eggshells for bone-tissue engineering, *Colloids Surf B Biointerfaces.* 172 (2018) 769–778, <https://doi.org/10.1016/j.colsurfb.2018.09.039>.
- [46] S. Lahrich, M. Abderrahim, E. Mhammedi, A. Siddharthan, S. Kumar, S.K. Seshadri, Synthesis and characterization of nanocrystalline apatites from eggshells at different Ca/P ratios, *Biomedical Materials.* 4 (2009), <https://doi.org/10.1088/1748-6041/4/4/045010>.
- [47] G.S. Kumar, A. Thamizhavel, E.K. Giriya, Microwave conversion of eggshells into flower-like hydroxyapatite nanostructure for biomedical applications, *Mater Lett.* 76 (2012) 198–200, <https://doi.org/10.1016/j.matlet.2012.02.106>.
- [48] C.F. Ramirez-Gutierrez, S.M. Londoño-Restrepo, A. del Real, M.A. Mondragón, M.E. Rodríguez-García, Effect of the temperature and sintering time on the thermal, structural, morphological, and vibrational properties of hydroxyapatite derived from pig bone, *Ceram Int.* 43 (2017) 7552–7559, <https://doi.org/10.1016/j.ceramint.2017.03.046>.
- [49] J.A. da Cruz, W.R. Weinand, A.M. Neto, R.S. Palácios, P. Palácios, A.J.M. Sales, P. R. Prezas, M.M. Costa, M.P.F. Graç, Advanced manufacturing for biomaterials and biological materials low-cost hydroxyapatite powders from tilapia fish, *JOM.* 72 (n.d.). Doi: 10.1007/s11837-019-03998-4.
- [50] W. Pon-On, P. Suntornsaratoon, N. Charoephandhu, J. Thongbunchoo, N. Krishnamra, I.M. Tang, Hydroxyapatite from fish scale for potential use as bone scaffold or regenerative material, *Materials Science and Engineering: C.* 62 (2016) 183–189, <https://doi.org/10.1016/j.msec.2016.01.051>.
- [51] P. Deb, A.B. Deoghare, Effect of pretreatment processes on physicochemical properties of hydroxyapatite synthesized from *Puntius conchionius* fish scales, *Bulletin of Materials Science.* 42 (2019), <https://doi.org/10.1007/S12034-018-1684-1>.
- [52] P. Terzioğlu, H. Öğüt, A. Kalemtaş, Natural calcium phosphates from fish bones and their potential biomedical applications, *Materials Science and Engineering: C.* 91 (2018) 899–911, <https://doi.org/10.1016/j.msec.2018.06.010>.
- [53] T. Goto, K. Sasaki, Effects of trace elements in fish bones on crystal characteristics of hydroxyapatite obtained by calcination, *Ceram Int.* 40 (2014) 10777–10785, <https://doi.org/10.1016/j.ceramint.2014.03.067>.
- [54] P. Shi, M. Liu, F. Fan, C. Yu, W. Lu, M. Du, Characterization of natural hydroxyapatite originated from fish bone and its biocompatibility with osteoblasts, *Materials Science and Engineering: C.* 90 (2018) 706–712, <https://doi.org/10.1016/j.msec.2018.04.026>.
- [55] S.C.P. Cachinho, R.N. Correia, Titanium scaffolds for osteointegration: Mechanical, in vitro and corrosion behaviour, *J Mater Sci Mater Med.* 19 (2008) 451–457, <https://doi.org/10.1007/S10856-006-0052-7/TABLES/3>.
- [56] A. Mukherjee, *Biomimetics Learning from Nature, Biomimetics Learning from Nature.* (2010), <https://doi.org/10.5772/198>.
- [57] G. Krishnamurthy, M.R. Murali, M. Hamdi, A.A. Abbas, H.B. Raghavendran, T. Kamarul, Characterization of bovine-derived porous hydroxyapatite scaffold and its potential to support osteogenic differentiation of human bone marrow derived mesenchymal stem cells, *Ceram Int.* 40 (2014) 771–777, <https://doi.org/10.1016/j.ceramint.2013.06.067>.
- [58] B. Mondal, S. Mondal, A. Mondal, N. Mandal, Fish scale derived hydroxyapatite scaffold for bone tissue engineering, *Mater Charact.* 121 (2016) 112–124, <https://doi.org/10.1016/j.matchar.2016.09.034>.
- [61] A. Olad, F. Farshi Azhar, The synergetic effect of bioactive ceramic and nanoclay on the properties of chitosan–gelatin/nanohydroxyapatite–montmorillonite scaffold for bone tissue engineering, *Ceram Int.* 40 (2014) 10061–10072, <https://doi.org/10.1016/j.ceramint.2014.04.010>.
- [62] X. yun Zhang, Y. ping Chen, J. Han, J. Mo, P. feng Dong, Y. hong Zhuo, Y. Feng, Biocompatible silk fibroin/carboxymethyl chitosan/strontium substituted hydroxyapatite/cellulose nanocrystal composite scaffolds for bone tissue engineering, *Int J Biol Macromol.* 136 (2019) 1247–1257. Doi: 10.1016/j.ijbiomac.2019.06.172.
- [63] W. Xiao, B. Sonny Bal, M.N. Rahaman, Preparation of resorbable carbonate-substituted hollow hydroxyapatite microspheres and their evaluation in osseous defects in vivo, *Materials Science and Engineering C.* 60 (2016) 324–332, <https://doi.org/10.1016/j.msec.2015.11.039>.
- [64] A. Szcześ, L. Hołysz, E. Chibowski, Synthesis of hydroxyapatite for biomedical applications, *Adv Colloid Interface Sci.* 249 (2017) 321–330, <https://doi.org/10.1016/j.cis.2017.04.007>.
- [65] Y. Tang, K. Zhao, L. Hu, Z. Wu, Two-step freeze casting fabrication of hydroxyapatite porous scaffolds with bionic bone graded structure, *Ceram Int.* 39 (2013) 9703–9707, <https://doi.org/10.1016/j.ceramint.2013.04.038>.
- [66] T. Jia, F. Zhou, H. Ma, Y. Zhang, A highly stable waste animal bone-based catalyst for selective nitriles production from biomass via catalytic fast pyrolysis in NH₃, *J Anal Appl Pyrolysis.* 157 (2021), <https://doi.org/10.1016/j.jaap.2021.105217>.
- [67] A. Buasri, T. Inkaew, L. Kodephun, W. Yenying, V. Loryuenyong, Natural Hydroxyapatite (NHAp) Derived from Pork Bone as a Renewable Catalyst for Biodiesel Production via Microwave Irradiation, *Key Eng Mater.* 659 (2015) 216–220, <https://doi.org/10.4028/WWW.SCIENTIFIC.NET/KEM.659.216>.
- [68] S.H. Rhee, H.N. Park, Y.J. Seol, C.P. Chung, S.H. Han, Effect of heat-treatment temperature on the osteoconductivity of the apatite derived from bovine bone, *Key Eng Mater.* 309–311 1 (2006) 41–44, <https://doi.org/10.4028/0-87849-992-X.41>.
- [69] A.S. Stanislavov, L.F. Sukhodub, L.B. Sukhodub, V.N. Kuznetsov, K.L. Bychkov, M.I. Kravchenko, Structural features of hydroxyapatite and carbonated apatite formed under the influence of ultrasound and microwave radiation and their effect on the bioactivity of the nanomaterials, *Ultrason Sonochem.* 42 (2018) 84–96, <https://doi.org/10.1016/j.ultsonch.2017.11.011>.
- [70] Z. Shi, X. Huang, Y. Cai, R. Tang, D. Yang, Size effect of hydroxyapatite nanoparticles on proliferation and apoptosis of osteoblast-like cells, *Acta Biomater.* 5 (2009) 338–345, <https://doi.org/10.1016/j.actbio.2008.07.023>.

Further reading

- [59] P. Deb, E. Barua, A.B. Deoghare, S. das Lala, Development of bone scaffold using *Puntius conchionius* fish scale derived hydroxyapatite: Physico-mechanical and bioactivity evaluations, *Ceram Int.* 45 (2019) 10004–10012, <https://doi.org/10.1016/j.ceramint.2019.02.044>.
- [60] J. Triyono, R. Alfiansyah, H. Sukanto, D. Ariawan, Y. Nugroho, Fabrication and characterization of porous bone scaffold of bovine hydroxyapatite-glycerin by 3D printing technology, *Bioprinting.* 18 (2020) e00078.

Publication II

Shukla, R., Sokkalingam, R., & Prashanth, K. G. (2023). Densification of the eggshell powder by spark plasma sintering. *Journal of Alloys and Compounds*, 962, 171079. <https://doi.org/10.1016/j.jallcom.2023.171079>



Contents lists available at ScienceDirect

Journal of Alloys and Compounds

journal homepage: www.elsevier.com/locate/jalcom

Densification of the eggshell powder by spark plasma sintering

Riddhi Shukla^a, R. Sokkalingam^b, K.G. Prashanth^{a,c,*}^a Department of Mechanical and Industrial Engineering, Tallinn University of Technology, Ehitajate tee 5, 19086 Tallinn, Estonia^b Department of Engineering and Physics, Karlstad University, SE-651 88 Karlstad, Sweden^c CBCMT, School of Mechanical Engineering, Vellore Institute of Technology, Vellore 632014, Tamil Nadu, India

ARTICLE INFO

Keywords:

Spark plasma sintering
Chicken eggshell
Bio-waste
Consolidation

ABSTRACT

Chicken eggshells (eggshells) are the bio-waste produced during day-to-day egg consumption by humans. The eggshell contains calcium carbonate (CaCO_3) along with several other elements such as Si, Mg, K, P, Na, etc., which enables its application for human bio-implants. Our research work aims to practically implement the eggshell powder as the bio-implant, for which, the study of the densification behavior of the eggshell powder is required. Hence, the present paper represents the densification behavior of the crystalline eggshell powder by spark plasma sintering. The eggshell powders were irregular in shape with a wide particle size distribution. The eggshell powder was sintered at six varying temperatures, i.e., 250 °C, 500 °C, 750 °C, 850 °C, 900 °C, and 1000 °C. The consolidated samples were characterized through SEM, FTIR, and XRD analysis, and the optimum spark plasma sintering temperature was determined. The consolidation of eggshells at 850 °C not only avoids the calcination process (due to the application of pressure) but gives optimum density and hardness making it an optimum condition for consolidating eggshells into compacts.

1. Introduction

Chicken eggs are widely consumed, both commercially and in households. Chicken eggs are composed of three main parts: the outer shell, which is made up of calcium carbonate (CaCO_3), i.e. ceramic; the second layer is a thin protein layer known as albumin; and the third, the inner core layer [1]. The only part of a chicken egg that is not useful in cooking is the eggshell causing wastage of very high calcium (Ca) containing products. Generally, the egg shells are disposed of on the land (as landfills) and in water. This creates a significant environmental concern owing to their microbial action [2]. In addition, dumping in land creates a financial concern owing to transportation and dumping land costs. In the past, researchers have tried to utilize eggshells in different products, such as wall tiles [3], and as calcium supplements [4]. Tizo et al. [5] and Hajji et al. [6] utilized eggshells for Cd- and Pb-like heavy metal removal. While Nassar et al. [7] attempted to utilize eggshells for Pd@CaO solar photocatalytic fabrication for wastewater treatment. Despite these facts, the utilization of eggshell waste remains a major concern for the environment as well as for the eggshell industry.

Eggshell is a source of calcium and human bones largely comprise calcium in salt, phosphate, and carbonate form (CaCO_3 : 94–95%). Apart from CaCO_3 , eggshell contains ~1% calcium phosphate ($\text{Ca}_3(\text{PO}_4)_2$,

~1% magnesium carbonate (MgCO_3), trace amounts of sodium (Na) (1512 ppm), magnesium (Mg) (3472–4500 ppm), strontium (Sr) (320–411 ppm), potassium (K) (525 ppm), sulfur (S) (589 ppm), and remaining ~4% organic matter [8–11]. Besides, natural bone also possesses trace amounts of Na, K, Mg, Sr, and Si along with Ca. Hence, naturally-derived Ca sources such as eggshells are an ideal choice for bone grafting materials [8]. One option is the direct use of CaCO_3 as the bone grafting material since CaCO_3 is bio-ceramic and possesses biocompatibility, bio-resorbability, and osteoconductivity [12–14]. Moreover, CaCO_3 is a biodegradable ceramic as compared to calcium phosphate forms [15,16]. The use of eggshells as a bone grafting material will eliminate the transportation of eggshells to landfills thereby saving the cost of transportation, cost for landfill, and CO_2 emission. Hence, this particular research work aims to utilize eggshell waste as a bone-grafting material.

Various studies have been conducted to densify CaCO_3 by powder metallurgical route through sintering. However, CaCO_3 is unstable above 800–900 °C, where it decomposes into calcium oxide (CaO) and carbon dioxide (CO_2) through calcination. This decomposition behavior of CaCO_3 poses issues with the densification and production of bone-grafting implants [17–22]. In order to address these issues, several researchers have attempted to dope CaCO_3 with a dopant (sintering aids)

* Corresponding author at: Department of Mechanical and Industrial Engineering, Tallinn University of Technology, Ehitajate tee 5, 19086 Tallinn, Estonia.
E-mail address: kprashanth@gmail.com (K.G. Prashanth).

<https://doi.org/10.1016/j.jalcom.2023.171079>

Received 24 April 2023; Received in revised form 10 June 2023; Accepted 20 June 2023

Available online 21 June 2023

0925-8388/© 2023 Elsevier B.V. All rights reserved.

that helps to produce dense CaCO_3 without decomposition. Tetrad and Assollant [23] doped CaCO_3 with Lithium Phosphate (Li_3PO_4) and achieved 98% relative density at 700 °C by pressureless sintering technique. Urabe et al. [24] tried to use LiF as an additive in order to densify CaCO_3 . Vlasov et al. [25] used 1–2% Lithium Carbonate (Li_2CO_3) with the aragonite phase of CaCO_3 and determined 620–650 °C as the optimum sintering temperature. Smirnov et al. [26] used ammonium carbonate for the sintering of the CaCO_3 to lower the sintering temperature. Ito et al. [27] used a eutectic mixture of KF-NaF-LiF system with CaCO_3 and succeed to produce a 99% dense compact. Despite this research, only limited information is available on the densification of CaCO_3 . The objective of the present study is to produce bio-implants from eggshell wastes in the form of CaCO_3 , for which eggshell powder must be densified.

Spark plasma sintering (SPS) is a promising method compared to conventional methods as compaction and sintering occur simultaneously. This not only achieves a higher density but also reduces the sintering time and lowers the sintering temperature. By extending its benefits, it is possible to avoid or limit the decomposition and crystallization phenomena happening in these eggshells [28–31]. SPS has been utilized to produce hydroxyapatite [29], tricalcium phosphate implants, and bioglass® owing to its densification at comparatively low temperatures. Moreover, SPS can consolidate a wide variety of materials from amorphous alloys, crystalline materials, composites, functionally graded materials, etc. [32–38]. For instance, Mechay et al. [39] used SPS for the production of hydroxyapatite bone implants and observed suppression of the sintering temperature from 1300 °C to 900 °C as compared to conventional sintering techniques. However, to date, there is no data reporting the SPS technique for the production of eggshells/ CaCO_3 bone implants. The present paper aims to study the sintering behavior of the CaCO_3 -rich eggshell and determine the optimum sintering temperature for bulk production.

2. Experimental details

The commercially produced eggshell powder was densified by SPS (HPD 10-GB, FCT System GmbH, Germany). A 10 mm diameter graphite mold with graphite spacers was used to avoid reactions between the graphite mold and the sample. The chamber was vacuumed and then filled with nitrogen in a nitrogen glow box, followed by SPS in the vacuum chamber. A uniaxial pressure of 50 MPa was applied and is followed by a simultaneous heating cycle. The heating rate was kept at 100 °C/min with 5 min holding time at the desired temperatures (i.e., 250 °C, 500 °C, 750 °C, 850 °C, 950 °C, and 1000 °C). The sintering temperature was measured using a K-type thermocouple inserted into the graphite mold wall. During the SPS process, the piston movement (punch displacement), pressure, current, voltage, and temperature were recorded precisely. The instantaneous change in the punch position can be calculated using Eq. (1). This instantaneous change in the punch position is directly correlated to the instantaneous change in density (hereafter relative density) using Eq. (2).

$$L = L_f + \Delta L_{\max} - \Delta L \dots \dots \dots (1)$$

$$D = \left(\frac{L_f}{L}\right) D_f \dots \dots \dots (2)$$

where L (mm) and L_f (mm) are the instantaneous and final heights of the sintered compacts, respectively. ΔL_{\max} (mm) and ΔL (mm) represented the maximum and instantaneous displacement of the upper punch, respectively. D (%) and D_f (%) were the instantaneous and final relative density of the powder compact, respectively [40–42].

The Chemical composition of the eggshell powder was analyzed using X-ray fluorescence spectroscopy (XRF) from Rigaku Primus II. Scanning Electron microscopy (SEM) of the eggshell powder and bulk sintered samples (compacts) was performed using a Hitachi Tabletop

SEM (TM-1000). The sintered compacts were polished with 4000-grid SiC papers before SEM characterization. ImageJ was used to analyze and extract statistical data (like powder particle size, and achieved theoretical density in compacts) from SEM images. Thermogravimetric analysis (TGA) of the eggshell powder was conducted using a NETZSCH STA 449 F3 Jupiter from room temperature to 1200 °C at a heating rate of 20 K/min under a nitrogen atmosphere, where ~9.5 mg eggshell powder was used in alumina crucibles without a lid. X-ray diffraction analysis (XRD) of the eggshell powder and compacts was carried out using Rigaku Smart Lab with Cu-K α , $\lambda = 1.5406 \text{ \AA}$, a step size of 0.02 and a scan speed of 5°/min from 20° to 60°.

The presence of structural and functional group constituents in the sintered compacts was measured by the Fourier transformed infrared spectroscopy (FTIR) using a Platinum-ATR Alpha FTIR spectrometer (Bruker Optic GmbH, Germany) using the attenuated total reflection (ATR) technique in the wavelength range of 50–2500 cm^{-1} . The microhardness of the eggshell compacts was measured using an Indentec 5030 kV Vickers hardness tester (Indentec Hardness Testing Machines Limited, West Midlands, UK) with a load of 50 g and dwell time of 10 s. The eggshell compact spark plasma sintered at 250 °C and 500 °C exhibited porosity, which directly affected the measurement of the indentation size and, as a result, hardness values. Hence, the compacts sintered at this temperature were avoided during the hardness test.

3. Results & discussion

3.1. Feedstock

The different elements in the eggshell powder were measured using the XRF technique and the results are furnished in Table 1. In general, the eggshell powder is considered calcareous, i.e., its main composition is CaCO_3 . Ca, O, and C are the three major constituents amounting to 32, 48, and 19 wt% respectively [10]. However, eggshells are also composed of other minerals, which was confirmed by the significant presence of Si and Mg, along with trace amounts of Al, Na, S, P, Cl, Sr, and Fe [2].

The morphology of the eggshell powder is shown in Fig. 1. The SEM images of eggshell powder (Fig. 1(a)) show the presence of irregularly shaped particles with a wide particle size distribution. This morphology is commonly observed in eggshell powders [43]. The higher-resolution SEM image (Fig. 1(b)) of an individual large particle reveals the presence of open pores within a particle. In nature, eggshells contain micropores between crystalline calcite crystals to allow the transfer of gases from inside to outside [44]. Fig. 1(c) shows the particle size distribution of the raw eggshell powder. The particle size of eggshell powder varies from 0.50 μm to 52.00 μm , with an average particle size of $18 \pm 12.00 \mu\text{m}$, showing a wide particle size distribution. The effect of temperature on the stability of eggshell powder was analyzed using thermogravimetric analysis (TGA). Fig. 1(d) shows the mass loss in eggshell powder with an increase in temperature at ambient pressure. Eggshell powder exhibited a mass loss in three different temperature zones. In each temperature zone, the mass loss of eggshell powder depicted a distinct mechanism. In the first zone of the TGA graph, i.e., room temperature to around 250 °C, 0.8% mass loss was observed, owing to the removal of moisture from the eggshell powder [18,45,46].

Eggshells can be considered as a composite biomaterial consisting of non-calcifying membranes (hereafter-organic matter) and a calcified shell matrix (mainly CaCO_3). The organic matter in the eggshell powder is metastable in nature and hence with increasing temperature it decomposes in the temperature range of 250 °C and 650 °C [18,19,45–47]. The decomposition of organic matter can be realized from Fig. 1(d) during the second segment of the mass loss, which corresponded to a mass loss of ~7.6% mass loss from the eggshell. The third segment, ~48.9% (Fig. 1(d)) mass loss was relevant to the decomposition of the CaCO_3 . The calcination reaction (see Eq. (3)) [20] restricts the consolidation of CaCO_3 . The calcination temperature of CaCO_3 varies between

Table 1
X-ray fluorescence analysis result of the raw eggshell powder.

Elements	C	O	Na	Mg	Al	Si	P	S	Cl	Ca	Fe	Sr
Concentration (wt%)	19.30	47.51	0.16	0.36	0.19	0.35	0.17	0.19	0.08	31.58	0.05	0.05

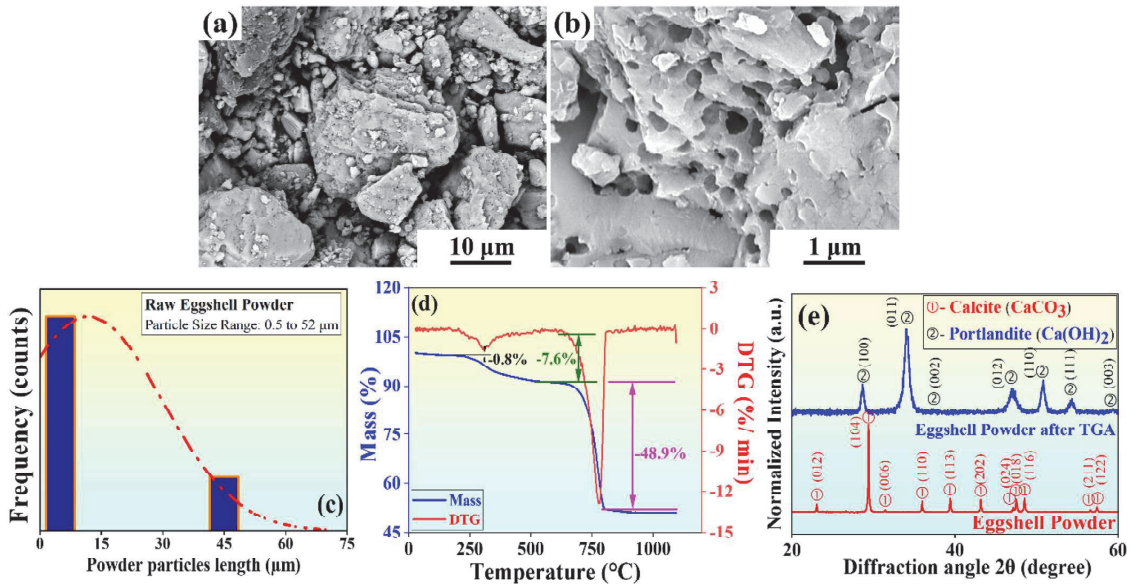


Fig. 1. Characterization of the feedstock eggshell powder (a), (b) scanning electron microscopy images, (c) particle size measurement plot, (d) thermogravimetric analysis plot, and (e) X-ray diffraction patterns of the eggshell powder.

800 and 900 °C, which mainly depends on the source of the CaCO₃, and heating conditions [48]. Generally, CaO is white in color along and is porous and fragile [2].



The eggshell powder before and after TGA was subjected to XRD analysis for determining the phases present in these materials. As shown in Fig. 1(e), the eggshell powder exhibited peaks at 23.05° (012), 29.41° (104), 35.98° (110), 39.42° (113), 43.17° (202), 47.52° (018), and 48.58° (116), which corresponds to the presence of calcite (CaCO₃), which is aligned with other reports [49]. However, calcite (CaCO₃) has three polymorphs namely calcite, aragonite, and vaterite. Among them, calcite is the most thermodynamically stable phase at room temperature and atmospheric pressure with a rhombohedral crystal structure, R $\bar{3}$ c [50]. In the diffraction pattern of CaCO₃, the most intense peak is observed for (104) plane, which corroborates to the calcite phase of CaCO₃ [51]. Moreover, no other crystalline phases were observed ensuring the presence of a single-phased calcite.

In contrast, the eggshell powder after TGA (Fig. 1(e)) observed major peaks at 28.66° (100), 34.08° (011), 47.06° (012), 50.79° (110), and 54.34° (111) respectively, which correspond to the portlandite structure, i.e., Ca(OH)₂ phase. CaO is hygroscopic, i.e., it rapidly reacts with moisture from the atmosphere and transforms into the more stable portlandite (Ca(OH)₂) phase, also known as the hydrated lime (see Eq. 4) [52]. During the TGA analysis, calcination process might have taken place and when CaO is exposed to the atmosphere, it reacts and further transforms to portlandite [45–47]. Portlandite has a hexagonal crystal structure (P $\bar{3}$ m1) with a : c ratio of 1:1.36 [53]. The appearance of the portlandite phase corroborates the decomposition of the CaCO₃ into CaO

and absorption of the moisture by CaO and conversion into Ca(OH)₂ (Eqs. (3) and (4)).



3.2. Characterization of bulk eggshell

The obtained relative density was plotted against the sintering time (Fig. 2(a)), sintering temperature (Fig. 2(b)), and holding time (Fig. 2(c)), which offers information about the densification process during spark plasma sintering. As seen in Fig. 2(a), during the sintering process, the densification takes place in several steps. Each step depends on the applied pressure and temperature. The first step relates to the application of initial pressure during the SPS process. The powders were subjected to a pressure of 50 MPa before heating, which is known as the pre-sintering/pre-pressing step. During the pre-pressing step, a mechanical load is applied to the particles, which is responsible for the fragmentation, and rearrangement of the particles, and to improve the contact between the particles. These major changes are of the utmost importance with respect to densification mechanisms, as the necking between the particles starts to grow and densifies the compact from the contact points between particles. Hence, a higher number of contact points/area provides higher activation energy for neck growth and consecutively densification [54].

After the pre-pressing step, the sintering process will be initiated, and a high current is passed through the compact following a joule heating phenomenon. The theory of SPS postulates that current passes through two adjacent particles, and generates plasma and electric arcs, which are responsible for the increase in the sintering temperature, neck

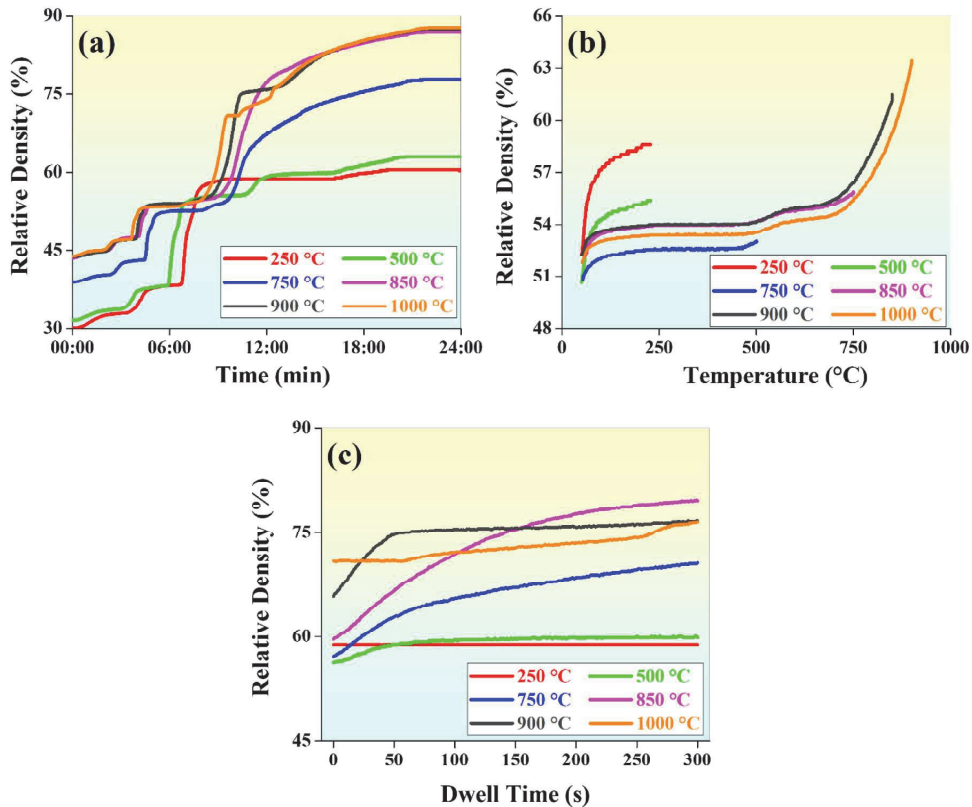


Fig. 2. Densification curves obtained for different the spark plasma sintered samples as a function of (a) sintering time, (b) temperature, and (c) dwell time.

formation, and pore reduction [55]. Therefore, this step in the SPS is of utmost importance from the point of view of densification. The changes in the densification with temperature during this stage are shown in Fig. 2(b). The temperature is a major driving force for various sintering mechanisms because it alters the activation energy. During sintering, six sintering mechanisms take place, among which three are non-densifying mechanisms and the other three are densifying mechanisms. Non-Densifying mechanisms involve surface diffusion, lattice diffusion from the surface, and vapor transport, which do not contribute to the densification of the compact and only increase its particle size. Whereas, densifying mechanisms include grain boundary diffusion, lattice diffusion from the grain boundary, and plastic flow to densify the compact and provide major shrinkage in the compacts (see Fig. 2(b)). Both mechanisms strongly depend on the sintering temperature, and both sintering mechanisms compete to dominate. Based on the activation energy, a higher sintering temperature mainly supports densifying mechanisms and achieves a higher relative density compared to a lower sintering temperature (Fig. 2(b)) [55]. Moreover, the 50 MPa pressure persisted throughout the sintering, which further assisted in increasing the contacts between particles, providing driving forces for several densifying sintering mechanisms. However, the non-densifying mechanisms that occur during sintering are largely unaffected by the applied pressure and changes invoked by pressure in the compact [56]. In addition to this, as simultaneous particle fragmentation and sintering changes the surface area of the particles persistently, which in turn alters the kinetics of the sintering process. Such changes will alter the decomposition or recrystallization temperature [57]. In general, the application of pressure during the hot consolidation process alter the

transformation temperature and mechanisms.

Once desired sintering temperature was achieved, the samples are held for desired time. Fig. 2(c) shows the effect of the holding temperature on the relative density. At relatively low sintering temperatures, i. e., 250 and 500 °C, the changes in the relative density were almost negligible. Although, the increase in density at higher holding temperatures was owing to the temperature and not correlated to the holding time. This signifies that densifying mechanisms are more prominent than non-densifying mechanisms with respect to increases in temperature, however unaffected by holding time [58]. The holding step was followed by the cooling step. It is worth mentioning that during cooling temperature decreases and thermal shrinkage mainly densifies the compact. As shown in Fig. 2(a), the thermal shrinkage and respective changes in the densification highly depend on the sintering temperature as higher sintering temperature expands the compact to a larger extent as compared to lower sintering temperatures. Therefore at lower sintering temperatures (250 and 500 °C), changes in the relative density are very small and the curve remains almost flat. Whereas, at higher sintering temperature (850, 900, and 1000 °C), changes in relative density is higher [54].

The SEM images of the eggshell samples sintered at six varying temperatures are shown in Fig. 3. Fig. 3 clearly distinguishes the density difference and porosity between the samples sintered at 250, 500, 750, and 850 °C. As seen, the eggshell powder sintered at 250 °C and 500 °C revealed the presence of individual particles after the SPS process, i. e., proper densification could not occur at 250 °C and 500 °C (63% and 60%). As the sintering temperature is increased, it densifies the compact due to various sintering mechanisms and due to reduction of particle

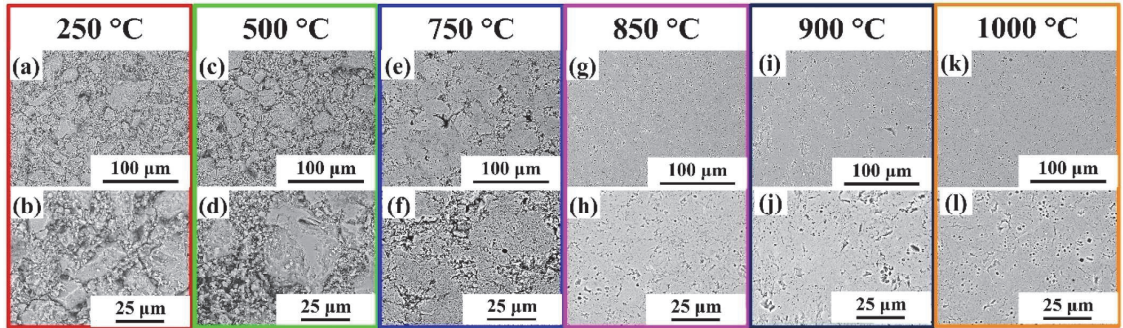


Fig. 3. Scanning electron microscopy images of the eggshell powder sintered at various temperatures (a), (b) 250 °C, (c), (d) 500 °C, (e), (f) 750 °C, (g), (h) 850 °C, (i), (j) 900 °C, and (k), (l) 1000 °C, respectively.

boundary, which almost disappear after 850 °C sintering temperature. However, at this condition, a network of closed porosity is observed [59]. The achieved densities are $60 \pm 1\%$, $63 \pm 2\%$, $78 \pm 0.1\%$, $87 \pm 1\%$, $88 \pm 3\%$, and $88 \pm 3\%$ respectively for the eggshell samples sintered at 250, 500, 700, 850, 900, and 1000 °C, respectively.

Fig. 4 shows the XRD patterns and FTIR data of the eggshell powder sintered as a function of various sintering temperatures. Fig. 4(a) shows the XRD graph of the sintered compacts. All peaks in the XRD graph of the sintered compacts corroborate the rhombohedral crystal structure corresponding to the calcite phase of CaCO_3 . All major peaks were observed near 29° , which is corroborated by the (104) plane of the Calcite phase. Despite sintering above the decomposition temperature (800 °C) of the CaCO_3 , no other peaks appear corresponding to CaO or Ca(OH)_2 . This implies that in SPS, the decomposition temperature is shifted above 1000 °C. These XRD patterns clearly advise that the bulk compacts are made of calcite phase and there was no phase transformation realized [2].

The FTIR spectra of eggshell compacts shown in Fig. 4(b) reveal information regarding several stretching and bending vibrations of the functional groups. All the spectra of the SPS eggshells show the presence of similar functional groups without any differences irrespective of the sintering temperature. The FTIR spectra of the eggshell powder showed four major peaks at 1410 cm^{-1} , 1084 cm^{-1} , 873 cm^{-1} , and 712 cm^{-1} , which are characteristic peaks of the carbonate group [19,60]. Eggshells mainly contain CaCO_3 with an ionic bond between the calcium and carbonate groups, whereas a covalent bond exists within the carbonate group. In carbonates, C is connected to three O atoms via a covalent

bond [61]. This C-O bond is responsible for the vibrations and peaks in the FTIR spectra [62]. If the C-O bond vibrates too-and-fro with the same intensity in each direction, it creates a symmetric vibration (ν_1), which is generally present at 1083 cm^{-1} . In the present spectra (Fig. 4(b)), ν_1 vibration was weakly present in the eggshell powder; however, with an increase in temperature, it significantly decreases as the peak intensity decreases, which is commonly reported for CaCO_3 [63]. The eggshell powder exhibited an intense peak at 1410 cm^{-1} , which corresponds to the asymmetric stretching of the carbonate group (CO_3^{2-}) molecular ion also known as the ν_3 vibration [64]. Asymmetric stretching can be identified as the to-and-fro moment of molecules towards each other, similar to symmetric stretching, but with different intensities in each direction [65]. Furthermore, the peaks observed at 712 and 873 cm^{-1} were sharp and narrow, corresponding to symmetric bending (in-plane bending ν_4) and asymmetric bending (out-plane bending ν_2), respectively [64]. These FTIR spectra are consistent with previously reported data and confirm the presence of carbonate, even if the compacts are sintered at higher temperatures like 1000 °C. As mentioned earlier, eggshells contain Mg, Na, and other trace elements, which can be in the carbonate form along with calcium carbonate and are responsible for the changes in the intensity of the peak with respect to sintering temperature.

The microhardness test result of the eggshell compacts is shown in Fig. 5. For the compact sintered at 850 °C, the highest microhardness value of $157 \pm 6 \text{ HV}_{0.05}$. However, the compacts sintered at 750 °C, 900 °C, and 1000 °C show similar hardness values of 149 ± 5 , 149 ± 7 , and $148 \pm 8 \text{ HV}_{0.05}$ respectively. In other words, an increase in the

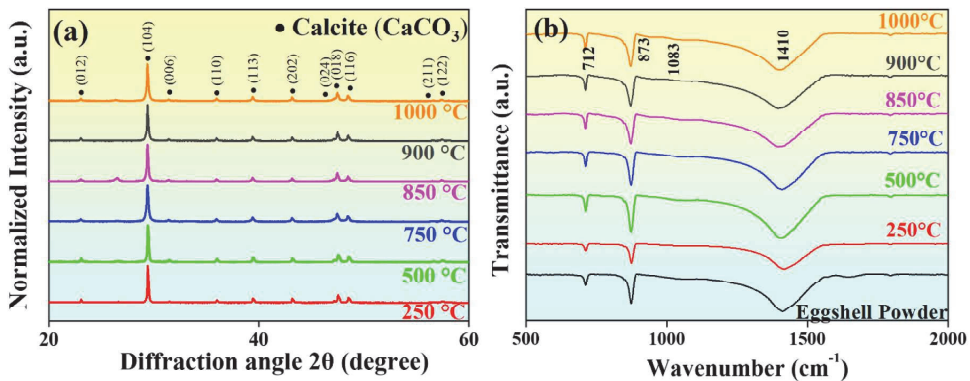


Fig. 4. (a) X-ray diffraction patterns and (b) Fourier transformed infrared spectroscopy traces of the eggshell powder spark plasma sintered at 250 °C, 500 °C, 750 °C, 850 °C, 900 °C, and 1000 °C, respectively.

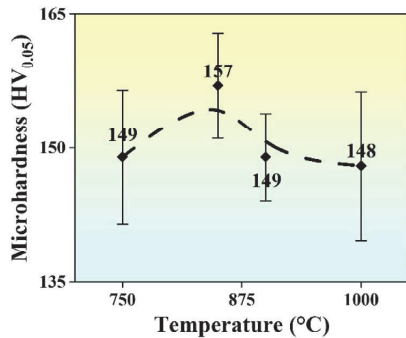


Fig. 5. Microhardness values of the spark plasma sintered eggshell powder at different temperatures: 750 °C, 850 °C, 900 °C, and 1000 °C.

sintering temperatures does not alter the microhardness values of the eggshell compacts. The hardness value is highly dependent on the density of the compacts. For compacts sintered at 850 °C, 900 °C, and 1000 °C, similar theoretical densities were observed (similar porosity levels); hence, the hardness values were nearly similar (also it is interesting to note that all these samples show the presence of similar phase that also attributes to the presence of similar hardness is these materials) [66,67]. The results are in agreement with other hardness values observed for the pure calcite phase (105–140 HV) [68–70].

Sintering is a temperature-dependent process, which produces denser samples at higher sintering temperatures by eliminating porosity. Therefore, the SPS graph of the eggshell powder sintered at higher temperatures, i.e., 850, 900, and 1000 °C (Fig. 2(b)) showed the highest possible density. XRF and XRD patterns confirm the presence of CaCO₃ in the form of calcite as the major phase even in the samples sintered at higher temperatures up to 1000 °C. According to the TGA analysis, the conversion of CaCO₃ into CaO should begin at 800 °C and pose difficulty to produce pore-free and denser samples sintered above 800 °C. However, the presence of pressure during sintering and simultaneous heating during the SPS process alters the kinetics of this decomposition reaction [57]. The XRD and FTIR analysis of the eggshell samples SPS above 800 °C (850 °C, 900 °C, and 1000 °C) showed the presence of the calcite phase without any calcination reaction, which is similar to the feedstock eggshell powder. This implies that the temperature for the decomposition reaction has been shifted to higher temperatures and could not take place even sintering at 1000 °C. Moreover, the best combination of densification and microhardness was achieved at 850 °C, which did not improve significantly by increasing the sintering temperature to 900 °C or 1000 °C. Also, it is reported that sintering the eggshell powder at higher temperatures did not achieve the best combination of the mechanical property. This signifies that for the compaction of the eggshell powder, 850 °C is found to be the optimum temperature, and eggshell compacts can be produced without the addition of any reactive phases.

4. Conclusion

The present study explored a unique technique for valorizing eggshell waste into a bone-grafting material. For the first time, eggshell powder in the form of CaCO₃ was effectively compacted using SPS without any additional sintering aids. SEM analysis revealed the presence of irregularly shaped eggshell particles with a wide particle size distribution. The decomposition of eggshell powder into CaO occurs in multiple stages, starting with the decomposition of organic matter at 500 °C, followed by calcination above 800 °C, resulting in the decomposition of CaCO₃ into CaO. The present study investigated the possibility of densification of eggshell powders by SPS as the combined action of pressure and temperature; the decomposition temperature

shifts to a higher value with the application of pressure during SPS. According to the TGA analysis, the decomposition should start at 850 °C; however, in spark plasma sintered samples at 850 °C, 900 °C, and 1000 °C, only CaCO₃ phase was observed in XRD and FTIR results. SEM images revealed that samples sintered at and above 850 °C exhibited saturation in density, i.e., 87–88% and did not help to improve the density of the compact. Hence, it can be concluded that 850 °C is the optimal temperature for achieving the maximum possible density in compacts fabricated using eggshell powder. The investigated method can be further expanded to produce calcium carbonate-based scaffolds for bone grafting applications because it offers better osseointegration and improved bio-compatibility. Hence, this research work opens an opportunity to incorporate eggshells into metallic bio-implants for example coating of the metallic bio-implant or eggshell-based scaffolds.

CRedit authorship contribution statement

Riddhi Shukla: Investigation, Methodology, Formal analysis, Writing – original draft. **R. Sokkalingam:** Methodology, Formal analysis, Writing – original draft. **K.G. Prashanth:** Conceptualization, Methodology, Resources, Validation, Writing – review & editing, Supervision, Funding acquisition, Project administration.

Declaration of Competing Interest

The authors declare that they have no known competing financial interests or personal relationships that could have appeared to influence the work reported in this paper.

Data availability

Data will be made available on request.

Acknowledgement

The authors acknowledge financial support from the Baltic Research Programme project no. EEA-RESEARCH-85 “Waste-to-resource: eggshells as a source for next generation biomaterials for bone regeneration (EGGSHELL)” under the EEA Grant of Iceland, Liechtenstein, and Norway no. EEZ/BPP/VIAA/2021/1.

References

- [1] M. Hicks, K. Anamthawat-Jónsson, Á. Einarsson, A. Þór Þórsson, The identification of bird eggshell by scanning electron microscopy, *J. Archaeol. Sci.* 151 (2023), 105712, <https://doi.org/10.1016/j.jas.2022.105712>.
- [2] N. Tangboriboon, R. Kuananruksapong, A. Sirivat, Preparation and properties of calcium oxide from eggshells via calcination, *Mater. Sci. -Pol.* 30 (2012) 313–322, <https://doi.org/10.2478/s13536-012-0055-7>.
- [3] M.N. Freire, J.N.F. Holanda, Characterization of avian eggshell waste aiming its use in a ceramic wall tile paste, *Cerâmica* 52 (2006) 240–244, <https://doi.org/10.1590/S0366-69132006000400004>.
- [4] S. Bhagat, S. Singh, Nanominerals in nutrition: Recent developments, present burning issues and future perspectives, *Food Res. Int.* 160 (2022), 111703, <https://doi.org/10.1016/j.foodres.2022.111703>.
- [5] M.S. Tizo, L. Andre, V. Blanco, C.Q. Cagas, B. Rangel, B. Dela Cruz, J.C. Encoy, J. V. Guinting, R.O. Arazo, V. Irvin, F. Mabayo, Efficiency of calcium carbonate from eggshells as an adsorbent for cadmium removal in aqueous solution, *Orig. Res. Artic.* (2018), <https://doi.org/10.1016/j.serj.2018.09.002>.
- [6] S. Hajji, N. Mzoughi, Kinetic, equilibrium and thermodynamic studies for the removal of lead ions from aqueous solutions by using low cost adsorbents: a comparative study, *J. Appl. Chem. (IOSR-JAC)* 11 (2018) 12–24, <https://doi.org/10.9790/5736-1107011224>.
- [7] A.M. Nassar, N.F. Alotaibi, Eggshell recycling for fabrication of Pd@CaO, characterization and high-performance solar photocatalytic activity, *Environ. Sci. Pollut. Res.* 28 (2021) 3515–3523, <https://doi.org/10.1007/S11356-020-10751-X/FIGURES/11>.
- [8] S. Mahdavi, A. Amirsadeghi, A. Jafari, S.V. Niknezhad, S.A. Bencherif, Avian Egg: A Multifaceted Biomaterial for Tissue Engineering, *Ind. Eng. Chem. Res* 60 (2021) 17348–17364, <https://doi.org/10.1021/acs.iecr.1c03085>.
- [9] T. Zaman, Mst.S. Mostari, Md.A. Al Mahmood, Md.S. Rahman, M.A. Al Mahmood, Md.S. Rahman, Evolution and characterization of eggshell as a potential candidate

- [58] M. Kermani, M. Razavi, M.R. Rahimpour, M. Zakeri, The effect of mechanical alloying on microstructure and mechanical properties of MoSi₂ prepared by spark plasma sintering, *J. Alloy. Compd.* 593 (2014) 242–249, <https://doi.org/10.1016/J.JALLCOM.2014.01.041>.
- [59] R. Shukla, A. Shrivastava, P. Chaudhuri, Effect of sintering parameters on surface morphology of Li₂TiO₃ compacts, in: Twenty Second DAE-BRNS Symposium on Thermal Analysis - Thermal Techniques for Advanced Materials, 2020.
- [60] P. Yilmaz, E. Öztürk Er, S. Bakirdere, K. Ülgen, B. Özbek, Application of supercritical gel drying method on fabrication of mechanically improved and biologically safe three-component scaffold composed of graphene oxide/chitosan/hydroxyapatite and characterization studies, *J. Mater. Res. Technol.* 8 (2019) 5201–5216, <https://doi.org/10.1016/J.JMRT.2019.08.043>.
- [61] T. Wong, Knoop microhardness anisotropy on the cleavage plane of single crystals with the calcite structure, 1991.
- [62] A. Shafiq Kamba, M. Ismail, T.A. Tengku Ibrahim, Z.A.B. Zakaria, Synthesis and characterisation of calcium carbonate aragonite nanocrystals from cockle shell powder (anadara granosa), *J. Nanomater* 2013 (2013), <https://doi.org/10.1155/2013/398357>.
- [63] Y. Kim, M.C. Caumon, O. Barres, A. Sall, J. Cauzid, Identification and composition of carbonate minerals of the calcite structure by Raman and infrared spectroscopies using portable devices, *Spectrochim. Acta A Mol. Biomol. Spectrosc.* 261 (2021), 119980, <https://doi.org/10.1016/J.SAA.2021.119980>.
- [64] M.E. Fleet, Infrared spectra of carbonate apatites: ν_2 -Region bands, *Biomaterials* 30 (2009) 1473–1481, <https://doi.org/10.1016/J.BIOMATERIALS.2008.12.007>.
- [65] N. Khan, D. Dollimore, K. Alexander, F.W. Wilburn, The origin of the exothermic peak in the thermal decomposition of basic magnesium carbonate, *Thermochim. Acta* 367–368 (2001) 321–333, [https://doi.org/10.1016/S0040-6031\(00\)00669-9](https://doi.org/10.1016/S0040-6031(00)00669-9).
- [66] J. Gong, Comment on “Measurement of hardness on traditional ceramics”, H. Kim and T. Kim, *J. Eur. Ceram. Soc.*, 22, 1437–1445 (2002), *J. Eur. Ceram. Soc.* 23 (2003) 1769–1772, [https://doi.org/10.1016/S0955-2219\(02\)00398-9](https://doi.org/10.1016/S0955-2219(02)00398-9).
- [67] Q. Tang, J. Gong, Effect of porosity on the microhardness testing of brittle ceramics: A case study on the system of NiO–ZrO₂, *Ceram. Int* 39 (2013) 8751–8759, <https://doi.org/10.1016/J.CERAMINT.2013.04.061>.
- [68] Mathweb, Calcium Carbonate, Calcite (CaCO₃), (n.d.). (<https://www.matweb.com/search/datasheet.aspx?matguid=bea4bfa9c8bd462093d50da5eebe78ac&ckck=1>) (accessed February 13, 2023).
- [69] J.R. Pandya, L.J. Bhagia, A.J. Shah, Microhardness of rhombohedral crystals: Calcite and sodium nitrate, *Bull. Mater. Sci.* 5 (1983) 79–82, <https://doi.org/10.1007/BF02822352>.
- [70] T. Wong, Knoop microhardness anisotropy on the cleavage plane of single crystals with the calcite structure, 1991.

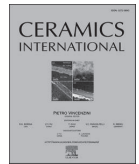
Publication III

Shukla, R., Yadav, M. K., Madruga, L. Y. C., Jaymani, J., Popat, K., Wang, Z., Xi, L., & Prashanth, K. G. (2024). A novel Ti-eggshell-based composite fabricated by combined additive manufacturing-powder metallurgical routes as bioimplants. *Ceramics International*. <https://doi.org/10.1016/j.ceramint.2024.12.073>



Contents lists available at ScienceDirect

Ceramics International

journal homepage: www.elsevier.com/locate/ceramint

A novel Ti-eggshell-based composite fabricated by combined additive manufacturing-powder metallurgical routes as bioimplants

Riddhi Shukla^a, Mayank Kumar Yadav^a, Liszt Yeltsin Coutinho Madruga^b, Jayamani Jayaraj^c, Ketul Popat^b, Zhi Wang^d, Lixia Xi^e, Konda Gokuldoss Prashanth^{a,f,*}

^a Department of Mechanical and Industrial Engineering, Tallinn University of Technology, Ehitajate tee 5, 19086, Tallinn, Estonia

^b Department of Bioengineering, George Mason University, Fairfax, 22030, Virginia, USA

^c Department of Materials Technology, Dalarna University, SE-79188, Falun, Sweden

^d National Engineering Research Center of Near-net-shape Forming for Metallic Materials, South China University of Technology, Guangzhou, 510641, China

^e Jiangsu Provincial Engineering Laboratory for Laser Additive Manufacturing of High-Performance Metallic Components, College of Materials Science and Technology, Nanjing University of Aeronautics and Astronautics, Yudao Street 29, Nanjing, 210016, China

^f Centre for Biomaterials, Cellular and Molecular Theranostics (CBCMT), Vellore Institute of Technology, School of Mechanical Engineering, Tamil Nadu, 632014, India

ARTICLE INFO

Handling Editor: Dr P. Vincenzini

Keywords:

Additive manufacturing
Powder metallurgy
Circular economy
Bioimplants
Composites

ABSTRACT

Eggshells are a biowaste and potential bio-ceramic due to the major calcium carbonate (CaCO_3) content, which offers bioactivity, bioresorbability, biocompatibility, and antibacterial properties. To benefit from the properties of the eggshell, this study explores the combined use of ceramic (eggshell) and ductile metal (CP-Ti as a hexagonal prism) as composites. A novel Ti-eggshell composite was fabricated by combining additive manufacturing and powder metallurgical routes. The novel Ti-eggshell composites were characterized for structural and microstructural analysis using X-ray diffraction and scanning electron microscopy. The hexagonal Ti struts deform marginally during composite manufacturing (minor variations in the strut dimensions may be observed) and the composites show the following compressive properties: yield strength of 123 ± 34 MPa and a Young's modulus of 47 ± 2 GPa within the range of natural human cortical bone. In addition, the Ti-eggshell composite offers non-cytotoxic and antibacterial behavior when tested with gram-negative-Pseudomonas. Aeruginosa and gram-positive-Staphylococcus. Aureus bacteria suggesting that such novel Ti-eggshell composites can be suitable members for bioimplant applications.

1. Introduction

The growing incidence of arthritis, accidents, and osteoporosis has led to the need for the development of novel and high-performance orthopedic implants [1]. Artificial orthopedic implants (made of ceramics, metals, polymers, or their combination) foster bone healing and re-establish interrupted bone healing processes [2,3]. For load-bearing applications, implants should not be cytotoxic, offer excellent corrosion resistance, and exhibit a good combination of properties including mechanical properties (like low modulus, adequate strength, appreciable ductility, good fatigue resistance, and good wear resistance). Generally, bio-implants are manufactured from SS316L (Elastic Modulus – $E \sim 210$ GPa), Co-Cr ($E \sim 230$ GPa), and Ti-based alloys ($E - 100-110$ GPa) [4]. Since developing biocompatible and high strength-to-weight ratio Ti6Al4V ELI (extra low interstitial impurity content) alloy. It has

become the preferred choice for the bio-implant and has been widely used [5]. Ti6Al4V ELI can be manufactured easily and offers flexibility to alter the microstructure. However, alloying elements like Al and V pose long-term issues in the human body, such as Alzheimer's disease, and other neurological side-effects [6,7]. On the other hand, commercially pure-Titanium (CP-Ti or Ti) is an unalloyed Ti with $\sim 0.1-0.3$ % oxygen and offers superior ductility and reduced elastic modulus (100–105 GPa) compared to Ti6Al4V (110 GPa) [8]. Moreover, CP-Ti offers better biocompatibility and corrosion resistance compared to Ti6Al4V. Hence, CP-Ti is a promising candidate to be utilized in the bio-medical field [6,9].

Natural bone is a composite, containing collagen tissue and hydroxyapatite ceramic, where collagen provides elastic strength and hydroxyapatite offers compressive strength [10]. Based on their composition, shape, size, and structures there are different types of

* Corresponding author. Department of Mechanical and Industrial Engineering, Tallinn University of Technology, Ehitajate tee 5, 19086, Tallinn, Estonia.
E-mail address: kgrashanth@gmail.com (K.G. Prashanth).

<https://doi.org/10.1016/j.ceramint.2024.12.073>

Received 10 September 2024; Received in revised form 30 November 2024; Accepted 5 December 2024

Available online 6 December 2024

0272-8842/© 2024 Elsevier Ltd and Techna Group S.r.l. All rights are reserved, including those for text and data mining, AI training, and similar technologies.

bones [11]. Human cortical bone is a highly dense bone that possesses elastic modulus in the range of 10–30 GPa [4], in comparison to metallic implants, it shows 5–10 times higher than human cortical bone. The difference in Young's modulus between natural bone and implant leads to bone resorption (due to the stress-shielding effect on the surrounding bone) and hence the need for revision surgery. To reduce stress shielding, it is necessary to lower Young's modulus, for which two approaches are commonly used. The first involves developing alloys with an elastic modulus in the range of natural bone, such as β -Ti [6,12–15]. However, it does not meet the requirement of a strength-modulus trade-off. The second approach involves the production of porous materials, which has gained considerable attention in recent years [16]. Here, the presence of porosity (open/closed) can significantly reduce the density of the implant, and its Young's modulus, resulting in a reduced stress-shielding effect [17]. There exist several techniques that can manufacture porous bio-implants, such as the space-holding technique, freeze-drying, gas foaming, etc. These methods can induce the desired level of porosity in implants; however, there exist issues with the control of the pore geometry and reproducibility. Additive manufacturing (AM) is a cutting-edge manufacturing technique, involving a layer-by-layer production strategy [18]. Hence, intricate and desired porosity can be made possible, and replications are also feasible [19]. With the development of AM, porosity can be tuned to meet patient-specific requirements [20]. Hence, to fabricate bio-implants with the desired elastic modulus, various lattice structures have been proposed and investigated [21–24].

Porous bio-implants can be categorized into two main types: strut-based and surface-based implants [25]. Studies have explored the pros and cons of different structures, but no consensus has been reached on the superiority of these structures for bone implant applications. The micro-architecture of the individual structure is important, including factors such as porosity, strut surface/thickness, compression strength, Young's Modulus, and interconnectivity [26]. Porous and non-porous CP-Ti can be manufactured using conventional/traditional manufacturing methods such as casting, powder metallurgy, and space holder technology [27]. However, the reactivity of Ti makes those processes time-consuming, energy-consuming, and expensive. AM of CP-Ti offers the production of complex shapes with controlled porosity, non-stochastic, and even patient-specific implants with requisite properties [6,12]. For the fabrication of Ti-based alloys, electron beam melting (EBM), laser powder-bed fusion (LPBF) process/selective laser melting (SLM), wire arc additive manufacturing (WAAM), directed energy deposition (DED) are generally employed [28,29]. LPBF offers a high cooling rate (10^4 – 10^6 K/s) that leads to the formation of martensitic microstructure in CP-Ti, which improves their mechanical properties [9]. Porous Ti-based implants show better osseointegration compared to solid implants as the porosity provides space for the human cell to grow and integrate with the body [30]. However, the bio-inert behavior of the Ti-based implant always perturbed the sole use of the Ti-based alloys. Conversely, ceramics-based biomaterials are known for their biocompatibility, corrosion resistance, and compressive strength, making them suitable for hard tissue applications. Bioactive ceramics, such as hydroxyapatite [31], tri-calcium phosphate [32], amorphous calcium phosphate (ACP) [33], or calcium carbonate (CaCO_3) show better bioactivity [34].

CaCO_3 in the natural bone along with hydroxyapatite and collagen facilitates the osseointegration process. The main advantage of using CaCO_3 -based implants is their bioresorbability. Bioresorbable materials also degrade like biodegradable materials but also release a controlled amount of Ca^{+2} and PO_4^{-3} , which act as therapeutic agents to heal bone injuries and increase bactericidal activity [35,36]. Chicken eggs are a daily food ingredient and are widely consumed in Europe and worldwide as a rich source of CaCO_3 . Approximately 7.0 million tons of eggs will be annually used in Europe alone in 2018 [37]. The inner core of the egg and the thin protein layer of the egg (albumin) are useful for food processing, while 11 % of the egg is made up of a ceramic shell (eggshell) ~2000 tons/day is discarded as it is not directly useful for food

production. This eggshell layer contains potential nutrients and elements such as CaCO_3 ~94–95 %, calcium phosphate ($\text{Ca}_3(\text{PO}_4)_2$) about 1 %, magnesium carbonate (MgCO_3) ~1 %, small amounts of sodium (Na) (1512 ppm), strontium (Sr) (320–411 ppm), magnesium (Mg) (3472–4500 ppm), sulfur (S) (589 ppm), potassium (K) (525 ppm), and ~4 % organic substances [38,39]. Disposal of eggshells not only results in the loss of these elements but also poses waste disposal issues. Dumping in land costs money, the decomposition of organic matter from the eggshell produces ammonia, methane, and hydrogen sulfide-like foul-smelling gases, as well as microbial action of the eggshell, threatens environmental concerns [40,41]. Utilizing eggshells as food calcium supplements has not eliminated waste disposal issues. Reports also show the use of eggshells in different applications such as wall tiles [41], Cd- and Pb-like heavy metal removal [42], solar photocatalytic fabrication for wastewater treatment [43], and polymer composite [44]. Nevertheless, a major concern still exists in effectively employing eggshells for value-added applications. This research aims to utilize eggshell waste in orthopedic bio-implants to produce sustainable bio-implants.

Valorizing eggshells in bio-implants will reduce environmental issues and promote sustainable production through a circular economy approach. However, implants made from these ceramics are prone to brittle failure and have inferior mechanical properties, which limits their applications. The inherent brittleness of ceramics poses a significant risk of early-stage implant failure under load-bearing conditions. This creates a critical need for biomaterials that offer both mechanical durability and effective biological performance [45,46]. This has led to growing interest in biocomposites that combine the strength and ductility of metals with the bioactivity of ceramics. Only a limited report deals with the fabrication of eggshell-doped biocomposites. Acharjee et al. [47] have developed Ti-doped waste eggshell-derived HAp for bone grafting applications, where eggshell-derived HAp was fabricated by mixing with 5 % Ti, and subsequently compacted and sintered at 900 °C. This process resulted in an apparent porosity of $\sim 27 \pm 1$ % with a 12–168 μm pore size distribution. In addition, the results show that these composites offer a higher degree of cell attachment to the bone implant suggesting that the doped eggshells exhibit increased bioactivity. Similarly, Husein et al. [48] have reinforced Mg and Mg-12r with 2.5 % eggshell using a powder metallurgy route to form a metal matrix composite, involving ball-milling and mixing, followed by uniaxial compaction and sintering at 450 °C for 2 h. Both composites exhibited bone-matching density. The striking feature of these composites is their corrosion rates. The corrosion rates in Hank's solution decrease from 12.1 mmpy to 3.81 mmpy, and 1.045 mmpy for pure Mg, Mg-2.5 ES, Mg-12r-2.5 ES composites, respectively. This highlights the enhanced anti-corrosion performance of the composites with the influence of eggshells.

Based on the detailed literature survey, the present research aims at a novel approach to use eggshells with AM-fabricated Ti-based hexagonal prism lattice using a combined LPBF and powder metallurgy (spark plasma sintering - SPS) approach. This paper for the first time integrates the use of CaCO_3 bio-ceramics/eggshells with Ti-based bio-implants. Ti-based bio-implants are prone to bacterial infection, hence bacterial adhesion and colonization are commonly observed [49,50]. If the implant lacks inherent antibacterial properties, bacteria can proliferate and form a biofilm on the implant surface, leading to implant-associated infections (IAI) [51]. IAI is a critical situation, as it may lead to revision surgery, antibiotic therapy, unnecessary suffering to patients, and in extreme cases, disability [51]. Therefore, minimization of IAI is desired for implants, and producing bio-implants with inherent antibacterial properties can be a preventive solution [52]. The addition of eggshell is two-fold; it is bio-resorbable, bio-active, and osseoinductive, additionally, it exhibits antibacterial properties and shows bactericidal activity. Recent advances in biomaterials research underscore the importance of developing implant surfaces that inherently resist bacterial attachment while promoting cell adhesion. Such surfaces can provide the immune system with additional time to eliminate infection-causing bacteria

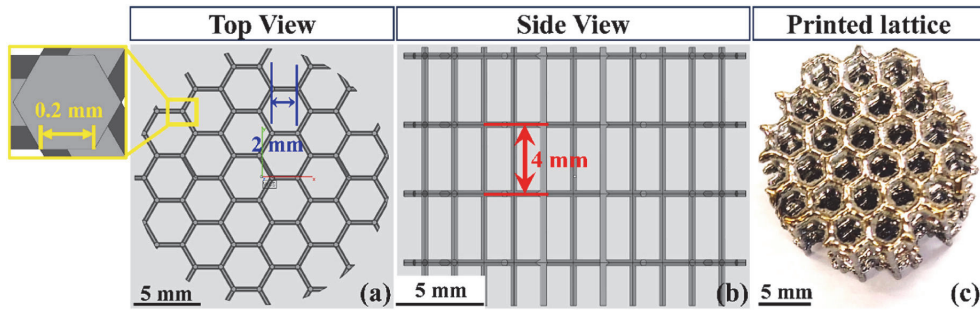


Fig. 1. Micro-architecture of the lattice structure, (a) Computer-aided design (CAD) showing the top view of the lattice and the inset showing the structure of an individual strut, (b) CAD design showing the side view of the lattice, and (c) optical microscopy image of the printed CP-Ti lattice.

before biofilm formation. Accordingly, this research aims to develop and characterize the Ti-eggshell composite for bone tissue engineering. By harnessing the unique properties of both materials, this composite aims to overcome the limitations of current implant technologies and enhance the performance and longevity of bone implants. Hence, the present study aims at a detailed characterization of the composite material followed by their mechanical and biomedical properties. The mechanisms involved in bacterial adhesion and growth will be elucidated.

2. Experimental details

2.1. Fabrication of the CP-Ti lattice

SLM280 machine (from SLM Solutions GmbH) equipped with a fiber laser was used to fabricate the CP-Ti-based lattice structures. The laser used in the manufacturing process has a maximum capacity of 700 W. A conical laser beam was employed that has a spot size of $\sim 80 \mu\text{m}$ at the substrate. Gas-atomized spherical CP-Ti powder (Grade 2) from Nanoshel (particle size $30\text{--}50 \mu\text{m}$) was used in this work. The following SLM parameters were employed in the present work: A laser power of 165 W, laser scan speed of 138 mm/s , hatch spacing of $110 \mu\text{m}$, layer thickness of $50 \mu\text{m}$, and a hatch rotation of 72° was used to fabricate the CP-Ti lattices [9]. Argon gas was used to purge the building chamber, and an argon atmosphere was maintained throughout the process to keep the oxygen levels below 100 ppm. The microarchitecture of the lattice structure designed to fabricate CP-Ti using LPBF is furnished in Fig. 1. In the current study, a hexagonal truss-like structure, or a hexagonal prism structure (hereafter HXP) was selected for implant design because the HXP structure (with $60\text{--}70\%$ porosity [53]) provides Young's modulus in the range of the cortical bone ($7\text{--}30 \text{ GPa}$) [21] and offers good compressibility and energy absorptivity [54]. The HXP lattice includes both vertical and horizontal struts, which are better achievable than inclined struts by LPBF [55]. Fig. 1(a and b) shows the CAD design of the HXP lattice designed using SolidWorks. As shown in the top view (Fig. 1(a)), the unit cell is 2 mm in length with a strut thickness of 0.2 mm (inset attached in Fig. 1(a)). Notably, the individual struts are also hexagonal with a strut thickness of 0.2 mm as it the minimum possible feature achievable using the LPBF method. The thin strut size was chosen to reduce the volume fraction of CP-Ti in the composite and to increase the volume fraction of eggshell powder. A hexagonal prism varies from a honeycomb structure in terms of its side view, as it has a truss-like structure (as seen in Fig. 1(b)) rather than a wall-like structure. The distance between two hexagonal layers is kept at 4 mm , resulting in a unit cell width-to-height ratio of $1:2$. The relative density of the lattice structure was calculated by dividing the lattice structure volume of the unit cell by the total volume of the unit cell [56]. This calculation yielded a relative density of 36% . Fig. 1(c) displays an optical image of the LPBF CP-Ti lattice replicating the CAD design within experimental

limits.

2.2. Fabrication of the Ti-eggshell composite

To fabricate the Ti-eggshell composite, the eggshell powder (procured from Xiamen Lichengda Technology Co. Ltd., Xiamen, Fujian province, China) was added to the lattice structure and is spark plasma sintered. Spark plasma sintering (SPS) was carried out using an SPS device (from HPD 10-GB, FCT System GmbH, Germany), which is placed inside a glove box (in a controlled environment). A 10 mm cross-section graphite outer ring and graphite punches were used during the SPS process. The graphite spacer was used to minimize interaction between the sample and the graphite mold. The presence of a graphite spacer helps in the easy removal of the sample from the mold. A uniaxial pressure of 50 MPa was applied, followed by a simultaneous heating cycle. As previously optimized [40], a maximum temperature of 850°C was achieved with a $100^\circ\text{C}/\text{min}$ heating rate, and the composite sample was held at the maximum temperature (850°C) for a dwell time of 5 min . The temperature measurement during the SPS process was carried out using a K-type thermocouple.

2.3. Materials characterization and mechanical testing

To determine the microstructure of the CP-Ti, a solid sample with 5 mm diameter and 5 mm height was produced along with the lattice. The produced solid samples were mounted in an epoxy resin. The standard metallographic procedures including grinding and polishing with different grades of emery papers were employed to remove all the scratches and mechanical imperfections in the sample surface. The mechanically polished surface was etched using a Kroll's reagent and observed under optical microscopy (Leica Microsystems) and high-resolution – scanning electron microscope (HR-SEM) (model – Zeiss GeminiSEM 450). The feedstock CP-Ti and eggshell powders were also examined using SEM evaluating the particle size distribution and shape. In addition, the microstructure of the Ti-eggshell composite was examined using an HR-SEM and subsequently analyzed using energy dispersive spectroscopy (EDS) (from INCA pental FETX3, Oxford instrument) fitted with the SEM device. High-resolution imaging was carried out using a transmission electron microscope (TEM) (from Tecnai G2 F20, FEI, Germany) equipped with a high-angle annular dark-field (HAADF) TEM using an FEI 80–300, and nano-diffraction.

The phases present in these samples (CP-Ti, eggshell, and CP-Ti-eggshell composites) were examined by X-ray diffraction (XRD) using a Rigaku smart lab equipment equipped with a $\text{Cu-K}\alpha$ radiation ($\lambda = 1.5406 \text{ \AA}$). A step size of 0.02° and a scan speed of $5^\circ/\text{min}$ were employed during the XRD measurements. The defect density (especially dislocation density) values are calculated from the XRD patterns using the conventional Williamson-Hall equation. The crystallographic

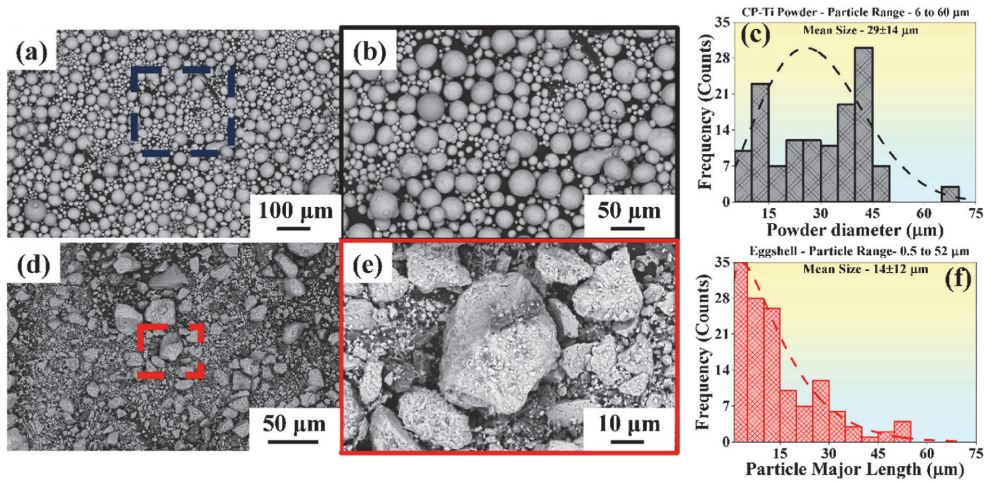


Fig. 2. Scanning electron microscopy images of the commercially pure Ti (CP-Ti) powder taken at (a) low magnification and (b) high magnification. (c) Plot showing the particle size distribution of the employed gas-atomized CP-Ti powders where the average particle size is observed to be $29 \pm 14 \mu\text{m}$. Scanning electron microscopy images of the raw eggshell powder taken at (d) low magnification and (e) high magnification. (f) The particle size distribution plot of the employed eggshell powders where the average particle size is observed to be $14 \pm 12 \mu\text{m}$.

information was extracted from the XRD data. The mechanical performance of the composites was evaluated in the form of compressive tests using an Instron test 5567 screw-driven universal testing machine at a strain rate of 10^{-3} mm/s. During the compression testing, the loading direction was co-axial with the building direction of the lattice.

2.4. Cytotoxicity and bacterial study

To compare the biological performance of the Ti-eggshell composite, eggshell compact produced by SPS and CP-Ti solids (of 6 mm height and 10 mm diameter) were utilized. To assess the cytotoxicity of the samples, the samples were immersed in the α -MEM media that contains 1 % penicillin-streptomycin and 10 % fetal bovine serum solution. The solution with 10 % fetal bovine serum and 1 % penicillin-streptomycin was centrifuged and filtered after 24 h before being added to the cell culture. Adipose-derived stem cells (ADSCs) at passage 6 were cultured in special flasks containing the α -MEM media. The cytotoxicity of samples was tested using a lactate dehydrogenase (LDH) assay (CyQUANT™ LDH Cytotoxicity Assay Kit). Upon reaching a confluency of 80 %, 20,000 cells/mL were seeded into each well (in a 24-well plate system) containing the filtered solution from different specimens. After incubation for 24 h at room temperature ($\sim 37^\circ\text{C}$) and 5 % CO_2 , from each well plate, a 50 μL solution was placed into a 96-well plate. The standard protocol for determining cytotoxicity was employed to evaluate the cytotoxicity of different surfaces. The cells grown in the polystyrene well plate was used as a positive control. On the other hand, the negative control employed here is the cells exposed to lysis buffer. The absorbance values of the samples are read in a microplate reader (from FLUOstar Omega, BMG LABTECH, Cary, NC, USA) with wavelengths of 490 nm and 680 nm. The results were evaluated using a two-way ANOVA analysis. The origin software was employed to evaluate the post-hoc Tukey's honestly significant difference (HSD) test, with significance defined as $p < 0.05$.

The antibacterial activity of the samples (surfaces) was carried out using the bacterial cultures of two different bacteria, namely, gram-negative *Pseudomonas aeruginosa* (ATCC 10145) (hereafter *P. aeruginosa*) bacteria and gram-positive *Staphylococcus aureus* (ATCC 6538) (hereafter *S. aureus*) bacteria. These bacteria were cultivated in 8 mL tryptic soy broth (TSB) from Sigma-Aldrich. They are then incubated at

room temperature (37°C) for a dwell time of 12 h. The solution containing the bacteria was then diluted until an optical density of 0.52 was achieved, corresponding to a concentration of 10^9 colony-forming units (CFU)/mL of TSB solution, measured at 562 nm wavelength. The sample surfaces were cleaned with DI water and sterilized under the UV light for 60 min and were then transferred to a 24-well plate. A 500 μL bacteria solution with a concentration of 10^6 CFU/mL was added to each well. The well plates were then incubated for two different time durations (6 h and 24 h) at room temperature (37°C), respectively. After the requisite incubation time, the bacterial solution was removed, and a PBS solution was used to rinse the surfaces. The bacteria present on the surfaces were fixed by immersing the surfaces in a fixative solution (composition of the solution: 3 % glutaraldehyde, 0.1 M sodium cacodylate, and 0.1 M sucrose in DI water) for a dwell time of 45 min. After fixing the bacteria, they were allowed to sit in a buffer solution (fixative solution without the presence of glutaraldehyde) for a dwell time of 10 min. The surfaces were then immersed subsequently in 35 %, 50 %, 70 %, and 100 % ethanol for a dwell time of 10 min each before being stored in a desiccator. To increase the conductivity for imaging, the surfaces were coated with 10 nm gold (Au). The bacterial morphology and the biofilm formation on the different sample surfaces were evaluated using the field emission SEM (JEOL JSM-6500).

3. Results and discussion

Fig. 2(a,b,d, and e) shows the SEM images of both CP-Ti and eggshell powders. The CP-Ti powder (Fig. 2(a and b)) employed in the present study is a gas-atomized powder with a spherical morphology. Some satellite particles (small spherical-shaped particles) are observed to be present on the boundaries of the large spherical particles. These satellite particles are common in gas-atomized powder due to the collision of the fine particles and partially molten particles because of gas circulation in the atomizing chamber [57]. The particle size distribution plot displayed in Fig. 2(c) indicates the presence of a wide range of particle sizes, with a mean size (d_{50}) of $29 \pm 13 \mu\text{m}$. On the other hand, the eggshell powders (Fig. 2(d and e)) exhibit the presence of irregularly shaped particles, where tiny particles stick to the surface of the large particles due to their large surface area. Fig. 2(f) presents a powder particle size distribution plot revealing that the large particles are in the range of $52 \mu\text{m}$, while the

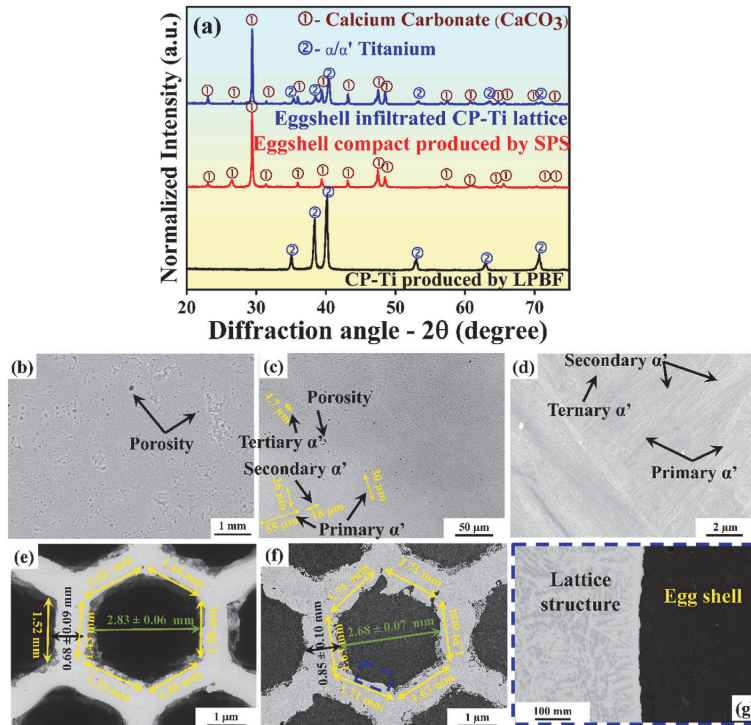


Fig. 3. (a) X-ray diffraction patterns of the CP-Ti produced by laser powder-bed fusion process, eggshell compact produced by SPS and Ti-eggshell composite, (b) Scanning electron microscopy image of the eggshell, (c) Optical Microscopy image, and (d) Scanning electron microscopy image of CP-Ti produced by laser powder-bed fusion process; (e) Scanning electron microscopy image of the CP-Ti lattice before SPS; (f) Scanning electron microscopy image of the CP-Ti-eggshell composite, (g) higher magnification Scanning electron microscopy image of the CP-Ti-eggshell composite interface.

small particles are in the range of $0.5 \mu\text{m}$, with a mean particle size (d_{50}) observed to be $14 \pm 12 \mu\text{m}$.

Fig. 3(a) shows the XRD patterns of the LPBF fabricated CP-Ti, SPS eggshell compacts, and Ti-eggshell composite. LPBF CP-Ti shows the presence of the major peaks at 35.06° (100), 38.36° (002), 40.11° (101), and 70.62° (103), respectively corresponding to the hexagonal close packed (HCP) crystal structure of the Ti having the space group: $P63/mmc$ (194) [9]. Since rapid cooling is involved during the fabrication of CP-Ti by the LPBF process, the solidification conditions favor the formation of a martensitic phase with the HCP structure [8]. Fig. 3(c and d) illustrates the microstructure of the LPBF fabricated CP-Ti, revealing the presence of a martensitic structure (α'). Attar et al. [9] and Gu et al. [58] have also reported a similar martensite microstructure in LPBF-CP-Ti samples. During the LPBF process, multiple scans create multiple cooling cycles, resulting in further modification of the martensitic structure. The modified martensite may be defined based on the dimensions of its major and minor axes. As marked with black arrows (in Fig. 3(c and d)), the plate with a major axis greater than $20 \mu\text{m}$ is marked as primary martensite. The plates with major axis dimensions between $10 \mu\text{m}$ and $20 \mu\text{m}$ are differentiated as secondary martensite, and all other plates with major axis dimensions falling between $1 \mu\text{m}$ and $10 \mu\text{m}$ are termed as ternary martensite [59].

The SPS fabricated eggshell compact (Fig. 3(a)) displays its major peaks at 29.40° (104), 47.46° (018), and 48.51° (116), respectively. The highest intense peak at (104) confirms the presence of the calcite phase of CaCO_3 , which has a rhombohedral crystal structure belonging to the $R\bar{3}c$ space group [60–62]. As depicted in Fig. 3(b), the SEM image of the SPS fabricated eggshell compact exhibits the presence of porosity, where

the compacts are observed to be $\sim 87 \pm 1\%$ dense [40]. According to Fig. 3(a), the XRD pattern of the Ti-eggshell composites showed the presence of all peaks of CP-Ti (HCP structure) and calcite phase. No additional peaks are observed suggesting there is no interfacial reaction taking place during the SPS process. Fig. 3(e) depicts the SEM image of the CP-Ti lattice before being subjected to the SPS consolidation process. The average length of the strut deviated from the CAD design by $\sim 23\%$. However, after SPS (Fig. 3(f)), the average length of the individual strut remained constant, with a higher average deviation. As evident from Fig. 3(f), the length of the strut varied, with certain areas being elongated and others contracted. This might be attributed to the influence of both the thermal and mechanical energies acting on these struts during the SPS process. Additionally, the width of the strut broadened after SPS, which resulted in a reduction of the distance between two parallel struts. During SPS, the applied pressure of 50 MPa (to densify the lattice) to such changes in the strut dimensions [63]. Moreover, the edges of the struts were wavy and not straight, which is a common geometric imperfection in horizontal struts [64], where they involve overhanging features. Overhanging features during the LPBF processing generally led to irregular surfaces and wavy edges. Strut waviness, dimensional and geometric deviation, and particle adhesion are more pertinent in thin wall/strut structures, which are mainly caused by gravitational factors as well as heat transfer properties. Furthermore, necking was observed at the nodal points, which is a typical defect that occurs when up to 5 struts merge at a single point. Necking is also a factor, which creates deviation from the original design and individual strut length [64]. In the present design, three struts merge from a single plane, while two struts merge from the perpendicular plane.

As shown in Fig. 3(g), the interface of the composite (CP-Ti and

Table 1

Table showing the average dimensions (length, width, and distance between two parallel struts) observed for the struts calculated from the scanning electron microscopy images and their variations as a function of processing conditions.

Description	Average length of the strut (n = 10) (mm)	Average width of the strut (n = 10) (mm)	Average distance between two parallel struts (n = 10) (mm)
CAD Design	2.0	0.5–0.7	3.1–3.2
As-built lattice	1.54 ± 0.09	0.68 ± 0.09	2.83 ± 0.06
Lattice after SPS	1.54 ± 0.15	0.85 ± 0.10	2.68 ± 0.07

eggshell) does not exhibit the presence of defects like porosity, which might be attributed to the effect of the processing parameters employed during the SPS consolidation process. In addition, no formation of new phases is observed at the interface (since no thermal reaction has taken place no intermetallic phase has formed) corroborating the XRD data. The original strut dimensions (involved during the CAD design), the strut dimensions after fabricating using the LPBF process, and the changes in the strut dimensions after being subjected to the SPS consolidation process are shown in Table 1. The table depicts the minor variations in the strut dimensions between the CAD model and the fabricated actual sample, which is related to the process capabilities. In addition, further changes in the strut dimensions after the SPS consolidation process (which is already discussed) are related to the application of both thermal and mechanical energies during the consolidation process. The dislocation density calculated for the LPBF-CP-Ti strut is found

to be $3.8 \pm 1 \times 10^{15} \text{ m/m}^3$. Such high dislocation densities are typical for LPBF-manufactured materials, even observed for other materials like Al-based, Ti-based, Co-based, and Ag-based alloys [65–67]. The high cooling rate observed during the process aids in rapid quenching of the material leading to the formation of meta-stable phases with a high degree of geometrically necessary dislocations (GNDs). The lattice parameters for the martensitic phase are observed to be $a = 2.9506 \text{ \AA}$, and $c = 4.6850 \text{ \AA}$ (leading to a c/a ratio of ~ 1.5878).

The lattice parameters show that the c/a ratio is well below the ideal value of 1.633, where the dimensions along the c -axis are reduced significantly compared to the a -axis. On the other hand, the fabrication of the composites by SPS involves the heating of the CP-Ti lattice along with the eggshell powders to $850 \text{ }^\circ\text{C}$ (below the beta transus temperature) for 5 min and subsequently cooled slowly inside a graphite die, a process very similar to annealing. Hence, the CP-Ti is subjected to an annealing kind of treatment during the composite fabrication process. Hence the concentration of dislocations (dislocation density) after the composite fabrication process and along the CP-Ti lattice reduces to $6 \pm 2 \times 10^{14} \text{ m/m}^3$. At the same time, the lattice parameters of CP-Ti also change, where a and c are found to be 2.9508 \AA and 4.6882 \AA , respectively leading to a c/a ratio of 1.5888. Generally, the c/a ratio Ti is observed to be 1.5888 instead of the ideal hcp c/a ratio of 1.633.

Fig. 4 shows the TEM images of the LPBF-processed CP-Ti. The selected area diffraction pattern (SAED – in Fig. 4(a)) of the CP-Ti shows the presence of a typical HCP phase, in the present case attributing to the martensitic phase formation. The SAED pattern is taken along the zone axis $[2\bar{1}\bar{1}0]$ and hence the angle between the planes A and B is observed

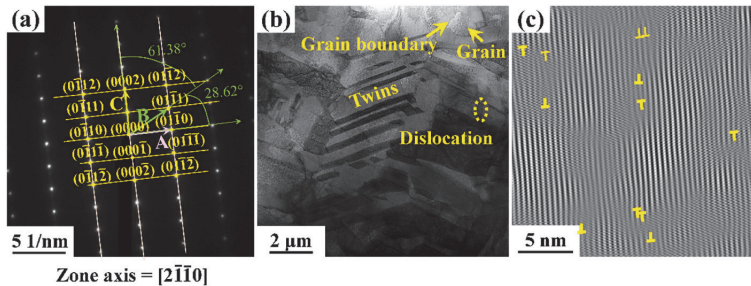


Fig. 4. The transmission electron microscopy images of the CP-Ti fabricated by laser power-bed fusion process. (a) Selected area diffraction pattern confirming the presence of a hexagonally closed packed structure. (b) Bright-field image showing the presence of imperfections like grain boundaries, twins, and dislocations. (c) Inverse Fourier-filtered image showing the presence of multiple edge dislocations.

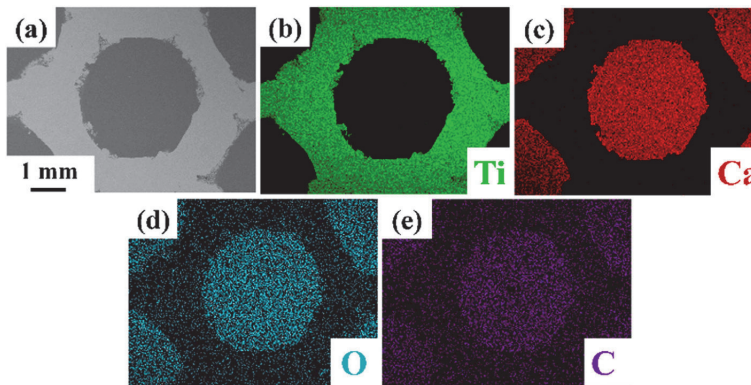


Fig. 5. The energy dispersive X-ray (EDX) maps taken along the Ti-eggshell composite (a) secondary electron image of the composite material. The EDX maps show the presence of elements like (b) Ti (CP-Ti lattice) and (c) Ca, (d) O, and (e) C (from eggshell).

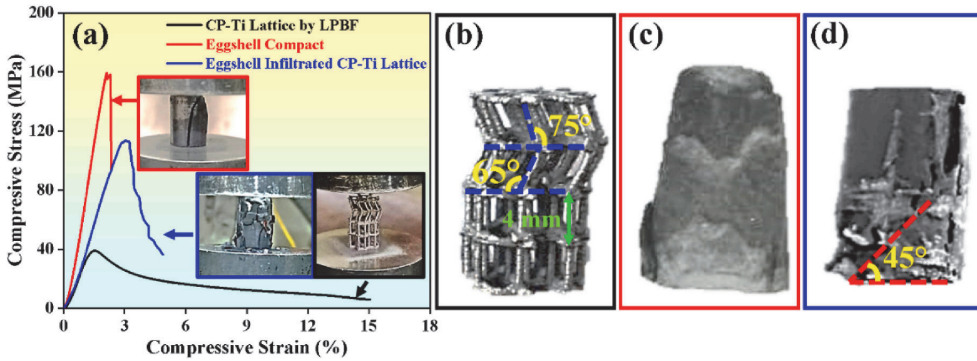


Fig. 6. (a) Room temperature uniaxial compressive stress-strain curves observed for the LPBF-fabricated CP-Ti lattice, eggshell compact, and CP-Ti-eggshell composites and the inset shows the fractured image of the samples. Optical images of the samples showing fractured impact after the compression test (b) LPBF-processed CP-Ti lattice (c) SPS-made eggshell compacts, and (d) Ti-eggshell composite.

Table 2

Table furnishing the Young's Modulus and the Yield Strength for the CP-Ti lattice, consolidated, and Ti-eggshell composites.

Description	Youngs Modulus (GPa)	Yield Strength (MPa)
CP-Ti	38 ± 1	37 ± 2
Eggshell	87 ± 11	155 ± 15
Composite – CP-Ti + Eggshell	47 ± 2	123 ± 34

to be 28.62° and BC is observed to be 61.38°. The SEAD pattern agrees with the XRD and SEM results, where α martensitic structure is observed in the CP-Ti lattice. The bright field image in Fig. 4(b) shows the different kinds of crystal defects that can be observed in a material. For instance, line defects in the form of dislocations are observed. The dislocations do not present isolated but are present in the form of lines, sometimes extending from one grain to another. Other surface defects like the grain boundaries and twins/twin boundaries are also observed in the LPBF-fabricated CP-Ti material. The presence of these defects may also be corroborated by the extreme cooling conditions that exist during

the LPBF processing of materials. Fig. 4(c) shows the inverse fast Fourier transform image (IFFT) displaying the presence of numbers of edge dislocations. The presence of both positive and negative edge dislocations is observed in the LPBF-processed CP-Ti. These dislocations are generated during the solidification process since these materials are not subjected to mechanical treatment. During solidification and on increasing strain over the solidifying surface (solidification solid/liquid interface), a few dislocation walls cut among themselves leading to the multiplication of two similar dislocation walls. As expected, the negative edge dislocation contributes to the generation of tensile stress on the microstructure and the positive edge dislocation induces compressive stress in return. A series of dislocation grids are observed over the entire surface where multiple positive and negative edge dislocations exist (Fig. 4(c)).

The energy dispersive X-ray (EDX) mapping of the Ti-eggshell composites is furnished in Fig. 5. It can be observed that the composite samples show the presence of elements like Ti, Ca, C, and O. The lattice rich in Ti is surrounded by the elements Ca, C, and O, which correspond to CaCO₃ phase. It is noteworthy to mention that the interfacial reaction between CP-Ti lattice and eggshell powder is absent and there is no diffusion at the interface under the optimized SPS conditions. Fig. 6(a) showcases the room temperature uniaxial engineering compressive stress-strain curve of the LPBF-fabricated CP-Ti, SPS-made eggshell compacts, and Ti-eggshell composite. The yield strength (σ_y) calculated for the CP-Ti sample is 38 ± 2 MPa, while for the eggshell compact, the σ_y is observed to be 155 ± 15 MPa and for the Ti-eggshell composite the σ_y is observed to be 123 ± 34 MPa (see Table 2). The images of the samples after the compression test are shown in Fig. 6(a) as inset and their enlarged view is shown in Fig. 6(b-d). The CP-Ti lattice after fracture shows the presence of a plateau, which is a common compressive behavior for porous structures as per ISO 13314 standards [54]. The smooth plateau region corroborates the ductile behavior of the lattice [17]. The fractured image of the hexagonal Ti lattice reveals that the struts of the top layer and the layer beneath it are bent at an angle of 75° and 65° respectively but in opposite directions, which is referred as sequential bending. The hexagonal lattice only contains the vertical struts (parallel to the loading direction) and horizontal struts (perpendicular to the loading direction) without any strut included at an angle to the loading direction. Previously, Choy et al. [54] reported that due to the nature of the loading direction, the horizontal struts are unaffected by the compression load. On the other hand, the horizontal struts are supported by the vertical struts resulting in the bending of vertical struts with an angle of 75° [54]. However, after the second layer from the top (Fig. 6(b)), the layer thickness remained consistent (4 mm as per design) owing to the sequential bending pattern [68].

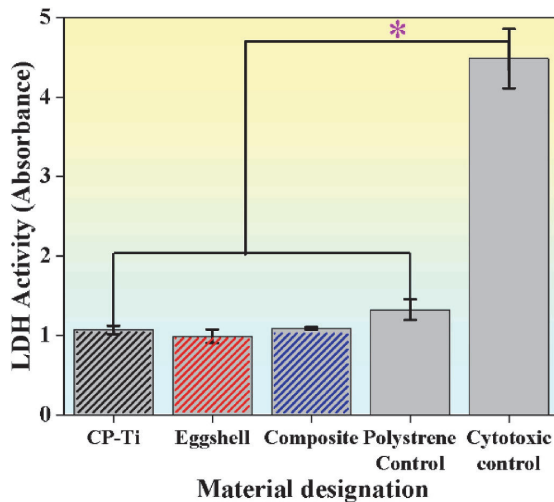


Fig. 7. The cytotoxicity analysis for the LPBF-processed CP-Ti lattice, eggshell compact, and Ti-eggshell composite on human adipose-derived stem cells. (*p ≤ 0.05).

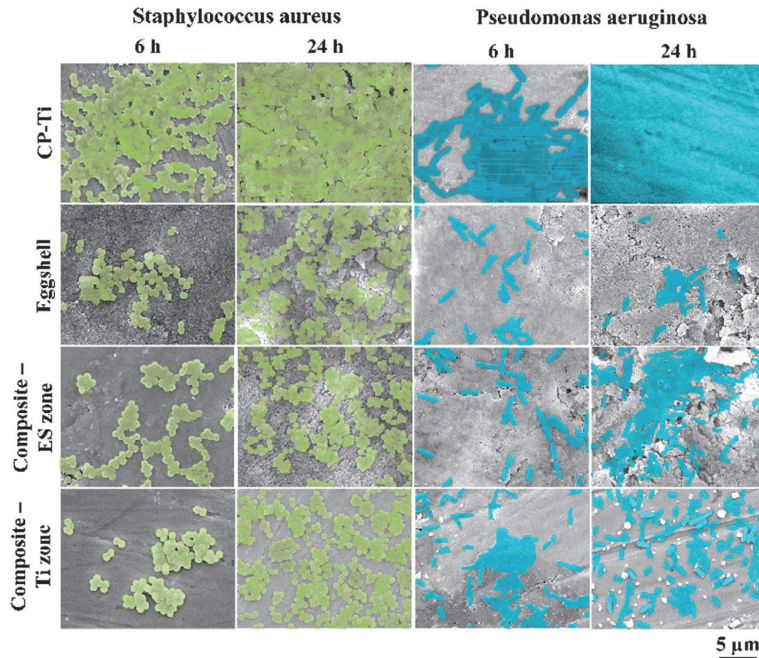


Fig. 8. Scanning electron microscopy images of the *Staphylococcus aureus* bacteria (false-colored green) and *Pseudomonas aeruginosa* bacteria (false-colored cyan) for the LPBF-fabricated CP-Ti, SPS-made eggshell compact, and the Ti-eggshell composite (abbreviated as composite). (For interpretation of the references to color in this figure legend, the reader is referred to the Web version of this article.)

The ‘saw-tooth’ behavior was observed in the plastic regime, which is common in brittle ceramic materials, which is pertinent to the emergence and densification of micro-cracks, ultimately failing the material. In the fractured eggshell sample (Fig. 6(a–c)), the serrated pattern is observed, which is attributed to brittle fracture [69,70]. The Ti-eggshell composite (Fig. 6(a–d)) displayed a combined compressive behavior of both CP-Ti and eggshell, which includes an increase in yield strength similar to eggshell compact whereas decrease in Young’s modulus similar to CP-Ti lattice. As a result, the Ti-eggshell composite demonstrated a compressive yield strength of $\sim 123 \pm 34$ MPa and Young’s modulus $\sim 47 \pm 1$ GPa, which is in the range of natural cortical bone (compressive yield strength = 100–130 MPa, and Young’s modulus = 5–30 GPa respectively) [71]. Fig. 6(d) shows the optical image of the Ti-eggshell composite after the compression test, which indicates that compressive failure occurred at an angle equivalent to $\sim 45^\circ$. Such 45° failure is attributed to shear and thus in the present case can be referred to as diagonal shear, corroborating a brittle fracture.

LDH is an enzyme present in cells and the cytotoxicity of the material can be identified from the LDH release caused by lysis due to material contact. The release of LDH enzyme to the media directly implies the cytotoxicity of the material, whereas the lower absorbance readings imply higher cytocompatibility [72]. Fig. 7 shows the cytotoxicity behavior of the CP-Ti, eggshell, and Ti-eggshell composite on adipose-derived stem cells (ADSCs). Eggshell exhibits the lowest absorbance (lowest LDH release), whereas CP-Ti and Ti-eggshell composite display similar absorbances. However, all the samples demonstrate lower cytotoxicity compared to the cytotoxic control and no statistical difference from the polystyrene control. Fig. 8 shows SEM images of the ATCC 6538 – *Staphylococcus aureus* (*S. aureus*) and ATCC 10145 – *Pseudomonas aeruginosa* (*P. aeruginosa*) bacteria after being grown for 6 h and 24 h, respectively. As depicted in Fig. 8, bacteria growth is higher on the CP-Ti surface (easy growth on the CP-Ti surface),

Table 3

Table furnishing the bacteria inhibition efficacy observed in the consolidated Ti-eggshell composites.

Description	<i>Staphylococcus aureus</i>		<i>Pseudomonas aeruginosa</i>	
	6 h	24 h	6 h	24 h
Eggshell	72	49	78	86
Composite (Ti + Eggshell) – ES zone	61	46	68	71
Composite (Ei + Eggshell) – Ti Zone	45	33	55	64

followed by Ti-eggshell composite and eggshell compacts. CP-Ti surface showed bacteria biofilm formation after 24 h of bacteria growth for both types of bacteria used. In the eggshell compact (refer to Fig. 8), bacteria growth is reduced due to the antibacterial activity of the CaCO_3 , especially against *P. aeruginosa*. Ti-eggshell composite contains both eggshell and CP-Ti surfaces, among this CP-Ti surface exhibited more bacteria growth compared to the eggshell regions. However, bacteria growth in the composite is significantly reduced compared to the CP-Ti and there are no signs of biofilm formation.

As presented in Table 3, the inhibition efficiency is most pronounced in the eggshell samples, followed by the eggshell-rich regions of the Ti-eggshell composite and the Ti-rich regions of the composite. Remarkably, the Ti-rich zones exhibit bacterial inhibition ranging from 33 % to 64 %, as depicted in Fig. 8, where biofilm formation is significantly reduced in these regions when compared to the CP-Ti surface. In contrast, the CP-Ti surface displays biofilm formation after 24 h of bacterial growth, indicating lower antibacterial efficacy. The plots below illustrate the percentage area covered by *Staphylococcus aureus* (Fig. 9(a)) and *Pseudomonas aeruginosa* (Fig. 9(b)) bacteria and then bacterial inhibition efficacy is furnished in Fig. 9. The hypothesis behind the antibacterial activity and interaction of bacteria on the surface is

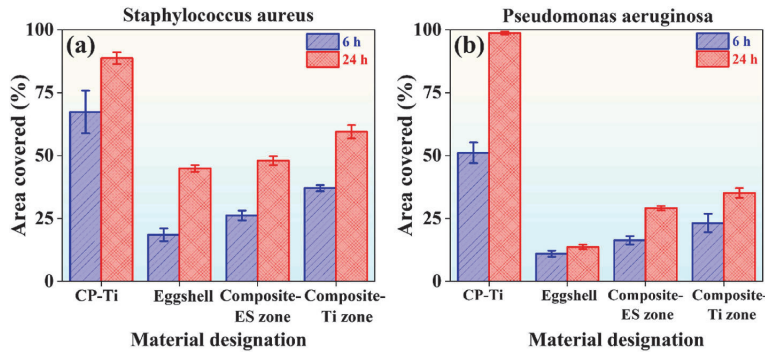


Fig. 9. Comparison of area coverage (%) on the LPBF-fabricated CP-Ti lattice, SPS-made eggshell compact, and the Ti-eggshell composite (abbreviated as composite) after 6 h and 24 h of incubation with (a) *Staphylococcus aureus*, and (b) *Pseudomonas aeruginosa* bacteria.

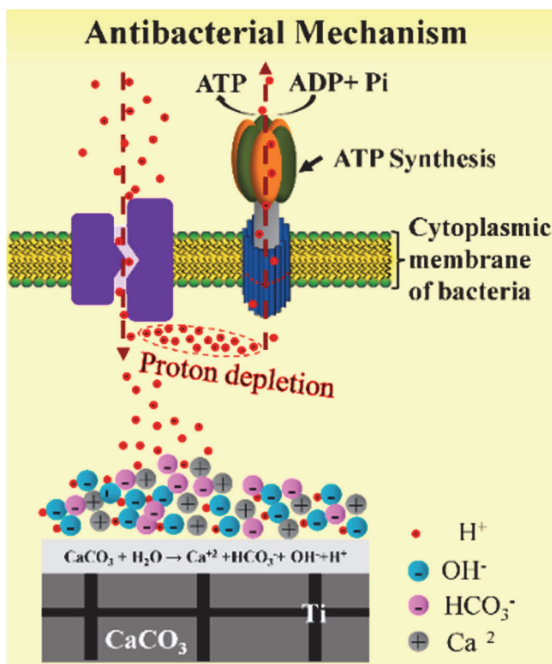


Fig. 10. Schematic diagram illustrating the micro-surface detailing the mechanism involved in the antibacterial behavior of the Ti-eggshell composite.

explained in Fig. 10.

Staphylococcus aureus (*S. aureus*) and *Pseudomonas aeruginosa* (*P. aeruginosa*) are two common types of gram-positive and gram-negative bacteria respectively [73]. The bacteria cell wall is the first layer to interact with the material surface. Both bacteria possess different cell wall structures, with the gram-negative being a highly complex structure with a thin layer of peptidoglycan [74]. It is shown in the literature that the calcium ions can interact and bind with both the cell walls, which could interrupt energy transport [75]. However, the ions can also pass through the cell wall and interact with the bacterial cytoplasmic membrane. In bacteria cells, H^+ ion (proton) exchanges constantly, which is known as the proton pump. This proton pump is essential to the synthesis of adenosine triphosphate (ATP). Eggshells are mainly composed of CaCO_3 , more specifically Ca^{+2} and CO_3^{-2} ions connected with ionic

bonds. CaCO_3 is highly alkaline. When it encounters a bacterial solution containing water (H_2O), it easily combines with the H^+ ion and produces HCO_3^- and OH^- ions. H^+ ion is mainly consumed to neutralize CaCO_3 , which produces the H^+ (proton) depleted zone. In the cell membrane, protons play a crucial role as the proton gradient produces ATP through the electron transport chain (ETC) (Schematics shown in Fig. 10). ATP is a powerhouse of the cell, and disruption in ATP synthesis adversely affects the bacterial growth, bacteria metabolism and as results in bacterial death. Briefly, the alkaline nature of the CaCO_3 inhibits bacterial growth and biofilm formation in eggshell-based bio-implants [76–78]. Whereas, in the case of CP-Ti, there are no such ions present to produce H^+ depleted zone. Moreover, compared to calcium, titanium is not strongly alkaline. An alkaline environment also acts similarly to inhibit bacterial growth. Hence, monolithic CP-Ti did not show such bactericidal activity but with the addition of eggshell the bactericidal activity increases in the composite. This suggests that the Ti-eggshell composite can be a good candidate for fabricating bactericidal surfaces and implants.

4. Summary

In the present manuscript, a novel Ti-eggshell composite was manufactured using a combined additive manufacturing-powder metallurgical (LPBF-SPS) approach. A CP-Ti hexagonal prism lattice was successfully fabricated using the LPBF process. As expected, with the extreme cooling conditions observed during the LPBF process, materials with a high degree of internal defects (especially dislocations) can be observed along with the metastable martensitic phase (α'). The eggshell powder was then introduced into the lattices of the CP-Ti and subjected to spark plasma sintering to fabricate these novel Ti-eggshell composites, effectively valorizing eggshell waste for use in bone-grafting materials. The composite retained the chemical composition and phases of calcium carbonate from the eggshell and titanium from the lattice. Room temperature uniaxial compression tests were conducted on these samples. The CP-Ti lattice failed by sequential bending, the eggshell compact failed by brittle fracture, and the Ti-eggshell composite failed by diagonal shear. Notably, the Ti-eggshell composite exhibited compressive strength and Young's modulus matching that of the natural human cortical bone. Furthermore, the Ti-eggshell composite was found to be non-cytotoxic to ADSCs and safe to be used as a biomaterial. Ti-eggshell composite demonstrated excellent antibacterial activity against both gram-positive bacteria (*S. aureus*) and gram-negative (*P. aeruginosa*). The antibacterial activity of the eggshell or eggshell-containing compacts is attributed to disruption in the proton pump. In conclusion, this study reports the successful valorization of eggshell waste (circular economy route) in bio-implants by introducing a CP-Ti lattice produced through additive manufacturing. The resulting Ti-eggshell composite

possesses mechanical properties comparable to that of natural human cortical bone, making it a promising material for biomedical (implant) applications.

CRedit authorship contribution statement

Riddhi Shukla: Writing – original draft, Methodology, Investigation, Formal analysis, Data curation, Conceptualization. **Mayank Kumar Yadav:** Writing – original draft, Methodology, Formal analysis, Data curation. **Liszt Yeltsin Coutinho Madruga:** Writing – original draft, Methodology, Investigation, Formal analysis, Data curation. **JJayamani Jayaraj:** Writing – review & editing, Validation, Resources. **Ketul Popat:** Writing – review & editing, Visualization, Supervision, Resources. **Zhi Wang:** Writing – original draft, Resources, Investigation, Formal analysis. **Lixia Xi:** Writing – original draft, Resources, Methodology, Investigation. **Konda Gokuldoss Prashanth:** Writing – review & editing, Validation, Supervision, Resources, Project administration, Funding acquisition, Conceptualization.

Data availability statement

The data published in the article may be available on reasonable request.

Declaration of competing interest

The authors declare that they have no known competing financial interests or personal relationships that could have appeared to influence the work reported in this paper.

Acknowledgments

The authors gratefully acknowledge funding from the National Natural Science Foundation of China (No. 52205382) for TEM studies and the Analytical Resources Core (RRID: SCR_021758) at Colorado State University for providing instrument access, training, and assistance with sample analysis.

References

- [1] C. Stewart, B. Akhavan, S.G. Wise, M.M.M. Bilek, A review of biomimetic surface functionalization for bone-integrating orthopedic implants: mechanisms, current approaches, and future directions, *Prog. Mater. Sci.* 106 (2019) 100588, <https://doi.org/10.1016/j.pmatsci.2019.100588>.
- [2] X. Li, P. Gao, P. Wan, Y. Pei, L. Shi, B. Fan, C. Shen, X. Xiao, K. Yang, Z. Guo, Novel bio-functional magnesium coating on porous Ti6Al4V orthopaedic implants: in vitro and in vivo study, *Sci. Rep.* 7 (1 7) (2017) 1–11, <https://doi.org/10.1038/srep40755>, 2017.
- [3] N. Singh, V. Edachery, M. Rajput, K. Chatterjee, S.V. Kailas, K.G. Prashanth, Ti6Al7Nb–TiB nanocomposites for ortho-implant applications, *J. Mater. Res.* 2022 (2022) 1–11, <https://doi.org/10.1557/S43578-022-00578-2>.
- [4] M. Geetha, A.K. Singh, R. Asokamani, A.K. Gogia, Ti based biomaterials, the ultimate choice for orthopaedic implants – a review, *Prog. Mater. Sci.* 54 (2009) 397–425, <https://doi.org/10.1016/j.pmatsci.2008.06.004>.
- [5] R. Rahmani, M. Antonov, L. Kollo, Y. Holovenko, K.G. Prashanth, Mechanical behavior of Ti6Al4V scaffolds filled with CaSiO₃ for implant applications, *Appl. Sci.* 9 (2019) 3844, <https://doi.org/10.3390/app9183844>.
- [6] M. Sarraf, E. Rezvani Ghomi, S. Alipour, S. Ramakrishna, N. Liana Sukiman, A state-of-the-art review of the fabrication and characteristics of titanium and its alloys for biomedical applications, *Biodes Manuf* 5 (2022) 371–395, <https://doi.org/10.1007/s42242-021-00170-3>.
- [7] H. Attar, S. Ehtemam-Haghighi, N. Soro, D. Kent, M.S. Dargusch, Additive manufacturing of low-cost porous titanium-based composites for biomedical applications: advantages, challenges and opinion for future development, *J. Alloys Compd.* 827 (2020) 154263, <https://doi.org/10.1016/j.jallcom.2020.154263>.
- [8] H. Attar, K.G. Prashanth, A.K. Chaubey, M. Calin, L.C. Zhang, S. Scudino, J. Eckert, Comparison of wear properties of commercially pure titanium prepared by selective laser melting and casting processes, *Mater. Lett.* 142 (2015) 38–41, <https://doi.org/10.1016/j.matlet.2014.11.156>.
- [9] H. Attar, M. Calin, L.C. Zhang, S. Scudino, J. Eckert, Manufacture by selective laser melting and mechanical behavior of commercially pure titanium, *Mater. Sci. Eng., A* 593 (2014) 170–177, <https://doi.org/10.1016/j.msea.2013.11.038>.
- [10] J. Neunzehn, T. Szuwart, H.P. Wiesmann, Eggshells as natural calcium carbonate source in combination with hyaluronan as beneficial additives for bone graft materials, an in vitro study, *Head Face Med.* 11 (2015) 1–10, <https://doi.org/10.1186/S13005-015-0070-0/FIGURES/7>.
- [11] S.A. Siddiqui, S.P. Srikanth, Y.S. Wu, T. Kalita, T.G. Ambartsumov, W. Tseng, A. P. Kumar, A. Ahmad, J.E. Michalek, Different types of algae beneficial for bone health in animals and in humans – a review, *Algal Res.* 82 (2024) 103593, <https://doi.org/10.1016/j.algal.2024.103593>.
- [12] L.-C. Zhang, H. Attar, M. Calin, J. Eckert, Review on manufacture by selective laser melting and properties of titanium based materials for biomedical applications, *Mater. Technol.* 31 (2016) 66–76, <https://doi.org/10.1179/1753555715Y.0000000076>.
- [13] N. Singh, P. Hameed, R. Ummethala, G. Manivasagam, K.G. Prashanth, J. Eckert, Selective laser manufacturing of Ti-based alloys and composites: impact of process parameters, application trends, and future prospects, *Mater Today Adv* 8 (2020) 100097, <https://doi.org/10.1016/j.mtadv.2020.100097>.
- [14] C.J. Burstone, A.J. Goldberg, Beta titanium: a new orthodontic alloy, *Am. J. Orthod.* 77 (1980) 121–132, [https://doi.org/10.1016/0002-9416\(80\)90001-9](https://doi.org/10.1016/0002-9416(80)90001-9).
- [15] Y.J. Liu, S.J. Li, H.L. Wang, W.T. Hou, Y.L. Hao, R. Yang, T.B. Sercombe, L. C. Zhang, Microstructure, defects and mechanical behavior of beta-type titanium porous structures manufactured by electron beam melting and selective laser melting, *Acta Mater.* 113 (2016) 56–67, <https://doi.org/10.1016/j.actamat.2016.04.029>.
- [16] M.A. Lopez-Heredia, E. Goyenvalle, E. Aguado, P. Pilet, C. Leroux, M. Dorget, P. Weiss, P. Layrolle, Bone growth in rapid prototyped porous titanium implants, *J. Biomed. Mater. Res.* 85 (2008) 664–673, <https://doi.org/10.1002/jbm.a.31468>.
- [17] X.P. Tan, Y.J. Tan, C.S.L. Chow, S.B. Tor, W.Y. Yeong, Metallic powder-bed based 3D printing of cellular scaffolds for orthopaedic implants: a state-of-the-art review on manufacturing, topological design, mechanical properties and biocompatibility, *Mater. Sci. Eng. C* 76 (2017) 1328–1343, <https://doi.org/10.1016/j.msec.2017.02.094>.
- [18] P.K. Gokuldoss, S. Kolla, J. Eckert, Additive manufacturing processes: selective laser melting, electron beam melting and binder jetting-selection guidelines, *Materials* 10 (2017) 672, <https://doi.org/10.3390/ma10060672>.
- [19] K. Prashanth, S. Scudino, R. Chatterjee, O. Salman, J. Eckert, Additive manufacturing: reproducibility of metallic parts, *Technologies* 5 (2017) 8, <https://doi.org/10.3390/technologies5010008>.
- [20] S. Liu, Y.C. Shin, Additive manufacturing of Ti6Al4V alloy: a review, *Mater. Des.* 164 (2019) 107552, <https://doi.org/10.1016/j.matdes.2018.107552>.
- [21] P. Hameed, C.-F. Liu, R. Ummethala, N. Singh, H.-H. Huang, G. Manivasagam, K. G. Prashanth, Biomimetic porous Ti6Al4V gyroid scaffolds for bone implant applications fabricated by selective laser melting, *Progress. Additive Manuf.* 6 (2021) 455–469, <https://doi.org/10.1007/s40964-021-00210-5>.
- [22] A.A. Raheem, P. Hameed, R. Whenshi, R.S. Elsen, A. G. A.K. Jaiswal, K. G. Prashanth, G. Manivasagam, A review on development of bio-inspired implants using 3D printing, *Biomimetics* 6 (2021) 65, <https://doi.org/10.3390/biomimetics6040065>.
- [23] B. Jagadeesh, M. Duraiselvam, K.G. Prashanth, Deformation behavior of metallic lattice structures with symmetrical gradients of porosity manufactured by metal additive manufacturing, *Vacuum* 211 (2023) 111955, <https://doi.org/10.1016/j.vacuum.2023.111955>.
- [24] J. Baskaran, D. Muthukannan, R. Shukla, P. Konda Gokuldoss, Manufacturability and deformation studies on a novel metallic lattice structure fabricated by Selective Laser Melting, *Vacuum* 222 (2024) 113065, <https://doi.org/10.1016/j.vacuum.2024.113065>.
- [25] H.M.A. Kolkien, S.J.P. Callens, M.A. Leeftang, M.J. Mirzaali, A.A. Zaidpoor, Merging strut-based and minimal surface meta-biomaterials: decoupling surface area from mechanical properties, *Addit. Manuf.* 52 (2022) 102684, <https://doi.org/10.1016/j.addma.2022.102684>.
- [26] Y. Tang, G. Dong, Q. Zhou, Y.F. Zhao, Lattice structure design and optimization with additive manufacturing constraints, *IEEE Trans. Autom. Sci. Eng.* 15 (2018) 1546–1562, <https://doi.org/10.1109/TASE.2017.2685643>.
- [27] K. Palka, R. Pokrowiecki, Porous titanium implants: a review, *Adv. Eng. Mater.* 20 (2018) 1700648, <https://doi.org/10.1002/adem.201700648>.
- [28] H. Attar, M.J. Bermingham, S. Ehtemam-Haghighi, A. Dehghan-Manshadi, D. Kent, M.S. Dargusch, Evaluation of the mechanical and wear properties of titanium produced by three different additive manufacturing methods for biomedical application, *Mater. Sci. Eng., A* 760 (2019) 339–345, <https://doi.org/10.1016/j.msea.2019.06.024>.
- [29] Y.S. Choi, C.L. Kim, G.H. Kim, B.S. Lee, C.W. Lee, D.G. Lee, Mechanical properties including fatigue of CP Ti and Ti-6Al-4V alloys fabricated by EBM additive manufacturing method, *Appl. Mech. Mater.* 873 (2017) 54–59, <https://dx.doi.org/10.4028/www.scientific.net/AMM.873.54>.
- [30] R. Alkentar, N. Kladovasilakis, D. Tzetzis, T. Mankovits, Effects of pore size parameters of titanium additively manufactured lattice structures on the osseointegration process in orthopedic applications: a comprehensive review, *Crystals* 13 (2023) 113, <https://doi.org/10.3390/cryst13010113>.
- [31] M. Kumar Yadav, R. Hiren Shukla, K.G. Prashanth, A comprehensive review on development of waste derived hydroxyapatite (HAP) for tissue engineering application, *Mater. Today: Proc.* (2023), <https://doi.org/10.1016/j.matpr.2023.04.669>.
- [32] M.K. Yadav, V. Pandey, K. Mohanta, V.K. Singh, A low-cost approach to develop silica doped Tricalcium Phosphate (TCP) scaffold by valorizing animal bone waste and rice husk for tissue engineering applications, *Ceram. Int.* 48 (2022) 25335–25345, <https://doi.org/10.1016/j.ceramint.2022.05.207>.
- [33] Q. Ma, K. Rubenis, Ö.E. Sigurjónsson, T. Hildebrand, T. Standal, S. Zemjane, J. Locs, D. Loca, H.J. Haugen, Eggshell-derived amorphous calcium phosphate: synthesis, characterization and bio-functions as bone graft materials in novel 3D

- osteoblastic spheroids model, *Smart Mater Med* 4 (2023) 522–537, <https://doi.org/10.1016/j.smaim.2023.04.001>.
- [34] G. Ryan, A. Pandit, D. Apatidis, Fabrication methods of porous metals for use in orthopaedic applications, *Biomaterials* 27 (2006) 2651–2670, <https://doi.org/10.1016/j.biomaterials.2005.12.002>.
- [35] A. Kumar, K. Biswas, B. Basu, Hydroxyapatite-titanium bulk composites for bone tissue engineering applications, *J. Biomed. Mater. Res.* 103 (2015) 791–806, <https://doi.org/10.1002/jbm.a.35198>.
- [36] J. Vuola, R. Taurio, H. Göransson, S. Asko-Seljavaara, Compressive strength of calcium carbonate and hydroxyapatite implants after bone-marrow-induced osteogenesis, *Biomaterials* 19 (1998) 223–227, [https://doi.org/10.1016/S0142-9612\(97\)00211-1](https://doi.org/10.1016/S0142-9612(97)00211-1).
- [37] J. Gautron, C. Dombre, F. Nau, C. Feidt, L. Guillier, Review: production factors affecting the quality of chicken table eggs and egg products in Europe, *Animal* 16 (2022) 100425, <https://doi.org/10.1016/j.animal.2021.100425>.
- [38] S. Mahdavi, A. Amiradeghi, A. Jafari, S.V. Niknezhad, S.A. Bencherif, Avian egg: a multifaceted biomaterial for tissue engineering, *Ind. Eng. Chem. Res.* 60 (2021) 17348–17364, <https://doi.org/10.1021/acs.iecr.1c03085>.
- [39] M.T. Hincin, Y. Nys, J. Gautron, K. Mann, A.B. Rodriguez-Navarro, M.D. McKece, The eggshell: structure, composition and mineralization, *Front. Biosci.* 17 (2012) 1266.
- [40] R. Shukla, R. Sokkalingam, K.G. Prashanth, Densification of the eggshell powder by spark plasma sintering, *J. Alloys Compd.* 962 (2023) 171079, <https://doi.org/10.1016/j.jallcom.2023.171079>.
- [41] M.N. Freire, J.N.F. Holanda, Characterization of avian eggshell waste aiming its use in a ceramic wall tile paste, *Cerâmica* 52 (2006) 240–244, <https://doi.org/10.1590/S0366-69132006000400004>.
- [42] M.S. Tizo, L. Andre, V. Blanco, C.Q. Cagas, B. Rangel, B. Dela Cruz, J.C. Encoy, J. V. Guntung, R.O. Arazo, V. Irvin, F. Mabayo, Efficiency of calcium carbonate from eggshells as an adsorbent for cadmium removal in aqueous solution, *Original Research Article* (2018), <https://doi.org/10.1016/j.asej.2018.09.002>.
- [43] A.M. Nassar, N.F. Alotaibi, Eggshell recycling for fabrication of Pd/CaO, characterization and high-performance solar photocatalytic activity, *Environ. Sci. Pollut. Control Ser.* 28 (2021) 3515–3523, <https://doi.org/10.1007/S11356-020-10751-X/FIGURES/11>.
- [44] A. Homavand, D.E. Cree, L.D. Wilson, Poly(lactic acid) composites reinforced with eggshell/CaCO₃ filler particles: a review, *Waste* 2 (2024) 169–185, <https://doi.org/10.3390/waste2020010>.
- [45] A. Kumar, T.J. Webster, K. Biswas, B. Basu, Flow cytometry analysis of human fetal osteoblast fate processes on spark plasma sintered hydroxyapatite-titanium biocomposites, *J. Biomed. Mater. Res.* 101 (2013) 2925–2938, <https://doi.org/10.1002/jbm.a.34603>.
- [46] C. Chu, X. Xue, J. Zhu, Z. Yin, In vivo study on biocompatibility and bonding strength of Ti/Ti–20 vol.% HA/Ti–40 vol.% HA functionally graded biomaterial with bone tissues in the rabbit, *Mater. Sci. Eng., A* 429 (2006) 18–24, <https://doi.org/10.1016/J.MSEA.2006.03.099>.
- [47] D. Acharjev, S. Mandal, S.K. Samanta, M. Roy, B. Kundu, S. Roy, P. Basak, S. K. Nandi, In vitro and in vivo bone regeneration assessment of titanium-doped waste eggshell-derived hydroxyapatite in the animal model, *ACS Biomater. Sci. Eng.* 9 (2023) 4673–4685, https://doi.org/10.1021/ACSBOMATERIALS.3C00060/ASSET/IMAGES/MEDIUM/AB3C00060_0013.GIF.
- [48] M.A. Hussein, M.A. Azeem, A.M. Kumar, N.M. Emar, Processing and in vitro corrosion analysis of sustainable and economical eggshell reinforced Mg and Mg-Zr matrix composite for biomedical applications, *Mater. Today Commun.* 32 (2022) 103944, <https://doi.org/10.1016/J.MTCOMM.2022.103944>.
- [49] H. Aoyagi, M. Okada, H. Yanagimoto, T. Matsumoto, Investigation on bacterial capture and antibacterial properties of acid-treated Ti surface, *Dent. Mater.* 40 (2024) 318–326, <https://doi.org/10.1016/J.DENTAL.2023.11.018>.
- [50] C. Song, Y. Chen, L. Liu, H. Lei, X. Yang, J. Hu, Q. Li, Y. Yang, Y. Li, In situ alloying Ti–Ag antibacterial biomaterials via laser powder bed fusion: microstructure, mechanical properties and bioperformance, *Mater Today Adv* 20 (2023) 100445, <https://doi.org/10.1016/J.MTADV.2023.100445>.
- [51] I. Ul Haq, T.A. Khan, K. Krukiewicz, Etiology, pathology, and host-impaired immunity in medical implant-associated infections, *J Infect Public Health* 17 (2024) 189–203, <https://doi.org/10.1016/J.JIPH.2023.11.024>.
- [52] S. Nilawar, K. Chatterjee, Surface decoration of redox-modulating nanoeria on 3D-printed tissue scaffolds promotes stem cell osteogenesis and attenuates bacterial colonization, *Biomacromolecules* 23 (2022) 226–239, <https://doi.org/10.1021/acs.biomac.1c01235>.
- [53] X. Li, C. Wang, W. Zhang, Y. Li, Fabrication and characterization of porous Ti6Al4V parts for biomedical applications using electron beam melting process, *Mater. Lett.* 63 (2009) 403–405, <https://doi.org/10.1016/j.matlet.2008.10.065>.
- [54] S.Y. Choy, C.N. Sun, K.F. Leong, J. Wei, Compressive properties of Ti–6Al–4V lattice structures fabricated by selective laser melting: design, orientation and density, *Addit. Manuf.* 16 (2017) 213–224, <https://doi.org/10.1016/J.ADDMA.2017.06.012>.
- [55] S. Van Bael, Y.C. Chai, S. Truscillo, M. Moesen, G. Kerckhofs, H. Van Oosterwyck, J.-P. Kruth, J. Schrooten, The effect of pore geometry on the in vitro biological behavior of human periosteum-derived cells seeded on selective laser-melted Ti6Al4V bone scaffolds, *Acta Biomater.* 8 (2012) 2824–2834, <https://doi.org/10.1016/j.actbio.2012.04.001>.
- [56] A. du Plessis, I. Yadroitsava, I. Yadroitsev, Ti6Al4V lightweight lattice structures manufactured by laser powder bed fusion for load-bearing applications, *Opt Laser Technol.* 108 (2018) 521–528, <https://doi.org/10.1016/J.OPTLASTEC.2018.07.050>.
- [57] P. Sun, Z.Z. Fang, Y. Zhang, Y. Xia, Review of the methods for production of spherical Ti and Ti alloy powder, *JOM* 69 (2017) 1853–1860, <https://doi.org/10.1007/s11837-017-2513-5>.
- [58] D. Gu, Y.-C. Hagedorn, W. Meiners, G. Meng, R.J.S. Batista, K. Wissenbach, R. Poprawe, Densification behavior, microstructure evolution, and wear performance of selective laser melting processed commercially pure titanium, *Acta Mater.* 60 (2012) 3849–3860, <https://doi.org/10.1016/j.actamat.2012.04.006>.
- [59] J. Yang, H. Yu, J. Yin, M. Gao, Z. Wang, X. Zeng, Formation and control of martensite in Ti–6Al–4V alloy produced by selective laser melting, *Mater. Des.* 108 (2016) 308–318, <https://doi.org/10.1016/J.MATDES.2016.06.117>.
- [60] S.C. Onwubu, S. Mhlongu, P.S. Mdluli, In vitro evaluation of nanohydroxyapatite synthesized from eggshell waste in occluding dentin tubules, *J. Appl. Biomater. Funct. Mater.* 17 (2019) 228080001985176, <https://doi.org/10.1177/2280800019851764>.
- [61] R. Chang, S. Kim, S. Lee, S. Choi, M. Kim, Y. Park, Calcium carbonate precipitation for CO₂ storage and utilization: a review of the carbonate crystallization and polymorphism, *Front. Energy Res.* 5 (2017), <https://doi.org/10.3389/feng.2017.00017>.
- [62] M.E. Hoque, M. Shehryar, K.M.N. Islam, Processing and characterization of cockle shell calcium carbonate (CaCO₃) bioceramic for potential application in bone tissue engineering, *J. Mater. Sci. Eng.* 2 (2013) 4, <https://doi.org/10.4172/2169-0022.1000132>.
- [63] R. Rahmani, N. Kamboj, M. Brojan, M. Antonov, K. Gokuldoss Prashanth, Hybrid metal-ceramic biomaterials fabricated through powder bed fusion and powder metallurgy for improved impact resistance of craniofacial implants, *Materialia (Oxf)* 24 (2022) 101465, <https://doi.org/10.1016/j.mta.2022.101465>.
- [64] L. Liu, P. Kamm, F. García-Moreno, J. Banhart, D. Pasini, Elastic and failure response of imperfect three-dimensional metallic lattices: the role of geometric defects induced by Selective Laser Melting, *J. Mech. Phys. Solid.* 107 (2017) 160–184, <https://doi.org/10.1016/j.jmps.2017.07.003>.
- [65] Z. Wang, M. Xie, Y. Li, W. Zhang, C. Yang, L. Kollo, J. Eckert, K.G. Prashanth, Premature failure of an additively manufactured material, *NPJ Asia Mater.* 12 (2020) 1–10, <https://doi.org/10.1038/s41427-020-0212-0>.
- [66] G. Wang, H. Ouyang, C. Fan, Q. Guo, Z. Li, W. Yan, Z. Li, The origin of high-density dislocations in additively manufactured metals, *Mater Res Lett* 8 (2020) 283–290, <https://doi.org/10.1080/21663831.2020.1751739>.
- [67] C. Zhao, Z. Wang, D. Li, L. Kollo, Z. Luo, W. Zhang, K.G. Prashanth, Cu–Ni–Sn alloy fabricated by melt spinning and selective laser melting: a comparative study on the microstructure and formation kinetics, *J. Mater. Res. Technol.* 9 (2020) 13097–13105, <https://doi.org/10.1016/j.jmrt.2020.09.047>.
- [68] X. Huang, S. Ding, L. Lang, S. Gong, Compressive response of selective laser-melted lattice structures with different strut sizes based on theoretical, numerical and experimental approaches, *Rapid Prototyp. J.* 29 (2023) 209–217, <https://doi.org/10.1108/RPJ-12-2021-0339>.
- [69] J. Pelleg, Deformation in ceramics, in: *Mechanical Properties of Ceramics*, first ed., Springer, Cham, Switzerland, 2014, pp. 281–350, https://doi.org/10.1007/978-3-319-04492-7_4.
- [70] K.G. Prashanth, S. Scudino, M.S. Khoshkhoo, K.B. Surreddi, M. Stoica, G. Vaughan, J. Eckert, Structural and mechanical characterization of Zr58.5Ti8.2Cu14.2Ni11.4Al17.7 bulk metallic glass, *Materials* 5 (2012) 1–11, <https://doi.org/10.3390/ma5010001>.
- [71] X. Wang, S. Xu, S. Zhou, W. Xu, M. Leary, P. Choong, M. Qian, M. Brandt, Y.M. Xie, Topological design and additive manufacturing of porous metals for bone scaffolds and orthopaedic implants: a review, *Biomaterials* 83 (2016) 127–141, <https://doi.org/10.1016/J.BIOMATERIALS.2016.01.012>.
- [72] S. Baghersad, L.Y.C. Madruga, A.F. Martins, K.C. Popat, M.J. Kipper, Expanding the scope of an amphoteric condensed tannin, tanfloc, for antibacterial coatings, *J. Funct. Biomater.* 14 (2023) 554, <https://doi.org/10.3390/jfb14110554>.
- [73] J.S. Lee, S.J. Lee, S. Bin Yang, D. Lee, H. Nah, D.N. Heo, H.-J. Moon, Y.-S. Hwang, R.L. Reis, J.-H. Moon, I.K. Kwon, Facile preparation of mussel-inspired antibiotic-decorated titanium surfaces with enhanced antibacterial activity for implant applications, *Appl. Surf. Sci.* 496 (2019) 143675, <https://doi.org/10.1016/j.apsusc.2019.143675>.
- [74] L.Y.C. Madruga, R.M. Sabino, E.C.G. Santos, K.C. Popat, R. de C. Balaban, M. J. Kipper, Carboxymethyl-kappa-carrageenan: a study of biocompatibility, antioxidant and antibacterial activities, *Int. J. Biol. Macromol.* 152 (2020) 483–491, <https://doi.org/10.1016/J.IJBIOMAC.2020.02.274>.
- [75] K.J. Thomas, C.V. Rice, Revised model of calcium and magnesium binding to the bacterial cell wall, *Biomaterials* 27 (2014) 1361–1370, <https://doi.org/10.1007/s10534-014-9797-5>.
- [76] A. Nostro, L. Cellini, M. Di Giulio, M. D’Arrigo, A. Marino, A.R. Blanco, A. Favaloro, G. Cutroneo, G. Bisignano, Effect of alkaline pH on staphylococcal biofilm formation, *APMIS* 120 (2012) 733–742, <https://doi.org/10.1111/j.1600-0463.2012.02900.x>.
- [77] S.K. Shukla, T.S. Rao, Effect of calcium on Staphylococcus aureus biofilm architecture: a confocal laser scanning microscopic study, *Colloids Surf. B Biointerfaces* 103 (2013) 448–454, <https://doi.org/10.1016/j.colsurf.2012.11.003>.
- [78] J. Tan, D. Wang, H. Cao, Y. Qiao, H. Zhu, X. Liu, Effect of local alkaline microenvironment on the behaviors of bacteria and osteogenic cells, *ACS Appl. Mater. Interfaces* 10 (2018) 42018–42029, <https://doi.org/10.1021/acsami.8b15724>.

Curriculum vitae

Personal data

Name: Riddhi Hirenkumar Shukla
Date of birth: 21/08/1996
Place of birth: India
Citizenship: Indian

Contact data

E-mail: riddhishukla2108@gmail.com

Education

2021–2024 Tallinn University of Technology, PhD
2017–2019 Master’s of Engineering (Metallurgical and Materials Engineering)
2013–2017 Bachelor of Engineering (Metallurgy Engineering)
2008–2013 High school

Language competence

English: Fluent
Hindi: Fluent
Gujarati: Mother Tongue

Research Visits

1.05.2023–04.09.2023 Colorado State University, Fort Collins, Colorado, USA
24.10.2022–28.10.2022 Esslingen University, Germany (Blended Intensive Program)
15.09.2022–30.09.2022 Dalarna University, Sweden

Research Experience

July 2021 – Present Early-stage researcher – Additive Manufacturing & Powder Metallurgy, Tallinn University of Technology (TalTech), Estonia
June 2018 – November 2019 Master’s Project – Powder Metallurgy, Institute for Plasma Research, Gandhinagar, India
July 2016 – April 2017 Intern – Metallurgical Engineering, National Metallurgical Laboratory, Jamshedpur, India

Extra-curricular work

2024 Runner-up in poster presentation on the topic “My day as a PhD student, Life of a materials engineer” in doctoral conference held on May 16, 2024, at TalTech (Tallinn University of Technology, Estonian Doctoral School)
<https://www.doktorikool.ee/en/karjaarikonverents/>
June 2024 Participated in EuroTeQ Collider at Ecole Polytechnique, Paris

Public Outreach

- Useless eggshells could be used to make artificial joints!
<https://researchinestonia.eu/2024/11/13/eggshells-to-joints/>
- Useless eggshells could be used to make artificial joints
<https://taltech.ee/en/news/useless-eggshells-could-be-used-make-artificial-joints>
- Useless eggshells could be used to make artificial joints
<https://novaator.err.ee/1609483741/kasututest-munakoortest-saaks-teha-tehisliigeseid>

Elulookirjeldus

Isikuandmed

Nimi: Riddhi Hirenkumar Shukla
Sünniaeg: 21/08/1996
Sünnikoht: India
Kodakondsus: India

Kontaktandmed

E-post: riddhishukla2108@gmail.com

Hariduskäik

2021–2024 Tallinn University of Technology, PhD
2017–2019 Master's of Engineering (Metallurgical and Materials Engineering)
2013–2017 Bachelor's of Engineering (Metallurgy Engineering)
2008–2013 High school

Keelteoskus

Inglise keel: kõrgtase
Hindi keel: ladus
Gudžarati keel: emakeel

Uurimiskülastused

1.05.2023–04.09.2023 Colorado osariigi ülikool, Fort Collins, Colorado, USA
24.10.2022–28.10.2022 Esslingeni ülikool, Saksamaa (segatud intensiivprogramm)
15.09.2022–30.09.2022 Dalarna Ülikool, Rootsi

Uurimiskogemus

juuli 2021 – praegu Varajases staadiumis uurija – lisaainetes tootmine, Tallinna Tehnikaülikool (TalTech), Eesti
juuni 2018 – november 2019 Magistriprojekt – pulbermetallurgia, Plasmauringute instituut, Gandhinagar, India
juuli 2016 – aprill 2017 Intern – metallurgiatehnika, Riiklik metallurgialabor, Jamshedpur, India

Õppekavaväline töö

2024 16. mail 2024 TalTechis (Tallinna Tehnikaülikool, Eesti Doktorikool) toimunud doktoriõppe konverentsil 2024. aasta teine posterettekannet teemal "Minu päev doktorandina, materjaliinseneri elu" <https://www.doktorikool.ee/et/karjaarikonverents/>
juuni 2024 Osalesin EuroTeQ Collideris Ecole Polytechnique'is Pariisis

Ühiskondlik panus

- Useless eggshells could be used to make artificial joints!
<https://researchinestonia.eu/2024/11/13/eggshells-to-joints/>
- Useless eggshells could be used to make artificial joints
<https://taltech.ee/en/news/useless-eggshells-could-be-used-make-artificial-joints>
- Useless eggshells could be used to make artificial joints
<https://novaator.err.ee/1609483741/kasutatutest-munakoortest-saaks-teha-tehisliigeseid>

ISSN 2585-6901 (PDF)
ISBN 978-9916-80-256-4 (PDF)